INVESTIGATION OF DRIVING MECHANISMS OF COMBUSTION INSTABILITIES IN LIQUID ROCKET ENGINES VIA THE DYNAMIC MODE DECOMPOSITION

A Thesis
Presented to
The Academic Faculty

by

John Mathew Quinlan

In Partial Fulfillment
of the Requirements for the Degree
Doctor of Philosophy in the
Guggenheim School of Aerospace Engineering

Georgia Institute of Technology
December 2015

INVESTIGATION OF DRIVING MECHANISMS OF COMBUSTION INSTABILITIES IN LIQUID ROCKET ENGINES VIA THE DYNAMIC MODE DECOMPOSITION

Approved by:

Ben T. Zinn, Advisor
Guggenheim School of Aerospace Engineering
Georgia Institute of Technology

Luca Dieci
School of Mathematics
Georgia Institute of Technology

Tim Lieuwen
Guggenheim School of Aerospace Engineering
Georgia Institute of Technology

Suresh Menon
Guggenheim School of Aerospace Engineering
Georgia Institute of Technology

Jerry M. Seitzman
Guggenheim School of Aerospace Engineering
Georgia Institute of Technology

Date Approved: August 10, 2015

To Professor Charles E. Mitchell—for with out his passion for combustion instabilities, I would not have found mine

and

To my parents—who made all of this possible with their support

and

To my wife, Laura and my kid(s), Gray. . . —for whom makes all of this worth the effort

Acknowledgments

To begin with, I must apologize for the length of the Acknowledgments—at least to the people near the end—but when you have been around as long as I have, there are a lot of people to thank. I will be forever in debt to many people who helped me during graduate school, both at Georgia Tech and at Colorado State. To begin, I must thank my advisors. First, I would like to thank the late Professor Charles E. Mitchell for starting me down this path. When I returned to Colorado State for my master's, he unknowingly set me on my current course with the simple question and a smile: "Have you ever heard of combustion instabilities?" After Professor Mitchell's passing, Professor Allen T. Kirkpatrick bravely took on the task of shepherding Dan Milano and I through the completion of our project and master's degrees. Similarly, while searching for a place to continue my education, Professor Ben T. Zinn (a former Princeton lab mate of Professor Mitchell, where they were both students of Professor Luigi Crocco) generously welcomed me into his group. Professor Zinn has supported my headlong dive into this and other work, including giving me enough time to deeply think and try new approaches. In addition, he has provided me with innumerable opportunities. I would also like to thank each of my committee members. Without the help of Professor Luca Dieci this work would not have been possible. His mathematical guidance was invaluable and his graciousness and humbleness unbounded (avoidable pun). Next, I must thank Professor Tim Lieuwen for his insightful questions and wealth of knowledge on hydrodynamics and combustion instabilities. It has also been invaluable to see how Professor Lieuwen's group is organized and functions as I move forward in academe. I would like to thank Professor Suresh Menon for graciously agreeing to serve on my committee and providing valuable insight into our problem. The final committee member to thank, Professor Jerry Seitzman, must be thanked for a wide range of items. Of course, I am thankful for his probing question into the heart of this work and his ever shaking or nodding head. Moreover, his passion for teaching is a gift to all of his students and deserves to be emulated. I owe gratitude to the Aerospace Engineering department head, Professor Vigor Yang for his support. I must also thank the plethora of teachers I have had both in university and in my formative years. For example, Professors Paul Heyliger (whom, I hope, I did not embarrass since leaving CSU), Paul

Wilbur, Dan Olsen, and Donald Radford (without whom I would have likely never made it into graduate school), while at Colorado State, prepared me for what lied ahead. And, I owe all of my math and science teachers, but, especially, Mrs. Rhea Pearlman who knew more about what I was made of when I was 17 than I did for many more years.

In addition to committee members and teachers, I must thank the generous support, financial and otherwise, from the Air Force Office of Scientific Research and contract monitor Dr. Mitat Birkan, NASA-Marshall and contract monitor Dr. Jeremy Kenny, and Pratt&Whitney-Rocketdyne/ Aerojet-Rocketdyne and Tim Hinerman.

Since coming to Georgia Tech, I have been fortunate to meet and closely interact with a large number of wonderful people. From that first day in the lab, James Cornacchio, one of the nicest guys I have ever met, made me feel right at home and he became a fast friend. I owe a huge amount of gratitude, and a ski vacation (not all inclusive), to Ben Wilde. Without Ben's influence and help, this work would not have been possible. Not only is he an incredibly talented scientist, his writing is superb—it is not fair to the rest of us mortals. You could not ask for a better officemate than Chris Foley. He must be thanked for always being a sounding board and supportive shoulder—but, more importantly—for being my partner in shenanigans and *Mo Bro*. I must thank all of the students that I have worked on projects with, including Yong Jea Kim, Martina Baroncelli (and for teaching us how to make tiramisu), Alex Damião, Ciprian Dumitrache and a number of undergraduate students. I learned a great deal through our interactions. For all of their help with and discussions about the diagnostics applied within this work, I am grateful for having Sasha Bibik and Ianko Chterev as resources. Next, are three people who are each brilliant and who I have learned so much from our deep discussions. First, I do not know anyone who has a better understanding of acoustics than David Scarborough. In addition, he has a truly unbelievable talent for viewing complex problems in a creative and simple manner—and with amazing results. Second, Ben Emerson is a incredibly talented scientist and one of the hardest workers I have ever met. Third, much of my knowledge of modern computing (rather than my old school FORTRAN 77) comes from my discussions with Matthew Clay. I am also grateful for the help of other research engineers around the lab, specifically, Bobby Nobel, Eugene Lubarsky, Bradley Ochs, Chris Ballance, and Shane Getchell. I will never forget my years sitting next to Jackie Crawford, III. Next, I must thank the members of our weekly

trivia team, including the afore mentioned Chris Foley, our lab's only Husband/Wife couple Brandon Sforzo (straordinario pizzaiolo) and Gina Magnotti, Dr. Rachel Geller and Rev. Andy Balicki, Ben and Nicole Knox, Sara Fort, Maggie McDonald, Marcin Morys, Chris Valenta, Katie Zach, and Metin Ozcan, and the *old guard* Kim, Josh, Brittany, Alison. During the last few years I have had the pleasure of sharing an office with a number of students, including Prabhakar Venkateswaran (a.k.a., Freddie Mercury or the Hulk—I miss hearing his laughter around the lab), Andrew Marshall (whose mass I obviously misjudged), and Aimee Williams (and her yummy confections). All of us in the lab have missed our lab *Mom*, Jackie O'Connor, over the last few years. For his guidance and help during this process I need to thank Professor Jeff Jagoda. From the administrative side of the Aerospace Department I would like thank Tiwanna Williams, Glenda Duncan, and Nelson Silverio. In addition, I am appreciative of the Aerospace Engineering machinists Scott Elliot, Scott Moseley, and Red Russell and their willingness to help me and all of the students in the lab. Also from Georgia Tech, I would like to thank all those whom I studied for *quals* and courses with and other interesting lab characters, including John Bennewitz, Daniel Foti, Nishant Jain, Caleb Cross, Mike Miles, Sean Dubsky, Jordan Blimbaum, Michael Aguilar, Anna Hotle , Danny Bloomer, Arun Radhakrishnan, Ryan Sullivan, David Wu, Michael Malanoski, Nick Magina, and Julia Lundrigan.

From my years at Colorado State and for years after, a number of other people influenced me significantly, namely, Jon Carter, Marty Malenshek, Justin Lisowski (and his imaginary wife Katie), and Veta Mitchell.

And, before that, I learned a great deal about being a practicing engineer from countless colleagues at Sturman Industries. Resorting to a list, Chris Cole (for taking a chance on me), Dan Giordano, Chad Jensen, Marc Wolverton (for summiting Mount Rainier with me), Guy Babbit (for having many a long night with me), Adam Mitchener (for being a dedicated friend), brewing instructors Larry Chaney, Keith Knoll, and Jeff Rogers, Khurshid Mirza (Rogers), Todd Barnet, Bob Pearson, Randal Strauss, Tibor Kiss, Chris Turner, Travis Johnson, Miguel Raimao, Dave Drury, Dave Saxon, Eric Cefus, Brian Cummings, Jeff Stewart, Bill Erickson, Jim Peña, Patrick Doyle, Evie Vance, Bruce Johnson, Jeff Gardner, Fredrik Bengtsson, Warren Salt, John Malik, Charles Klose, Eric Drummond, Carol and Eddie Sturman, and Tim Kranz. In addition, from International Truck and Engine, I will always remember my hours spent with Russ Zukouski.

Reaching even further back, I learned a great deal about engineering and working as a team (and how to do all of that on little to no sleep) from Fred Basin, John Beshears, Tavin Dille, Will Francis, Chris Ladd, Tom Urbanek, and Lucas Weidner. Also, I must thank a father/son team for teaching me about machining, losing at softball, and keeping it shiny side up, Keith Senkow Sr. and Keith Senkow Jr. I learned a lot of intuition about good engineering while working with Hank Hayes—and how to build a awesome Chevy 350 in the kitchen. Mark Buckland has been a great friend who is always up for an adventure and we have tried to show him a good time when he shows up in Atlanta. One of the most supportive friend we have had through the years—and our personal vet when needed—is Sadie (Mercedes) Maybach. I would be remiss to not mention my high school locker mate (and dear friend), Kevin Szepe. He taught me many things over the years, including how to eat a piece of cheese cake with ones jaw wired shut and how to aim high.

Turning to my family, I must thank my entire family for their encouragement throughout this process and the knowledge that I have gained from each of them over the years. I could never forget to mention my sisters, Tia and Lalenia. You could not ask for two better big sisters growing up—even if they dressed me up in a tutu. While I beat Tia to the doctorate, she became a Professor before me. Lalenia has been ever supportive and her advice over the last year has been especially helpful. My view into academe was at least partially defined by my cousin Dr. Dr. Shelley McDonald (Ph.D./M.D.), it has been a pleasure getting to know her. Next, I must thank my parents for—basically—everything. From my Mom, Sue, I learned not to take yourself too seriously and to ignore others who do, to have fun, and the difference between good art and *bad* art. From my Dad, John (one of many Johns in the family—obviously), I learned work ethic, how to build anything, lawn maintenance, and above all—how to use my brain. I need to thank my late grandmother, Lottie Guthrie, for supporting my budding engineer ways, who, when I helped her with something, paid me with a screwdriver—with which I undoubtedly used to take things apart around the house. I should also thank her for the clan tartan—or, at least I should thank my late grandfather, John Guthrie (yes, another one) for the clan name. For much of my graduate career, our dog Magnus kept me company while studying—she is greatly missed.

I am so lucky to have an amazing son, (John) Gray, with whom to share the last year of my thesis work. He helped shred any drafts returned from Professor Zinn, hopefully, after they were no

longer needed. I am also thankful for any future sons or daughters that find there way into our home, although, I can't specifically name them yet.

Finally, the most important thanks goes to Laura, my wife, who has supported me in every way through the last 20 years. Without her continued support, words of encouragement, flexibility, understanding, toughness, love, and patience throughout this process I would have been unable to pursue my doctorate degree. I am fortunate to be her *Papa Bear*; she is my best friend.

J. Matt Quinlan

Grand Lake, Colorado

July 5th, 2015

TABLE OF CONTENTS

LIST OF TABLES

LIST OF FIGURES

NOMENCLATURE

LRE	Liquid Rocket Engine.
1T	First tangential mode.
1W	First full cycle widthwise mode.
CI	Combustion Instability.
DMD	Dynamic Mode Decomposition.
DOF	Degrees of Freedom.
EFD	Ensemble Floquet Decomposition.
FD	Floquet Decomposition.
FFT	Fast Fourier Transform.
FWHM	Full-Width Half-Max.
LIF	Laser Induced Fluorescence.
ODE	Ordinary Differential Equation.
PDF	Probability Density Function.
PIV	Particle Image Velocimetry.
PLIF	Planar Laser Induced Fluorescence.
POD	Proper Orthogonal Decomposition.
PSD	Power Spectral Density.
SDD	Simultaneous Dynamic Decomposition.
SIAR	Single Injector Acoustic Rig.
SVD	Singular Value Decomposition.

Variables and symbols

$\boldsymbol{a}$	Coefficient vector.
A	Evolution operator or finite dimensional approximation of the Koopman operator.
a_i	i^{th} coefficient.
a_j	j^{th} Galerkin coefficient.
AU	Arbitrary units.
B	Invertible constant Floquet stability matrix or system forcing matrix [N].

$\boldsymbol{c}$	DMD modal coefficients.
C	Damping coefficient matrix [N s/m].
c	Speed of sound [m/s].
$\boldsymbol{d}$	Generalized state space forcing vector.
$\hat{\boldsymbol{e}}_i$	Unit vector in the i^{th} direction.
E	Energy-like L^2 norm of the state vector.
$\tilde{f}$	Acoustic frequency [Hz].
$\boldsymbol{f}$	Force vector [N].
$f(t)$	Periodic function of time.
$f(u_h')$	Hydrodynamic/combustion to acoustic subsystem coupling function.
G	Compact heat release matrix.
g	Gravitational acceleration constant [m/s^2].
$g(p')$	Acoustic to hydrodynamic/combustion subsystem coupling function.
I	Identity matrix.
K	Stiffness coefficient matrix [N/m].
L_1	Left length of SIAR rig [m].
L_2	Right length of SIAR rig [m].
$\dot{m}$	Mass flow rate [g/s].
$\tilde{M}$	Black diagonal, repeated monodromy matrix.
M	Monodromy matrix, evolution operator, or mass coefficient matrix [N].
m	Mass [kg] or number of rows in a matrix.
n	Number of columns in a matrix.
N	Complex combustion response, number of time intervals, or noise matrix.
N_p	Complex combustion response or periodic function associated with acoustic pressure.
N_u	Complex combustion response or periodic function associated with acoustic velocity.
N_ϕ	Complex combustion response or periodic function associated with equivalence ratio.
$\bar{\mathcal{P}}$	Mean pressure [Pa].
$\mathcal{P}$	Poincaré map.

P	Rank of matrix $\tilde{S}$.
p'	Acoustic pressure [Pa].
$P(t)$	τ-periodic matrix function.
$\dot{q}'$	Oscillatory heat release [kJ/kg s].
$\boldsymbol{q}$	Generalized state space coordinates.
Q	Orthogonal matrix.
$\boldsymbol{r}$	Residual vector.
R	Upper triangular matrix or specific gas constant.
r	Rank of pseudoinverse or number of measurements within one period.
$\tilde{S}$	DMD matrix.
S	Companion matrix or swirl number.
SF	SDD data component scale factor.
Δt	Time step [s] or PIV shot time offset [s].
T	Temperature [K] or System coefficient matrix.
t	Time [s].
$\bar{U}$	Mean velocity [m/s].
$\boldsymbol{u}_k$	DMD uncoupled coordinate vector for the k^{th} time step—normal coordinates.
U	Left singular vector matrix.
u	Solution variable.
u'	Acoustic velocity [m/s].
$\boldsymbol{v}_k$	Data snapshot at k^{th} time step.
V	Data matrix/Krylov sequence.
W	Right singular vector matrix.
$\Delta \boldsymbol{x}$	PIV displacement vector [m].
$\boldsymbol{x}$	Solution or state vector.
X	Mole fraction [-].
x	Transverse direction [mm] or Displacement [m].
y	Injection direction [mm].

Z_L	Left eigenvector matrix.
Z_R	Right eigenvector matrix.
$\bar{(\cdot)}$	Temporal mean.
$\dot{(\cdot)}$	Differentiation with respect to time.
Im	Imaginary part of complex number.
Re	Real part of complex number.
$\mathcal{G}$	Observation operator.
$\mathcal{K}$	Koopman operator.
$\mathcal{LR}_j$	Local Rayleigh index for mode j.
$\mathcal{N}$	Nonlinear acoustic operator.
$\mathcal{R}_j$	Rayleigh index for SDD mode j.
$\mathcal{RI}_j$	Rayleigh integral for mode j.
$\mathcal{SI}_j$	Spatially integrated Rayleigh index for mode j.
$\mathcal{T}$	Time-stepping operator.

Greek

α	Arbitrary constant.
β	Heat kernel scale factor or arbitrary constant.
γ	Ratio of specific heats.
ϵ	Parametric term scale factor.
η_i	i^{th} Floquet multiplier.
κ	Coefficient of stiffness [N/m].
Λ	Diagonal Ritz value matrix.
λ	Complex Ritz value.
μ	Eigenvalue of Floquet multiplier.
ν	Coefficient of damping [N s/m].
Ω	Diagonal eigenvalue matrix.
ϕ	Right eigenvectors of $\tilde{S}$.
ϕ'	Oscillatory equivalence ratio.

$\tilde{\phi}$	Left eigenvectors of $\tilde{S}$.
ψ	Eigenvectors of A.
ρ	Floquet exponents.
$\bar{\rho}$	Average density [kg/m^3].
Σ	Diagonal singular value matrix.
σ	Singular values.
τ	Time delay [s].
ϕ_j	j^{th} Galerkin basis function or Floquet multiplier.
ϕ^+	Positive frequency real Floquet mode.
ϕ^-	Negative frequency real Floquet mode.
Φ	Matrix solution.
ω	Complex angular frequency [rad/s].
$\tilde{\omega}$	Natural acoustic angular frequency [rad/s].

Superscripts

-1	Inverse or Moore-Penrose pseudoinverse.
H	Hermitian.
T	Transpose.
$*$	Complex Conjugate.

Subscripts

i	i^{th} index.
j	j^{th} index.
k	Time step k.
ac	Acoustic.
chemi	Chemiluminescence.
$hydro$	Hydrodynamic.
N	Total number of snapshots.
p	With respect to acoustic pressure.
ϕ	With respect to equivalence ratio.

u	With respect to acoustic velocity.
0	Initial condition.
∞	With respect to far field.

SUMMARY

Combustion instability due to feedback coupling between unsteady heat release and natural acoustic modes can cause catastrophic failure in rocket engines. Predicting the onset of combustion instability in practical devices requires understanding the interaction between the fluid flow, chemical reactions, and the acoustic field. Researchers have studied combustion instabilities both experimentally and analytically since the 1950's. Based on this work, linear and nonlinear models have been proposed, and strategies to mitigate combustion instabilities have been developed and successfully demonstrated in certain applications. Many important questions remain unresolved even today, however, due to the high cost of testing, the limited diagnostic access inside practical devices, and the inability of existing data analysis techniques to fully explain the coupling mechanisms that drive combustion instability. Given these limitations, the primary objective of this study was to develop techniques to elucidate specific combustion instability driving mechanisms through development of experimental facilities and methods for processing data collected using modern time-resolved diagnostics.

The first part of this work focused on the development of a laboratory-scale facility that could be used to study full-scale like combustion instabilities while maintaining the correct acoustic frequencies and the correct transverse orientation of the acoustic field with respect to the the mean flow direction. In addition, the developed experimental facility needed to be highly accessible for diagnostic measurements, allowing the acquisition of simultaneous high-speed data to characterize the swirling, reacting flow and acoustic field. The developed rig exhibited a transverse combustion instability near 170 Hz for one length configuration of the acoustic duct and high-speed (10 kHz), simultaneously acquired data was taken. The specific diagnostics measurements applied were: particle image velocimetry to find the flow velocities in a plane through the centerline of the injector; planar laser induced fluorescence of the OH combustion radical to locate the reaction zone and combustion products on the same plane; chemiluminescence of the CH^* combustion radical as a

qualitative, line-of-sight heat release indicator; and, dynamic pressure measurements to characterize the acoustic field within the combustor.

The second part of this work focused on the development of an approach to analyze the simultaneous diagnostic data for extracting coupled modes/physical phenomena using the newly developed dynamic mode decomposition algorithm. By applying this method, the simultaneous dynamic decomposition, to the simultaneous particle image velocimetry, planar laser induced fluorescence, chemiluminescence, and dynamic pressure data for the unstable experiment dataset it was found that the reaction zone oscillations were closely coupled with the inner shear layer dynamics. Furthermore, it was found that there was a nearly neutrally stable, annular or helical hydrodynamic mode at 1017 Hz, which had large acoustic amplitude and a negative or stable Rayleigh criterion. Rather than being driven by the combustion heat release, this mode is likely driven by the high-speed fluid flow. On the other hand, this technique was unable to locate the acoustically observed, combustion instability near 170 Hz. This shortcoming led us to hypothesize that the governing physics were not well described by a constant evolution operator, as prescribed by the dynamic mode decomposition method. Physically, this result suggests that the often assumed—and sometimes successful—constant linear relationship between heat release and either the acoustic pressure or acoustic velocity is unrealistic in some combustors.

The final part of this work focused on the extension of the dynamic mode decomposition to systems whose governing equations vary with time. With this aim in mind, rather than requiring the governing evolution operator to be constant, we developed a new approach for analyzing data where the operator was allowed to be periodic in time. This goal was accomplished by combining the theory for time-periodic, linear systems of equations, Floquet theory, with mathematical manipulations similar to those of the dynamic mode decomposition. As a result, we were able to develop a technique, the Floquet decomposition, to approximate from experimental data the largest moduli Floquet multipliers, which determine the stability of the periodic solution trajectory of the system. The unstable experiment dataset was studied with this technique and with an estimated time period of 1 ms. In these results, again, no modes were located near the 170 Hz observed combustion instability having a large acoustic amplitude. This led to the further development of an ensemble average version of the time-periodic operator analysis technique, the ensemble Floquet decomposition. This analysis

technique combines the sampled data from different phases of the operator's period into larger data vectors allowing improved approximations of the largest magnitude Floquet multipliers. Then, it proceeds similarly to the Floquet decomposition algorithm to calculate the approximate Floquet multipliers and their associated modes. Next, the method separates the large, composite modes and phase corrects the differently phased modal components. Finally, the phase corrected components are averaged to yield improved spatial mode structures. The unstable experiment dataset was analyzed with this technique and the analysis found a nearly neutrally stable mode with frequency of 169.6 Hz, which also had a large acoustic amplitude. Furthermore, the approximate Rayleigh criterion indicated that this mode was unstable with respect to combustion instability.

Overall, based on the positive findings that the ensemble Floquet decomposition was able to locate an unstable combustion mode at 170 Hz when the operator's periodic frequency was set to 1000 Hz, we believe that the 1017 Hz mode parametrically forces the 170 Hz mode, resulting in what could be characterized as a parametric combustion instability.

CHAPTER I

INTRODUCTION

This research investigates new approaches for studying, in a laboratory environment, the mechanisms that drive transverse, acoustically coupled combustion instabilities (CIs). For decades, CIs have hindered the development and operation of propulsion systems, power generation systems, and energy intensive industrial processes. These CIs manifest themselves as large amplitude oscillations of one or more natural acoustic modes of the combustor and are driven by feedback processes that couple combustion heat release oscillations with the excited acoustic mode oscillations. Generally, these heat release fluctuations are associated with fluid dynamic and thermodynamic property oscillations, e.g., pressure, velocity, and equivalence ratio oscillations, see Fig. 1. While the initial perturbations of these properties might be small, the oscillations grow when the system becomes unstable. This growth continues until the oscillations attain a constant amplitude, called a limit cycle, when the energy supplied to the oscillations during a cycle equals the energy dissipated per cycle by the damping processes. An example of these large amplitude CI waves is shown in Fig. 2a, where the amplitude of the oscillation is approximately 10 MPa (1450 psi) peak to peak. Large amplitude oscillations shorten hardware life and can cause catastrophic failure, see Fig. 2b.

In an attempt to prevent CIs through the interruption of the feedback mechanisms or by increasing the system damping, the driving and damping of CIs have been studied both analytically and experimentally since the 1950's. Many of the early studies of driving mechanisms were performed

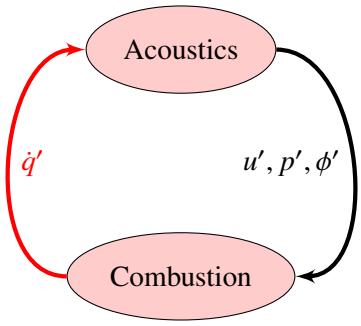

Figure 1: CI feedback cycle

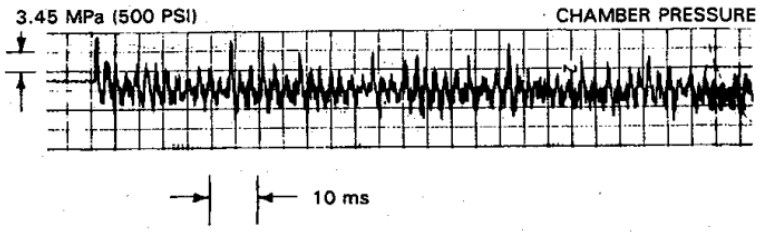

(a) Typical pressure time history for F-1 engine exhibiting high-amplitude CI [2]

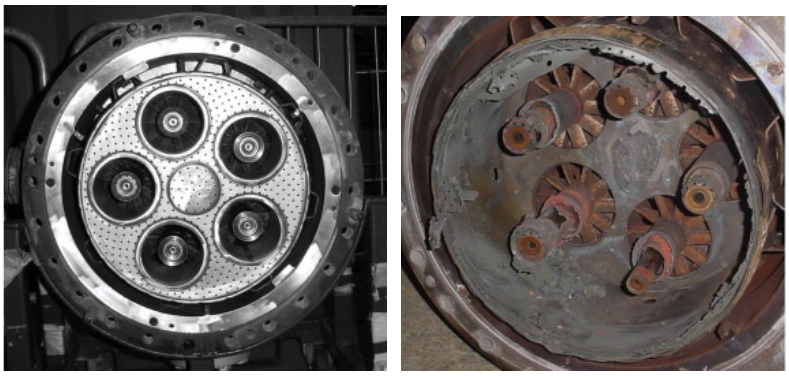

(b) Damage to gas turbine burner due to uncontrolled CI [3]

Figure 2: Typical high-amplitude CI

by the Liquid Rocket Engine (LRE) community and are documented by Crocco and Cheng [4] and in the NASA publication SP-194 [5]. More recent work on LRE CI is found in a compiled volume by Yang and Anderson [6] and details of many developments from the Russian community are given by Natanzon [7]. In addition, a recent review paper discusses the work to connect acoustics, hydrodynamics, and flame response in transverse CIs [8]. While we have amassed a fair amount of heuristic knowledge about acoustically coupled CIs, many of the details remain unknown.

A key difficulty in developing a better understanding of CIs is identifying the feedback pathways that link the flow and thermodynamical property oscillations to the oscillatory heat release. This requires that the instability be investigated under operating conditions similar to those encountered in full-scale engines. These conditions are difficult to achieve in practice because operating a full-scale LRE or gas turbine is expensive and the ability to perform needed diagnostics is very limited. Therefore, most studies of the CI driving mechanisms have been performed in sub-scale rigs. These small rigs are, however, unable to simulate the full-scale CI driving physics because of their inability to simulate the frequencies and overall acoustic environment of full-scale CIs. As a result, a new technique for designing laboratory-scale rigs is needed.

In addition, most previous studies were performed before the widespread use of high-speed imaging and laser based diagnostic techniques. As a result, very little is known about the detailed fluid dynamic and combustion processes involved in CIs. Now, these modern high-speed diagnostic techniques can be applied to optically accessible combustors to probe the reacting flow field for velocities and reaction rates, which allow us to study the coupling between pressure, velocity, and combustion heat release oscillations.

With the advent of modern diagnostic techniques has come the development of advanced data analysis techniques. In part, these developed analysis techniques have been born from the massive quantity of data generated by high-speed imaging and large-scale simulations. In the study of CIs, to find the coupling mechanisms from the large amounts of high-speed diagnostics data (many gigabytes of data are generated per second of testing), these data must be analyzed and *reduced* to find the portion of the data that represents the phenomena of interest.

Therefore, we have identified the proper sub-scale testing, use of modern diagnostics, and use of advanced data analysis techniques as three enabling technologies for the study of CIs. Specifically, to elucidate the fundamental processes that drive CIs in LRE, we apply modern diagnostic and data analysis techniques to measure and analyze data from an optically accessible, small-scale combustor that exhibits full-scale-like transverse CIs.

With this aim in mind, we designed and built an optically accessible, small-scale rig that simulates the conditions found in unstable, full-scale engines. Next, we used modern high-speed diagnostic techniques to probe the reacting flow field under different operation conditions. Finally, the experimentally acquired data was analyzed using the recently developed dynamic mode decomposition (DMD) [9] and a number of techniques based on the DMD to study the CI driving mechanism found in the small-scale rig.

* * *

Returning to the proper simulation of full-scale CIs in sub-scale facilities in more detail, a scale comparison between the size of a full-scale LRE and small-scale simulator is schematically shown in Fig. 3. In this figure the full-scale and sub-scale facilities are the Rocketdyne F-1 engine [2] and a NASA 40 element rig [10], respectively. The F-1 has a diameter of 1 m, about 7 times the diameter

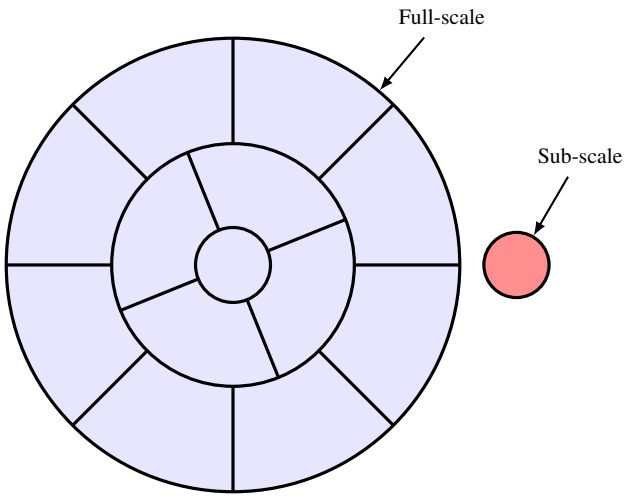

Figure 3: Scaled LRE sizes, full-scale: Rocketdyne F-1 (blue) and sub-scale: NASA 40 element (red)

of the 40 element rig (0.144 m), a large ratio in spite of the fact that the latter is a relatively large sub-scale engine. This sub-scale engine exhibits a first-tangential (1T) acoustic CI at 5080 Hz [11], which is far removed from the 440–540 Hz CI excited in the F-1 LRE [2]. The large discrepancy in the CI frequency experienced in these rigs highlights the need to develop methods that would allow us to simulate the acoustic conditions of full-scale engines in small-scale rigs.

In addition to replicating the correct frequency in a sub-scale rig, it is particularly important to simulate the full-scale acoustic pressure and velocity fields in the vicinity of the injectors where the propellant injection and mixing processes are especially sensitive to acoustic oscillations [5, 12]. While the pressure field near an injector is similar for both axial and transverse acoustic oscillations, the acoustic velocities differ substantially. In the case of axial CI, the acoustic velocity near the injector plate is essentially zero because of the high axial acoustic impedance boundary condition at the injector plate. In contrast, in the case of transverse CI, the direction of the acoustic velocities near the injector plate are perpendicular to the mean flow direction and may vary in magnitude from one location to another (from velocity node to velocity anti-node), thus exposing different injectors to different transverse acoustic velocities. There is evidence that these transverse acoustic velocity oscillations perturb the reactant injection and mixing processes and may, thus, strongly affect the mechanism that drives the CI.

This study presents an approach that overcomes typical sub-scale rig limitations and enables investigation of transverse CIs in a laboratory environment. The approach discussed in this research

is applicable to a wide range of combustion systems, but focuses specifically on instabilities in large-scale LREs, which are particularly susceptible to detrimental, transverse CIs.

Figure 4a shows schematically how a small-scale rig could simulate the transverse acoustic environment of a full-scale engine. The light blue circle represents a transverse cross-section of a full-scale LRE experiencing a 1T CI whose acoustic pressure anti-nodes (+ and −) are located at the top and bottom of the cross-section and the direction of the acoustic velocity field inside the chamber is shown as arrows parallel to the acoustic motion. The red portion of Fig. 4a represents a rectangular

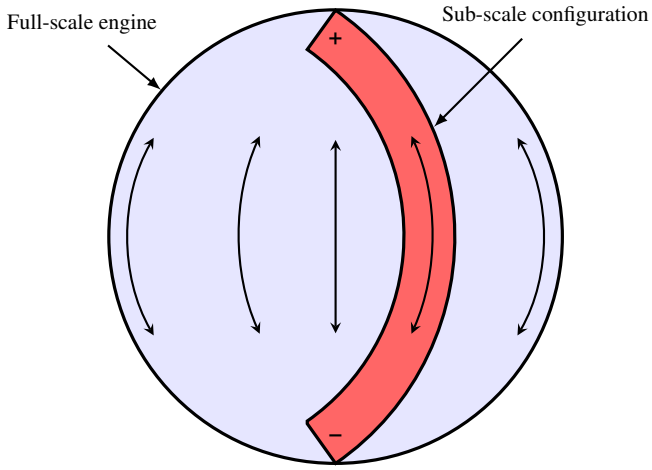

(a) Full-scale transverse acoustic emulation

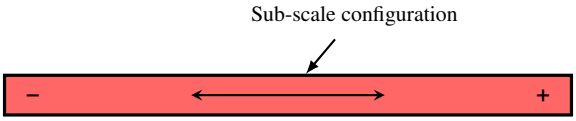

(b) Sub-scale configuration with proper acoustic frequency and wave alignment

Figure 4: Full-scale engine vs. sub-scale concept, full-scale (light blue), sub-scale (red)

arc section of the full-scale LRE that experiences acoustic velocity oscillations that are directed along its curved axis and has acoustic pressure anti-nodes at both ends. Assuming that the arc width is small compared with the chamber diameter, the acoustic oscillations along the axis would appear to be nearly one dimensional. *Extracting* this arc from the full-scale LRE and *straightening* it yields the configuration shown in Fig. 4b. This simplified configuration could serve as a small-scale rig for the study of a full-scale CI because it provides the proper orientation between the acoustic velocity and the mean flow directions while maintaining the correct oscillatory frequency. This concept forms the basis for the small-scale rig that was developed and used in this study. The developed small-scale rig is shown in Fig. 5 and additional details about the rig are presented in the following chapter.

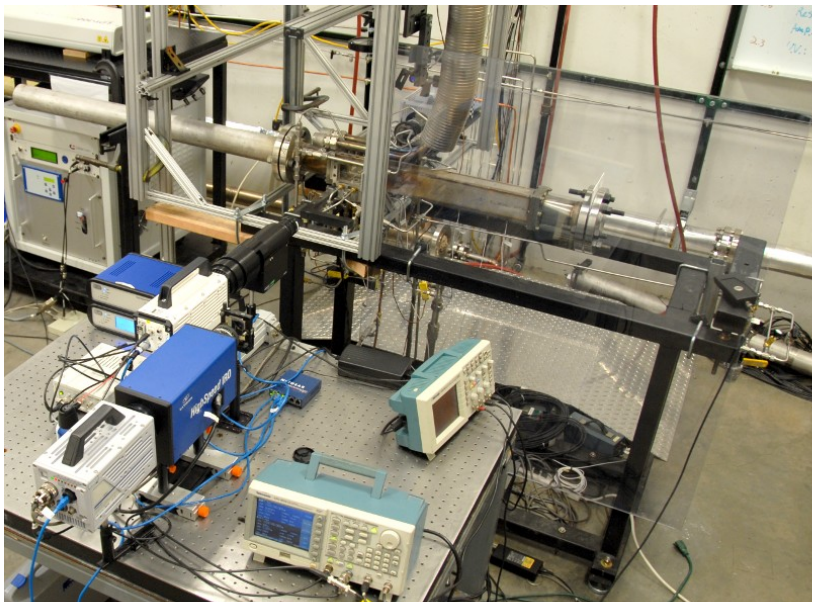

Figure 5: Experimental facility

Small-scale rigs must also provide capabilities for using modern diagnostic techniques, e.g., particle image velocimetry (PIV), planar laser induced fluorescence (PLIF), chemiluminescence, and dynamic pressure measurements, to obtain spatial and temporal descriptions of the reacting flow. These data can be processed using data analysis techniques to further the understanding of the mechanisms that drive CIs. In addition to processing data with common techniques, the diagnostic data will be analyzed using the DMD method. The DMD will be used in this study because it can highlight important phenomena/processes as shown by the work of Schmid, Violato, and Scarano [13]; others have begun using the DMD to study reacting flows [14].

Specifically, to demonstrate the suitability of the DMD method for studying CIs we can compare the DMD algorithm foundation to a common CI model equation. We will show in Section 3.1 that the DMD method approximates the most unstable eigenvalues and associated eigenvectors of the evolution operator or matrix, A, for systems taking the form:

$$\boldsymbol{v}_{k+1} = A\boldsymbol{v}_k, \tag{1}$$

where $\boldsymbol{v}_k$ is the k^{th} measurement vector, or, snapshot, of the system.

Additionally, we will show in Section 5.1 that the CI problem may be written as an inhomogeneous wave equation for the acoustic pressure, driven by the rate of unsteady heat release:

$$\frac{\partial}{\partial x}\left(c^2\frac{\partial p'}{\partial x}\right) - \frac{\partial^2 p'}{\partial t^2} = -(\gamma - 1)\,\bar{\rho}\frac{\partial \dot{q}'}{\partial t}. \tag{2}$$

In Eq. (2), the heat release term must be modeled due to its complex dependence on many state variables and parameters. For example, this term may be modeled by assuming that the oscillatory heat release is proportional to the oscillatory velocity, $\dot{q}' \propto u'$:

$$\frac{\partial}{\partial x}\left(c^2\frac{\partial p'}{\partial x}\right) - \frac{\partial^2 p'}{\partial t^2} = -(\gamma - 1)\,\bar{\rho} N_u \frac{\partial u'}{\partial t}, \tag{3}$$

where N_u is the proportionality constant. If we rewrite $\frac{\partial \dot{u}'}{\partial t}$ in terms of p' using conservation of momentum and expand the acoustic pressure spatially into a Galerkin mode expansion [15, 16], then Eq. (3) can be written in terms of the Galerkin mode coefficients, $\boldsymbol{a}$, as:

$$\ddot{\boldsymbol{a}} + \tilde{M}\boldsymbol{a} = 0. \tag{4}$$

Furthermore, Eq. (4) can be rewritten as a first order system of equations by defining the state vector as $\boldsymbol{x} \equiv [\boldsymbol{a} \quad \dot{\boldsymbol{a}}]^T$, yielding:

$$\dot{\boldsymbol{x}} = M\boldsymbol{x}, \tag{5}$$

where the evolution operator is:

$$M = \begin{bmatrix} \mathbf{0} & I \\ -\tilde{M} & \mathbf{0} \end{bmatrix}. \tag{6}$$

Equation (5) represents the dynamical systems of equation form of the governing equations, a viewpoint recently taken by a number of authors to study CIs [17–23].

The general solution to Eq. (5), from the initial conditions $\boldsymbol{x}_0$ is:

$$\boldsymbol{x}_k = \boldsymbol{x}(t_k) = e^{Mk\Delta t}\boldsymbol{x}_0 = \left(\prod_k e^{M\Delta t}\right)\boldsymbol{x}_0. \tag{7}$$

By considering a single small time step, Δt, from an *initial* condition of $\boldsymbol{x}_k$, Eq. (7) is:

$$\boldsymbol{x}_{k+1} = e^{M\Delta t}\boldsymbol{x}_k, \tag{8}$$

which has nearly the same form as Eq. (1).

If the measurements taken from the system governed by Eq. (8) evolve in a similar fashion, i.e., $A \equiv \mathcal{G}\left(e^{M\Delta t}\right)$, where $\mathcal{G}$ is some measurement operator:

$$\boldsymbol{v}_{k+1} = A\boldsymbol{v}_k, \tag{9}$$

then we see Eq. (9) is in exactly the form as Eq. (1), as desired. The DMD can, therefore, approximate the most unstable eigenvalues and eigenvectors of the measurement evolution operator, A, as will be shown in Chapter 3. These modes are related, through $\mathcal{G}$, to the eigenvalues and eigenvectors of $e^{M\Delta t}$. For example, if the state vector of a system is completely measurable, i.e., $\mathcal{G} = I$, the identify operator, then the DMD directly approximates the eigenvalues and eigenvectors of the governing evolution operator, $e^{M\Delta t}$. Owing to the fact that our model CI problem can be manipulated into a form suitable for analysis with the DMD, to elucidate the physical modes responsible for the experimentally observed CI, we used the DMD method to process the high-speed, simultaneously acquired data from the unstable combustor.

The initial aim of this work was to explore whether the DMD analysis could locate these fundamental modes. In pursuing this aim, in Chapter 4, we unexpectedly discovered that the DMD was incapable of locating the desired modes from our experimental data. This led us to hypothesize that the operator governing the system was, in fact, not constant. Rather, we modified our assumption, allowing the measurement's evolution operator to be periodic in time. We will demonstrate in Chapter 5 why we might expect the CI governing system of equations to behave periodically. With this modified assumption in mind, we were able to develop a new data analysis technique. This new approach—based on Floquet theory—approximates the quantities knows as the Floquet multipliers, which determine the periodic system's stability, along with the associated modes. With this new technique, in Chapter 6, we were able to experimentally analyze the CI mechanism for a case where it appears that the governing equations are periodic. The results of this approach provide evidence that the observed CI is due to *parametric excitation* and, thus, we might refer to the observed CI as a *parametric* CI.

CHAPTER II

EXPERIMENTAL FACILITY AND DIAGNOSTICS

In this chapter, we describe the laboratory-scale facility that was developed to simulate full-scale CIs, experimental conditions investigated, and diagnostic capabilities along with examples of the high-speed diagnostics data acquired.

2.1 Experimental Facility

This section describes the experimental facility developed to explore the suitability of small-scale rigs to study the driving mechanisms of transverse CIs in full-scale engines. This small-scale rig was designed to provide the following capabilities:

1. Excite large amplitude oscillations at the frequencies of full-scale transverse CIs; i.e., the direction of the acoustic oscillation is perpendicular to that of the injection process and mean flow

2. Relatively inexpensive to construct and operate

3. Provide access for optical diagnostics and acoustic pressure measurements

A small-scale combustor with a single element, full-scale like injector was developed to meet the aforementioned goals, see Fig. 6. The rig, which is an extension of the concept described in Fig. 4b, is shown schematically in Fig. 6a. Notably, the velocity oscillations are parallel to the long axis of the duct and perpendicular to the direction of the mean flow and injector axis. The fuel and oxidizer enter the optically accessible combustion chamber through an injector in the bottom wall of the duct and the products are exhausted through a nozzle at the upper wall. This facility consists of a combustion chamber, a sensing section, and two adjustable length duct sections. It is possible to vary the frequency of the oscillations and the location of the combustion process relative to the excited oscillations by moving the pistons at both ends of the rig. Thus, combustion can occur near a pressure anti-node, a velocity anti-node, or somewhere in between these two locations, which allows

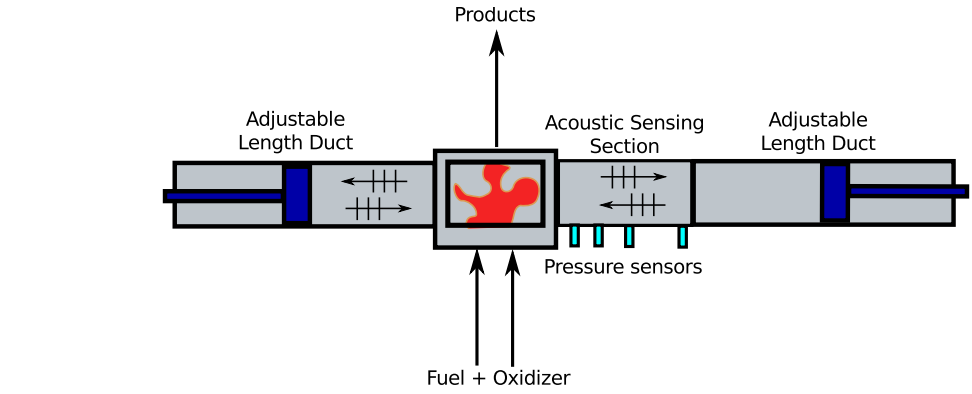

(a) Rig concept

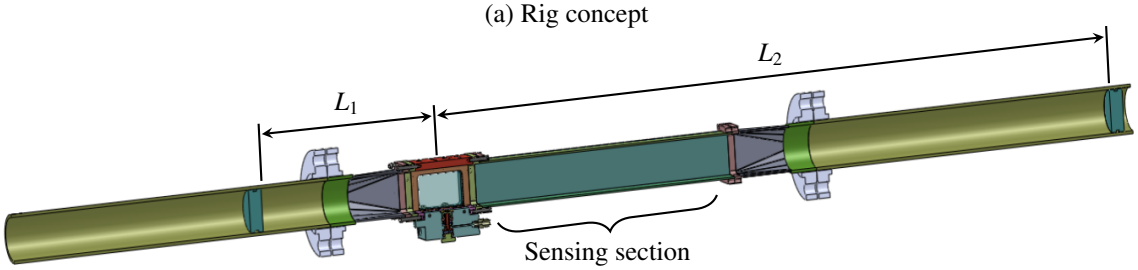

(b) Rig solid models

Figure 6: Experimental facility concept and details

one to determine the relative sensitivity of the combustion driving process to pressure and velocity oscillations.

Using the concept in Fig. 6a as a guide, a rig was designed and developed, see Fig. 6b. The rig has a sensing section for determining the properties of the excited, transverse, acoustic field and two adjustable length sections for setting the geometric length. Note that the cross-sectional area of the developed rig is nearly constant along the major axis of the rig. Specifically, the combustor and sensing sections have a rectangular cross-section (height: 76.2 mm, depth: 2.36 mm) and are connected to the round cross-section adjustable ducts (with approximate internal diameter of ø73.7 mm) via a rectangular-to-round transition. For convenience, we refer to the rig as the SIAR (Single Injector Acoustic Rig) in the ensuing discussion.

Fuel and oxidizer are introduced via an adjustable swirl injector, which is detailed in Appendix B. The oxidizer used in all experiments was air supplied by a high-pressure system and metered through a critical orifice. The orifice selected was ø1.6 ± 0.013 mm, yielding the nominal mass flow rate of 11 g/s at a supply pressure of 3450 kPa. The fuel system supplies a mixture of hydrogen, H_2, and methane, CH_4, to the combustor. The fuel combination resulted in a highly reactive system, due to the

presence of H_2, while retaining the ability to perform methylidyne radical, CH^*, chemiluminescence as a qualitative heat release indicator, as discussed in Appendix C.4. Thus, the CH_4 may be regarded as a fuel dopant to allow CH^* chemiluminescence measurements.

Figure 7a shows the experimental facility, laser systems, and high-speed cameras. Figure 7b provides a close-up view of the main combustor section. Also shown in Fig. 7b are the window cooling systems and the exhaust ejector to protect optical equipment, e.g., the laser sheet forming optics, which, are located just above the combustor. The SIAR configuration and a second configuration based on active impedance boundary control are discussed in more detail by Quinlan and Zinn [24].

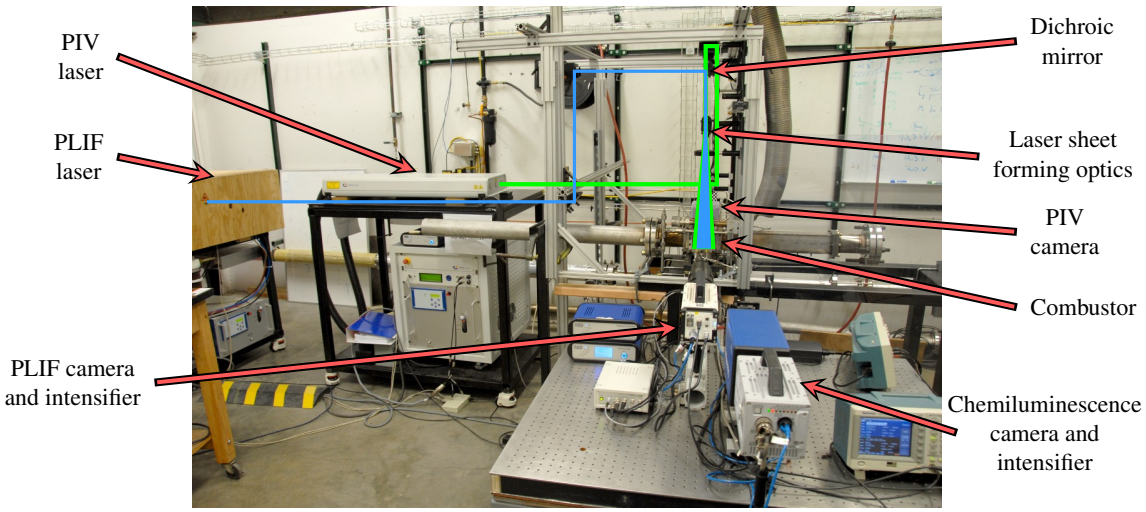

(a) Overall facility and diagnostic setup

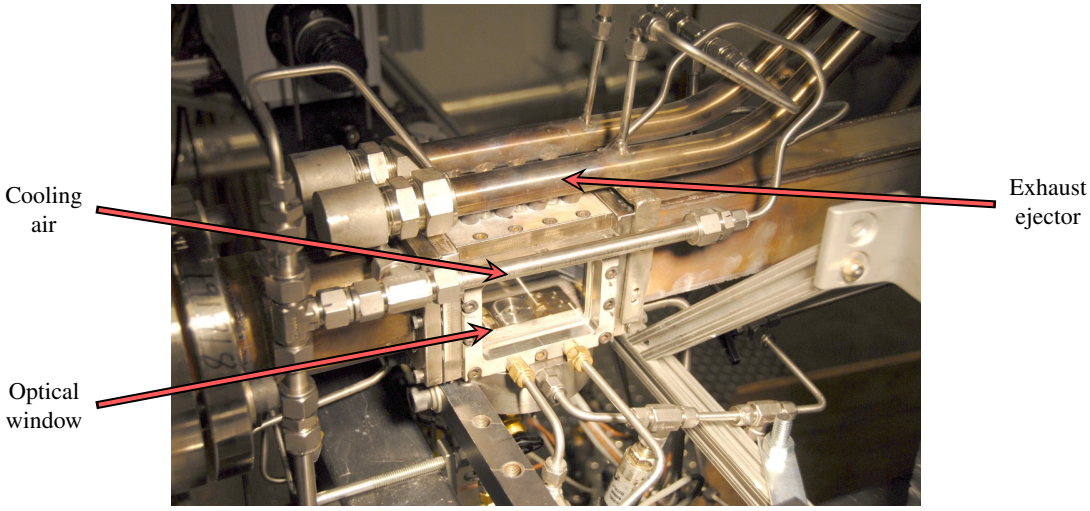

(b) Combustor, cooling, and exhaust ejector

Figure 7: Photos of experimental facility and components

2.2 Experimental Conditions

To better understand CIs we focus primarily on the differences between two experimental test conditions in this work. The conditions will be referred to as the *stable* and *unstable* cases. The only significant change in the test facility between the stable and unstable cases was the length of the left duct, which was $L_1 = 0.262\,\text{m}$ and $L_1 = 0.914\,\text{m}$, respectively (see Fig. 6b). The sensing section side of the transverse duct had a constant length of $L_2 = 1.016\,\text{m}$. Other operational parameters of interest are listed in Table 1. The *swirl* percentage is defined by the mass flow rate of air through the outer high-swirl number path relative to the total mass flow of air. The geometric swirl numbers were calculated in Appendix B to be 13.7 and −25.8 for the inner and outer swirl paths, respectively. The negative sign for the outer path indicates that the swirl is in the counter-clockwise direction when viewing the injector from the exit, towards the swirler generators. The net swirl of the flow depends on the mass flow rate through each of the swirl paths. For example, if 20% of the total mass flow is through the outer, high swirl path, the total geometric swirl number can be approximated as:

$$S_{\text{total}} = \frac{\dot{m}_{\text{inner}} S_{\text{inner}} + \dot{m}_{\text{outer}} S_{\text{outer}}}{\dot{m}_{\text{total}}}, \tag{10}$$

resulting in a total geometric swirl number of approximately 5.78 for the conditions studied in this work.

The primary measured acoustic mode is one half of a full-cycle along the major axis of the rig, and, to not confuse this with a tangential or longitudinal mode, this mode will be called the first widthwise mode (1W). The 1W frequency ($\tilde{f}$) is listed in Table 1, along with the magnitude of the power spectral density (PSD) of the acoustic pressure at $\tilde{f}$.

Table 1: Experimental conditions

Case	Total length	$\dot{m}_{air}$	$\dot{m}_{H_2}$	$\dot{m}_{CH_4}$	Swirl	T_{air}	$\tilde{f}$	PSD
-	m	g/s	g/s	g/s	%	K	Hz	kPa^2/Hz
stable	1.27	11.56	0.188	0.297	20.8	327.4	253.9	0.0035
unstable	1.93	11.58	0.189	0.313	21.1	316.6	169.7	0.0807

2.3 *Diagnostic Data*

The specific high-speed diagnostics applied to the SIAR rig are: dynamic pressure sensing, PIV, PLIF, and chemiluminescence, which are described in detail in Appendix C. A sample of the time history of the acoustic data is shown in Figs. 8a and 8b and the PSD in Figs. 8c and 8d for the stable and unstable datasets, respectively. The PSDs show that in both cases there is a large amount of spectral content in the 1 kHz range. Since in both experiments the approximately 1 kHz spectral peak is wide, we attribute this mode to the flow noise of the air system being filtered by the natural acoustic modes of the system. One pressure sensor is located in the duct and two are very near the injector. Specifically, pressure sensors, p'_1, p'_3, and p'_5 are located at $x = 0.336$ m, $x = 0.0263$ m, and $x = -0.0263$ m, respectively.

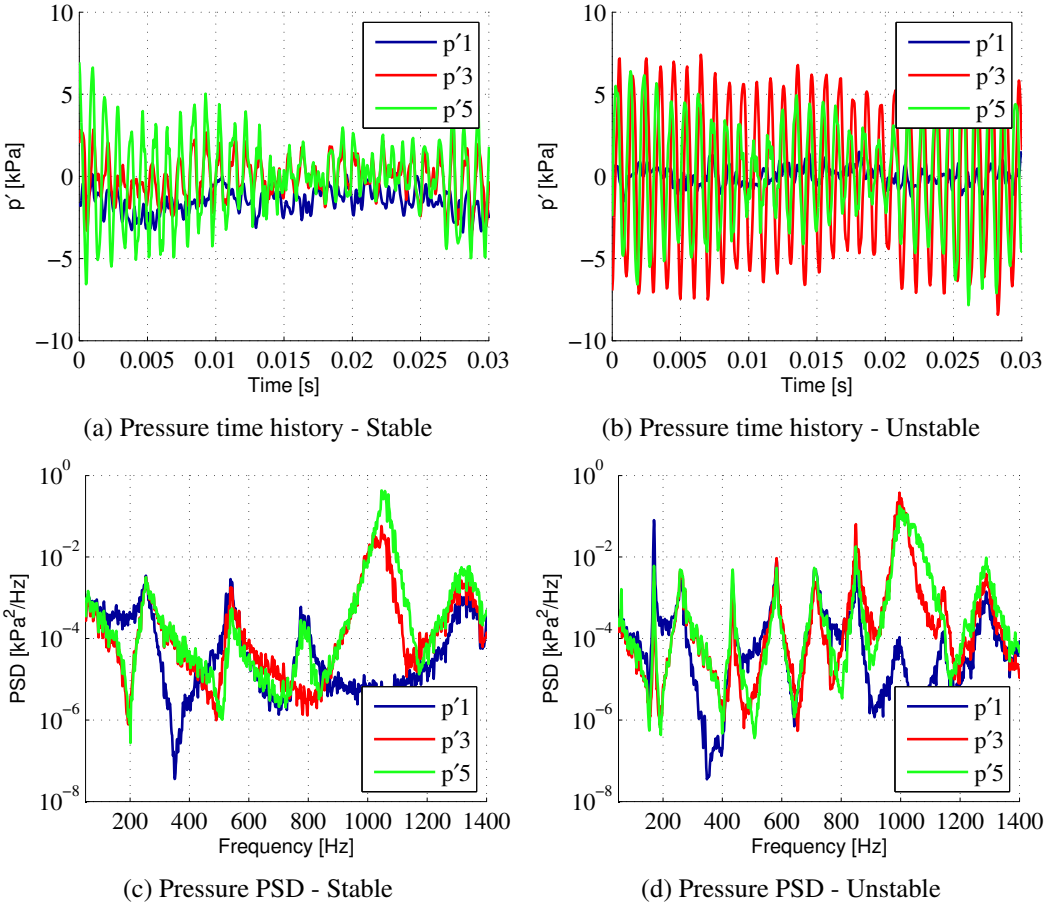

(a) Pressure time history - Stable

(b) Pressure time history - Unstable

(c) Pressure PSD - Stable

(d) Pressure PSD - Unstable

Figure 8: Acoustic pressure measurements

2.3.1 Acoustic Measurements

Assuming for a moment that the acoustic field may be represented by a one dimensional wave equation with a constant, effective speed of sound, and that the walls on either end of the duct can be modeled as perfectly rigid, then the natural acoustic mode frequencies are evenly spaced. Using consecutive peaks in the PSD in the 2 to 3 kHz frequency range, we have estimated the effective speed of sound for the stable and unstable experimental configurations as 668.17 m/s and 549.01 m/s, respectively. The associated fundamental frequency (for the 1 W mode) for each of these cases is 263.06 Hz and 142.23 Hz and higher modes are integer multiples of these frequencies. In Figs. 9a and 9b are plotted the PSDs from 100 to 6000 Hz and in Figs. 9c and 9d the PSDs from 100 to 1400 Hz. We have also included dashed vertical lines at each of the simplistically calculated acoustic mode frequencies. The vast majority of peaks in the acoustic PSD align very well with the equally spaced, predicted acoustic mode frequencies. Two exceptions to the overall accurate matching are the first two peaks in the PSD from the unstable experimental dataset, where the predicted frequencies are 142 and 284 Hz and the measured frequencies are approximately 170 and 264 Hz, respectively. There are two possible reasons that the predicted and measured frequencies differ: the first possibility is that the speed of sound is non-constant, taking this into account changes both the predicted mode shape and the predicted mode frequency (this effect will be examined in Section 2.3.2); the second possibility is that the oscillatory heat release, which we will see appears as a forcing term in the acoustics, not only affects the stability of the system, but also the oscillatory frequencies (this effect will be qualitatively examined in Section 2.3.3).

2.3.2 Calculated and Measured Acoustic Frequencies

A linear acoustic model can be created by assuming that the magnitude of state variable oscillations are much less than their mean values and neglecting mean flow allows us to write the conservation of mass, momentum, and energy as:

$$\frac{\partial \rho'}{\partial t} + \frac{\partial}{\partial x}\left(\bar{\rho} u'\right) = 0, \tag{11}$$

$$\bar{\rho}\frac{\partial u'}{\partial t} + \frac{\partial p'}{\partial x} = 0, \tag{12}$$

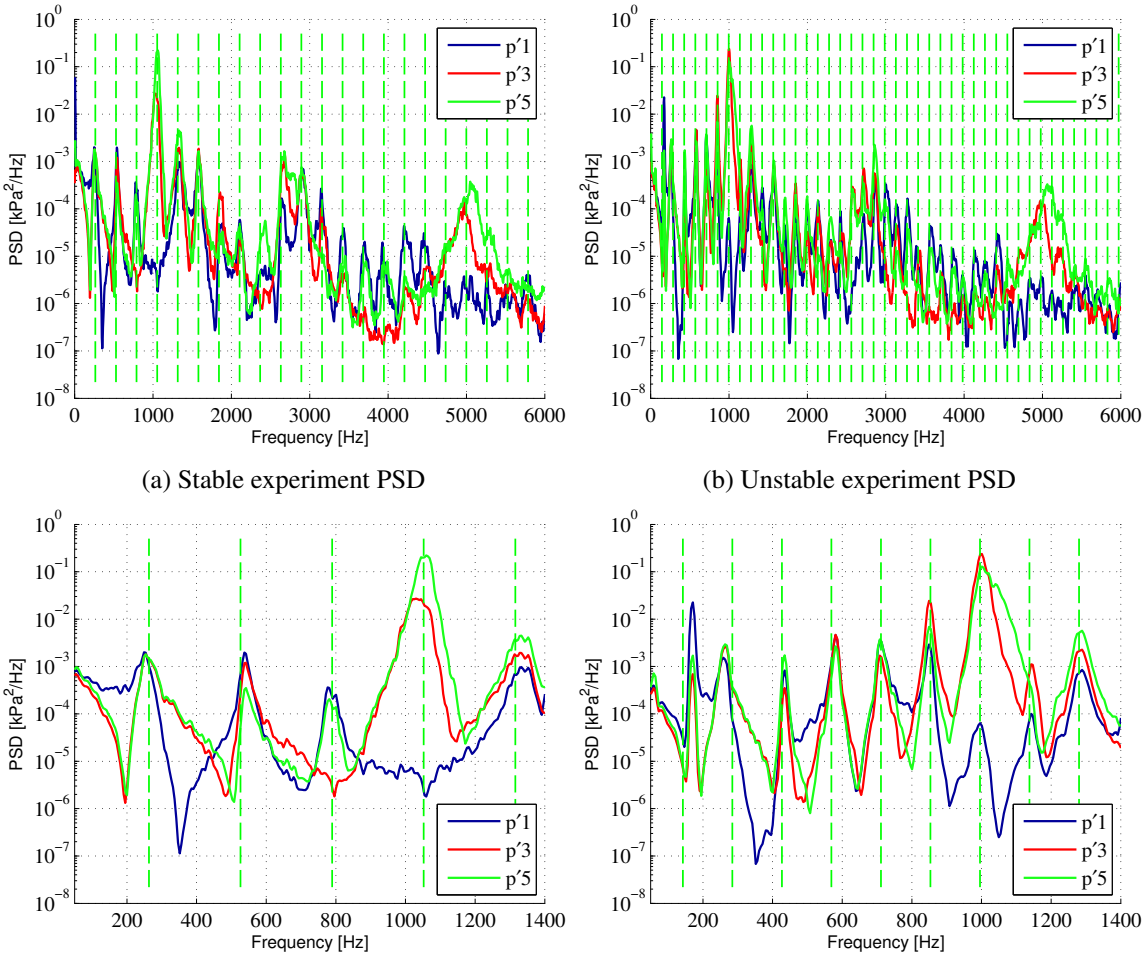

(a) Stable experiment PSD

(b) Unstable experiment PSD

(c) 50 to 1400 Hz Stable experiment PSD

(d) 50 to 1400 Hz Unstable experiment PSD

Figure 9: Acoustic pressure measurements (PSD) and calculated transverse acoustic modes (vertical light green dashed lines); Fundamental frequency, mean speed of sound, and effective mean temperature: Stable experiment: 263.06 Hz, 668.17 m/s, 1097.6 K; Unstable experiment: 142.23 Hz, 549.01 m/s, 740.99 K

and

$$\frac{\partial p'}{\partial t} + \gamma \bar{\mathcal{P}} \frac{\partial u'}{\partial x} = (\gamma - 1)\,\bar{\rho}\dot{q}', \tag{13}$$

respectively. Additionally we will use the perfect gas state equation:

$$\bar{\mathcal{P}} = \bar{\rho} R \bar{T}. \tag{14}$$

Under our these assumptions, the speed of sound may be written:

$$c = \sqrt{\gamma R \bar{T}}\,. \tag{15}$$

Here we may interpret c as $\bar{c}$, the temporal mean speed of sound, but we will allow the speed of sound to be a function of spatial location, $c = c(x)$.

To simplify the application of these equations we will begin by multiplying Eq. (12) by $\gamma\bar{\mathcal{P}}$ and divide through by $\bar{\rho}$:

$$\gamma\bar{\mathcal{P}}\frac{\partial u'}{\partial t} + \frac{\gamma\bar{\mathcal{P}}}{\bar{\rho}}\frac{\partial p'}{\partial x} = 0. \tag{16}$$

We recognize that within Eqs. (14) and (15) that $c^2 = \gamma\bar{\mathcal{P}}/\bar{\rho}$ (which we will allow to be a function of x) and take the partial x-direction derivative, yielding:

$$\gamma\bar{\mathcal{P}}\frac{\partial^2 u'}{\partial x t} + \frac{\partial}{\partial x}c^2\frac{\partial p'}{\partial x} = 0, \tag{17}$$

Next, we take the partial derivative with respect to time of Eq. (13):

$$\frac{\partial^2 p'}{\partial t^2} + \gamma\bar{\mathcal{P}}\frac{\partial^2 u'}{\partial t x} = (\gamma - 1)\,\bar{\rho}\frac{\partial \dot{q}'}{\partial t} \tag{18}$$

Since u' is smooth, $\frac{\partial^2 u'}{\partial t x} = \frac{\partial^2 u'}{\partial x t}$, so we can subtract Eqs. (17) and (18) and upon canceling terms yields the following wave equation:

$$\frac{\partial}{\partial x}\left(c^2\frac{\partial p'}{\partial x}\right) - \frac{\partial^2 p'}{\partial t^2} = -(\gamma - 1)\,\bar{\rho}\frac{\partial \dot{q}'}{\partial t} \tag{19}$$

Assuming that the pressure and heat release variables are harmonic in time, i.e., $p'(x,t) = p(x)e^{-i\omega t}$ and $\dot{q}'(x,t) = q(x)e^{-i\omega t}$ and canceling the common $e^{-i\omega t}$ in each term yields a forced Helmholtz equation:

$$\frac{\mathrm{d}}{\mathrm{d}x}\left(c^2\frac{\mathrm{d}p}{\mathrm{d}x}\right) + \omega^2 p = i\omega\bar{\rho}\,(\gamma - 1)\,q \tag{20}$$

Due to the fact that the functional form of q is complicated or unknown in most systems, the oscillatory heat release is typically heuristically modeled. As a qualitative model we will assume that q is simply p with a gain and phase applied. In complex equations, this gain and phase can be achieved by multiplying by a complex number, N, which we will call the *complex combustion response*. Defining N as:

$$N \equiv \frac{\bar{\rho}\,(\gamma - 1)\,q}{2p} \tag{21}$$

and substituting into Eq. (20) yields:

$$\frac{\mathrm{d}}{\mathrm{d}x}\left(c^2\frac{\mathrm{d}p}{\mathrm{d}x}\right) + \omega^2 p = i\omega 2Np. \tag{22}$$

We can collect terms in p:

$$\frac{\mathrm{d}}{\mathrm{d}x}\left(c^2\frac{\mathrm{d}p}{\mathrm{d}x}\right)+\left(\omega^2-i\omega 2N\right)p=0. \tag{23}$$

By defining $\tilde{\omega}^2 \equiv \omega^2 - i\omega 2N$, we see that Eq. (23) is an eigenvalue problem for $\tilde{\omega}_k^2$ and the mode shapes of the pressure, p_k:

$$\frac{\mathrm{d}}{\mathrm{d}x}\left(c^2\frac{\mathrm{d}p_k}{\mathrm{d}x}\right)+\tilde{\omega}_k^2 p_k=0. \tag{24}$$

where the integer k identifies one of an infinite number of modes. We can interpret $\tilde{\omega}$ as the *natural acoustic mode* angular frequency and ω as the angular frequency at which the forced system actually oscillates. Given the appropriate boundary conditions, Eq. (24) can be solved analytically for the case when c is constant. Typically, when c is not a constant, the system must be solved numerically. For example, if c is constant for a duct of nondimensional length, $L = 1$ and the duct has hard wall terminations, i.e.:

$$\frac{\mathrm{d}p}{\mathrm{d}x}=0 \quad \text{at} \quad x=0,1 \tag{25}$$

then:

$$\tilde{\omega}_k = k\pi c \quad \text{for} \quad k=0,1,2,\ldots. \tag{26}$$

and

$$p_k = a_k\cos\left(\frac{\tilde{\omega}_k}{c}t\right) \quad \text{for} \quad k=0,1,2,\ldots. \tag{27}$$

From Figs. 9a and 9b we see that the vertical dashed lines, representing the simplified, constant speed of sound calculated frequencies, align well with the peaks in the measured acoustic spectra for frequencies up to around 4 kHz. The frequency known as the cutoff frequency is the lowest frequency at which the duct can support acoustic modes in the plane of the cross-section. Above the cutoff frequency we might expect the 1-D acoustic assumption to break down. We will return to the cutoff frequency momentarily, after making another observation about the predicted and measured modal frequencies. While most of the predicted and measured frequencies match reasonably well, there are a few modes whose measured frequencies are not well predicted by the constant c calculations, e.g., the first two modes in Figs. 9c and 9d.

These two observations, have led us to estimate the average cross-sectional temperature as a function of the position along the duct length, $T(x)$, allowing us to estimate the cutoff frequency and speed of sound with respect to location in the duct. Figure 10 shows the estimated temperature and

the resulting cutoff frequencies for the stable and unstable experimental setups. The peak temperature was chosen to be 600 K below the adiabatic flame temperature (to account for averaging over the cross-section and heat losses) and the coolest temperature was fixed at 375 K. In addition, we assumed a temperature profile based on the steady solution to compact heat source/heat transfer—the *heat kernel*—as a simple/qualitative temperature distribution to examine the differences in predicted mode frequencies. Specifically, we estimated the temperature as:

$$T(x) = T_{max} \exp\left(\frac{-x^2}{\beta}\right) + T_{\infty}, \tag{28}$$

where β equals 0.143 and 0.02871 for the stable and unstable experiments, respectively. We selected β to match the predicted and measured natural acoustic mode frequencies over the $2 - 3$ kHz range, where the measured peaks are nearly evenly spaced.

To estimating modal frequencies with the above defined temperature profiles we must again solve Eq. (24), allowing $c = c(x)$. To solve this system we have employed the Ritz-Galerkin method (a type of global variational method). Specifically, we expand the independent variable, p_k, as a linear combination of predefined, known functions, which are called *basis functions*, ϕ_j:

$$p_k(x) = \sum_{j=1}^{n} a_j \phi_j(x), \tag{29}$$

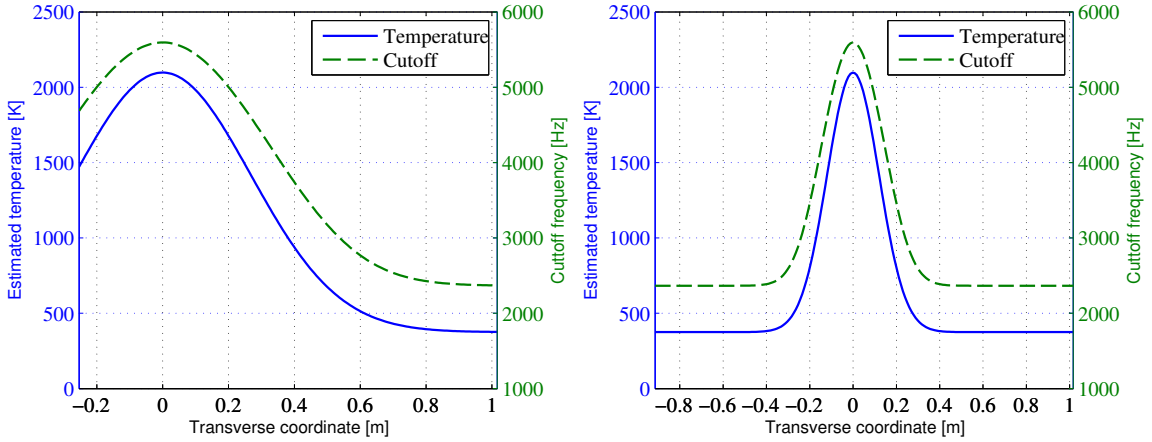

(a) Stable experiment

(b) Unstable experiment

Figure 10: Qualitatively estimated temperature and acoustic cuttoff frequencies along transverse duct

where a_j are the expansion coefficients that must be solved for. Substituting Eq. (29) into Eq. (24) yields:

$$\frac{\mathrm{d}}{\mathrm{d}x}\left(c^2\frac{\mathrm{d}\sum_{j=1}^{n}a_j\phi_j}{\mathrm{d}x}\right)+\tilde{\omega}_k^2\sum_{j=1}^{n}a_j\phi_j=0. \tag{30}$$

Assuming the series expansions are finite dimensional and the basis or test functions are smooth, then we can exchange the order of summation and differentiation:

$$\sum_{j=1}^{n}a_j\left[\frac{\mathrm{d}}{\mathrm{d}x}\left(c^2\frac{\mathrm{d}\phi_j}{\mathrm{d}x}\right)+\tilde{\omega}_k^2\phi_j\right]=0. \tag{31}$$

Rather than solving Eq. (31) directly, we instead solve the *weak form* [25] of Eq. (31). There are a number of reasons to seek the solution to the weak form rather than the original differential equation. First, a weak formulation reduces the differentiability requirements on the basis functions. For example, the Helmholtz equation has a spatial second derivative, so the strong solution must be twice differentiable, but we can approximate the weak solution by basis functions that are only once differentiable, using the weak form. Second, the weak form often leads to solution techniques that are easily implemented on a computer, e.g., the finite element method. Third, some boundary conditions, like the rigid wall boundary condition in our case, naturally appear in the formulation and thus are very easy to implement. Lastly, there is often a useful weak solution in cases when there is no classical, strong solution. All this being said, typically the weak solution is a very good approximation to the solution of the original differential equation.

The first step in finding the weak form, or the weighted residual form, of the governing equation is to multiply the equation (Eq. (31) in this case) by what are known as *weight function*, w_i, and integrated over the spatial domain. There are a number of possible choices for weight functions, which result in slightly different formulations (Ritz-Galerkin, Petrov-Galerkin, collocation, leasts squares, etc.), see, for example, Reddy [25]. We have chosen $w_i = \phi_i$ (the Ritz-Galerkin formulation). Specifically, multiplying Eq. (31) by the weight function ϕ_i and integrating over the non-dimensional tube length yields:

$$\int_0^1\phi_i\sum_{j=1}^{n}a_j\left[\frac{\mathrm{d}}{\mathrm{d}x}\left(c^2\frac{\mathrm{d}\phi_j}{\mathrm{d}x}\right)+\tilde{\omega}_k^2\phi_j\right]\mathrm{d}x=0. \tag{32}$$

Again, since we are working in finite dimensions and p_k is smooth, the order of integration and summation may be exchanged:

$$\sum_{j=1}^{n} a_j \int_0^1 \phi_i \left[\frac{\mathrm{d}}{\mathrm{d}x}\left(c^2 \frac{\mathrm{d}\phi_j}{\mathrm{d}x} \right) + \tilde{\omega}_k^2 \phi_j \right] \mathrm{d}x = 0. \tag{33}$$

In Eq. (33), the first term in the summation requires the derivative of c and the second derivative of ϕ_j to be continuous. The weak form reduces the required smoothness of the solution by exchanging the differentiation from ϕ_j to ϕ_i through integration by parts:

$$\int_0^1 \phi_i \frac{\mathrm{d}}{\mathrm{d}x}\left(c^2 \frac{\mathrm{d}\phi_j}{\mathrm{d}x} \right) \mathrm{d}x = -\int_0^1 \frac{\mathrm{d}\phi_i}{\mathrm{d}x} c^2 \frac{\mathrm{d}\phi_j}{\mathrm{d}x}\, \mathrm{d}x + \left[\phi_i c^2 \frac{\mathrm{d}\phi_j}{\mathrm{d}x} \right]_{x=0}^{1}. \tag{34}$$

But, from our boundary condition, Eq. (25), we have $\left[\frac{\mathrm{d}\phi_j}{\mathrm{d}x}\right]_{x=0,1} = 0$, thus the boundary terms are identically zero and Eq. (33) may be written as:

$$\sum_{j=1}^{n} a_j \int_0^1 \left[-c^2 \frac{\mathrm{d}\phi_i}{\mathrm{d}x} \frac{\mathrm{d}\phi_j}{\mathrm{d}x} + \tilde{\omega}_k^2 \phi_i \phi_j \right] \mathrm{d}x = 0. \tag{35}$$

Defining:

$$K_{ij} \equiv \int_0^1 c^2 \frac{\mathrm{d}\phi_i}{\mathrm{d}x} \frac{\mathrm{d}\phi_j}{\mathrm{d}x}\, \mathrm{d}x \tag{36}$$

and

$$M_{ij} \equiv \int_0^1 \phi_i \phi_j \, \mathrm{d}x, \tag{37}$$

Eq. (35) may be written:

$$\sum_{j=1}^{n} a_j \left[-K_{ij} + \tilde{\omega}_k^2 M_{ij} \right] = 0. \tag{38}$$

Taking $i = 1, 2, \ldots, n$ in Eq. (38) gives n equations for n unknowns (the a_j's) and we can write this system of equations in matrix form:

$$-\boldsymbol{K}\boldsymbol{a} + \tilde{\omega}_k^2 \boldsymbol{M}\boldsymbol{a} = 0 \tag{39}$$

or

$$\boldsymbol{K}\boldsymbol{a} = \tilde{\omega}_k^2 \boldsymbol{M}\boldsymbol{a}. \tag{40}$$

Equation (40) is in the form of a *generalized eigenvalue problem* where $\tilde{\omega}_k^2$ is the eigenvalue and $\boldsymbol{a}$ is the eigenvector associated to that eigenvalue. While many good solution techniques exist of

generalized eigenvalue problems, we can rewrite Eq. (40) as a standard eigenvalue problem. This is accomplished by left multiplying Eq. (40) by M^{-1} and defining $\tilde{K} \equiv M^{-1}K$, yielding:

$$\tilde{K}\boldsymbol{a} = \tilde{\omega}_k^2 \boldsymbol{a}. \tag{41}$$

Practically, we almost never find the inverse of a matrix due to its high computational cost, but with our chosen formulation and basis functions, M is diagonal. So, the inverse of M may be simple constructed by taking the reciprocal of the diagonal entries of M.

While often the chosen basis functions are polynomials, in this case by choosing a cosine series we can recover the simple Fourier series like results when the speed of sound is constant. Again, the basis functions must meet the specified boundary conditions, hence why we use a cosine series rather than a full cosine/sine series. Specifically, we choose the basis—and weight functions in this case—to be:

$$\phi_k = \cos(k\pi x), \tag{42}$$

where $k = 0, 1, 2, \ldots$ and x is in $[0, 1]$. Notice that $k = 0$ yields $\phi_0 = \cos(0) = 1$, resulting in a zero eigenvalue, which represents a *bulk* mode. The bulk acoustic mode is essential to the operation of a Helmholtz absorber, but in our problem it has no consequences and is only retained for to meet the *completeness* requirements of the method.

We must select the number of terms, n, to use in our approximation. The first of two convenient features of this approach is that the n by n matrices can be constructed recursively from the $n-1$ by $n-1$ matrices and explicit calculation of the n^{th} row/column, which in this case are simply transposes of each other; this recursive construction and the overall low number of term needed for accurate results makes global variation methods very efficient for calculations like these. The second advantageous feature is that the approximated frequencies will always be overestimated and as more terms are added to the calculation, the error in the frequency monotonically decreases. Also, the eigenvalues of the lowest frequency modes are estimated more accurately than higher modes' eigenvalues. With all of these features in mind, we will assume that the difference in the eigenvalue with two different values of n, from a large n to a lower value of n is a measure of the error for the latter case. Specifically, we found that the largest change in the lowest 30 eigenvalues between

$n = 80$ and $n = 60$ was less than 2.8×10^{-9} Hz. Owing to this extremely low value, with $n = 60$ we have confidence in the numerical solution technique for the low frequency modes of interest.

Substituting the speed of sound, Eq. (28), into Eq. (36), we can perform the integrations required to form the matrices K and M and hence $\tilde{K}$. This was accomplished via a Python code and the eigenvalues and eigenvectors were calculated with SciPy.

The resulting frequencies are marked as blue dot-dashed lines on the PSD spectra in Fig. 11 and the first 22 are listed in Table 2. The first item of note is that the majority of the frequencies are very close to the evenly spaced, constant speed of sound values shown by the green dashed lines. On the other hand, the frequency for the first two modes in the unstable experiment configuration are both shifted an appreciable amount, Fig. 11b. The constant and non constant speed of sound frequencies for the first two modes were 142.23 and 156.27 Hz and 284.46 and 275.59 Hz, respectively. Although the shift amplitudes are not as large as measured, the shift direction for these two modes, shifted up and down in frequency, respectively, is correct. In addition to not predicting large enough frequency shifts for these two modes, it appears that the estimated temperature effects do not explain other frequency shifts. For example, it does not explain why the fundamental mode for the stable experiment case, Fig. 11a, have nearly identical calculated frequencies for the constant and non constant speed of sound cases and neither matches the measured peak in the PSD. Potentially the true temperature field has stronger gradients, causing the shift to be larger, but the changing speed of sound is still unlikely to fully account for the frequency shifts. As a result, there is another source that might explain the shifts—coupling with the unsteady heat release.

But, before discussing the affect of heat release on the frequency, we have plotted a number of acoustic mode shapes in Fig. 12. In each plot, the location of the injector along the duct is marked with a green dot-dashed line. In addition, in each of the figures, the constant and non constant speed of sound mode shapes are shown in red dashed and solid blue lines respectively. Note that the frequencies between the two mode shapes are slightly different, e.g., in Fig. 12c the constant and non constant speed of sound modes occur at nondimensional frequencies of π and 3.320, respectively. Throughout this work we will be interested in modes with natural mode frequencies near 170, 270, and 1000 Hz. As such, we have plotted two modes from the stable experiment configuration, 266.91 and 1053.9 Hz, and three from the unstable experiment configuration, 156.27, 275.59, and 996.06 Hz.

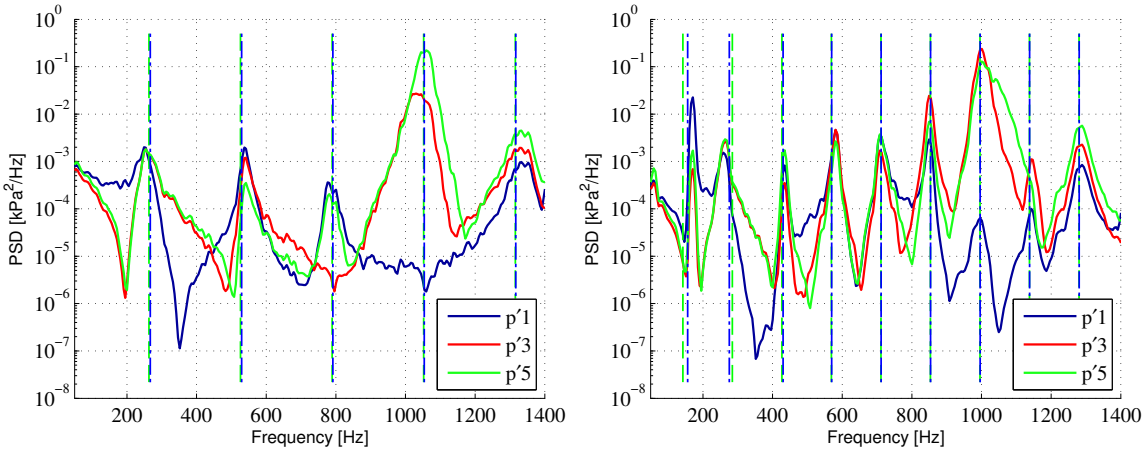

(a) 50 to 1400 Hz Stable experiment PSD

(b) 50 to 1400 Hz Unstable experiment PSD

Figure 11: Acoustic pressure measurements (PSD), constant temperature calculated transverse acoustic modes (vertical light green dashed lines), and Ritz-Galerkin estimated non-constant temperature transverse acoustic modes (vertical dark blue dot-dashed lines); Temperature distribution coefficient β: Stable experiment: $\beta = 0.143$; Unstable experiment: $\beta = 0.02871$

In all of these modes the general character of the wave is the same whether the speed of sound was constant or not. On the other hand, locally the wave field is substantially modified by the temperature effects. One point to keep in mind about the fundamental acoustic modes for each experimental configuration, Figs. 12a and 12c, is that injector is located near a pressure anti-node/velocity node for the 266 Hz mode and a velocity anti-node/pressure node for the 156.27 Hz mode.

2.3.3 Calculated and Measured Acoustic Frequencies—Effect of Heat Release

We now return to the idea that the unsteady heat release is somehow responsible for the unexplained frequency shifts in the acoustic PSD and will attempt to qualitatively explain the results. To begin our discussion, starting with Eqs. (23) and (24), we can see how the combustion effects the measured angular frequency and the stability through the real and imaginary parts of the complex angular frequency of the system, ω:

$$\tilde{\omega}_k^2 = \omega_k^2 - i\omega 2N \quad \Rightarrow \quad \omega_k^2 - i\omega 2N - \tilde{\omega}_k^2 = 0. \tag{43}$$

This is a quadratic equation for ω whose solutions are:

$$\omega_k = iN \pm \sqrt{N^2 + \tilde{\omega}_k^2}. \tag{44}$$

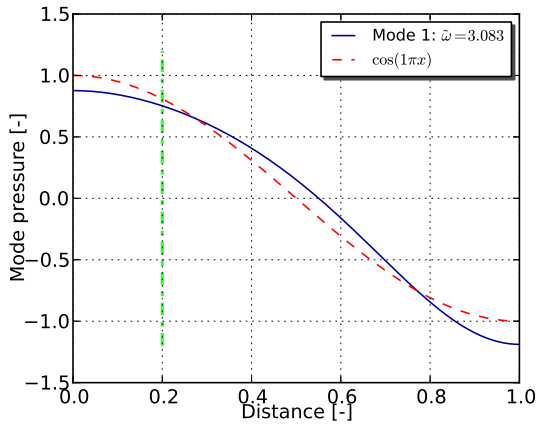

(a) Stable mode 1: 266.91 Hz

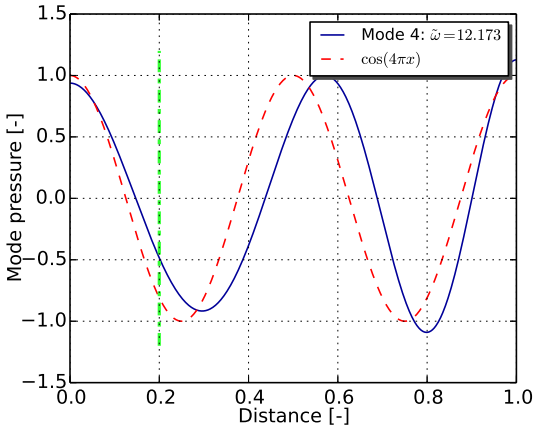

(b) Stable mode 4: 1053.9 Hz

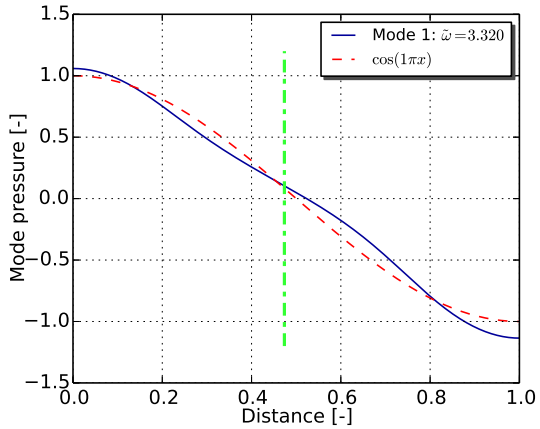

(c) Unstable mode 1: 156.27 Hz

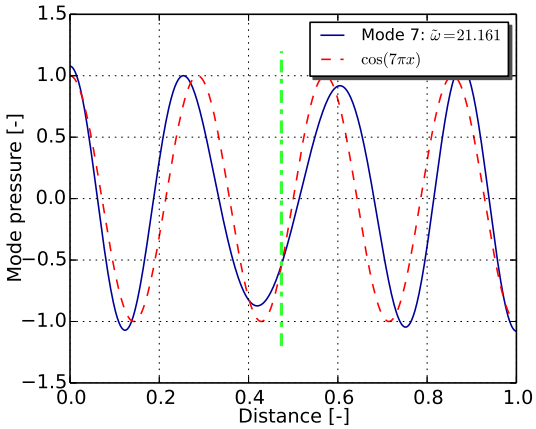

(d) Unstable mode 7: 996.06 Hz

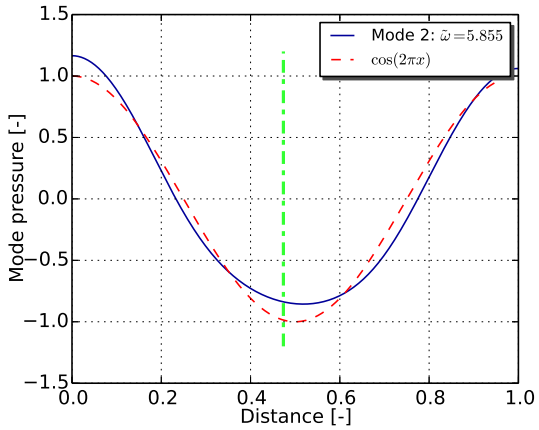

(e) Unstable mode 2: 275.59 Hz

Figure 12: Select acoustic pressure mode shapes for the constant (red dashed lines) and non constant speed of sound calculations. The injector location along duct is marked by vertical green dot-dashed line

Table 2: Acoustic mode frequencies calculated with Ritz-Galerkin expansion for the stable and unstable experiments

Mode -	f_s Hz	f_u Hz
1 W	266.91	156.27
2 W	529.41	275.59
3 W	791.35	430.24
4 W	1053.92	569.59
5 W	1316.73	711.70
6 W	1579.65	853.88
7 W	1842.62	996.06
8 W	2105.63	1138.26
9 W	2368.66	1280.46
10 W	2631.71	1422.68
11 W	2894.77	1564.90
12 W	3157.84	1707.13
13 W	3420.91	1849.35
14 W	3683.99	1991.58
15 W	3947.08	2133.82
16 W	4210.17	2276.05
17 W	4473.26	2418.28
18 W	4736.35	2560.52
19 W	4999.45	2702.76
20 W	5262.55	2844.99
21 W	5525.64	2987.23
22 W	5788.75	3129.47

If N, the complex combustion response, is much less than the *acoustic* or unforced angular frequency squared, $\tilde{\omega}_k^2$, which is real and nonnegative (positive for any case of interest), then the binomial expansion yields:

$$\omega_k = iN \pm \sqrt{\tilde{\omega}_k^2} - \frac{N^2}{2\sqrt{\tilde{\omega}_k^2}} - \frac{N^4\sqrt{\tilde{\omega}_k^2}}{32\tilde{\omega}_k^2} + O\left(N^5\right) \tag{45}$$

or

$$\omega_k = iN + \tilde{\omega}_k - \frac{N^2}{2\tilde{\omega}_k} - \frac{N^4}{32\tilde{\omega}_k} + O\left(N^5\right). \tag{46}$$

Moreover, assuming that $N \ll 1$, the higher order terms in N can be neglected to identify the leading influence of N on the angular frequency and growth rate. In other words, the complex frequency is approximately:

$$\omega_k \approx iN + \tilde{\omega}_k. \tag{47}$$

Breaking Eq. (47) into its real and imaginary parts yields:

$$\mathrm{Re}\{\omega_k\} = \omega_R \approx -N_I + \tilde{\omega}_k \tag{48}$$

and

$$\mathrm{Im}\{\omega_k\} = \alpha \approx N_r, \tag{49}$$

where N_R and N_I are the real and imaginary parts of the complex combustion response.

As can be seen from Eq. (48), for very small oscillatory heat additions, the angular frequency at which the system oscillates is the predicted *acoustic* angular frequency minus the imaginary part of the complex combustion response. Depending on the sign of N_I, positive or negative, the measured frequency will be below or above the acoustic frequency, respectively. Equation (49) shows that for small N, the real part of the complex combustion response is the linear growth rate of the system, α.

With this in mind, we can conceptually interpret N in the complex plane as driving if the value of N is in the right half-plane and the measured frequency will be below or above the calculated acoustic frequency if the imaginary part of N is above or below the real axis, see Fig. 13.

Again, considering the first two modes for the unstable experiment dataset and their spectral peak widths, we believe that the 1 W mode is unstable, while the 2 W mode is stable. In fact, we will support these assertions in Chapter 6. Furthermore, the measured frequency for the 1 W and 2 W modes are higher and lower than the calculated natural acoustic mode frequency, respectively. Given

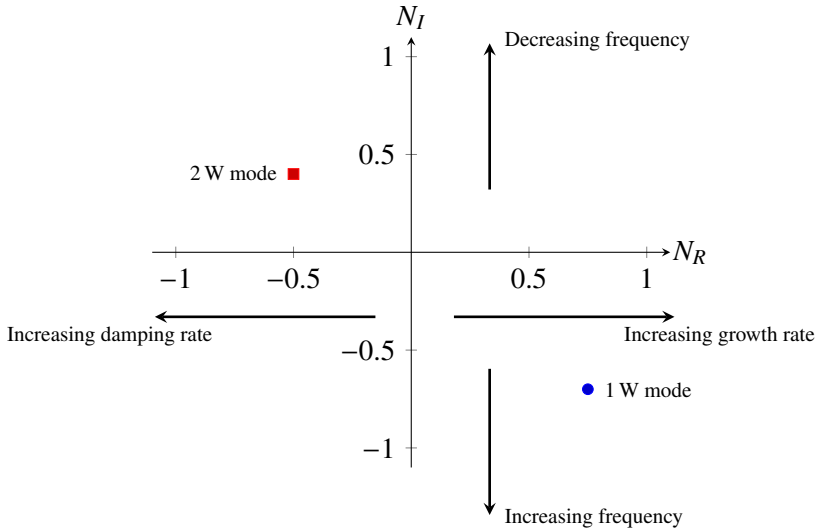

Figure 13: Effect of complex combustion response on linear stability and measured frequency

these observations, in Fig. 13, we can qualitatively plot which quadrants of the complex plane the value of N takes for each of these modes, the forth and second quadrants.

2.3.4 Optical Diagnostics

An example of the instantaneous data collected by each of the optical techniques is shown in Fig. 14. Note that each of these images represents the same sampling period of the unstable dataset, hence they are *simultaneous* images. The axes scales are in mm, the injector nozzle is located at approximately $y = 0$ mm and has diameter 10.9 mm, and the injector axis/mean flow direction is from bottom to top.

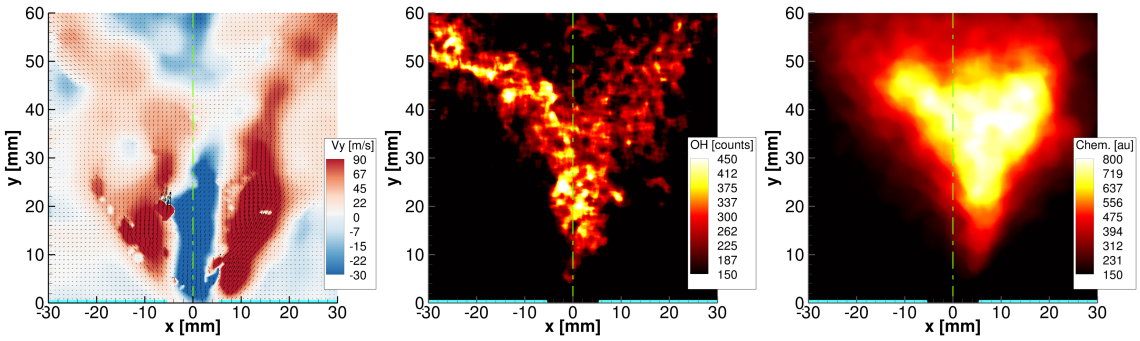

(a) Raw PIV vectors (b) Raw PLIF intensity (c) Raw chemiluminescence intensity

Figure 14: Example of instantaneous diagnostic data

The first image, Fig. 14a, shows the calculated PIV velocity field found from a Mie scattering image pair. Note, the velocity field has some areas where the vectors appear to be unusually large or small, evidence of the noise often encountered with PIV data. This noise is unavoidable and the data reduction approaches employed must be resilient to the presence of such noise. The instantaneous PLIF and chemiluminescence images are shown in Figs. 14b and 14c. Note that PIV and PLIF are planar diagnostics where as chemiluminescence is a line of sight technique.

CHAPTER III

DATA ANALYSIS VIA THE DYNAMIC MODE DECOMPOSITION

One of the main objectives of this study is to apply modern data analysis techniques to *extract* as much useful information as possible from large quantities of measured experimental data. Specifically, we seek features that may affect the CI mechanisms, e.g., coherent vortical structures, and the frequency and growth/decay rate of the features using a *data only* approach. This chapter lays the ground work for applying the DMD analysis to high repetition rate (10 kHz) simultaneous diagnostic data obtained by such methods as PIV, PLIF, and chemiluminescence.

This chapter consists of two parts. The first part introduces the DMD approach, including key terminology, interpretation of the method, and practical algorithms for application based on the singular value decomposition (SVD) [26] that allows for a noise reduction scheme. The second part demonstrates the application of the DMD approach and its relationship to systems of first-order ordinary differential equations (ODEs) by analyzing the dynamics of a spring-mass-damper system.

3.1 Mathematical Theory for the DMD

This section describes the theoretical development of the DMD method, which is grounded in nonlinear dynamical systems theory [27], and seeks to find coherent, mono-frequency, spatial modes that describe the evolution of the system. We begin by looking at systems that may possess infinite dimensions and then show how a similar approach may be applied to practical finite dimensional systems, which are of interest in this study. Further, since our interest lies in the application of the DMD in the analysis of experimental data, the focus will be on discrete-time rather than continuous-time systems.

Consider a dynamical system whose state is described by a potentially infinite dimensional vector, $\boldsymbol{x}_k$, at the k^{th} time step, and has an operator, $\mathcal{T}$, that maps the system from one time step to the next:

$$\boldsymbol{x}_{k+1} = \mathcal{T}(\boldsymbol{x}_k). \tag{50}$$

Further, imagine that the state vector, $\boldsymbol{x}_k$, may not be measured directly, but can be related to the measured quantities or *observables*, $\boldsymbol{v}_k$, at time step k by the observation operator, $\mathcal{G}$:

$$\boldsymbol{v}_k = \mathcal{G}(\boldsymbol{x}_k). \tag{51}$$

Next, we introduce the *Koopman operator* [28, 29], $\mathcal{K}$, that relates two consecutive observations, $\boldsymbol{v}_k$ and $\boldsymbol{v}_{k+1}$ at time k and $k+1$ respectively, much like the time stepping operator related two consecutive state vectors:

$$\boldsymbol{v}_{k+1} = \mathcal{K}(\boldsymbol{v}_k). \tag{52}$$

We are interested in $\mathcal{K}$ because the DMD method approximates some of its eigenvalues and eigenvectors from measured data—telling us about the evolution of the system without having to know $\mathcal{T}$ explicitly. Starting from Eq. (52), the relationship between the Koopman operator, the time-stepping operator, and the observation operator is found by employing Eq. (51) to change from observation space to state space:

$$\mathcal{G}(\boldsymbol{x}_{k+1}) = \mathcal{K}[\mathcal{G}(\boldsymbol{x}_k)]. \tag{53}$$

Substituting Eq. (50) into the left hand side of Eq. (53) yields:

$$\mathcal{G}[\mathcal{T}(\boldsymbol{x}_k)] = \mathcal{K}[\mathcal{G}(\boldsymbol{x}_k)]. \tag{54}$$

To appreciate the relationship between $\mathcal{K}$ and $\mathcal{T}$, imagine we could directly observe the state of the system, $\boldsymbol{x_k}$; in other words, if $\mathcal{G} = I$, then we see from Eq. (54) that in this case $\mathcal{K} = \mathcal{T}$. Thus, the closer we come to observing the state of the system, the more direct $\mathcal{K}$ is linked to the governing physics. The idea of improving the observation operator as a way to improve the relationship between the Koopman operator and the time-stepping operator has two practical implications. First, it motivates the experimentalist to make a large number of high-quality measurements of the system at each time step. Second, by processing multiple diagnostics simultaneously, a more complete representation of the system's state is obtained.

To apply the general concepts presented above to experimental or numerical data, which must have finite dimensions, we introduce the following finite dimensional operator, A, which is analogous

to $\mathcal{K}$ in Eq. (52), and relates measured data at two consecutive time steps k and $k+1$:

$$\boldsymbol{v}_{k+1} = A\boldsymbol{v}_k. \tag{55}$$

The vector $\boldsymbol{v}_k$ contains a finite number of observations (e.g., measured velocities) at the k^{th} time step and is commonly called the k^{th} *snapshot* of the system. While this finite dimensional operator, A, does not contain the infinite number of eigenvalues of $\mathcal{K}$, it approximates a portion of the spectra of the Koopman operator [30]. Thus, A may be considered a finite dimensional approximation to the Koopman operator. Henceforth, for convenience, we will refer to A as the finite dimensional Koopman operator, or simply as the Koopman operator when there is no possibility of confusion.

Following the discussion of Schmid [9], snapshot vectors provided by experiments or numerical simulations at equally spaced time intervals may be arranged column-wise in a matrix:

$$V \equiv \{\boldsymbol{v}_1 \;\; \boldsymbol{v}_2 \;\; \cdots \;\; \boldsymbol{v}_N\}. \tag{56}$$

Using the definition of the finite dimensional Koopman operator, A (see Eq. (55)), the data matrix, V, may be rewritten in the following form:

$$V = \left\{\boldsymbol{v}_1 \;\; A\boldsymbol{v}_1 \;\; A^2\boldsymbol{v}_1 \;\; \cdots \;\; A^{N-1}\boldsymbol{v}_1\right\}. \tag{57}$$

In this representation, we can see that the columns of V form a *Krylov sequence* defined by the repeated multiplication of a vector by a matrix, e.g., $\boldsymbol{v}_2 = A\boldsymbol{v}_1$, $\boldsymbol{v}_3 = A^2\boldsymbol{v}_1$, etc. Taking all linear combinations of a Krylov sequence forms a linear vector space called a *Krylov subspace* [31]. By this definition of a Krylov subspace, we see that the column space of V, or Span(V), forms an N dimensional Krylov subspace. The implication of the observed form of Eq. (57) is that the DMD method is related to a powerful set of mathematical tools, namely the Arnoldi and Lanczos methods, based on Krylov subspaces to approximate eigenmodes [32].

In the DMD method, we will use two Krylov sequences, $V_{1:N-1}$ and $V_{2:N}$, defined by:

$$V_{i:j} = \left\{A^{i-1}\boldsymbol{v}_1 \;\; A^i\boldsymbol{v}_1 \;\; \cdots \;\; A^j\boldsymbol{v}_1\right\} = \left\{\boldsymbol{b} \;\; A\boldsymbol{b} \;\; A^2\boldsymbol{b} \;\; \cdots \;\; A^{j-i-1}\boldsymbol{b}\right\}, \tag{58}$$

where $\boldsymbol{b} = A^{i-1}\boldsymbol{v}_1$ was substituted into the right hand side of Eq. (58) to show that any $V_{i:j}$ is a Krylov sequence and can generate a Krylov subspace. By applying Eq. (55) to each column of the Krylov

sequence $V_{1:N-1}$, we find that the two Krylov sequences $V_{1:N-1}$ and $V_{2:N}$ are related by the finite dimensional Koopman operator, A:

$$AV_{1:N-1} = V_{2:N}. \tag{59}$$

Equation (59) will serve as the starting point for a number of different DMD developments that follow.

We seek to find, from observations only, some approximate eigenvalues and eigenvectors, i.e., *Ritz values* and *Ritz vectors*, of the matrix A to gain insight into the spatial and temporal dependencies of the physical processes that may contribute to the investigated CI. Two approaches for finding this information are possible. The first uses the sequential nature of Eq. (59) to find a similar matrix whose eigenmodes may be calculated. The second employs a series of methods based on matrix factorization to obtain the eigenproblem of interest. The first approach is presented to show one way of conceptualizing the DMD method, but is impractical due to numerical conditioning issues.

In the first DMD approach to find the approximate eigenmodes, we write the last snapshot $\boldsymbol{v}_N$ as a linear combination of the preceding $N-1$ snapshots, i.e., $\boldsymbol{v}_1 \ \cdots \ \boldsymbol{v}_{N-1}$, as:

$$\boldsymbol{v}_N = a_1\boldsymbol{v}_1 + a_2\boldsymbol{v}_2 + \cdots + a_{N-1}\boldsymbol{v}_{N-1} + \boldsymbol{r} = V_{1:N-1}\boldsymbol{a} + \boldsymbol{r}, \tag{60}$$

where a_i represents the coefficient of the i^{th} snapshot and $\boldsymbol{r}$ is the residual that is in the null space of the Krylov subspace, Span($V_{1:N-1}$).

Next, substituting Eq. (60) for the last snapshot in Eq. (59) yields:

$$AV_{1:N-1} = V_{2:N} = \{\boldsymbol{v}_2 \ \ \boldsymbol{v}_3 \ \ \cdots \ \ \boldsymbol{v}_{N-1} \ \ V_{1:N-1}\boldsymbol{a} + \boldsymbol{r}\} = \{\boldsymbol{v}_2 \ \ \boldsymbol{v}_3 \ \ \cdots \ \ V_{1:N-1}\boldsymbol{a}\} + \boldsymbol{r}\cdot\hat{\boldsymbol{e}}_{N-1}, \tag{61}$$

where $\hat{\boldsymbol{e}}_{N-1}$ is a unit vector in the $N-1$ direction. Since, with the exception of the last column, the columns of $V_{2:N}$ are identical to the columns of $V_{1:N-1}$ shifted by one column, Eq. (61) may be rewritten in terms of $V_{1:N-1}$, $\boldsymbol{v}_N$, $\boldsymbol{a}$, and the residual in the form:

$$AV_{1:N-1} = V_{2:N} = V_{1:N-1}\begin{bmatrix} 0 & 0 & \cdots & 0 & a_1 \\ 1 & 0 & \cdots & 0 & a_2 \\ 0 & 1 & \ddots & \vdots & \vdots \\ \vdots & \ddots & \ddots & 0 & a_{N-2} \\ 0 & \cdots & 0 & 1 & a_{N-1} \end{bmatrix} + \boldsymbol{r}\cdot\hat{\boldsymbol{e}}_{N-1} = V_{1:N-1}S + \boldsymbol{r}\cdot\hat{\boldsymbol{e}}_{N-1}, \tag{62}$$

where the matrix S has a special structure and is generally referred to as a *companion matrix*. As discussed by Schmid [9] and Ruhe [33], while the eigenvalues of the companion matrix are the same as the eigenvalues of the matrix A, they will not be calculated using this approach due to numerical stability difficulties in calculating the eigenvalues of the companion matrix. In addition, this formulation may also be disproportionately influenced by error in the first and last snapshots, as has been numerically confirmed [34].

While the DMD formulation based on the companion matrix could theoretically provide dynamic information about the Koopman operator, it fails as a practical algorithm. To develop formulations that are more numerically robust and, thus, less sensitive to errors in the data, we turn our attention to matrix factorizations methods. To derive useful DMD formulations we will present the following three approaches using combinations of QR factorization and SVD:

1. QR factorization of $V_{1:N-1}$, inversion of triangular matrix R, and an eigenproblem solution.
2. QR factorization of $V_{1:N-1}$, inversion of triangular matrix R via the SVD, and an eigenproblem solution.
3. SVD decomposition of $V_{1:N-1}$ and an eigenproblem solution.

Although each of these approaches yield a data only method for finding the Ritz values and Ritz vectors of the finite dimensional Koopman operator, only two of them can practically analyze large systems. We will also assume at this point that the length of the snapshots, v, is greater than the number of snapshots by at least one, i.e., $m > N - 1$. Thus, the matrix $V_{1:N-1}$ is *tall*.

3.1.1 DMD by QR Factorization and Direct Inversion

This approach starts by substituting the *economic* QR factorization of the tall matrix $V_{1:N-1}$ (i.e., $V_{1:N-1} = QR$) into Eq. (59) to obtain:

$$AQR = V_{2:N}. \tag{63}$$

Next, right multiplying Eq. (63) by R^{-1} and left multiplying by Q^H yields:

$$Q^H A Q = Q^H V_{2:N} R^{-1} \equiv \tilde{S}_1. \tag{64}$$

Since the matrix Q is semi-unitary (i.e., $Q^H Q = I$, but $QQ^H \neq I$), it follows that the spectrum of $\tilde{S}_1$ approximates a portion of the spectrum of A [35]. The inversion of the triangular matrix R is, however, computationally challenging due to the high effort involved in finding the inverse. In contrast, we may compute the action of the inverse of a triangular matrix quite efficiently because we find it by a *triangular solve* rather than through explicit inversion [35]. In other words, solving $R\boldsymbol{x} = \boldsymbol{b}$ for $\boldsymbol{x}$ may be done quite efficiently compared to finding R^{-1}. No such numerical improvement is available for this approach, hence this method is impractical for large systems; this issue will be addressed by the next approach.

3.1.2 DMD by QR Factorization and SVD

Since finding the inverse of R in Eq. (64) is computationally costly, we substitute the SVD of the matrix R (i.e., $R = U\Sigma W^H$) into Eq. (63), to obtain:

$$AQU\Sigma W^H = V_{2:N}. \tag{65}$$

Note that since we have assumed $V_{1:N-1}$ is tall it follows that U and W are unitary and Q is a semi-unitary matrix (e.g., $U^H U = UU^H = W^H W = WW^H = Q^H Q = I$, but $QQ^H \neq I$). Also since Σ is a diagonal matrix—hence its inverse is found by taking the reciprocal of the diagonal entries—we may right multiply Eq. (65) by W and then by Σ^{-1} and left multiplying by Q^H and then by U^H, yielding the following equation:

$$U^H Q^H AQU = U^H Q^H V_{2:N} W\Sigma^{-1} \equiv \tilde{S}_2. \tag{66}$$

As in the discussion of $\tilde{S}_1$ above, due to the unitary and semi-unitary nature of U and Q, respectively, it follows that $\tilde{S}_2$ approximates a portion of the spectrum of A.

While there is additional computational cost to perform the SVD, the approach given by Eq. (66) has two advantages over Eq. (64): the inverse operation required in this approach is computationally inexpensive and allows us to introduce a noise rejection technique, which will be described in Section 3.1.4.

For systems where the dimension of $\boldsymbol{v_k}$ is much larger than the number of snapshots N, e.g., in the case of large simulations where the number of observables is very large but the number of time steps may be limited (i.e., the matrix $V_{1:N-1}$ is *tall*), this DMD formulation is especially attractive.

3.1.3 DMD by SVD

If the data matrix of the system of interest is not tall, there is no advantage in performing the QR factorization and the following third approach may offer an attractive solution formulation. Again, starting with Eq. (59) and taking the economic SVD of $V_{1:N-1}$ (i.e., $V_{1:N-1} = U\Sigma W^H$) yields:

$$AU\Sigma W^H = V_{2:N}. \tag{67}$$

If $V_{1:N-1}$ is tall then W is unitary and U is semi-unitary (e.g., $U^HU = W^HW = WW^H = I$, but $UU^H \neq I$) and if $V_{1:N-1}$ is not tall or square then U is unitary and W is semi-unitary (e.g., $U^HU = UU^H = W^HW = I$, but $WW^H \neq I$). Right multiplying Eq. (67) by W and then Σ^{-1} and left multiplying by U^H gives:

$$U^HAU = U^HV_{2:N}W\Sigma^{-1} \equiv \tilde{S}_3. \tag{68}$$

Again, the matrix $\tilde{S}_3$ approximates a portion of the spectrum of matrix A due to the semi-unitary character of U. Similar to the second approach, a noise rejection technique can be readily implemented. Henceforth, if the system is *tall* we will use Eq. (66), otherwise, Eq. (68) will be used. Recovering the approximate eigenvalues and eigenvectors of A with any of these approaches is discussed in Section 3.1.5.

3.1.4 SVD and noise rejection

A critical feature of the last two approaches is the ability to incorporate a robust noise rejection technique. To understand why noise can cause problems, consider two nearly identical snapshots from a dataset where the first is assumed to represent a linearly independent vector and the second, the difference of the two snapshots, represents another independent vector. Due to the resemblance of the two snapshots, the second vector would have very little content and would be susceptible to noise and numerical errors. Addressing these issues, we do not calculate the inverse of Σ in Eqs. (66) and (68) exactly. In fact, the main reason we use a SVD based method is that it exists for all matrices and the process is "unsurpassed" [36] for robustness with regards to its capability to find solutions for ill-conditioned or nearly rank-deficient systems.

We implement the noise reduction technique by first taking the economic SVD of the $m \times n$ matrix B ($B = U\Sigma W^H$), in this case, $B = R$ or $B = V_{1:N-1}$. To reduce the noise, we seek a low-rank

approximation to B in some sense, here the least squares sense or equivalently in the Frobenius norm [37,38]. The approximation's rank, r, is less than m and n and is selected to balance the number of DMD modes we find and the amount of information rejected as noise. To find the approximation to B, we take the singular value matrix:

$$\Sigma = \text{diag}\left(\sigma_1, \sigma_2, \ldots, \sigma_n\right), \tag{69}$$

with

$$\sigma_1 \geq \sigma_2 \geq \ldots \geq \sigma_n \geq 0, \tag{70}$$

and zero the singular values with index greater than r:

$$\tilde{\Sigma} = \text{diag}\left(\sigma_1, \sigma_2, \ldots, \sigma_r, 0, \ldots, 0\right). \tag{71}$$

Therefore, the *best* approximation in the least squares sense to B is:

$$\tilde{B} = U\tilde{\Sigma}W^H. \tag{72}$$

Since some of the diagonal entries of $\tilde{\Sigma}$ are zero, the matrix is singular and hence non-invertible, but, we can find the Moore-Penrose pseudoinverse [39]:

$$\tilde{\Sigma}^{-1} = \text{diag}\left(\sigma_1^{-1}, \sigma_2^{-1}, \ldots, \sigma_r^{-1}, 0, \ldots, 0\right). \tag{73}$$

So, in Eqs. (66) and (68) we use $\tilde{\Sigma}^{-1}$ rather than Σ^{-1}.

If the data snapshots have zero temporal mean, although not the case for our data, then the above process is equivalent to projecting the matrix $V_{1:N-1}$ into the first r POD modes.

3.1.5 DMD Modes

The remaining step is to find the DMD modes from one of the approaches presented above. As mentioned, the spectra of the defined $\tilde{S}$ matrix approximates a portion of the spectra of the Koopman operator. In other words, the Ritz values of $\tilde{S}$ represent a subset of the eigenvalues of A, giving insight into the dynamics of the system from a *data only* analysis.

In addition to the approximate eigenvalues, we seek to find approximate eigenvectors of the system. The relationship between the approximate eigenvectors of A and those found by solving for the Ritz vectors of $\tilde{S}$ may be obtained by comparing the two eigenproblems:

$$A\boldsymbol{\psi}_i = \mu_i\boldsymbol{\psi}_i, \tag{74}$$

and:

$$\tilde{S}\,\boldsymbol{\phi}_i = \mu_i \boldsymbol{\phi}_i. \tag{75}$$

Because the matrices A and $\tilde{S}$ are similar the eigenvalues in both eigenproblems are the same. Substituting the left hand side of Eq. (64), Eq. (66), or Eq. (68) for $\tilde{S}$ into Eq. (75) and rearranging into the form of Eq. (74) yields the following relationships:

$$\begin{aligned} \boldsymbol{\psi}_i &= Q\boldsymbol{\phi}_i \quad \text{for method 1,} \\ \boldsymbol{\psi}_i &= QU\boldsymbol{\phi}_i \quad \text{for method 2,} \\ \text{and} \quad \boldsymbol{\psi}_i &= U\boldsymbol{\phi}_i \quad \text{for method 3.} \end{aligned} \tag{76}$$

Notably, while the eigenvectors $\boldsymbol{\psi}$ are the standard *right* eigenvectors, we will on occasion require the less common *left* eigenvectors, $\tilde{\boldsymbol{\psi}}$, due to the lack of symmetry of A, which are given by:

$$\tilde{\boldsymbol{\psi}}_i A = \mu_i \tilde{\boldsymbol{\psi}}_i, \tag{77}$$

and:

$$\tilde{\boldsymbol{\phi}}_i \tilde{S} = \mu_i \tilde{\boldsymbol{\phi}}_i. \tag{78}$$

In these equations μ_i are again the same eigenvalues as those calculated from the right eigenproblem. The left eigenvectors are useful, when properly scaled, because the left and right eigenvectors possess the property known as biorthonormality, i.e.:

$$\tilde{\boldsymbol{\phi}}_i^H \cdot \boldsymbol{\phi}_j = \delta_{ij}. \tag{79}$$

3.2 DMD and Spring-Mass-Damper-System Example

To illustrate the DMD method, we apply the technique to the two degree of freedom (DOF) spring-mass-damper system shown in Fig. 15. The advantage of analyzing such a simple system is that it can be studied both analytically and by using the DMD method. By writing a free-body diagram for each of the masses and applying *Newton's second law*, the system in Fig. 15 is found to be governed by the following two, coupled, second-order ODEs:

$$\begin{aligned} m_1\ddot{x}_1 + (\nu_1 + \nu_2)\,\dot{x}_1 - \nu_2\dot{x}_2 + (\kappa_1 + \kappa_2)\,x_1 - \kappa_2 x_2 &= f_1 \\ m_2\ddot{x}_2 - \nu_2\dot{x}_1 + \nu_2\dot{x}_2 - \kappa_2 x_1 + \kappa_2 x_2 &= f_2, \end{aligned} \tag{80}$$

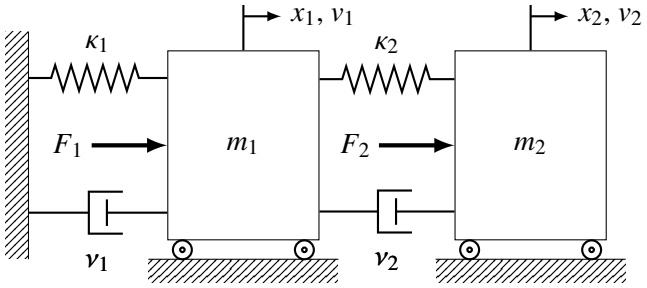

Figure 15: Two degree of freedom spring-mass-damper system

where the over-dot, $(\dot{})$, represents differentiation with respect to time. In matrix form, this system may be rewritten as:

$$M\ddot{\boldsymbol{x}} + C\dot{\boldsymbol{x}} + K\boldsymbol{x} = \boldsymbol{f}. \tag{81}$$

To analyze this system, we transform the equations from the physical coordinates, or *configuration space*, to a system of first-order ODEs using the *state space* representation with generalized coordinates [40]. While the choice of generalized coordinates ($\boldsymbol{q}$) is not unique, a logical set is the displacement and velocity vectors, $\boldsymbol{q} = \{\boldsymbol{x}(t) \;\; \dot{\boldsymbol{x}}(t)\}^T$. To transform the system into state space, we supplement Eq. (81) with the identity $\dot{\boldsymbol{x}} = \dot{\boldsymbol{x}}$ and write as:

$$\begin{aligned} \dot{\boldsymbol{x}} &= \dot{\boldsymbol{x}} \\ \ddot{\boldsymbol{x}} &= -M^{-1}C\dot{\boldsymbol{x}} - M^{-1}K\boldsymbol{x} + M^{-1}\boldsymbol{f}. \end{aligned} \tag{82}$$

Note that for lumped mass systems the mass matrix, M, is diagonal and, thus, mathematically trivial to invert. Making use of the generalized coordinates, Eq. (82) may be rewritten as:

$$\dot{\boldsymbol{q}} = T\boldsymbol{q} + B\boldsymbol{d}, \tag{83}$$

where $\boldsymbol{d} = \{\boldsymbol{0} \;\; \boldsymbol{f}\}^T$ and

$$T = \begin{bmatrix} 0 & I \\ -M^{-1}K & -M^{-1}C \end{bmatrix} \quad \text{and} \quad B = \begin{bmatrix} 0 \\ M^{-1} \end{bmatrix}. \tag{84}$$

Applying Eq. (83) to the system shown in Fig. 15 yields:

$$T = \begin{bmatrix} 0 & 0 & 1 & 0 \\ 0 & 0 & 0 & 1 \\ -\frac{1}{m_1}(\kappa_1 + \kappa_2) & \frac{\kappa_2}{m_1} & -\frac{1}{m_1}(\nu_1 + \nu_2) & \frac{\nu_2}{m_1} \\ \frac{\kappa_2}{m_2} & -\frac{\kappa_2}{m_2} & \frac{\nu_2}{m_2} & -\frac{\nu_2}{m_2} \end{bmatrix} \quad \text{and} \quad B = \begin{bmatrix} 0 & 0 \\ 0 & 0 \\ \frac{1}{m_1} & 0 \\ 0 & \frac{1}{m_2} \end{bmatrix}. \tag{85}$$

Two advantages of the state space representation are that the system is uniquely quantified by the state vector, $\boldsymbol{q}$, and that it can handle systems with general damping, rather than the more restrictive proportional damping case, $C = \alpha M + \beta K$, that we are often limited to in configuration space approaches. Unfortunately, the coefficient matrices are no longer symmetric in this representation. The consequences of this loss of symmetry include: (i) the eigenvalues are in general complex and (ii) the right eigenvectors are no longer orthogonal. The first of these is actually an advantage as the eigenvalue gives both the angular frequency and the growth/decay rate of the mode. The second point is addressed by the biorthonormality property of the right and left eigenvectors as discussed in the previous section.

If we assume that the system in Fig. 15 is unforced, the solution of Eq. (83), in discrete time, can be expressed in the following form [40]:

$$\boldsymbol{q}_{k+1} = e^{T\Delta t}\boldsymbol{q}_k, \tag{86}$$

where Δt is the time step. "In spite of the above apparent simplicity," Jack Hale [41] warns, "the matrix e^{At} is a rather complicated individual." One approach for handling much of this complication is through an eigenmode decomposition:

$$\boldsymbol{q}_{k+1} = e^{T\Delta t}\boldsymbol{q}_k = Z_L e^{\Lambda\Delta t} Z_R^H \boldsymbol{q}_k, \tag{87}$$

where Z_L and Z_R are matrices composed of the left and right eigenvectors of T, respectively, placed column-wise in the matrices, and Λ is a diagonal matrix containing the eigenvalues of T. Thus, in the right hand side of Eq. (87) much of the complication is shifted to finding the left and right eigenvectors and their normalization. Equation (87) also shows that given the initial state of the system, the solution can be constructed if the eigenvalues and eigenvectors of the coefficient matrix are known.

Next we will relate the eigenmode decomposition and the DMD/Koopman operator. From Eqs. (52) and (87) and since in this case $\mathcal{G}$ is equal to the identity operator it follows that $A = \mathcal{K} = \mathcal{T} = e^{T\Delta t}$. Further, the eigenvalues and eigenvectors of T may be related to the DMD modes by considering the eigenproblems $T\psi = \lambda\psi$ and $e^{T\Delta t}\phi = \mu\phi$. Expanding the matrix exponential, e^T, into its power series, it may be shown that the eigenvectors, ψ and ϕ, are identical and that the eigenvalues

of the T matrix (λ) are related to the eigenvalues of the Koopman operator (μ) by the relationship:

$$\lambda = \frac{\ln(\mu)}{\Delta t}. \tag{88}$$

To demonstrate the ability of the DMD approach to calculate a system's eigenmodes, the state vector will be calculated at equally spaced time intervals and these data will be used as the observations/snapshots for input into the DMD method. Using the system parameters shown in Table 3 and performing an eigenvalue analysis of the associated matrix, T, the true eigenvalues of the operator are found and are listed in the first row of Table 4.

Table 3: Example system parameters

Parameter	m_1	m_2	ν_1	ν_2	κ_1	κ_2	Δt	N
Units	[kg]	[kg]	[N s/m]	[N s/m]	[N/m]	[N/m]	[s]	[-]
Value	1	1	0.1	0.1	1	1	0.01	2500

With the initial conditions, $\boldsymbol{q}(0) = \{1 \;\; 0 \;\; 0 \;\; 0\}^T$, the DMD was performed using Eqs. (68), (75), and (76) as described in the previous section, and the resulting eigenvalues, which have been transformed with Eq. (88) into the more typical form (λ), are given in the second row of Table 4. The error for the first and second pair of eigenvalues is $-1.51 \cdot 10^{-7} \pm 1.88 \cdot 10^{-6} i$ and $-4.86 \cdot 10^{-9} \pm 1.96 \cdot 10^{-8} i$. Consistent with this example, Duke et al. [34] found that the DMD method typically reproduces the angular frequency more accurately than the growth/decay coefficient. They also found—like we expected from the Krylov origin if this method—that good results could be obtained from a relatively short total data sample length; for linear systems, such as our example, one quarter of a wavelength may provide an adequate length dataset [34]. The results in Table 4 show that: (i) the Ritz values occur in complex conjugate pairs due to the real nature of the coefficient matrix, and (ii) the real part of each value is negative, as expected, due to the damped nature of the system.

The calculated DMD based Ritz vectors are compared with the true eigenvectors of the system's coefficient matrix in Fig. 16. It shows that the DMD reproduces the system eigenvectors. For the four modes, we define the normed error as $||\phi - \tilde{\phi}||_{L2}$, resulting in errors of 0.0588, 0.1558, 0.0278, and 0.0730.

Table 4: Comparison of system eigenvalues

Source	λ_1, λ_2	λ_3, λ_4
T matrix	$-0.13090170 \pm 1.61273021i$	$-0.01909830 \pm 0.61773883i$
DMD	$-0.13090476 \pm 1.61273021i$	$-0.01909831 \pm 0.61773884i$

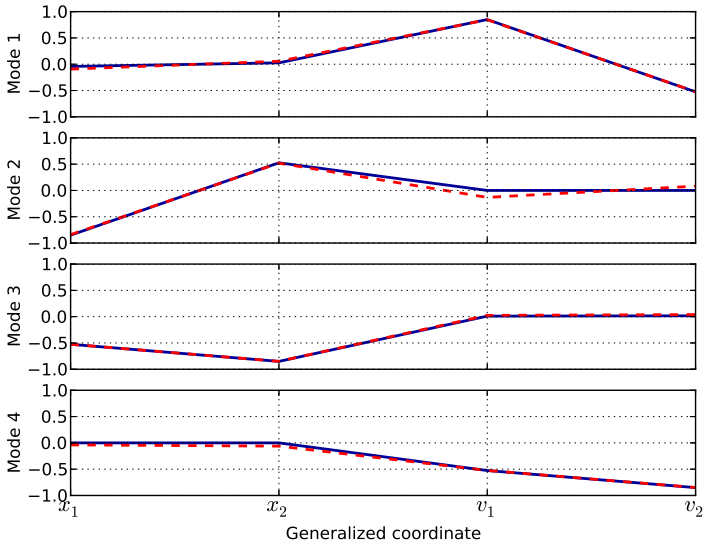

Figure 16: True eigenvectors (solid blue lines) and DMD synthesized modes (dashed red lines)

Using the DMD method, we also investigate the DMD modal coefficients to allow reconstruction of the original data (with the aid of the SVD based noise reduction technique). We begin from the definition of $\tilde{S}$, in this case Eq. (68), and recognizing that using an eigenvalue decomposition:

$$\tilde{S} = Z_R \Omega Z_L^H = Z_R \Omega Z_R^{-1}, \tag{89}$$

where the matrix Ω is the diagonal matrix with the calculated Ritz values of $\tilde{S}$, μ, as its entries. Equations (68) and (89) are equated and rearranged to solving for Ω:

$$\Omega = Z_R^{-1} U^H Q^H A U Q Z_R \tag{90}$$

This equation shows that $Z_R^{-1} U^H Q^H$ is the matrix that diagonalizes A, suggesting that we transform our snapshots ($\boldsymbol{v}_k = \boldsymbol{q}_k$) using this matrix. Defining this transformed vector at time step k as:

$$\boldsymbol{u}_k \equiv Z_R^{-1} U^H Q^H \boldsymbol{q}_k. \tag{91}$$

The original state vector may be written as $\boldsymbol{q}_k = QUZ_R\boldsymbol{u}_k$ and using this form to replace both the k^{th} and $(k+1)^{\text{th}}$ snapshot in Eq. (55) yields:

$$QUZ_R\boldsymbol{u}_{k+1} = AQUZ_R\boldsymbol{u}_k. \tag{92}$$

Rearranging Eq. (92) to isolate $\boldsymbol{u}_{k+1}$ and comparing the resulting expression with Eq. (90) we find:

$$\boldsymbol{u}_{k+1} = \Omega\boldsymbol{u}_k. \tag{93}$$

Equation (93) shows the original coupled ODEs have been decoupled, i.e., the solution evolves for each DMD mode independently. This finding suggests that $\boldsymbol{u}_i$ may be expanded in terms of the eigenvalues and eigenvectors as follows:

$$\boldsymbol{u}_k = c_1\mu_1^{k-1}\phi_1 + \ldots + c_P\mu_P^{k-1}\phi_P = \sum_{j=1}^{P} c_j\mu_j^{k-1}\phi_j = \Omega^{k-1}Z_R\boldsymbol{c}. \tag{94}$$

In this equation P is the number of eigenmodes found from $\tilde{S}$, which is equal (like in this example) or less than (typical) the dimension of the matrix A, and $\boldsymbol{c}$ is the vector containing the coefficient $(c_1, c_2, \ldots)$ for each DMD mode. In principle, if $P = \text{Dim}(A)$ (not typical) and the eigenvalues are unique, then the coefficients should be constant in time and may be found by rearranging Eq. (94) and substituting Eq. (91) for $\boldsymbol{u}_k$, to give:

$$\boldsymbol{c} = Z_R^{-1}\Omega^{-(k-1)}Z_R^{-1}U^HQ^H\boldsymbol{q}_k. \tag{95}$$

Using Eq. (95) and the initial snapshot to find the coefficients yields:

$$\boldsymbol{c} = Z_R^{-1}\Omega^0Z_R^{-1}U^HQ^H\boldsymbol{q}_1 = Z_R^{-2}U^HQ^H\boldsymbol{q}_1. \tag{96}$$

For our example, the initial DMD modal coefficient vector is found to be $\boldsymbol{c} = \{-0.034+0.566i,\ -0.074+0.051i,\ 0.013-0.929i,\ -0.063-0.264i\}^T$. With these coefficients, the state of the system can be found at any time step, k, by rearranging Eq. (95) into the following form:

$$\tilde{\boldsymbol{q}}_k = QUZ_R\Omega^kZ_R\boldsymbol{c}, \tag{97}$$

where $\tilde{\boldsymbol{q}}_k$ is the synthesized time history of the state vector, which has been calculated without explicitly requiring the coefficient matrix T. Figure 17 compares the positions and velocities obtained by numerically integrating the system (solid lines with blue for mass 1 and green from mass 2) with

those calculated using the DMD method (thick dashed lines with green for mass 1 and blue from mass 2). For the limited simulation time, the numerically integrated data and the DMD synthesized data are indistinguishable.

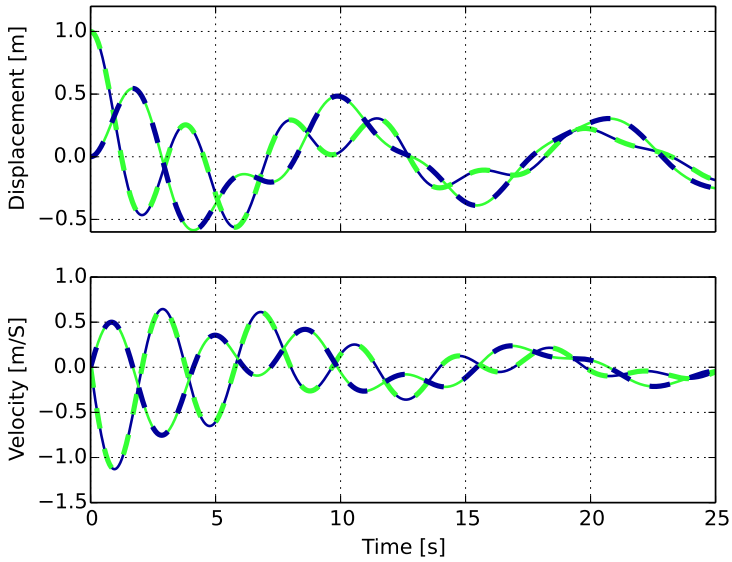

Figure 17: Time history of system state — solid lines: numerically integrated solution; dashed lines: DMD prediction based on calculated modes and initial state coefficients

For this simple case, where we had complete, noise-free data, the DMD method captured all of the system dynamics; i.e., the four DMD modes/Ritz values pairs reproduce the numerically integrated data very accurately. Forming a relative error in the L_∞ sense, the error is found to be less than $3 \cdot 10^{-6}$ for each of the four states.

While it is not clear yet whether the DMD can be used in general to find specific system parameters, much can be learned about the system if the DMD generates a complete basis, i.e., when the number of DMD modes equals the dimension of the governing ODE. If this is the case and there are no repeated eigenvalues, as in our example, we suggest a new approach that can reconstruct the system coefficient matrix from observations only using the relation $T = Z_R \Lambda Z_L^H = Z_R \Lambda Z_R^{-1}$. The

exact matrix, T, and the DMD synthesized matrix, $\tilde{T}$ are presented in Eq. (98):

$$T = \begin{bmatrix} 0 & 0 & 1 & 0 \\ 0 & 0 & 0 & 1 \\ -2 & 1 & -0.2 & 0.1 \\ 1 & -1 & 0.1 & -0.1 \end{bmatrix}$$

$$\tilde{T} = \begin{bmatrix} -2.76137325 \times 10^{-6} & 1.10482747 \times 10^{-6} & 9.99999371 \times 10^{-1} & -2.03497078 \times 10^{-7} \\ 1.69993459 \times 10^{-6} & -6.92936225 \times 10^{-7} & 3.93414590 \times 10^{-7} & 1.00000013 \\ -2.00000096 & 1.00000041 & -2.00002655 \times 10^{-1} & 1.00000031 \times 10^{-1} \\ 1.00000059 & -1.00000025 & 1.00001631 \times 10^{-1} & -1.00000033 \times 10^{-1} \end{bmatrix}. \tag{98}$$

The data in Eq. (98) show that the differences between elements of T and $\tilde{T}$ are less than $3 \cdot 10^{-6}$. Using the definition of the matrix T (Eq. (85)) and the DMD calculated $\tilde{T}$ matrix, a system of equations may be derived for the mass, stiffness, and damping coefficients. Since this system of equations is linear and homogeneous, its solution can only be determined up to a constant factor. Assuming $m_1 = 1.0\,\text{kg}$ is known, the remaining system parameters are found to be: $\tilde{m}_2 = 1.00000016\,\text{kg}$, $\tilde{k}_1 = 1.00000055\,\text{N/m}$, $\tilde{k}_2 = 1.00000041\,\text{N/m}$, $\tilde{\nu}_1 = 0.10000262\,\text{N s/m}$, $\tilde{\nu}_2 = 0.10000004\,\text{N s/m}$. The damping coefficient ν_1 was found to have the worst error, but it was less than $3 \cdot 10^{-5}$, where the error is defined for each parameter as $|\tilde{x} - x|/x$. The effects of noise and inability to directly observe the state vector have not yet been quantified for these findings.

This example has shown that under optimal conditions that the DMD was able to reproduce the system eigenvalues and eigenvectors from a data only approach. We have also found the modal coefficients that allow for the time history of the system to be reconstructed and if the governing equation is known, system parameters may be found. These positive findings support further exploring the DMD method for larger, nonlinear, and noisy systems.

CHAPTER IV

DYNAMICS MODE DECOMPOSITION METHOD ANALYSIS RESULTS

In the previous two chapters, we have discussed the development of a laboratory-scale combustor to simulate full-scale CIs, discussed the high-speed diagnostic data that were acquired under stable and unstable operating conditions, and discussed the use of the DMD method in the processing of large datasets in the search of important dynamical system features. In this chapter, we apply the DMD method to analyze experimental data in an effort to elucidate the mechanisms that drive CIs in our laboratory-scale combustor as an analogy to CIs in full-scale LREs. We seek to find how the diagnostics of the measured velocities, pressures, and OH and CH^* radicals are related and how this information can be used to find the key steps of the CI feedback mechanism. This mechanism will likely depend on the acoustic field, flow field, reaction rates, reaction zone anchoring, and coherent structure convective velocities.

In search of these important steady and dynamic features of the system, we first processed the data using traditional averaging techniques, e.g., finding the temporal mean of each diagnostic at each spatial location, allowing us to extract time-averaged features from the flow field. Next, we analyzed the data with the DMD method, as discussed in Chapter 3, to find the coherent dynamic content from each of the diagnostic measurements. But, this will lead us to a shortcoming of processing simultaneously acquired data in a non-simultaneous fashion—potentially leading us to the wrong conclusions. This shortcoming suggests that we process the data simultaneously with the DMD method; we will call this technique the simultaneous dynamic decomposition (SDD). This concept was suggested by Schmid [9] and we will discuss our developed technique in Section 4.3. We have since found similar work by Richecoeur et al. [42]. Next, we compare the data acquired from the stable and unstable experimental conditions and build a conceptual feedback mechanism that might explain the observed CI. In the remainder of this chapter, we analyze the combustion stability for a 1017 Hz SDD mode by calculating the mode's Rayleigh index and Rayleigh integral. Our

calculations show this mode is stable, but in Chapter 6 we will show that this mode still plays an important role in the CI observed in the experiment.

4.1 Frequency Domain and Statistical Data Reduction Approaches

Focusing first on the PIV and PLIF data as we build our understanding of CI mechanisms, we begin by using standard data analysis techniques—such as statistical and frequency domain based approaches—to analyze the datasets from the stable and unstable experiments. Initially we determined the temporal mean for each dataset, for each diagnostic, at each spatial location. These mean images for the unstable case dataset are shown in Figs. 18a and 18b. The first plot, Fig. 18a, shows the spatial distribution of the velocity vectors and the contour coloring represents the y-component of the velocity to highlight different regions of the flow field. The mean velocity data show a well defined inner recirculation zone, along with inner and outer shear layers of the swirling reacting flow. The inner recirculation zone is produced by vortex breakdown along the centerline of the flow. The locations of the shear layers are important because hydrodynamic instabilities of these shear layers grow into large scale vortical structures, which are responsible for large scale mixing. The second plot, Fig. 18b, shows the spatial dependence of the mean OH intensity. It shows that a conical reaction zone is stabilized below the central recirculation zone in the low velocity/stagnation region associated with the reverse flow. Near the injector, the reaction zone is collocated with the inner shear layer. Notably, Figs. 18a and 18b show that while the inner shear layer diverges slightly from the axis with downstream distance, the reaction zone divergence is significant. This situation is similar to that observed by Emerson et al. who studied bluff body stabilized flames and noted that when the low density region spread faster than the shear layer, there were strong hydrodynamic shear layer instabilities [43]. This finding could provide a mechanism for nonlinear growth of perturbations near the anchor point as they propagate downstream. Figures 18a and 18b also show the velocity and combustion fields are not perfectly symmetric, especially the velocity field. Swirl stabilized flames are often asymmetric, especially in confined environments, due to the highly three dimensional structure of the inner recirculation zone [44]. The time-averaged features that we have identified are shown schematically in Fig. 18c.

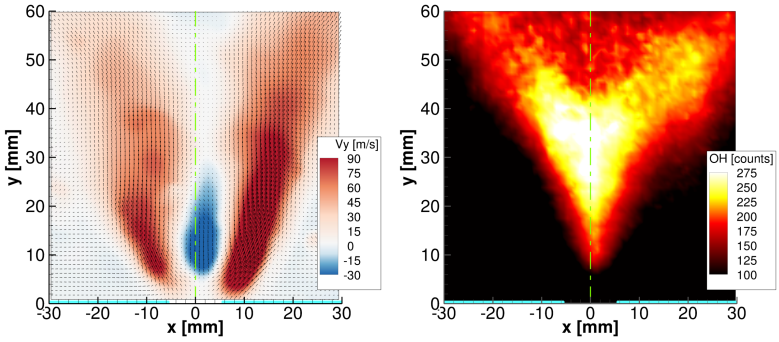

(a) PIV temporal mean (b) PLIF temporal mean

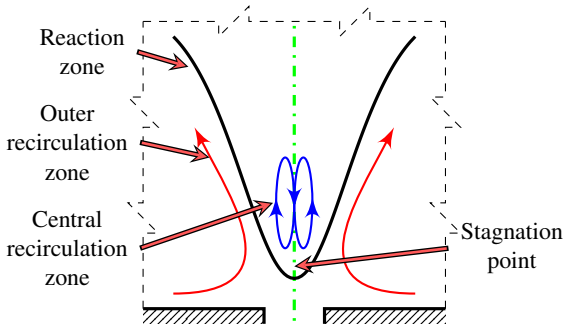

(c) Time-averaged structure

Figure 18: Unstable dataset temporal means and time-averaged structure schematic

Much like our analysis of the acoustic data in Section 2.3.2, we performed a frequency domain analysis to identify significant frequencies in the PIV and PLIF data and begin to identify the physical processes associated with these frequencies. The time history of the PIV and PLIF data at each spatial location was analyzed to find the PSD at that point by Welch's method using four ensembles with zero overlap and Hanning windowing [45]. The PSDs at each point were averaged over the spatial domain for each of the cases and diagnostics, see Fig. 19. The *solid* lines and the *dash-dot* lines represent the stable and unstable PSD, respectively.[1] We examine the data from the unstable experiment first. The unstable acoustic mode near 170 Hz is visible in each of the three diagnostic measurements. These data also show a second peak at 440 Hz, which may be due to the 3W acoustic mode, which from calculations shown in Table 2 is near 430 Hz, or vortex/exhaust nozzle interaction as we will discuss later. In contrast to the unstable combustor data, the stable combustor spectra show no large spike at the combustor's natural acoustic frequency of 267 Hz or at the previously

[1]The PLIF data have been scaled so that the noise floor of the stable case is similar to that of the stable x-direction velocity data to present the data on the same plot.

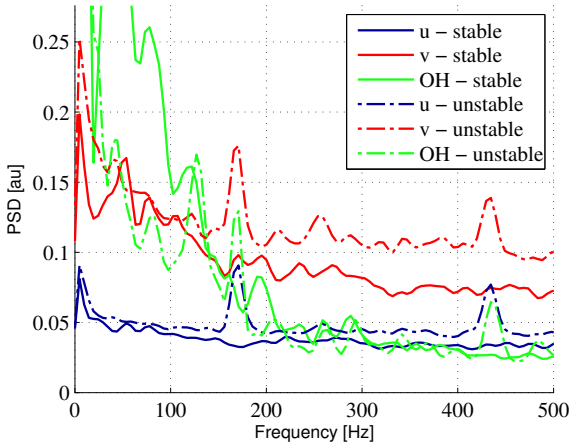

Figure 19: PSD of velocity and scaled PLIF data for both the stable and unstable datasets

observed 170 Hz instability, although 170 Hz is not a natural acoustic mode of the shorter combustor configuration. As we might expect, using only the data from the stable measurements we cannot identify the potential instability that may result from changing the system's acoustic length.

To investigate whether important spatial structures in the investigated combustion process can be found using traditional methods, we analyze the PSD results from the unstable combustor by plotting the difference of the power spectrum at 170.9 Hz and the noise floor at 183.1 Hz, as shown in Fig. 20. It shows the PSD content of the x-direction velocity components and the OH intensity at each spatial location. The x-component velocity PSD, Fig. 20a, has a well organized spatial structures oscillating at 170 Hz that could be important to the CI mechanism. The areas of high amplitude oscillations are relatively far from the injector, but as we will discuss later these regions may not be the most important regions when considering the transverse velocity. The OH intensity PSD, Fig. 20b, shows significant combustion fluctuations at 170 Hz throughout the reaction zone, again with the largest amplitudes occurring downstream of the injector, near the shear layers.

The PSD identifies the important frequencies from the data and even the location of high amplitude oscillations, but the technique is limited in its ability to provide a complete description of the spatial and temporal dynamics. One limitation, due to the second order statistical nature of the technique, is that the phase data are lost. Hence, we will explore additional techniques to aid in our understanding of CIs.

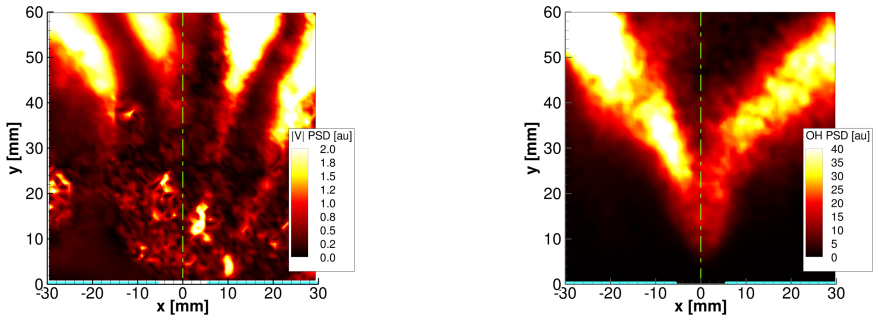

(a) PIV power spectrum

(b) PLIF power spectrum

Figure 20: Unstable combustor PSD at 170.9 Hz minus noise floor at 183.1 Hz

While these basic approaches have provided some understanding of the system behavior, other less commonly used techniques are available that may provide additional information. For example, the kurtosis may be used to analyze the data. The kurtosis is one measure of a probability density function (PDF) and its departure from a normal Gaussian distribution. Since random noise is expected to have a Gaussian distribution, according to the mean value theorem, values of kurtosis far from the Gaussian value of 3 may indicate the presence of something other than random noise or turbulent fluctuations. The kurtosis of the PIV and PLIF data for the unstable experiments are shown in Figs. 21a and 21b. In both figures, white represents values near the Gaussian value of 3, with red and blue representing values greater than and less than 3, respectively. The x-velocity component data (Fig. 21a) show that the kurtosis is greater than 3 almost everywhere. The PDFs of the PIV data have tall narrow peaks and wide tails. The wide tails show us that extreme values occur more frequently than we would expect for a normal distribution. This is likely due to noise in the PIV data, making the kurtosis not very useful here. In contrast, the OH data, Fig. 21b, show a well defined region of low kurtosis that is located near the edge of the time-averaged reaction zone. This low value of the kurtosis indicates the PDFs have a broad peak or even bimodal distribution, without frequently occurring extreme events. By comparing the OH data kurtosis and the OH data PSD at 170 Hz, we find the kurtosis indicates there may be important oscillatory features in the flow that are closer to the injector than those identified by the PSD data. Likely, small fluctuations near the stagnation point, which are difficult to measure, grow nonlinearly downstream and become more pronounced and easier to find in the PSD.

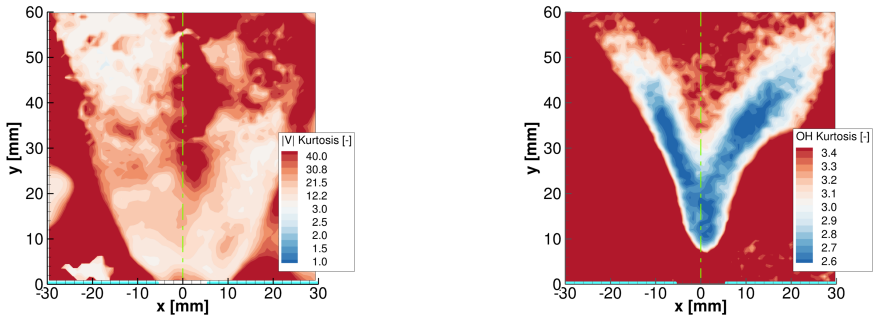

(a) PIV velocity magnitude kurtosis

(b) PLIF kurtosis

Figure 21: Unstable dataset kurtosis

4.2 DMD Analysis of Individual Diagnostic Datasets

The DMD method offers useful capabilities for studying nonlinear physics while maintaining many of the advantages of a linear analysis. In this section, we will use the DMD method to analyze the PIV and then the PLIF data, separately.[2] Then, in the following section, we will present an approach that allows for these datasets to be simultaneously analyzed.

4.2.1 DMD Analysis of PIV Data

Initially, the DMD was used to analyze the unstable PIV data to find the Ritz values and Ritz vectors (i.e., approximate eigenvalues and eigenvectors) of the velocity field. The resulting modes, an example of which is shown in Fig. 22, suggest the presence of an outer shear layer instability. Figures 22a and 22b show the real and imaginary parts of a complex Ritz vector, respectively. The second image may be thought of as the same mode shown in the first image, phase-shifted by 90°, which are conceptually analogous to the sine and cosine functions. This oscillatory pattern, spatially shifted between the two phases, shows the traveling wave nature of these modes. The contour coloring for these figures represent the x-direction component of the normalized velocity (the eigenmode has been normalized to have an L^2 norm of 1) and the alternating bands of transverse velocity are indicative of vortical structures. The offset in phase of the vortical structure from the left to right half planes in Fig. 22 may be due to the presence of a helical vortex core wrapped around the

[2]Only representative results will be given here, while a thorough discussion of typical DMD results will be postponed until Section 4.3.2.1.

inner recirculation zone, as shown by the POD mode analysis of Steinberg et al. [46] and the LES study of Roux et al. [47].

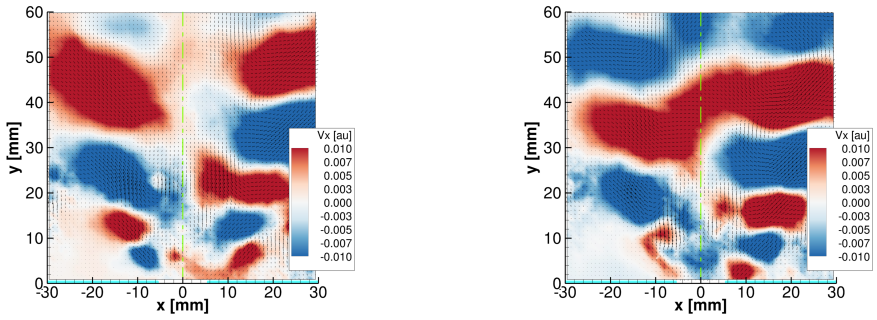

(a) Real velocity at 984 Hz (b) Imaginary velocity at 984 Hz

Figure 22: Example of a DMD mode from the unstable experiment PIV (x-component) data

4.2.2 DMD Analysis of PLIF Data

Next we used the DMD technique to analyze the unstable OH-PLIF dataset. One resulting mode is shown in Fig. 23. Again, a comparison of the mode's real and imaginary parts suggests that this is a traveling wave mode. These modes show that the high OH intensity oscillations are primarily confined to a region near the outer edge of the time average reaction zone, near the inner shear layer. In addition, the mode plotted is much stronger on the left hand side of the injector axis, but similar modes exist that are stronger on the right hand side, which have slightly different frequencies and growth rates.

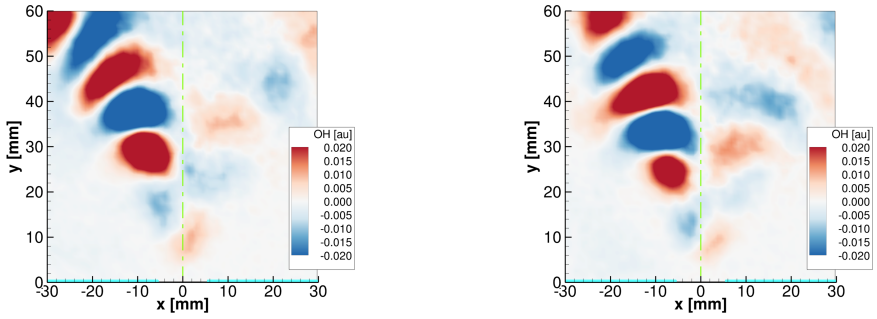

(a) Real OH intensity at 2385 Hz (b) Imaginary OH intensity at 2385 Hz

Figure 23: Example of an unstable PLIF dataset DMD mode

The above discussion suggests that applying the DMD method to the PIV and PLIF datasets separately, one may conclude that an outer shear layer instability drives combustion oscillations near

the inner shear layer, which may not be the case. To illustrate the potentially unrelated nature of the outer shear layer instability and the combustion oscillations, we plotted, see Fig. 24, the Ritz values found in the separate analyses of the PIV and PLIF data for the unstable condition. In this figure the x-axis and y-axis represents the growth or decay parameter and the real angular frequency of the modes, respectively. Examination of Fig. 24 shows that the PIV (black circles) and PLIF (red squares) spectra significantly differ from one to another except for the Ritz value at the origin, which represents a non-dynamic *steady* mode. Since the two sets of Ritz values are considerably different, we may conclude that the outer shear layer instability and the combustion oscillations are not necessarily related. To investigate potential coupling between the PIV and PLIF data—which we expect intuitively—another approach must be used to analyze the system.

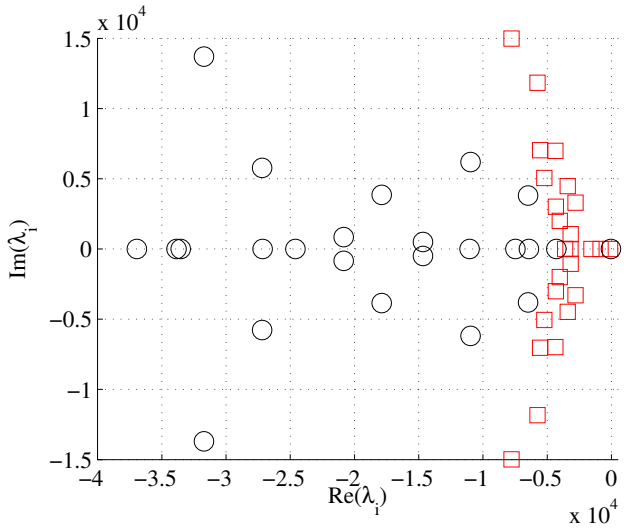

Figure 24: Ritz values for separate PIV (black circles) and PLIF (red squares) datasets

4.3 Simultaneous Dynamic Decomposition

This section presents a new approach that we have developed for analyzing the simultaneously acquired data, the SDD method. This effort was motivated by the inability of the previously used techniques to identify the salient dynamic features of the investigated CI mechanism from the separately processed data and the more subtle idea that the closer the measurement vector is to the state vector, the better the DMD approximates the governing physics of the system, see Section 3.1.

4.3.1 The SDD Concept

In this study, we developed a DMD based approach for analyzing simultaneously acquired, high-speed, diagnostic data. To demonstrate this concept, we present the method through an example utilizing the simultaneously measured PIV and PLIF data discussed earlier. Then, in Section 4.3.3 the SDD method is used to analyze the PIV, PLIF, chemiluminescence, and acoustic data together.

Figure 25 shows a diagram that describes the manner in which the DMD method may be used to analyze simultaneously acquired data. Again, while this concept was developed independently during this study, it is similar to the approach presented by Richecoeur et al. [42]. The SDD method begins, at each time step, by reshaping into column vectors and scaling (if necessary) the two dimensional data matrices (i.e., images) that represent the x-direction and y-direction velocity components and the OH-PLIF intensity. These vectors are then concatenated into a single, larger vector. Since the DMD method is invariant to row exchanges, the ordering of data within the vectors is arbitrary but must be consistent. Recalling that the input vectors for the DMD are commonly referred to as *snapshots*, the new vector containing the simultaneously measured data will be referred to as a *super-snapshot*. Returning to the diagram, the super-snapshots from each time step become the input into the DMD algorithm.

From Chapter 3 we recall that the input to the DMD algorithm was a series of snapshots equally spaced in time and the output was a set of complex Ritz values, each of which is associated with a Ritz vector. The Ritz values describe the modal angular frequency and growth or decay rate and the Ritz vectors represent the spatial dependence of the mode. In the SDD algorithm, the Ritz vectors calculated by the DMD method contain information from both the velocity and OH intensity snapshots. In fact, the vectors have the same component-wise structure as the input super-snapshots, i.e., if the j^{th} component of the super-snapshots corresponded with the y-direction velocity component at location (13 mm,47 mm), then the j^{th} component of the Ritz vectors corresponds to the (normalized) y-direction velocity component at location (13 mm,47 mm) for each mode. As a result, for each Ritz value, the Ritz vectors may be broken back into smaller vectors and reshaped into images corresponding to the coupled x-direction velocity component, y-direction velocity component, and OH-PLIF intensity.

Conceptually, if we use the DMD method as discussed in Sections 4.2.1 and 4.2.2—which analyzed each diagnostic dataset separately—then the Ritz values and Ritz vectors we find depend only on the analyzed dataset, as demonstrated by Eq. (99):

$$\begin{aligned} \boldsymbol{v}_{PIV} &\rightarrow DMD \rightarrow \lambda_{PIV}(\boldsymbol{v}_{PIV}),\ \boldsymbol{\phi}_{PIV}(\boldsymbol{v}_{PIV}) \\ \boldsymbol{v}_{PLIF} &\rightarrow DMD \rightarrow \lambda_{PLIF}(\boldsymbol{v}_{PLIF}),\ \boldsymbol{\phi}_{PLIF}(\boldsymbol{v}_{PLIF}). \end{aligned} \tag{99}$$

On the other hand, the SDD method finds a single set of Ritz values that is dependent on both sets of diagnostic data:

$$\boldsymbol{v} = \begin{Bmatrix} \boldsymbol{v}_{PIV} \\ \boldsymbol{v}_{PLIF} \end{Bmatrix} \rightarrow DMD \rightarrow \lambda(\boldsymbol{v}_{PIV}, \boldsymbol{v}_{PLIF}),\ \boldsymbol{\phi}(\boldsymbol{v}_{PIV}, \boldsymbol{v}_{PLIF}) = \begin{Bmatrix} \boldsymbol{\phi}_{PIV}(\boldsymbol{v}_{PIV}, \boldsymbol{v}_{PLIF}) \\ \boldsymbol{\phi}_{PLIF}(\boldsymbol{v}_{PIV}, \boldsymbol{v}_{PLIF}) \end{Bmatrix}. \tag{100}$$

Equation (100) shows that the Ritz modes $\boldsymbol{\phi}_{PIV}$ and $\boldsymbol{\phi}_{PLIF}$ are now dependent on both the PIV and PLIF data. In other words the modes found by the SDD method, $\boldsymbol{\phi}$, represent the coupled oscillation of both the velocity, $\boldsymbol{\phi}_{PIV}$, and OH intensity, $\boldsymbol{\phi}_{PLIF}$, at the complex frequency λ. Showing two things, this method of processing simultaneously measured data preserves the spatial and temporal relationship between the multiple diagnostic measurements and locates modes with common dynamics (λ) in the physical phenomena represented by the data.

4.3.2 SDD Analysis of PIV and PLIF Data

To illustrate the advantages of the SDD method, we will use it to analyze the simultaneously measured, high-speed, PIV and PLIF data from the stable and unstable tests. The SDD input data was scaled to

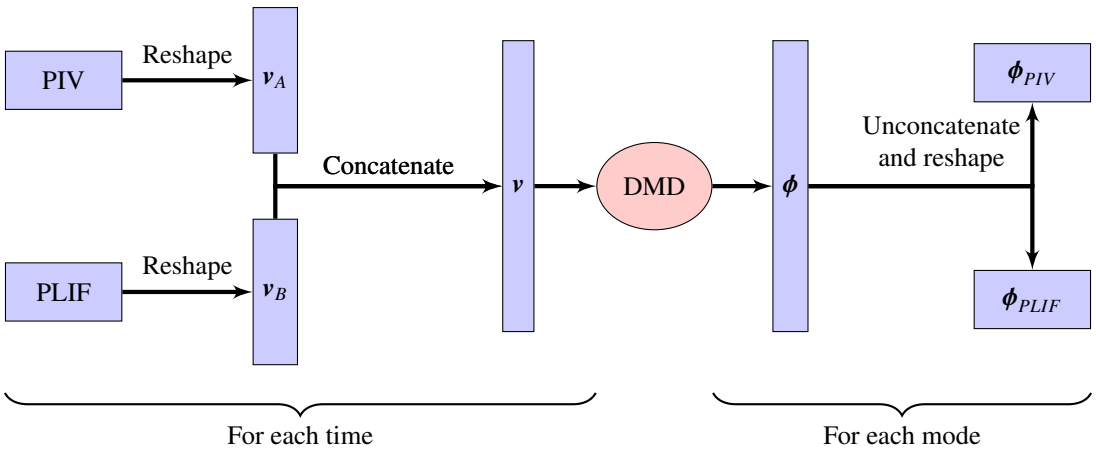

Figure 25: The SDD conceptual data flow

make the time average PIV and PLIF vectors have a L^2 norm of $1/3$ and 1, respectively; this choice will be discussed in Section 4.3.3.

4.3.2.1 Typical Results

We present SDD results for the unstable test data and discuss the results in detail to show what type of information may be accessed by this approach. The stable and unstable experimental measurements will be discussed in the next section.

Figure 26 shows data obtained from the unstable case consisting of the singular value distributions, a Ritz value map, and Ritz vectors. Figure 26a presents the normalized singular values, plotted on a log-log scale. The x-axis represents the index of the singular value and the y-axis the singular value magnitude normalized by the largest singular value. In this example, the relative singular value threshold used was equal to 0.03 for forming the pseudoinverse. Any singular values below this threshold are regarded as noise. The analysis showed that there were 21 singular values that exceeded this threshold value. As a result, the DMD algorithm produces 21 approximate eigenvalues and eigenvectors. These complex Ritz values were converted from the *exponential* form (μ) to the more typical *time-stepper* form (λ) by Eq. (88) and were plotted on the complex plane in Fig. 26b where the x-axis is the growth or decay factor and the y-axis is the real angular frequency. Three points are highlighted on this plot: the diamond at the origin, labeled *c-d*, represents the steady mode, see Figs. 26c and 26d, which is approximately equivalent to the (scaled) temporal mean; the square box, labeled *e-f*, shows the Ritz value of the Ritz mode displayed in Figs. 26e and 26f; and the circled Ritz value, labeled *g-h*, is associated to the mode in Figs. 26g and 26h. Each oscillatory image pair represents the real normalized velocity and real normalized OH intensity of a single Ritz mode—associated with a single Ritz value. Since the real and imaginary parts of the oscillatory modes are similar in structure and represent a $\pm\pi/2$ phase shift in the mode, we will typically show only the real or imaginary part of a mode when the physical interpretation of the two parts is similar. The first pair of images, shown in Figs. 26c and 26d, describe the spatial distribution of the steady mode. The contours represent the y-direction velocity component to highlight the central recirculation zone and the steady OH intensity image employs a false colormap to highlight the time-average reaction zone. In Figs. 26e to 26h the red-blue color in the left plots represents

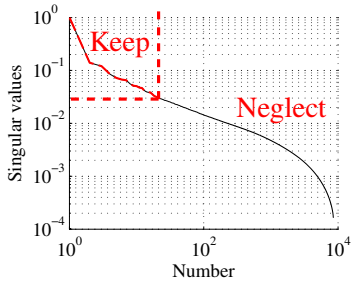

(a) Singular values

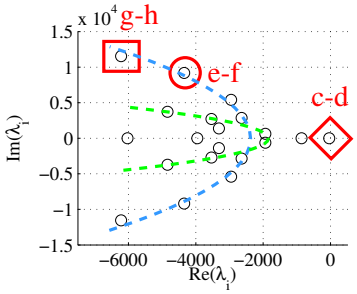

(b) Ritz values

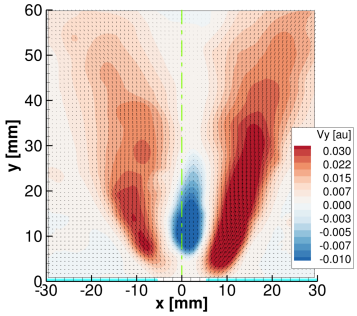

(c) Steady velocity

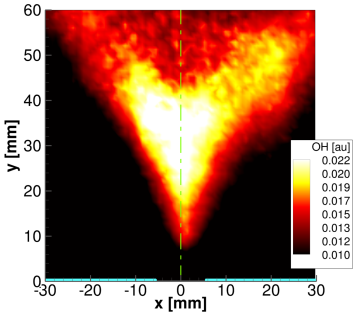

(d) Steady OH

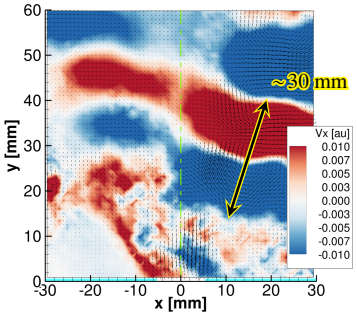

(e) Velocity at 1460 Hz

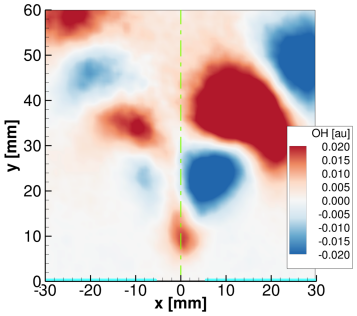

(f) OH at 1460 Hz

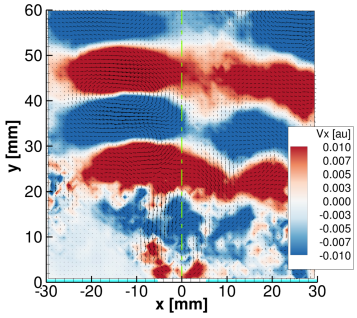

(g) Velocity at 1837 Hz

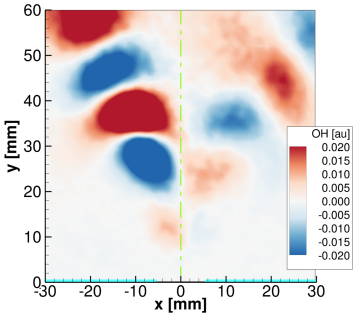

(h) OH at 1837 Hz

Figure 26: Typical SDD data

positive-negative x-velocities, respectively, to highlight vortical structures. The red-blue color in the right plots represents more-less OH intensity than the steady mode.

The first oscillatory mode, shown in Figs. 26e and 26f, has a frequency of 1460 Hz and both the velocity and OH intensity exhibit similar spatial structures; i.e., this mode represents a coupled oscillation in the velocity and OH intensity at 1460 Hz. The structure has a wavelength, shown in Fig. 26e, of approximately 30 mm. Thus, using the wavelength and frequency it is possible to calculate a *convective velocity* for this structure. Such calculations for this and other modes showed that the convective velocity approximately equals 36 m/s. Turning to the second oscillatory mode, Figs. 26g and 26h, at 1837 Hz, a similar structure is found but with a shorter characteristic wavelength, approximately 20 mm. Again the convective velocity is approximately 36 m/s. This sequence of similar structures with increasing frequency and deceasing size, which progressively have their largest amplitudes closer to the injector, is a characteristic of related DMD modes found in a parabolic arc like series of values on the eigenvalue map. Two such parabolas are shown by dashed lines in Fig. 26b. Furthermore, in both oscillatory modes there is a positive correlation between the x-velocity and increased OH intensity on the right of the injector centerline and a negative correlation on the left. The change in sign of the correlation is due to the change in the direction of the velocity with respect to the flame propagation direction on the opposite sides of the injector axis. We interpret this finding physically as the x-direction velocity component of vortical structures alternately push the reaction zone in on itself—decreasing OH intensity—and push the reaction zone into fresh reactants—enhancing combustion. The reaction zone augmentation by the vortical structures is shown schematically in Fig. 27.

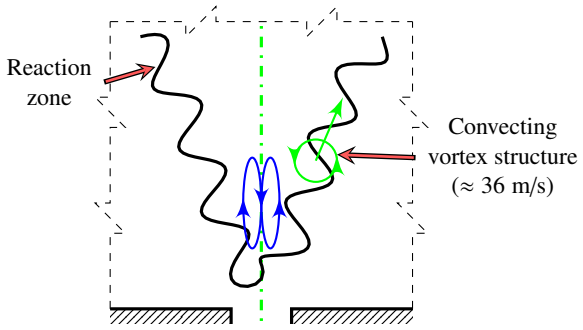

Figure 27: Hydrodynamic and combustion interaction

With the identification of the convective velocity of the vortical structures above, we can explain the presence of the 440 Hz peak in the PSDs of the unstable data. Using the SDD based convective velocity and the axial height of the combustor (76.2 mm), we can find the time for a vortical structure to originate at the injector exit and propagate to the exhaust nozzles, where the structure is accelerated, acting as an acoustic source. Furthermore assuming the acoustic wave propagates at a roughly uniform speed of sound (estimated as 549 m/s) upstream back to the injector exit, then we can calculate the acoustic propagation time. This returning acoustic wave perturbs the shear layers, creating a disturbance that grows into a vortical structure, hence completing the cycle. In addition, this process occurs at a frequency very near the 3W acoustic mode. We estimate the combined hydrodynamic and acoustic cycle frequency by the reciprocal of the total time:

$$f = \frac{1}{\tau_{\text{hydro}} + \tau_{\text{ac}}}, \tag{101}$$

where τ_{hydro} and τ_{ac} have been estimated as 0.0021 s and 0.00014 s, respectively. With this equation we find the estimated frequency of this feedback cycle is 443.4 Hz, quite close to the observed frequency in the unstable PSDs.

Recalling from Eq. (96) that a snapshot, $\boldsymbol{v}_k$ (which is an approximation to the state vector), we can find the DMD modal coefficients of the system. Then using Eq. (97) we can reconstruct or *synthesize* an approximation to $\boldsymbol{v}_k$ that has been filtered through the DMD modes. As an example, we project a raw (noisy) instantaneous velocity field (shown in Fig. 28a) and OH intensity field into the 21 SDD modes found above. We use the coefficients from this projection to reconstruct the instantaneous velocity and OH fields. These fields have been simplified by the process as we can see in the velocity field shown in Fig. 28b.

Some of the features in the raw image appear to be missing from the reconstructed image, but the reconstructed image only retains the coherent mono-frequency dynamic structures found within the 21 SDD modes. More dynamical modes, more features, and more noise would be retained if more singular values are retained when forming the pseudoinverse. We have added green streamlines to Fig. 28b to highlight the tight vortical structure wrapped around the inner recirculation zone, which is hard to identify in the more complex velocity field of Fig. 28a. This process of projection and

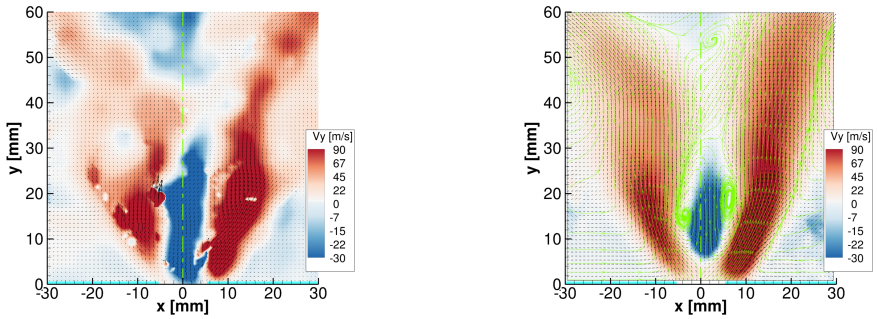

(a) Raw images (b) Reconstructed images

Figure 28: Noise reduction and coherent mode dynamic highlighting with DMD synthesis

synthesis allows us to identify the important dynamical features more easily than possible from the original noisy data.

4.3.2.2 Stable vs. Unstable Experimental Datasets

To identify key similarities and differences between the stable and unstable combustor configurations described in Section 2.2, the PIV and PLIF data from two experiments were analyzed with the SDD method. Both datasets were processed using the SDD method described in Section 4.3.1, with a normalized singular value threshold of 0.03, which yielded 25 modes in the stable case and 21 modes in the unstable case. Figure 29 shows the combined PIV and PLIF spectra for the stable (red squares) and unstable (black circles) datasets. Inspecting this figure we find that a large number of Ritz values in one spectra have a corresponding mode in the second spectra that has a similar Ritz value. We did not expect this similarity because of the considerably difference in stability between the two cases. Furthermore, this similarity may indicate that some of the key fluid dynamics and combustion processes are largely the same in both the stable and unstable cases.

Figures 30 and 31 show a selection of oscillatory modes from the stable and unstable combustor configurations, respectively, taken from the upper parabolic arc like structure found in Fig. 29. The mode shown in Figs. 30a and 30b has a similar Ritz value as the mode shown in Figs. 31a and 31b and so on. Comparing these figures we find that not only are the Ritz values similar, but the mode shapes are also similar—especially comparing the high frequency modes from each figure. This correspondence between modes further supports the conclusion that the hydrodynamic and combustion processes are similar in the stable and unstable cases. So, if we can identify and model

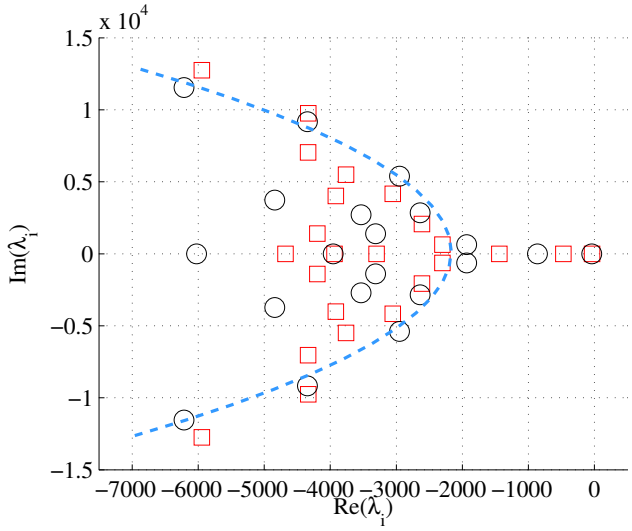

Figure 29: Ritz values from the SDD method, stable (red squares) and unstable (black circles) experiments

the differences between these two cases, in the future, it may be possible to use data acquired from stable experiments to predict unstable operation.

Up to this point, we have not identified how the high-frequency hydrodynamic modes and induced combustion oscillations can provide energy to lower frequency acoustic modes. To see how this transfer might occur, we continue the discussion started in Section 4.3.2.1 about how the modes along an arc in the Ritz value complex plane have related structures with high-frequency/short wavelength structures closer to the injector and low-frequency/long wavelength structures further downstream. Physically, as a coherent structure propagates downstream (away from the injector) it grows in size due to diffusion/viscous effects and the pairing of two or more vortical structures into a larger structure. This growth in structure size and decrease in frequency is likely a key link between the higher frequency hydrodynamic oscillations and the lower frequency, transverse acoustic modes. For example, if the coherent structures grow in size to the point where their characteristic frequency is close to that of an acoustic natural frequency, the oscillatory motion of the coherent structure would make the heat release fluctuate, which acts as a source of energy for the natural acoustic mode.

Analyzing the unstable experimental dataset, we found SDD modes with frequencies of 101 Hz and 221 Hz, which are near the CI frequency of 170 Hz. The 221 Hz mode is shown in Fig. 32. While not directly related to the 170 Hz acoustic mode, the SDD mode structure oscillates mainly

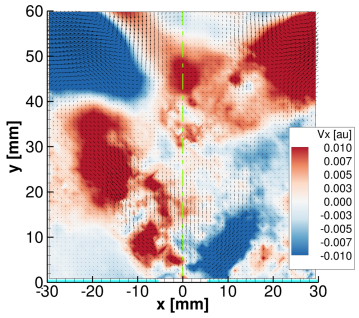

(a) Velocity at 329 Hz

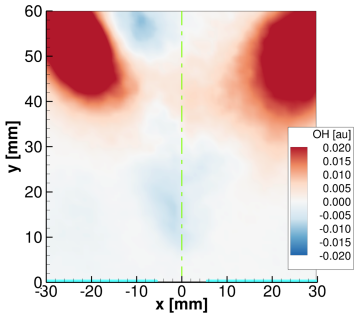

(b) OH at 329 Hz

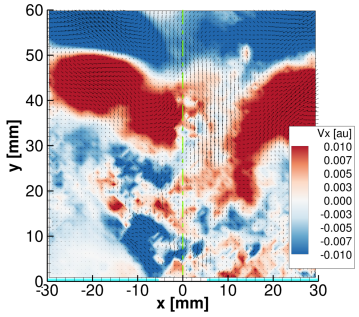

(c) Velocity at 875 Hz

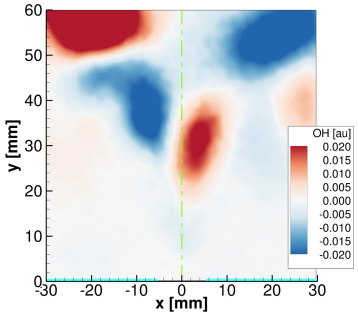

(d) OH at 875 Hz

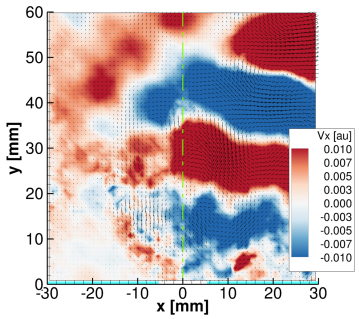

(e) Velocity at 1554 Hz

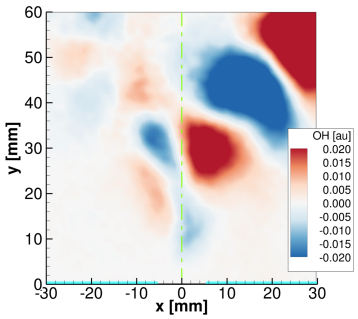

(f) OH at 1554 Hz

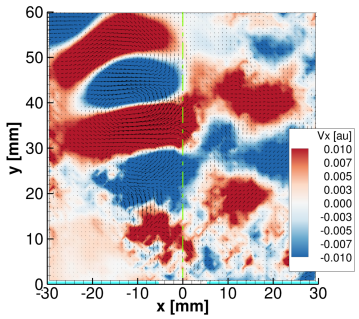

(g) Velocity at 2029 Hz

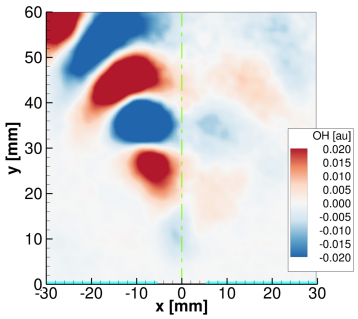

(h) OH at 2029 Hz

Figure 30: SDD modes from stable configuration

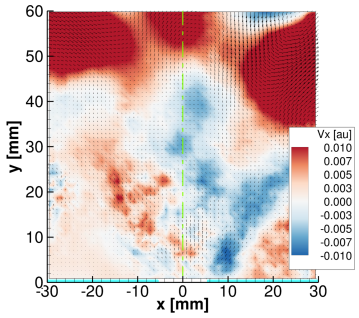

(a) Velocity at 454 Hz

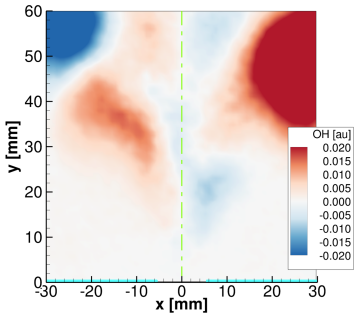

(b) OH at 454 Hz

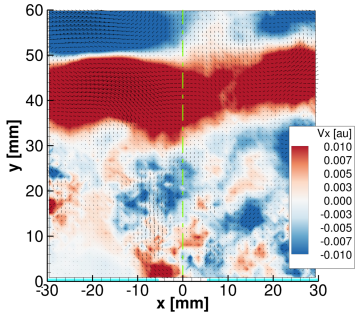

(c) Velocity at 859 Hz

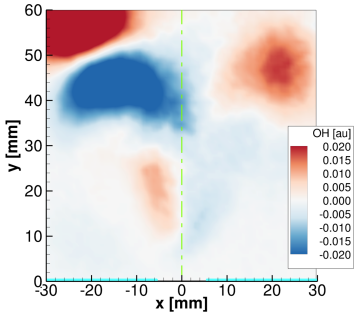

(d) OH at 859 Hz

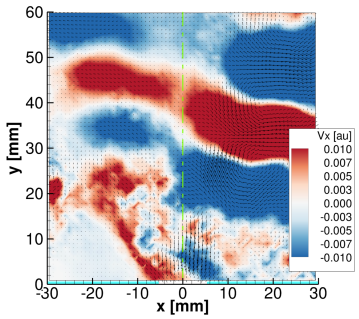

(e) Velocity at 1460 Hz

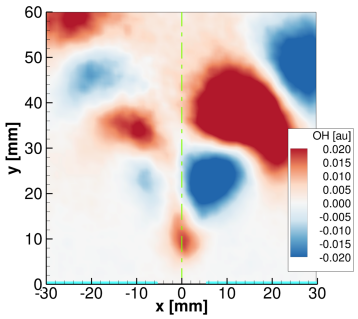

(f) OH at 1460 Hz

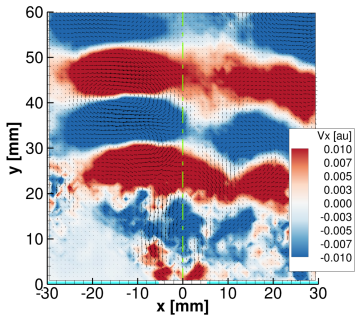

(g) Velocity at 1837 Hz

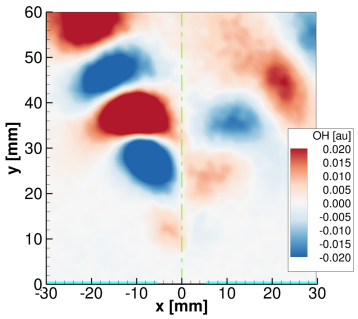

(h) OH at 1837 Hz

Figure 31: SDD modes from unstable configuration

downstream of the injector in the x or transverse direction and is similar to the structure found in the velocity data PSD at 170 Hz (see Fig. 20a). Linear theory predicts that there will be no transfer of energy between modes at different frequencies, but the system is nonlinear and energy transfer between modes of differing frequencies can occur when the frequency difference is not too large. Conceptually this is similar to the energy transfer by nonlinear terms in the turbulent energy cascade [48]. So the similar structures and frequencies of the SDD mode and the 170 Hz PSD might indicate that it is possible for nonlinear transfer of energy between these modes.

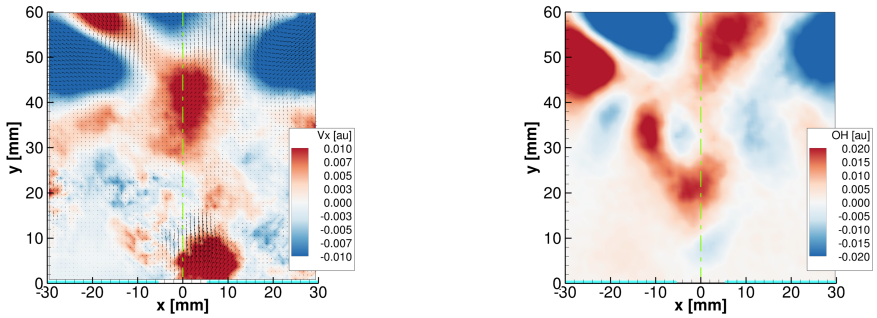

(a) Imaginary velocity

(b) Imaginary OH intensity

Figure 32: DMD mode at 221 Hz from unstable dataset

The above discussed observations and the previously discussed combustion zone structure, see Fig. 18c, suggest a feedback process that may be responsible for the observed CI. Recalling from Fig. 20b that there were 170 Hz oscillations in OH intensity throughout the reaction zone, but that the fluctuations were larger in amplitude further downstream. These larger OH intensity oscillations are not likely due to direct perturbation from the transverse acoustic field because the magnitude of the fluid dynamic velocities in this region may be on the order of 50 m/s, while the transverse acoustic velocities are orders of magnitude smaller. However, near the stagnation/reaction zone anchor point, the acoustic velocity is large compared to the local fluid dynamic velocities. Hence, this important region of the flow field may be directly influenced by the acoustic waves.

We begin our description of the proposed CI feedback mechanism with the perturbation of the reaction zone anchor point. First, the stagnation point of the aerodynamically stabilized reaction zone is perturbed by the transverse acoustic velocity field. This perturbation of the inner recirculation zone may then excite hydrodynamic waves of the inner shear layer that convect—at an approximate velocity of 36 m/s—downstream. As they convect downstream, these waves grow into large scale structures,

which perturb the reaction zone. The processes of acoustic perturbation of the reaction zone anchoring and coherent structure propagation are shown schematically in Fig. 33. The perturbation of the unstable shear layer results in a nonlinear growth through which the small hydrodynamic waves become large enough to affect the combustion process, although initially at the high frequencies of the hydrodynamic instability. The growth and pairing processes then cause the frequency to drop to the point where energy may be transfered nonlinearly to the transverse acoustic modes. The combustion heat release oscillations cause an unsteady volumetric expansion, which acts as an acoustic source. If some of the new acoustic energy goes into the 170 Hz acoustic mode (at the correct phase) then the feedback cycle is complete.

Since the SDD analyses revealed that many of the modes were similar when the combustor was operating in the stable and unstable configurations, it is necessary to understand why CI was not excited in the stable case. Recalling that in the stable configuration the combustor was shorter and its natural acoustic mode frequencies larger, it is possible that in this case the heat release oscillations could not couple with the natural acoustic modes of the combustor. Likely, due to an incompatibility of the oscillatory combustion frequencies/phases and the natural acoustic modes as dictated by the sign of the Rayleigh index (positive: driving, negative: damping):

$$\mathcal{R}_j = \int_{cycle} \dot{q}'_j p'_j \, \mathrm{d}t. \tag{102}$$

Also, because the combustor geometry was different between the two cases, the location of the combustion relative to the standing acoustic velocity and pressure fields are different. The change

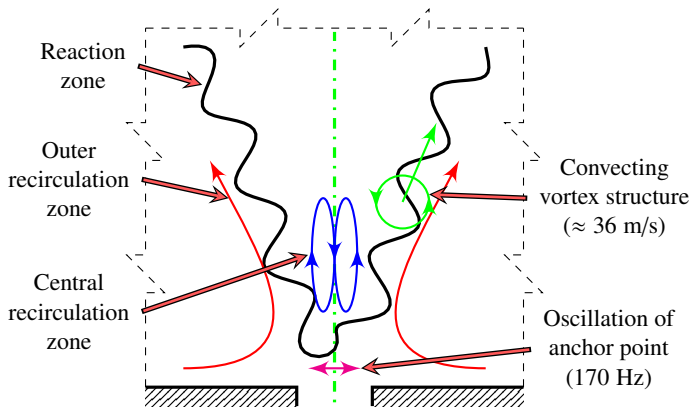

Figure 33: System dynamics

in pressure field directly influences the Rayleigh index and the acoustic velocity oscillations likely effect the oscillatory combustion—again potentially changing the Rayleigh index.

The overall combustion stability is given by the sign of the volumetric integral of the Rayleigh index, known as the Rayleigh integral:

$$\mathcal{RI}_j = \int_{\mathcal{V}} \int_{\text{cycle}} \dot{q}'_j p'_j \, \mathrm{d}t \, \mathrm{d}\mathcal{V} = \int_{\mathcal{V}} \mathcal{R}_j \, \mathrm{d}\mathcal{V}. \tag{103}$$

Meaning, if for mode j that $\mathcal{RI}_j > 0$, then net energy is added to the mode during the cycle through the combustion process and the system is linearly unstable.

Another view of the Rayleigh integral is possible by exchanging the order of the integrations with respect to time and volume:

$$\mathcal{RI}_j = \int_{\text{cycle}} \int_{\mathcal{V}} \dot{q}'_j p'_j \, \mathrm{d}\mathcal{V} \, \mathrm{d}t = \int_{\text{cycle}} \mathcal{SI}_j \, \mathrm{d}t, \tag{104}$$

where $\mathcal{SI}_j$, the spatially integrated Rayleigh index in defined as:

$$\mathcal{SI}_j \equiv \int_{\mathcal{V}} \dot{q}'_j p'_j \, \mathrm{d}\mathcal{V}. \tag{105}$$

Using this view of the Rayleigh integral, $\mathcal{SI}_j$ describes the total driving or damping as a function of time—or equivalently as a function of phase of the mode. In this work, we have assumed that the unsteady heat release is proportional to the intensity of the CH^*-chemiluminescence, i.e., $\dot{q}'_j \propto I_{\text{chemi}}$ and due to the line of sight integrating nature of the measurement Eq. (105) may be written:

$$\mathcal{SI}_j \equiv \int_{\mathcal{V}} \dot{q}'_j p'_j \, \mathrm{d}\mathcal{V} \propto \int_{\text{x,y}} I_{\text{chemi}} p'_j \, \mathrm{d}x \, \mathrm{d}y. \tag{106}$$

We will continue the Rayleigh integral discussion at the end of the next section.

4.3.3 SDD Analysis of PIV, PLIF, Chemiluminescence, and Acoustic Data

Up to this point, the results we have shown have been for the combined PIV and PLIF datasets. In this section, we extend the SDD technique to include the chemiluminescence and acoustic data. To accomplish this, we discuss how acoustic data has been treated slightly differently than other datasets, discuss our chosen scaling for each data type, and apply the SDD method in an attempt to elucidate the 170 Hz combustion instability.

The dynamic pressure measurements, as discussed in Section 2.3 and Appendix C, were acquired at 20 kHz and anti-aliased with a low pass filter, while the optical diagnostic techniques were limited to acquisition rates of 10 kHz and are subject to aliasing in the temporal domain. These facts allowed us to treat the pressure data slightly differently than the optical data, and as we look at the combined data in the following paragraphs, we rely on the high-quality, antialiased acoustic data more heavily than other data types.

First, the three pressure sensors employed were downsampled from 20 kHz to 10 kHz, forming the first three signals within the acoustic dataset. But, this employees only half of the acquired data and, more importantly, only characterizes half of the acoustic state variables, namely p' and u' or equivalently p' and $\mathrm{d}p'/\mathrm{d}t$. Continuing with our desire to include as much state variable information as possible into the analyses, we used a fourth order finite difference algorithm to estimate $\mathrm{d}p'/\mathrm{d}t$ at 10 kHz for each of the three pressure signals and included these three new signals into the total acoustic pressure dataset.

$$v_{AC} = [p'_1 \quad p'_2 \quad p'_3 \quad \dot{p}'_1 \quad \dot{p}'_2 \quad \dot{p}'_3]^T \tag{107}$$

To maintain similar numerical values for the pressure and its derivatives, the derivative was multiplied by the sampling frequency, 10,000.

As we discussed briefly in Section 4.3.1, the scaling of each data point is somewhat arbitrary, meaning that if the signal from one pressure sensor was multiplied by a scaling factor, the resulting SDD mode point corresponding to this pressure would also be scaled by the same factor. But, the choice of scaling for each data point does affect the overall SDD results. We have chosen to keep the data within specific data types scaled as measured, but we will apply scale factors to each data type to shift the importance placed on each of these datasets in the SDD analyses. The scale factors were defined to require the norm of the temporal average of the absolute value at each point within the data type to be equal to the prescribed scale factor. For example, the absolute value of the PLIF data at each spatial location j is temporarily averaged and the resulting vector is scaled so that its norm is equal to the prescribed scaling factor, i.e.,:

$$\mathrm{SF}_{PLIF} = \|\langle|\phi_{PLIF,j}|\rangle\| \tag{108}$$

Since we can scale all of the data by a common factor and not change the results we have chosen the PLIF scale factor to be equal to one. In the previous results in this chapter, we found good results when the PIV data was scaled so that it was less important in the SDD analyses. We believe that overall improved modal structures in both the PIV and PLIF components of the mode was due to the deemphasis of the noisy PIV data when determining the Ritz values of the system. Specifically we have chosen the PIV scale factor to be one-third. Since the chemiluminescence data appears to be of good quality and represent similar phenomenon to the OH PLIF data, we have chosen the chemiluminescence scale factor to also equal one. Lastly, due to the high quality, antialiased nature of the acoustic data and its vital importance in the CI, we have chosen a scale factor of three for the acoustic data type. The scale factors are summarized in Table 5. The sensitivity to different scale factors is examined in Section 6.2.3.

Since our primary interest is elucidating the observed CI we primarily focus on analyzing the unstable experiment dataset. Applying the scale factors in Table 5 to the unstable dataset, combining the data into super-snapshots with the SDD approach, and performing the analysis yields the Ritz value spectra shown by crosses in Fig. 34. The two sub figures represent the same data displayed in two different ways, related by Eq. (88). Figures 34a and 34b show the exponential, μ, and time stepper, λ, forms of the approximate eigenvalues, respectively. In the latter plot, points to the left and right (if there were any) of the y-axis represents stable and unstable modes, respectively, while in the first plot, modes whose modulus is less than one and greater than one represent stable and unstable modes, respectively. In this figure we have included the unit circle for reference.

The frequency and modulus of the two largest modulus dynamic modes (largest $|\mu|$ not on the y-axis) are listed in Table 6 under the heading *unfiltered* and the PIV, PLIF, and chemiluminescence components of these modes are shown in Figs. 35 and 36. Figure 35 represents a nearly neutrally stable mode, which is perhaps due to a helical vortex structure, albeit not perfectly symmetric, as

Table 5: Relative scale of different data types during SDD combination process; each data vector type scaled so the norm of their temporal averages equals the value given

Data type	PIV	PLIF	Chemiluminescence	Acoustic
Norm/scale of data	1/3	1	1	3

Table 6: SDD predicted frequencies and moduli of estimated exponential eigenvalue of the two leading dynamic modes from analysis using unfiltered and filtered acoustic data (all other data used in the same way)

Acoustic data	Unfiltered	Filtered
f [Hz]	1016.94	22.85
$\|\eta\|$	0.9395	0.9688
f [Hz]	549.79	565.15
$\|\eta\|$	0.8167	0.8121

seen in Figs. 35a and 35b. Similar to our discussions in Section 4.3.2, the transverse velocity shown in Figs. 35a and 35b and the regions of more or less OH intensity shown in Figs. 35c and 35d appear to correlate well, negatively and positively on the left and right side of the injector axis, respectively. For the first time, in this figure, we see that there are regions where the OH PLIF and the CH^* chemiluminescence look similar, but with some differences. The first difference between these two measurements, assuming that the flame is nearly premixed, is that while CH^* exists primarily in the heat release zone of the flame, the OH radical is generated near this zone, but has a longer lifetime and thus exists in appreciable content in hot exhaust products. This difference may not be evident in the Ritz vectors because the dynamic modes represent the difference from the temporally steady portion of the data and both the CH^* and OH radicals are generated in similar spatial locations and, thus, have a steep gradient in similar spatial locations. Likely, some of the small differences—like the larger region of high (red) combustion on the right hand side of Fig. 35f compared to that found in Fig. 35d—are due to the planar versus line of sight integrated nature of the two measurements. The acoustic amplitude for the three pressure signals for the 1017 Hz mode can be found in Fig. 37 (the crosses). The red and green markers represent the pressure sensors that are attached to the combustion chamber on either side of the injector via standoff tubes for protection against the high temperatures, while the blue markers represent a sensor in the acoustic duct away from the combustor. From Fig. 37, we see that highest average dynamic chamber pressure (average of red and green crosses) that is found from this analysis corresponds to the 1017 Hz mode. This results checks well with our PSD results shown in Fig. 8.

It is interesting to note that the 1017 Hz mode corresponds well to an estimate of the rotational frequency of the swirling flow. Assuming that the maximum rotational velocities are 1.1 to 1.2 times

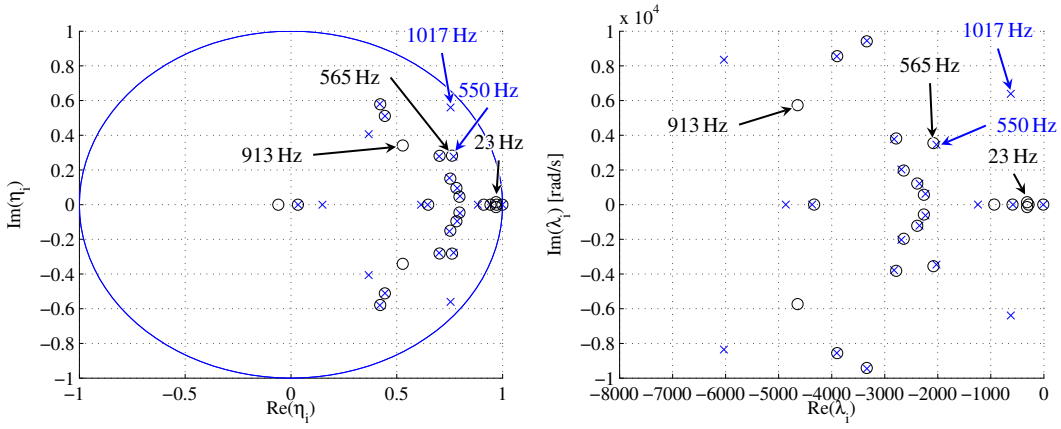

(a) Approximate exponential eigenvalues (b) Approximate time-stepper eigenvalues

Figure 34: SDD spectra for unstable experimental dataset using unfiltered and filtered acoustic data

the maximum axial velocities for this range swirl number and that the tangential velocities peak near the outer shear layer [47], then we can estimate the rotational period of the swirl as:

$$\tau = \frac{(2\pi)(0.016\,\text{m})}{(1.15)(90\,\text{m/s})} = 0.000971\,\text{s}, \tag{109}$$

which corresponds to a frequency of 1029.5 Hz.

Turning to the 550 Hz mode shown in Fig. 36, we see that the PIV and PLIF portions of the mode have similar a structure to the 1017 Hz mode we found in Fig. 35. In fact, the apparently helical or annular hydrodynamic structure is stronger in the 550 Hz mode. On the other hand, while the PLIF and chemiluminescence portions of the 1017 Hz mode were similar, these two mode portions in the 550 Hz mode are substantial different, indicating large out of plane content in the 550 Hz mode. Comparing the acoustic amplitude for these two modes, see Fig. 37, yields that the average dynamic chamber pressure for the 550 Hz mode is approximately half that of the 1017 Hz mode. While the modal frequencies of these two modes are not integer multiples of each other, they likely represent a single combined hydrodynamic/combustion/acoustic oscillation related to the 4 W and 7 W natural acoustic modes.

Figure 37b shows the same acoustical mode data as Fig. 37a, but limited to the frequency range of 0 to 300 Hz. As we see, none of the modes are at the acoustically observed combustion instability frequency of 170 Hz. At this point we would like to explore whether the 1017 Hz mode is dominating the analysis technique and thus we are missing the desired 170 Hz mode. To suppress the 1017 Hz

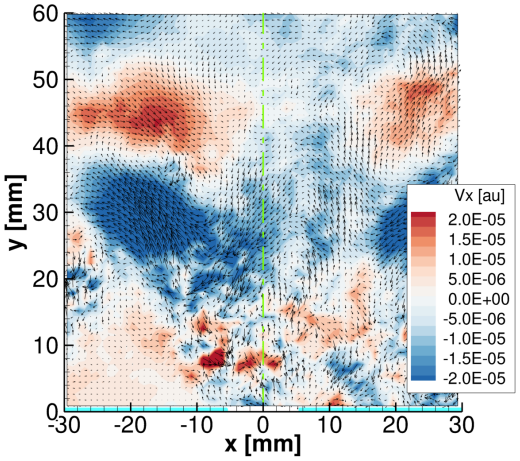

(a) Real part of PIV component of SDD mode

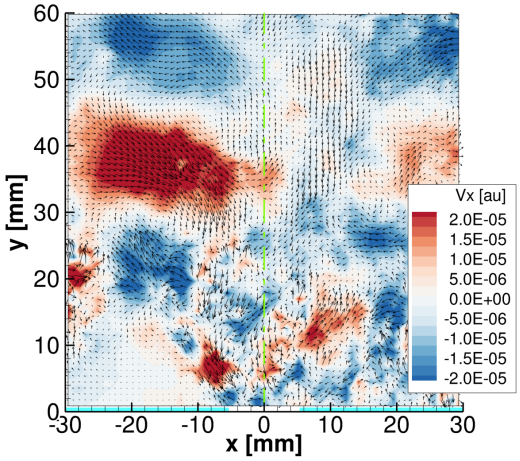

(b) Imaginary part of PIV component of SDD mode

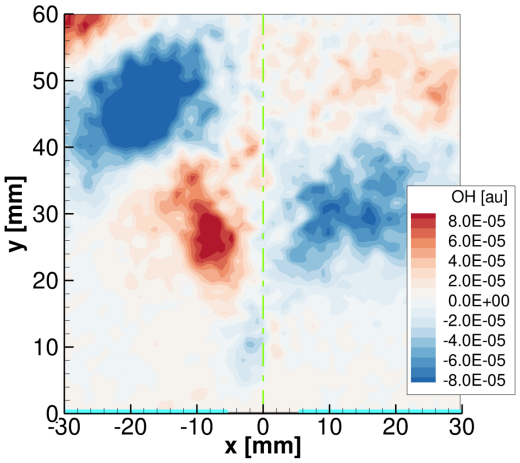

(c) Real part of PLIF component of SDD mode

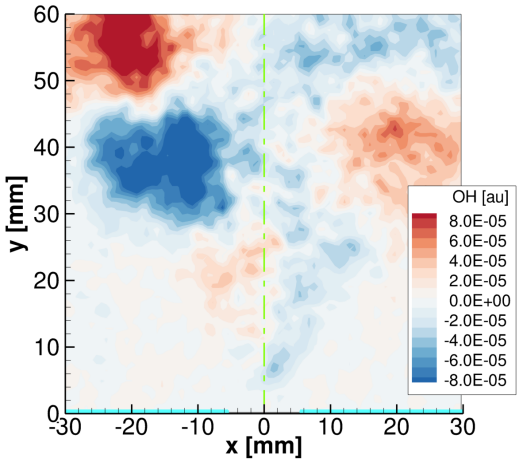

(d) Imaginary part of PLIF component of SDD mode

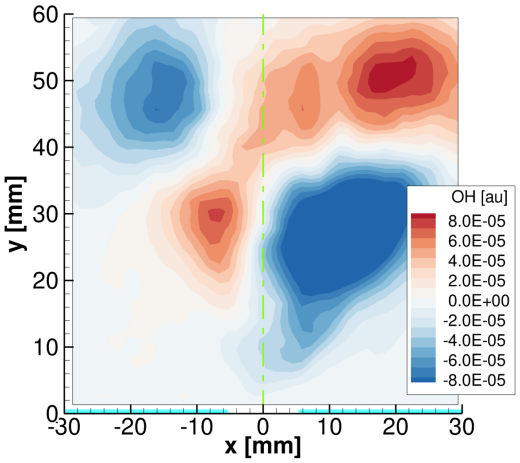

(e) Real part of chemiluminescence component of SDD mode

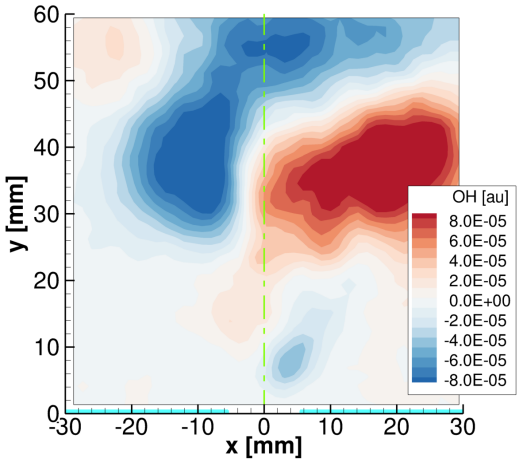

(f) Imaginary part of chemiluminescence component of SDD mode

Figure 35: Unstable dataset SDD mode components. Frequency: 1016.94 Hz

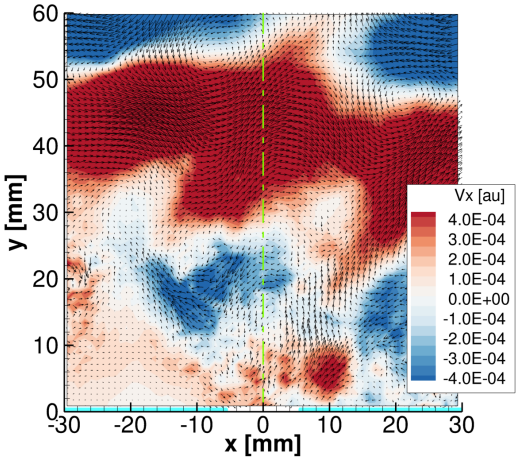

(a) Real part of PIV component of SDD mode

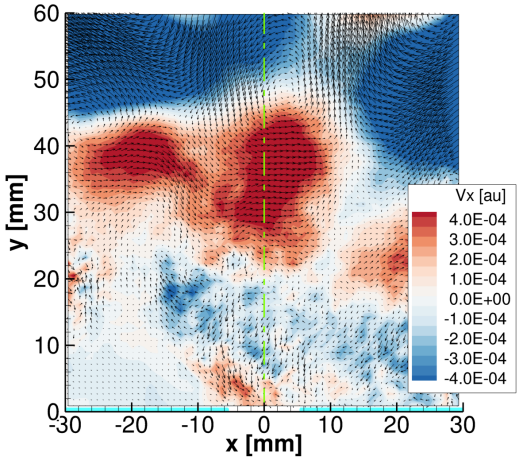

(b) Imaginary part of PIV component of SDD mode

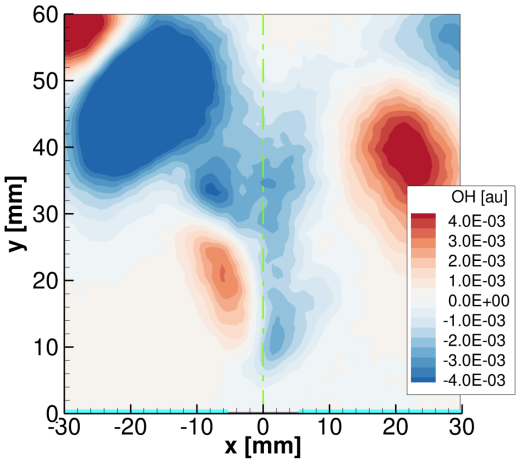

(c) Real part of PLIF component of SDD mode

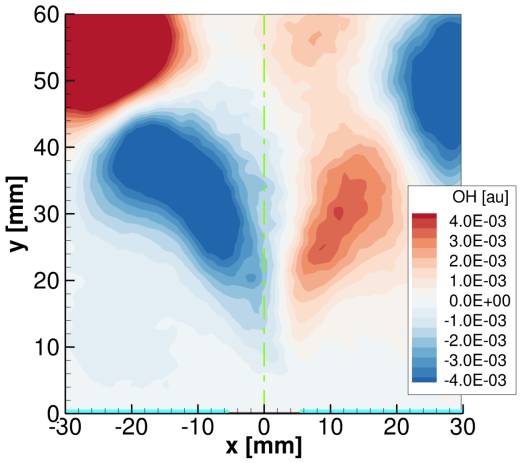

(d) Imaginary part of PLIF component of SDD mode

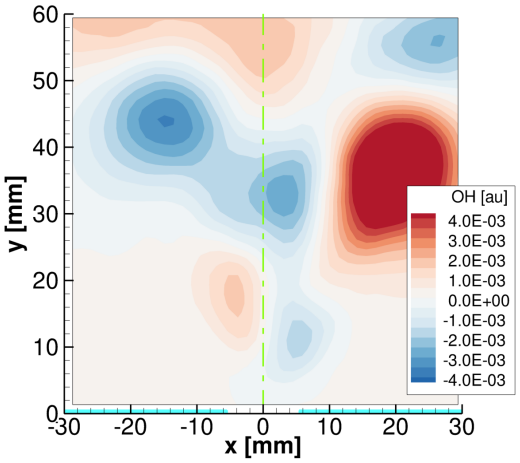

(e) Real part of chemiluminescence component of SDD mode

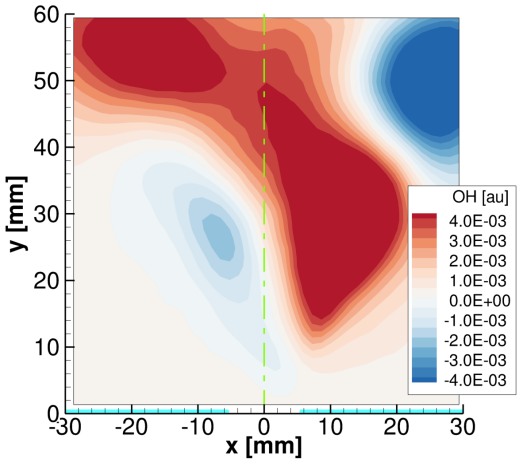

(f) Imaginary part of chemiluminescence component of SDD mode

Figure 36: Unstable dataset SDD mode components. Frequency: 549.79 Hz

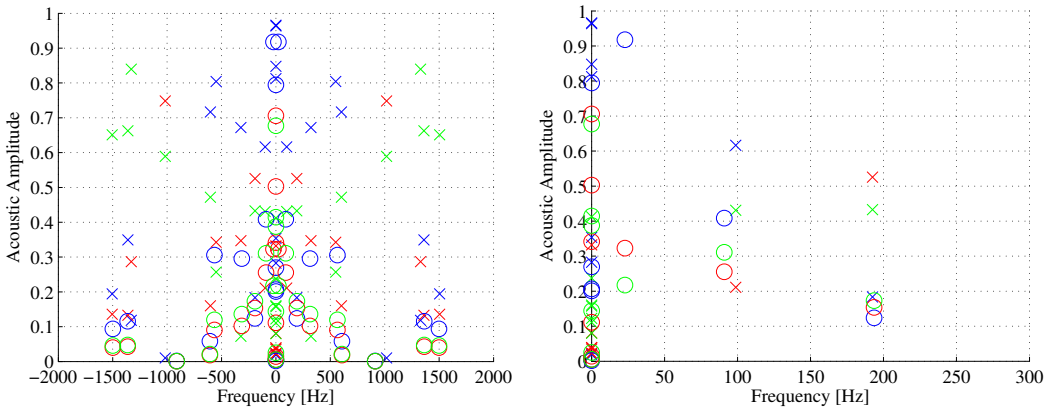

(a) Acoustic amplitude for all modes

(b) Acoustic amplitudes for modes with $f \in [0, 300]$ Hz

Figure 37: Predicted modal acoustic amplitudes from SDD analyses: unfiltered acoustic data (crosses), filtered acoustic data (circles). Dynamic pressure sensor location: p'_1 at $x = 0.336$ m (blue), p'_3 at $x = 0.0263$ m (red), p'_5 at $x = -0.0263$ m (green)

mode, the acoustic data have been low-pass filtered with a cutoff frequency of 300 Hz and high pass filtered with a cutoff frequency of 80 Hz. We have employed a *forward-backwards* Butterworth filtration scheme to minimize the phase distortion caused by this bandpass filtering. Replacing the original unfiltered (other than low-pass filtering for anti-aliasing) acoustic data with the bandpass filter acoustic data and running the SDD analysis on the unstable experiment dataset yields the circular data points in Figs. 34 and 37. Again, the two largest modulus Ritz value modes are listed in Table 6 and their PIV, PLIF, and chemiluminescence mode components are plotted in Figs. 38 and 39.

From Fig. 34b we see the nearly neutrally stable 1017 Hz mode from the *unfiltered* data analysis appears to have been damped in the *filtered* data analysis to a mode with frequency of approximately 913 Hz. Otherwise, most modes in the SDD spectra are nearly unchanged by the acoustic filtering; the change to the modes' structure is also small. For example, comparing the previous 550 Hz mode with the new 565 Hz mode, Figs. 36 and 38, respectively, there is little difference except for the phase of the mode. In addition to the damped 1017 Hz mode, in the filtered data analysis there is a new very low frequency, 23 Hz, dynamical mode. In fact, the 23 Hz mode is now the largest modulus Ritz value mode, see Table 6. From Fig. 39 it appears that the 23 Hz mode is in part due to the anchoring

point of the swirling reaction zone lifting and dropping relative to the injection plane, see Figs. 39d and 39f.

Returning to Fig. 34b, again we seek a large modulus Ritz value corresponding to a modal frequency of 170 Hz, but the applied filtering technique has not yielded a new mode near the desired frequency. In both the filtered and unfiltered data, there is a mode near 190 Hz, albeit not a large modulus approximate exponential eigenvalue, that could be related to the observed instability, but there is no way to tell without more information.

The inability of the SDD analysis to locate a 170 Hz mode that is responsible for the CI is likely due to one of two possibilities: there is a shortcoming of the method, e.g., the data is too noisy for the method to find the underlying mode; or, the method enforces improper assumptions about the physical system, e.g., the DMD algorithm assumes that the operator A in Eq. (55) is a constant, although this may not be true in the physical system. We will explore the latter possibility in the next chapter.

Finally, we would like to explore whether or not the 1017 Hz mode is *stable* in the sense of CIs. For the 1017 Hz mode, the combustion chamber pressure and the spatially integrated Rayleigh index (as defined by Eq. (106)) are shown in Fig. 40. From Fig. 40b, we see that the Rayleigh index is negative nearly the entire cycle. The modal stability with respect to CI is given by the Rayleigh integral, Eq. (103), (see Table 7) and for this mode is -0.2738 AU, negative, therefor this mode is damped. Although this mode is *stable*, we believe that this mode is integral to the 170 Hz observed CI. To demonstrate that this is indeed the case, new analysis techniques are required.

4.4 Conclusions

The simultaneously measured PIV and PLIF data were analyzed with common techniques, e.g., time-averaging and frequency content analysis. First, we analyzed the data with simple statistical

Table 7: SDD predicted combustion stability based on modal Rayleigh integral for the unstable experiment dataset

f [Hz]	1016.94
Rayleigh Integral [AU]	-0.2738
Modal combustion stability	Stable

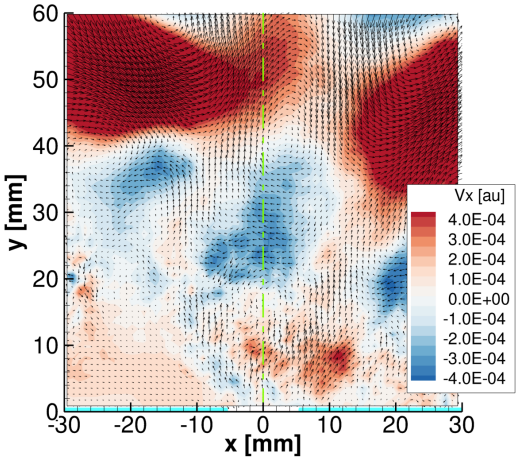

(a) Real part of PIV component of SDD mode

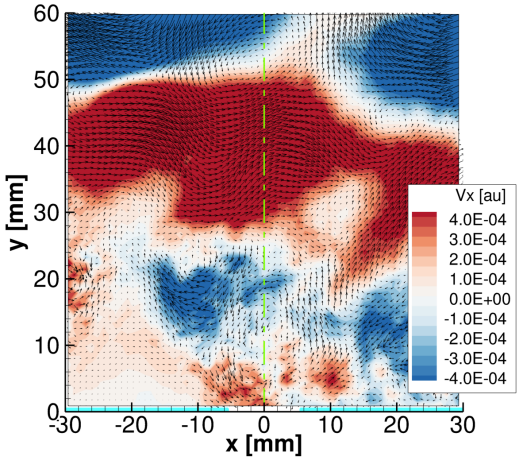

(b) Imaginary part of PIV component of SDD mode

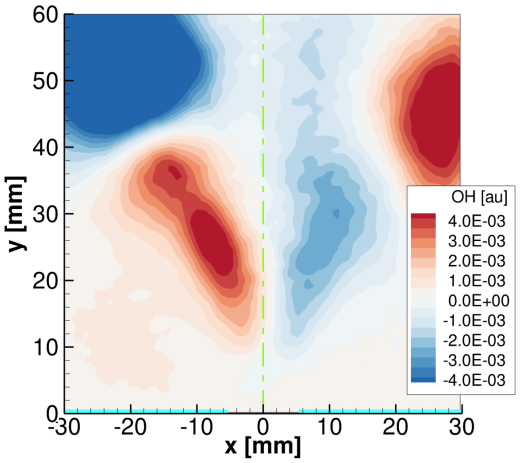

(c) Real part of PLIF component of SDD mode

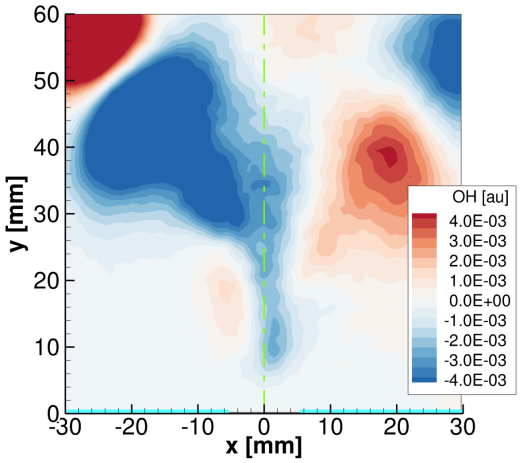

(d) Imaginary part of PLIF component of SDD mode

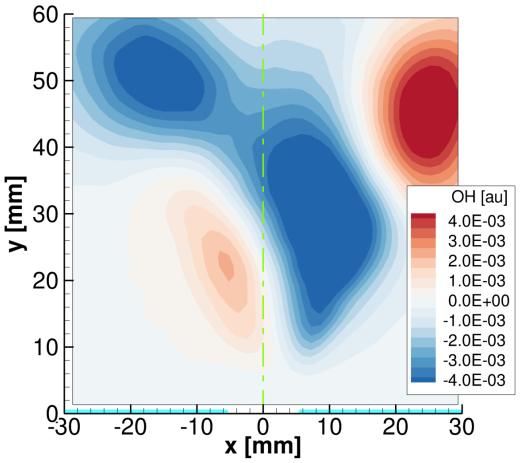

(e) Real part of chemiluminescence component of SDD mode

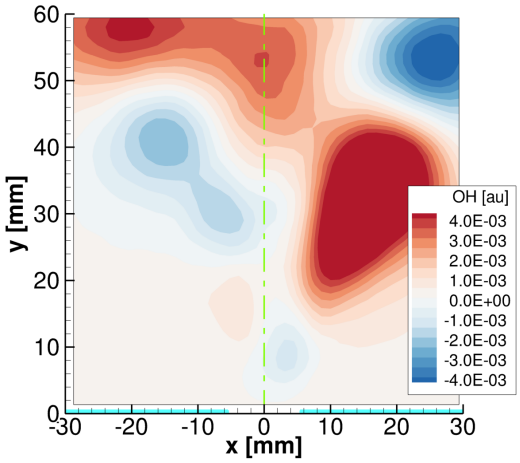

(f) Imaginary part of chemiluminescence component of SDD mode

Figure 38: Unstable dataset SDD mode components. Frequency: 565.15 Hz

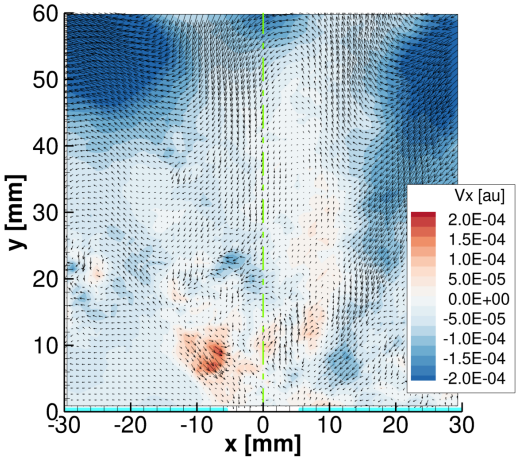

(a) Real part of PIV component of SDD mode

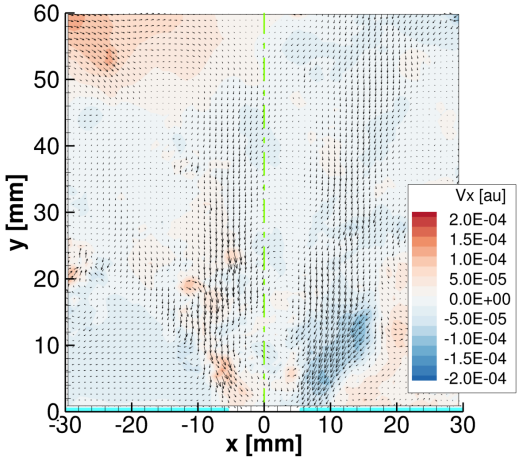

(b) Imaginary part of PIV component of SDD mode

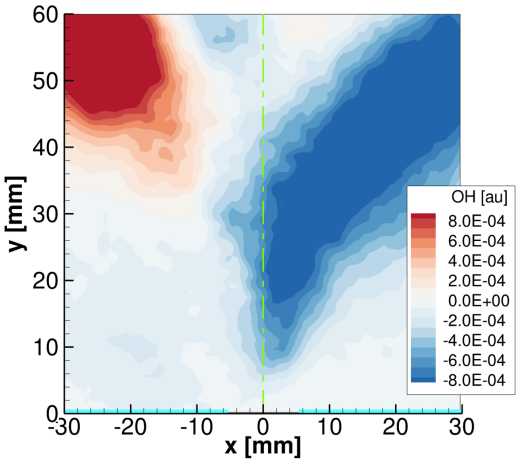

(c) Real part of PLIF component of SDD mode

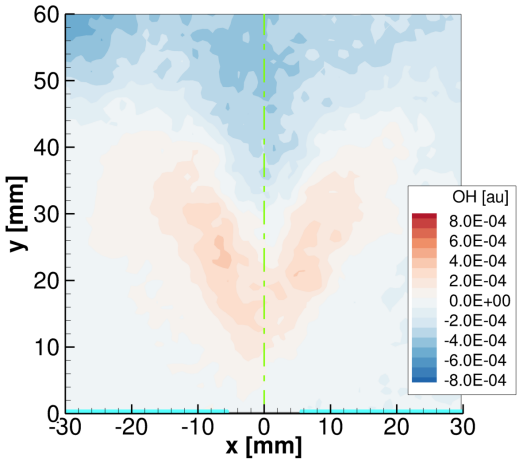

(d) Imaginary part of PLIF component of SDD mode

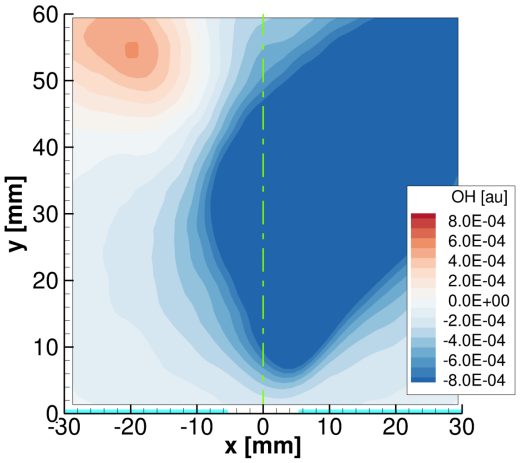

(e) Real part of chemiluminescence component of SDD mode

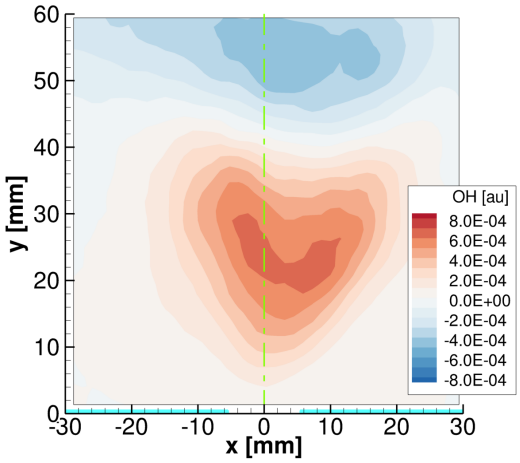

(f) Imaginary part of chemiluminescence component of SDD mode

Figure 39: Unstable dataset SDD mode components. Frequency: 22.85 Hz

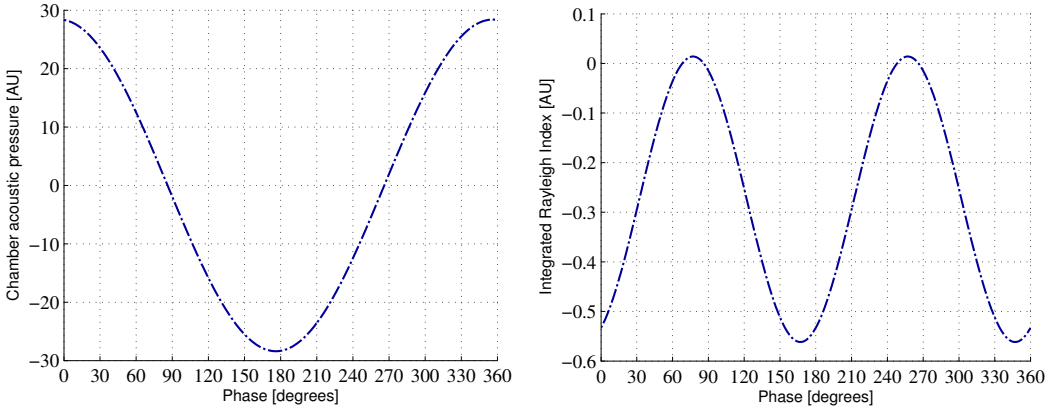

(a) Combustion chamber acoustic pressure

(b) Spatially integrated Rayleigh index

Figure 40: Combustion chamber acoustic pressure and spatially integrated Rayleigh index versus mode phase for the unstable experiment at 1017 Hz

methods showing the time-average structure of the reaction zone, recirculation zones, and shear layers. The PSD at the CI frequency of 170 Hz showed the OH intensity fluctuations were strongest well downstream of the inner recirculation zone, but due to the small amplitude of the acoustic velocity oscillations there appears to be a nonlinear amplification mechanism related to the inner shear layer instability.

Next we showed that analyzing the PIV and PLIF datasets separately with the DMD method shows important dynamical content in both diagnostics—such as high-frequency OH fluctuations and an outer shear layer instability. But, the modes from each of the analyses are allowed to have independent dynamical information, i.e., the modes found in each analysis can have unrelated frequencies. Since the frequencies, in general, differ from the PIV to PLIF analyses, we have no way to determine if the modes are related.

This suggested that we analyze the data in such a way as to maintain the simultaneous nature of the data. This was accomplished by forming composite input vectors for the DMD algorithm to ensure that a dynamic mode output from the algorithm had the same frequency and growth factor for the both the PIV and PLIF data. Some of these modes, in both the stable and unstable operation cases, showed what appears to be an inner shear layer instability and closely related combustion zone oscillations. We found these modes had a nearly constant convective velocity of approximately 36 m/s. Furthermore, the SDD method showed the hydrodynamics and combustion were relatively unchanged regardless of the system's stability; suggesting that the fundamental difference between

the stable and unstable cases is due to the energy feedback into the natural acoustic mode. If we can establish this link it may be possible to create a general framework—including making measurements of a combustor operating in a stable manner and modeling the acoustic feedback mechanism—to predict and prevent detrimental CIs.

Finally, we analyzed the PIV, PLIF, chemiluminescence, and acoustic data with the SDD method for the unstable experiment case and found the largest modulus exponential Ritz value, μ—the dominate mode—had a frequency near 1017 Hz. Using the chemiluminescence data as an approximation for heat release and the combustion chamber acoustic pressure, the Rayleigh integral for this mode was negative and hence, *stable* with respect to CI. Also, we found no definitive evidence of the unstable 170 Hz CI and over the next two chapters we will propose an approach to overcome this shortcoming.

CHAPTER V

STUDY OF PERIODIC SYSTEMS WITH DYNAMIC MODE DECOMPOSITION BASED TECHNIQUES

In Chapter 4, it was shown that SDD analyses could identify coupling between fluid dynamical and combustion processes, see, e.g., Figs. 30 and 31. However, the DMD/SDD analyses were not able to couple the fluid mechanical and combustion processes with the acoustic modes of the unstable combustor. We believe that the inability of the DMD/SDD analyses to elucidate this coupling is related to the fact that the DMD/SDD approach assumes that the operator A, see Eq. (55), is constant, which probably is not the case in unstable combustors.

It is likely that in unstable combustors the operator A is a function of time, i.e., $A = A(t)$. While it would be desirable to develop an analysis technique for the general case that allows for any time dependence of $A(t)$, little is known about systems with arbitrary time dependence and we are investigating unstable combustors that exhibit nearly periodic time behavior. Therefore, the next step in this study was to investigate systems with operators that are both linear and periodic. With this aim in mind, we explored techniques based on the Floquet theory, because the theory provides a well developed framework for such systems. It has been shown [41, 49] that Floquet theory can be applied to study the stability of linear and sometimes nonlinear systems that exhibit solutions that are periodic or nearly periodic (quasiperiodic), similar to those exhibited by unstable combustors.

Periodic systems of equations are capable of exhibiting instabilities due to the oscillatory nature of the system's *parameters*. These instabilities are known as parametric instabilities [50–53]. Periodic systems of equations and the resulting parametric instabilities often occur when the system is composed of two or more subsystems, each potentially oscillating at its own natural frequencies. Since CIs likely involve coupling between a hydrodynamic/combustion subsystem and an acoustic subsystem in a feedback loop, it is possible that the CI observed in our experiments is, in fact, a parametric instability.

In this chapter, using the DMD/SDD method, we develop a data analysis technique based on the Floquet theory that allows us to find the stability of oscillatory systems from an analysis of measured data without a priori knowledge of the governing equations. In Chapter 6, we will apply the techniques developed in this chapter to our experimental datasets and explore the possibility that the observed CI is a parametric CI.

5.1 Motivation: Parametric Combustion Instabilities

In this section we will demonstrate that CIs are possible caused by parametric instabilities. We begin our discussion from the inhomogeneous wave equation, Eq. (19), repeated here:

$$\frac{\partial}{\partial x}\left(c^2\frac{\partial p'}{\partial x}\right) - \frac{\partial^2 p'}{\partial t^2} = -(\gamma-1)\bar{\rho}\frac{\partial \dot{q}'}{\partial t} \tag{110}$$

The functional form of the unsteady heat release, $\dot{q}'$, is generally an unknown function of the state variables of the system and its geometric configuration:

$$\dot{q}' = \dot{q}'\left(p', u', \omega, \bar{U}, X, \bar{T}, \bar{P}, c, \ldots\right). \tag{111}$$

A common heat release model is to assume that the total response is the sum of three contributions proportional to the acoustic pressure, the acoustic velocity, and the incoming mixture fraction perturbation [54]:

$$\dot{q}' = N_p p' + N_u u' + N_\phi \phi'. \tag{112}$$

In this equation, the N's represent complex proportionality constants or gain and phase differences between their respective state variables and their contribution to the unsteady heat release.

Due to the configuration of our system and to simplify the discussion, we will limit the discussion to the velocity coupling term on the right-hand side of Eq. (112). Substituting Eq. (112) into Eq. (110) and absorbing the constant $(\gamma-1)$ into N_u gives:

$$\frac{\partial}{\partial x}\left(c^2\frac{\partial p'}{\partial x}\right) - \frac{\partial^2 p'}{\partial t^2} = -N_u\bar{\rho}\frac{\partial u'}{\partial t} \tag{113}$$

which with conservation of momentum, Eq. (12), can be rewritten as a function of p:

$$\frac{\partial}{\partial x}\left(c^2\frac{\partial p'}{\partial x}\right) - \frac{\partial^2 p'}{\partial t^2} = N_u\frac{\partial p'}{\partial x} \tag{114}$$

Much like we did in Chapter 2, we will use the Ritz-Galerkin method to discretized the spatial derivatives. In Chapter 2 we did this to turn our ODE/Helmholtz equation into a linear algebra problem, which was easy to solve with a computer. Here we discretize the spatial derivatives to yield a system of ODEs, which can then be studied.

We represent the acoustic pressure, $p' = p'(x,t)$, as a sum of time varying coefficients and spatial basis function:

$$p'(x,t) = \sum_{j=1}^{n} a_j(t)\phi_j(x). \tag{115}$$

Substituting this expansion into Eq. (114) and simplifying yields:

$$\sum_{j=1}^{n} \left\{ a_j \frac{\partial}{\partial x}\left(c^2 \frac{\partial \phi_j}{\partial x}\right) - \frac{\partial^2 a_j}{\partial t^2}\phi_j - a_j N_u \frac{\partial \phi_j}{\partial x} \right\} = 0. \tag{116}$$

Next, Eq. (116) is multiplied by a trial function, here chosen from the same set of basis functions, and the equation is integrated over the nondimensional domain, $x \in [0,1]$:

$$\sum_{j=1}^{n} \left\{ a_j \int_0^1 \phi_i \frac{\partial}{\partial x}\left(c^2 \frac{\partial \phi_j}{\partial x}\right) \mathrm{d}x - \frac{\partial^2 a_j}{\partial t^2} \int_0^1 \phi_i \phi_j \mathrm{d}x - a_j \int_0^1 N_u \phi_i \frac{\partial \phi_j}{\partial x} \mathrm{d}x \right\} = 0. \tag{117}$$

If we assume that the heat release zone is compact compared with the acoustic wavelength, then N_u is only nonzero at one x-location, x_{inj} and with the generalized function, the Dirac delta function, Eq. (117) can be written:

$$\sum_{j=1}^{n} \left\{ a_j \int_0^1 \phi_i \frac{\partial}{\partial x}\left(c^2 \frac{\partial \phi_j}{\partial x}\right) \mathrm{d}x - \frac{\partial^2 a_j}{\partial t^2} \int_0^1 \phi_i \phi_j \mathrm{d}x - a_j \int_0^1 N_u \delta\left(x - x_{\mathrm{inj}}\right) \phi_i \frac{\partial \phi_j}{\partial x} \mathrm{d}x \right\} = 0, \tag{118}$$

which, with the properties of integrals of the Dirac function becomes:

$$\sum_{j=1}^{n} \left\{ a_j \int_0^1 \phi_i \frac{\partial}{\partial x}\left(c^2 \frac{\partial \phi_j}{\partial x}\right) \mathrm{d}x - \frac{\partial^2 a_j}{\partial t^2} \int_0^1 \phi_i \phi_j \mathrm{d}x - a_j \left[N_u \phi_i \frac{\partial \phi_j}{\partial x} \right]_{x=x_{\mathrm{inj}}} \right\} = 0, \tag{119}$$

Further, as discussed in Chapter 2, we will use integration by part to lower the continuity requirements on the basis functions, forming the weak form of the equation:

$$\sum_{j=1}^{n} \left\{ -a_j \int_0^1 c^2 \frac{\partial \phi_i}{\partial x} \frac{\partial \phi_j}{\partial x} \mathrm{d}x - \frac{\partial^2 a_j}{\partial t^2} \int_0^1 \phi_i \phi_j \mathrm{d}x - a_j \left[N_u \phi_i \frac{\partial \phi_j}{\partial x} \right]_{x=x_{\mathrm{inj}}} \right\} = 0. \tag{120}$$

Multiplying through by -1, allowing i to take on values from 1 to n, and defining:

$$K_{ij} \equiv \int_0^1 c^2 \frac{\mathrm{d}\phi_i}{\mathrm{d}x} \frac{\mathrm{d}\phi_j}{\mathrm{d}x} \mathrm{d}x, \tag{121}$$

$$M_{ij} \equiv \int_0^1 \phi_i \phi_j \, \mathrm{d}x, \tag{122}$$

and

$$G_{ij} \equiv \left[\phi_i \frac{\partial \phi_j}{\partial x} \right]_{x=x_{\mathrm{inj}}}, \tag{123}$$

then Eq. (120) may be written in matrix form:

$$K\boldsymbol{a} + M\ddot{\boldsymbol{a}} + N_u G\boldsymbol{a} = 0. \tag{124}$$

Again, like in Chapter 2, if we choose a cosine series to match the hard wall boundary condition, due orthogonality of the functions, the matrix M is diagonal, so its inverse is simply the reciprocal of its diagonal entries. Left multiplying Eq. (124) by M^{-1} and collecting yields:

$$\ddot{\boldsymbol{a}} + \left(M^{-1}K + N_u M^{-1} G \right) \boldsymbol{a} = 0. \tag{125}$$

Assuming, as is typical, that N_u is a constant (frequency response function approach) or a function of amplitude and frequency (describing function approach) [55, 56], Eq. (125) represents linear or quasi-linear, constant coefficient system. Oscillations at one natural frequency in linear constant coefficient systems are independent from oscillations at any other frequency. In other words, these systems can exhibit linear instabilities, which only depend on the oscillation at the instability frequency. On the other hand, if we assume that N_u is not constant, but rather that it is periodic in time, the system is now a linear periodic system.

As an example of a linear periodic system, assuming for a moment that $N_u = \epsilon \cos(\hat{\omega} t)$, then Eq. (125) becomes:

$$\ddot{\boldsymbol{a}} + \left(M^{-1}K + \epsilon \cos(\hat{\omega} t) \, M^{-1} G \right) \boldsymbol{a} = 0. \tag{126}$$

Further taking the one-term expansion to see the leading behavior of the system, $n = 1$, Eq. (126) simplifies to:

$$\ddot{a} + \left(\frac{k}{m} + \epsilon \frac{g}{m} \cos(\hat{\omega} t) \right) a = 0, \tag{127}$$

Equation (127) is a form of the equation known as the Mathieu equation, which we will show in this chapter is capable of exhibiting parametric instabilities.

5.2 Background for Periodic Systems

A large number of physical systems exhibit periodic, oscillatory behavior. For example, consider a pendulum whose support is moved vertically as a periodic function of time that is described by the function $f(t)$. The governing equation describing the dynamics of the pendulum's angle relative to the vertical axis, u, is [57]:

$$\ddot{u} + (\kappa + f(t)) \sin(u) = 0, \tag{128}$$

where $\kappa = \omega_0^2 = g/L$ and g and L are the gravitational constant and pendulum length, respectively. We can think of this system as having its gravitational acceleration augmented by the acceleration of the support. Further, Eq. (128) may be linearized by assuming u oscillates with a small amplitude about the angle $u = 0$ or $u = \pi$, expanding $\sin(u)$ ($\sin(u) \approx u$) to obtain:

$$\ddot{u} + (\kappa + f(t))u = 0. \tag{129}$$

The pendulum system becomes linear if the pendulum is either nearly directly below or above its support, respectively, and $f(t)$ is not a function of the state variable. Equation (129) is a form of Hill's equation. There has been extensive analysis of this equation, see, e.g., the work of Magnus and Winkler [58]. Often, Hill's equation is specialized by setting $f(t)$ to be a time-harmonic function, yielding the Mathieu's equation:

$$\ddot{u} + (\kappa + \epsilon \cos(t))u = 0. \tag{130}$$

This system is forced, in some sense, by the oscillation of the support point. From the support, energy can be transfered to and from the system, which can cause the oscillations to grow or decay in time. But, this equation is not forced in the traditional way; in contrast to Eq. (130), a *forced* pendulum is governed by:

$$\ddot{u} + \kappa u = \epsilon \cos(t). \tag{131}$$

The difference between Eq. (131) and Eq. (130) appears subtle at first glance. They are both linear, but they belong to two different classifications for systems of differential equations, autonomous and nonautonomous, respectively. A system of equations is said to be autonomous if the system does not depend explicitly on the independent variable t; in other words, $\dot{\boldsymbol{x}} = A\boldsymbol{x}$ is autonomous and $\dot{\boldsymbol{x}} = A(t)\boldsymbol{x}$ is not.

Rewriting Eq. (131) and Eq. (130) in state space, where $\boldsymbol{x} = \{u, \dot{u}\}^T$, yields:

$$\dot{\boldsymbol{x}} = \begin{bmatrix} 0 & 1 \\ -\kappa & 0 \end{bmatrix} \boldsymbol{x} + \begin{bmatrix} 0 \\ \epsilon \cos(t) \end{bmatrix}, \tag{132}$$

and

$$\dot{\boldsymbol{x}} = \begin{bmatrix} 0 & 1 \\ -\kappa - \epsilon \cos(t) & 0 \end{bmatrix} \boldsymbol{x}, \tag{133}$$

respectively.

At this point we restrict our discussion to the homogeneous form of Eq. (132). To find the stability of solutions to Eq. (132) we need only find the eigenvalues of the coefficient matrix, which are given by:

$$\det \begin{bmatrix} 0 - \lambda & 1 \\ -\kappa & 0 - \lambda \end{bmatrix} = 0. \tag{134}$$

The eigenvalues of Eq. (134) are:

$$\lambda_{1,2} = \pm \sqrt{-\kappa} = \pm \sqrt{-\omega_0^2}. \tag{135}$$

For nondegenerate (nonrepeated) eigenvalues, the solution of a 2-dimensional autonomous set of first-order equations takes the form $x(t) = \alpha e^{\lambda_1 t} + \beta e^{\lambda_2 t}$. Therefore, the solution is asymptotically stable if and only if the real part of each eigenvalue is less than zero or, equivalently, the imaginary part of ω_0 must be less than zero. If the real part of each eigenvalue is zero, then the system oscillates at the angular frequency $\omega = \pm \sqrt{\mathrm{Im}(\lambda)}$ with constant amplitudes, α and β, which are chosen to match the problem's initial conditions. This case is referred to as marginally stable.

Returning to the Mathieu equation, Eq. (133), the coefficient matrix is not constant in time and, thus, the eigenvalues of the matrix are not constant. In fact, the stability of nonautonomous equations have little to do with the coefficient matrix: "there is no obvious relation between the (time-dependent) eigenvalues of a time-dependent matrix and the stability of the zero solution of the corresponding first-order linear differential equation." [59] Rather than depending on eigenvalue problem solutions, the stability of solutions for the Mathieu equation and other nonautonomous equations requires more involved solution techniques.

Again, our goal is to leverage the well developed dynamical system theory and apply some of the key techniques to our experimental dataset to elucidate the physical processes that control the

investigated CI. First, we examine the mathematical theory of periodic systems. Then, we show how the theory may be applied in a new technique to experimental datasets. Next, we give a number of examples—some which may be relatively easily treated theoretically, e.g., the Mathieu equation—to show what we might expect from our new technique. Lastly, we use discuss the choice of analysis period for the developed technique for cases where it is not known a priori. In the following chapter, the theory developed here is employed to analyze the experimental datasets described previously and discuss the implications of the results.

5.3 Floquet Theory

Much of this section is based on Floquet's theory developed in 1883 [60]. While this theory is presented here without proof, it is discussed in detail in many references [41, 49, 61, 62]. We develop the theory in this section first for periodic linear systems, keeping in mind that at least some of the findings are applicable to a much boarder class of problems.

First, we consider a first-order, homogeneous, linear system of equations:

$$\dot{u} = A(t)u, \quad u(0) = u_0. \tag{136}$$

The general solutions of this linear system are given by [49]:

$$u(t) = \Phi(t, 0)\Phi(0, 0)u_0, \tag{137}$$

where $\Phi(t, 0)$ is a matrix solution from time 0 to t, which is defined as the solution of the system of equation:

$$\begin{cases} \dot{\Phi}(t, 0) = A(t)\Phi(t, 0) \\ \Phi(0, 0) : \text{linearly independent columns} \end{cases} \tag{138}$$

Since the columns of $\Phi(t, 0)$ must be linearly independent solutions, the initial conditions, $\Phi(0, 0)$, must be chosen to be linearly independent. The above definition of a matrix solution allows for an infinite number of matrix solutions, which are all related by nonsingular matrices. For example, if we have a second matrix solution, $\Psi(t, 0)$, we will find that $\Phi(t, 0) = \Psi(t, 0)C$, where C is some nonsingular matrix. Given this flexibility, we can arbitrarily choose the initial conditions to be $\Phi(0, 0) = I$. For this reason, we define the principal or fundamental matrix solution, $\Phi(t, 0)$, as the

one given by the solution of the following homogeneous, linear, initial value problem:

$$\dot{\Phi}(t,0) = A(t)\Phi(t,0), \quad \Phi(0,0) = I, \tag{139}$$

and the general solution becomes:

$$u(t) = \Phi(t,0)u_0. \tag{140}$$

While very little is known about the solutions of linear, homogeneous systems where the matrix function $A(t)$ is an arbitrary function of time, much more is known about the solutions of systems whose governing operator, $A(t)$, is periodic in time. With this in mind, we assume $A(t)$ is τ-periodic and as a result Eq. (136) may be written:

$$\begin{cases} \dot{u} = A(t)u, \quad u(0) = u_0, \\ A(t+\tau) = A(t). \end{cases} \tag{141}$$

If we evaluate the fundamental matrix solution at $t = \tau$, the resulting matrix is known as the *monodromy* matrix:

$$M \equiv \Phi(\tau, 0). \tag{142}$$

While Chicone [59] has pointed out that the time-dependent eigenvalues of the time-dependent coefficient matrix have no direct relationship with the stability of nonautonomous systems, Floquet has shown that the stability of the orbits found in nonautonomous systems is related to the eigenvalues of the monodromy matrix. The eigenvalues of the monodromy matrix, μ, are called the Floquet multipliers and their values are directly related to the stability of the system. There are three different stability cases: if all of the Floquet multipliers lie within the unit circle of the complex domain, then the system in asymptotically stable; if any of the Floquet multipliers lie outside the unit circle of the complex domain, then the system is unstable; if the largest magnitude Floquet multipliers lie on the unit circle of the complex domain, then the system is Lyapunov stable. By Lyapunov stable we mean that if the initial state of the solution is started near a Lyapunov stable solution, it will remain near the Lyapunov solution as $t \to \infty$.

Similar to our discussion of Eq. (88) in Section 3.2, the Floquet multipliers satisfy the following relationship:

$$\rho = \frac{\ln(\mu)}{\tau}, \tag{143}$$

where the transformed form of the Floquet multipliers, ρ, are referred to as Floquet exponents. One of the advantages of this form is that the real part of ρ is the growth/decay factor and the imaginary part is the angular frequency, ω. We must, however, be careful here. Specifically, due to the properties of the complex logarithm and its *branch cuts*, the Floquet multipliers are unique, but the Floquet exponents are not. The nonuniqueness occurs because the true angular frequency of the *mode* is the imaginary part of ρ—or—accounting for different branch cuts of the logarithm:

$$\omega = \mathrm{Im}\left\{\rho + i2\pi k/\tau\right\}, \tag{144}$$

for any integer k. While the drawback of this nonuniqueness is that we must be careful to identify the correct frequency, it potentially allows us to apply these techniques to oscillations above the traditionally limiting Nyquist cutoff frequency.

Floquet's theorem tells us that we can express the monodromy matrix as a product of a τ-periodic matrix function and a matrix exponential, i.e.:

$$\Phi(\tau, 0) = M = P(t)e^{Bt}, \tag{145}$$

where the matrix function $P(t)$ is τ-periodic:

$$P(t + \tau) = P(t), \tag{146}$$

and B is an invertible constant matrix. The theorem also tells us that the eigenvalues of B are the Floquet multipliers provided by the monodromy matrix. The structure of Eq. (145) indicates that the largest modulus eigenvalue of B (or equivalently the largest modulus Floquet multiplier) determines the stability of the solution, $u(t)$.

The Floquet theory decomposes the solution into a periodic part, $P(t)$, and an exponential part, e^{Bt}. Since the exponential part may be complex, it can contribute to the periodic behavior of the solution. The product of these two contributions may produce mathematically rich solutions that include exponential growth/decay, periodic solutions, and quasiperiodic solutions.

One of the drawbacks of using the monodromy matrix is that it can be difficult to determine, often requiring solving the system n times from n independent initial conditions, where n is the dimension of the system. An approximation of the monodromy matrix can be found by expanding

$A(t)$ in a Taylor series and only retaining the constant term. This approach yields a form similar to the solution of an autonomous, first-order system of equations that may be written as:

$$u(t_k) = e^{Ak\Delta t}u_0 = \prod_k e^{A\Delta t}u_0. \tag{147}$$

The Taylor series expansion shows that if we divide the period into N small intervals, $\Delta t = \tau/N$, then we may approximate $A(t)$ on each interval as a constant operator, $A(t_k)$. By taking this approach, the approximate monodromy matrix is [63, 64]:

$$M \approx \prod_{k=1}^{N} e^{A(t_k)\Delta t}. \tag{148}$$

This approximation for the monodromy matrix should be accurate whenever $\partial A(t)/\partial t$ and/or Δt is small.

Returning to the quantification of stability of an orbit, we can determine the stability from the largest magnitude Floquet multiplier. Assuming we have ordered the Floquet multipliers from largest to smallest magnitude, $|\mu_1| \geq |\mu_2| \geq \ldots \geq |\mu_n|$, then the stability criterion is given by:

$$\text{if} \quad |\mu_1| \quad \begin{cases} < 1 & \text{the orbit is asymptotically stable} \\ = 1 & \text{the orbit is Lyapunov stable} \\ > 1 & \text{the orbit is unstable} \end{cases} . \tag{149}$$

Since we only need to know μ_1 to determine the stability of the system and since the monodromy matrix is often practically intractable, it follows that Krylov based methods might be used to find the largest magnitude Floquet multiplier effectively. We will address this idea in the following section, Section 5.4.

Before we leave the Floquet theory, let's discuss another result associated with the Floquet multipliers. That is, if at least one of the Floquet multipliers is equal to one, i.e., $\mu_i = 1$, then there exists a periodic orbit with period τ. In fact, if the periodic solution was found through linearization, then there will be a Floquet multiplier equal to one. Also, if at least one of the Floquet multipliers is equal to minus one, i.e., $\mu_i = -1$, then there exists a periodic orbit with period 2τ. Interestingly, if the system continues to experience this type of period doubling, the system may exhibit chaotic behavior [65–69].

5.4 *Floquet Decomposition*

We now consider the case for which we cannot determine the monodromy matrix and may not even know the governing equations of the system. It has been suggested by Schmid that a DMD like calculation can give the Floquet multipliers of the system [9]. We developed a new technique that can indeed find *some* of the Floquet multipliers and that these multipliers are, in fact, those that determine the stability of the system.

Since most real systems are nonlinear, we will present some properties of nonlinear systems that have motivated our approach before we present our analysis.

To determine the stability of orbits found in nonlinear systems, we often use linearization about an orbit or the Poincaré map. Briefly examining the latter, the Poincaré map describes the time-evolution of intersections of a system's solution orbits and a plane transverse to the solution's trajectory. In fact, it describes the solution in a space whose dimension has been reduced by one from the dimension of the original system. A schematic of one period of the solution is shown in Fig. 41. Here the Poincaré map shows that point A has been transformed (or *mapped*) to point B, during the time between intersections with the Poincaré section, i.e., $\mathcal{P}(A) = B$. From this figure we can see why the Poincaré map is sometimes referred to as the *first return* map.

In autonomous nonlinear systems, the local stability of a *fixed point* (equilibrium) solution is given by the eigenvalues of the Jacobian matrix linearized about the fixed point. The stability of the fixed point is asymptotically stable or unstable if the sign of the real part of all of the eigenvalues are strictly less than zero or if the real part of any eigenvalue is greater than zero, respectively. Similarly, the stability of periodic a orbit in a nonlinear system is given by the eigenvalues of the derivatives of the Poincaré map. In some ways, the periodic orbit in the Poincaré section appears

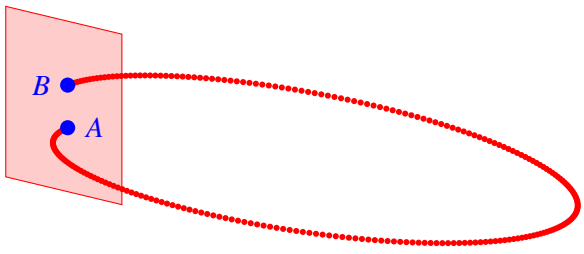

Figure 41: Poincaré map schematic

to be a fixed point solution in this reduced dimensional space. While in Section 5.3, we developed and discussed the Floquet theory based on linear systems, it turns out that the Floquet multipliers are the eigenvalues of the Poincaré map derivatives. Thus, the local stability of the orbit is given by the Floquet multiplier—even for nonlinear systems as long as the solution is nearly periodic. As a result, whether the system to be analyzed is linear and nonautonomous or nonlinear and exhibits quasiperiodic solutions, the largest modulus Floquet multiplier can be used to determine the stability of the solution.

In addition, whether using Poincaré or Floquet theories, the analysis begins by examining the data once per cycle. Hence, we conceptually perform a measurement once each period and place these data into a matrix. For the Mathieu equation, Eq. (133), the proper analysis period τ is the period of the cycle of perturbations as one subsystem perturbs another, e.g., $\omega = 1\,\text{rad/s}$, so $\tau = 2\pi/\omega = 2\pi\,\text{s}$. If the high-speed data has been acquired with a sampling period of Δt (the inverse of the sampling rate), then there are r measurements during one period, $r = \tau/\Delta t$. Given the matrix $V_{1:N} = [v_1 \quad v_2 \quad v_3 \quad \dots \quad v_N]$ containing all of the measured data, the periodically sampled data matrix is:

$$\tilde{V}_{1:k} = [v_1 \quad v_{r+1} \quad v_{2r+1} \quad \dots \quad v_{(k-1)r+1}], \tag{150}$$

where $k = \text{floor}((N-1)/r)$ is the number of complete periods within the original data matrix.

Recall that for the constant linear operator case, $\dot{x} = Ax$, the solution is *propagated* by the operator $e^{A\Delta t}$, i.e.:

$$\begin{aligned} x_1 &= e^{A\Delta t} x_0 \\ x_2 &= e^{A\Delta t} e^{A\Delta t} x_0 = e^{A2\Delta t} x_0 \\ &\vdots \\ x_N &= e^{AN\Delta t} x_0 \end{aligned} \quad . \tag{151}$$

In contrast, when $A = A(t)$ is time dependent, the solution evolution is considerably more complex. For a linear periodic system, Eq. (141), recalling that the fundamental matrix solution $\Phi(\cdot,\cdot)$ is

defined by Eq. (139), we can write the solution as:

$$\begin{aligned} x(\Delta t) &= x_1 &&= \Phi(\Delta t, 0)x_0 \\ x(2\Delta t) &= x_2 &&= \Phi(2\Delta t, \Delta t)\Phi(\Delta t, 0)x_0 = \Phi(2\Delta t, 0)x_0 \\ &\vdots \\ x(\tau) &= x_r &&= \Phi(r\Delta t, (r-1)\Delta t)\ldots\Phi(\Delta t, 0)x_0 = \Phi(r\Delta t, 0)x_0 = \Phi(\tau, 0)x_0 = Mx_0 \end{aligned} \quad . \tag{152}$$

This indicates that the periodically sampled data matrix, Eq. (150), may be rewritten with the monodromy matrix ($M = \Phi(\tau, 0)$) as:

$$\tilde{V}_{1:k} = [v_1 \quad Mv_1 \quad M^2v_1 \quad \ldots \quad M^kv_1]. \tag{153}$$

We now relate the subsets of data $\tilde{V}_{1:k-1}$ to $\tilde{V}_{2:k}$, yielding:

$$\tilde{V}_{2:k} = M\tilde{V}_{1:k-1}. \tag{154}$$

Taking the SVD of the data matrix on the right-hand side, $\tilde{V}_{1:k-1} = U\Sigma W^H$, gives:

$$\tilde{V}_{2:k} = MU\Sigma W^H. \tag{155}$$

Right multiplying Eq. (155) by W and then by the rank j pseudoinverse of $\Sigma \rightarrow \tilde{\Sigma}^{-1}$, as discussed in Section 3.1.4, and then left multiplying by U^H gives:

$$U^HMU = U^H\tilde{V}_{2:k}W\Sigma^{-1} \equiv \tilde{S}_F. \tag{156}$$

Similar to the discussion of the DMD method in Chapter 3, some of the eigenvalues of the monodromy matrix—especially the ones with largest modulus—are approximated by the eigenvalues of matrix $\tilde{S}_F$, which we can find without knowledge of the monodromy matrix and, more importantly, without knowing $A(t)$. Again, these largest Floquet multipliers are in fact exactly what is required to determine the stability of the orbit. We will refer to this analysis technique as the Floquet decomposition (FD).

To perform the FD analysis, we must first choose the appropriate analysis period, τ. The correct choice of period depends, however, on the problem being solved. We will discuss three possible situations. The first situation is when a nonautonomous parametric forcing term, similar to the $\epsilon\cos(t)$ term in the Mathieu equation, has a frequency that is known a priori. In this case, the appropriate time period is the reciprocal of this frequency. The second situation is when the parametric forcing

term's frequency is not known. In this case, it will be difficult to find the appropriate time period from theory alone. The third situation is when the system consists of two or more subsystems, each characterized by its own frequencies, whose interactions can produce a parametric instability. In this case, since the parametric instability coupling term depends on the state variables it follows that the time period may presumably be found by analyzing the state variables. Under these conditions, two techniques for finding the time period are to use the PSD of a state variable or to find the peak autocorrelation of a state variable or the state vector. We will discuss the choice of analysis period further in Section 5.7.

5.5 Ensemble Floquet Decomposition

It will be shown in Section 6.1 that the FD analysis suffers from some shortfalls; To address these issues we need to develop an extension of the FD method, which is described in this section.

The process described by Eqs. (153) to (156) provides an approach to approximate the largest modulus Floquet multiplier of a system without knowledge of the governing equations. This method will be applied to the experimental datasets in Section 6.1, where we will show that, similarly to the SDD results that are described in the previous chapter, the modes exhibit considerable noise—especially in the velocity fields. In addition, the PIV and PLIF measurements are planar and, thus, cannot describe the full 3-D, swirling velocity and chemical state of the system, respectively. As a consequence, it is necessary to find a way to improve the results when the measurements are noisy and/or do not fully describe the state variable, i.e., planar instead of volumetric measurements.

We were motivated by a number of concepts during the development of the following method. The first is that we conceptually know that our results will be better the closer the measurements are to the state vector. The FD method does not require the data to be taken at the sampling frequency, potentially leaving some useful data unused if the sampling period is much longer than the FD analysis period. In addition, for a linear periodic system, the Floquet multipliers are constant and, as a consequence, do not depend on the initial conditions—or conceptually the chosen Pioncaré map surface as long as it is transverse to the solution orbit. And, of course, averaging makes everything better.

Consider a periodic solution in the space $\mathbb{R}^n$. Taking a Pioncaré section, the periodic solution appears to be a fixed point (solution) of the Pioncaré map in the $\mathbb{R}^{n-1}$ hyperplane. With this conceptual hyperplane and the FD method, we can determine the stability of the orbit. In addition, we should be able to pick a second Pioncaré section, employ the FD and again approximate the largest Floquet multipliers. Figure 42 shows a periodic orbit and four Pioncaré sections on which the FD analysis can be performed. If we *average* the results obtained by processing the data at all of the Pioncaré sections, we may be able to improve the overall approximation.

We could simply run the FD method repeatedly starting from r consecutive snapshots, thus using all of the data, then appropriately averaging the approximate Floquet multipliers and modes. This would be much like analyzing the PIV and PLIF data separately, which we found in Section 4.2 gave less than ideal results, partly due to the fact that the modes we found did not have the same Ritz values and thus could not be directly compared. Equivalently, due to the different Floquet multipliers, the EFD based modes could not be easily averaged. Therefore, we apply a similar approach to the one we employed in the SDD method discussed in Section 4.3.1, rearranging the data into larger vectors and simultaneously processing them with the FD algorithm. The advantage of this approach is that the approximated Floquet multipliers for each *ensemble* are identical and were determined from the collective data. Now we average each ensemble, after correcting for the phase difference caused by taking the initial data snapshot from r consecutive time steps. We will call this method of processing data the ensemble Floquet decomposition (EFD).

If we can exploit this repeated approximation, there are two conditions under which the result could improve on the FD method. The first condition is when the measured data matrix is noisy,

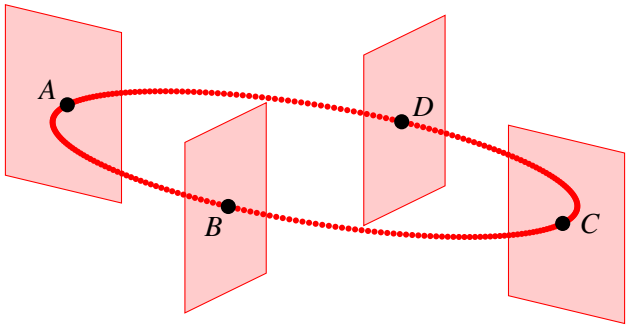

Figure 42: Ensemble Floquet Decomposition schematic

then the FD method approximates the Floquet multipliers of a *noisy* monodromy matrix. If the noise is random, it is reasonable to expect that averaging the repeated application of the FD method should reduce the influence of the noise. The second condition where we might expect improved results is when the measurements at any particular time or phase do not fully quantify the state of the system. In this case, the partially complete data taken from intersections of the solution trajectory with different Pioncaré sections could yield additional information about the state variable and, thus, improve our approximation of the Floquet multipliers.

The first step in this method is to construct the data matrices for each hypothetical Pioncaré section. Assuming there are j equally spaced Pioncaré sections and there are a total of k complete periods within the dataset, then we may write the individual periodic datasets from each section as:

$$\begin{aligned}
\tilde{V}_A \equiv \tilde{V}_{1:k} &= [v_1 \quad v_{1+r} \quad v_{1+2r} \quad \dots \quad v_{1+(k-1)r} \quad] \\
\tilde{V}_B \equiv \tilde{V}_{1+r/j:k+r/j} &= [v_{1+r/j} \quad v_{1+r+r/j} \quad v_{1+2r+r/j} \quad \dots \quad v_{1+(k-1)r+r/j} \quad] \\
\tilde{V}_C \equiv \tilde{V}_{1+2r/j:k+2r/j} &= [v_{1+2r/j} \quad v_{1+r+2r/j} \quad v_{1+2r+2r/j} \quad \dots \quad v_{1+(k-1)r+2r/j} \quad] \\
&\vdots
\end{aligned} . \tag{157}$$

Rewriting Eq. (157) using Eq. (153) yields:

$$\begin{aligned}
\tilde{V}_A \equiv \tilde{V}_{1:k} &= [v_1 \quad Mv_1 \quad M^2v_1 \quad \dots \quad M^kv_1 \quad] \\
\tilde{V}_B \equiv \tilde{V}_{1+r/j:k+r/j} &= [v_{1+r/j} \quad Mv_{1+r/j} \quad M^2v_{1+r/j} \quad \dots \quad M^kv_{1+r/j} \quad] \\
\tilde{V}_C \equiv \tilde{V}_{1+2r/j:k+2r/j} &= [v_{1+2r/j} \quad Mv_{1+2r/j} \quad M^2v_{1+2r/j} \quad \dots \quad M^kv_{1+2r/j} \quad] \\
&\vdots
\end{aligned} . \tag{158}$$

Often we take $j = r$, simplifying the equations and using all of the acquired data.

Concatenating the data matrices from Eq. (158) into a larger matrix, much like we discussed in Section 4.3, allows us to define a single dataset on which we will apply the FD method:

$$\tilde{V} \equiv \begin{bmatrix} \tilde{V}_A \\ \tilde{V}_B \\ \tilde{V}_C \\ \vdots \end{bmatrix} = \begin{bmatrix} v_1 & Mv_1 & M^2v_{1j} & \dots & M^kv_1 \\ v_{1+r/j} & Mv_{1+r/j} & M^2v_{1+r/j} & \dots & M^kv_{1+r/j} \\ v_{1+2r/j} & Mv_{1+2r/j} & M^2v_{1+2r/j} & \dots & M^kv_{1+2r/j} \\ \vdots & & & & \end{bmatrix} . \tag{159}$$

From the structure of Eq. (159), we define an abstracted *snapshot*, $\tilde{v}$ as:

$$\tilde{v} \equiv \begin{bmatrix} v_1 \\ v_{1+r/j} \\ v_{1+2r/j} \\ \vdots \end{bmatrix} \tag{160}$$

and rewrite the abstracted data matrix as:

$$\tilde{V} = \left[\begin{bmatrix} v_1 \\ v_{1+r/j} \\ v_{1+2r/j} \\ \vdots \end{bmatrix} \quad \tilde{M}\begin{bmatrix} v_1 \\ v_{1+r/j} \\ v_{1+2r/j} \\ \vdots \end{bmatrix} \quad \tilde{M}^2\begin{bmatrix} v_1 \\ v_{1+r/j} \\ v_{1+2r/j} \\ \vdots \end{bmatrix} \quad \dots \quad \tilde{M}^k\begin{bmatrix} v_1 \\ v_{1+r/j} \\ v_{1+2r/j} \\ \vdots \end{bmatrix}\right] = \left[\tilde{v} \quad \tilde{M}\tilde{v} \quad \tilde{M}^2\tilde{v} \quad \dots \quad \tilde{M}^k\tilde{v}\right]. \tag{161}$$

where

$$\tilde{M} \equiv \begin{bmatrix} M & 0 & \dots & 0 \\ 0 & M & \dots & \vdots \\ 0 & 0 & \ddots & 0 \\ \vdots & & 0 & M \end{bmatrix}. \tag{162}$$

In an idealized case, the measurements are free of noise and the analysis associated with each Pioncaré section provides the same M matrix. In this case, the EFD method, during the SVD decomposition step, would produce a series of repeated singular values. Once sorted, as is typical from high to low, we would find a stair step series of values in the normalized singular value plot. An example of the idealized FD and EFD analyses singular value plots are shown in Fig. 43. In addition, if we include only the largest singular values in the pseudoinverse process, we will enhance the contribution of the largest singular values to the FD multipliers and modes, while diminishing the contribution of the remaining values. While an apparent disadvantage, this approach only analyzes the *leading* behavior it should be kept in mind that the stability of these periodic systems only depends on this leading behavior.

In the following chapter, we will apply the EFD method to analyze experimental data; this application of the EFD method differs from the idealized case in two key ways. First, real measurements include noise, the amplitude of which can be small for clean signals or very large for some

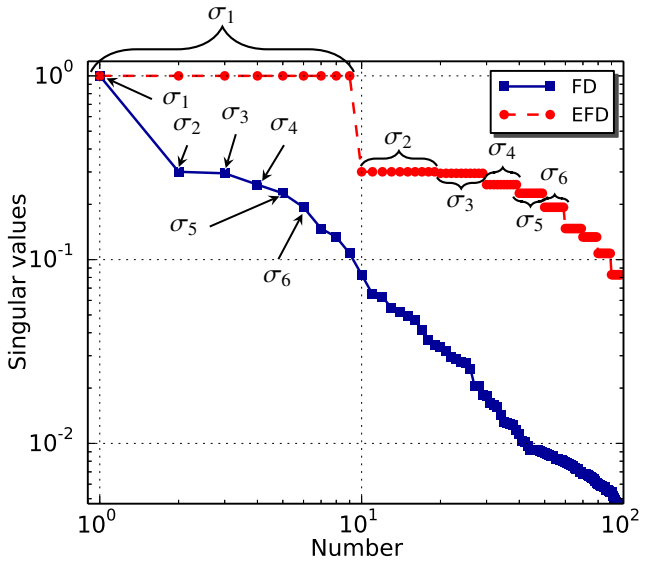

Figure 43: Conceptual normalized singular values obtained from the FD method and the singular values generated by EFD methods with 10 perfect ensembles with complete state data

measurements. If the only effect that we had to deal with was noise addition to the true measurements, then Eq. (162) would have a series of noise matrices, N_k, added to each M matrix on the diagonal. In this case, the EFD method would enhance the large singular values, thus reducing the effect of noise on them.

The second difference is that we do not have full state space data at any given time. For example, the planar diagnostics provide information at one cross-section (or slice) of a complex swirling flow and taking different slices would yield different portions of the total state vector for the system. This second effect changes our interpretation of Eq. (162) somewhat. Including the lack of full state measurement effect only, the diagonal matrices in Eq. (162) would not be M, they would instead be a series of low dimension approximations to M. Here, the EFD method would not produce a series of repeated singular values because each submarix contains different information about the true monodromy matrix. In this case, we expect the SVD of $\tilde{M}$ to not only enhance the leading singular values, but to better describe the leading singular value decomposition of the true M matrix.

Including the effects of noise addition and incomplete state variable description, we might rewrite Eq. (162) as:

$$\tilde{M} \equiv \begin{bmatrix} \hat{M}_1 + N_1 & 0 & \dots & 0 \\ 0 & \hat{M}_2 + N_2 & \dots & \vdots \\ 0 & 0 & \ddots & 0 \\ \vdots & & 0 & \hat{M}_k + N_k \end{bmatrix}, \tag{163}$$

where, $\hat{M}_j$ is the noise-free, reduced dimension, approximation to M and N_j is the measurement noise. We will use this interpretation in comparing the FD and EFD methods when they are used to analyze our experimental data in Section 6.2.1.

If, for example, we used two Pioncaré sections, A and B, and we knew the appropriate time period, τ, then we could apply the DMD algorithm to these data, yielding approximate Floquet multipliers, η, and the associated Floquet modes, $\boldsymbol{\phi}$. Or,

$$\boldsymbol{v} = \begin{Bmatrix} \boldsymbol{v}_A \\ \boldsymbol{v}_B \end{Bmatrix}, \tau \quad \rightarrow \quad DMD \quad \rightarrow \quad \eta(\boldsymbol{v}_A, \boldsymbol{v}_B), \;\; \boldsymbol{\phi}(\boldsymbol{v}_A, \boldsymbol{v}_B) = \begin{Bmatrix} \boldsymbol{\phi}_A(\boldsymbol{v}_A, \boldsymbol{v}_B) \\ \boldsymbol{\phi}_B(\boldsymbol{v}_A, \boldsymbol{v}_B) \end{Bmatrix}. \tag{164}$$

Much like our discussion in Section 4.3.1, the accuracy of the approximate Floquet multipliers depends on the information obtained from each of the input vectors that, in this case, are the data from the different Poincaré sections. Also, in a manner similar to the discussion of the calculated Ritz vectors, the mode, $\boldsymbol{\phi}$, is a composite of modes that have the same structure as the input vectors. Here, these composite modes represent different realizations or ensembles of the analysis, at the different Pioncaré sections in some sense. However, since both $\boldsymbol{\phi}_A$ and $\boldsymbol{\phi}_B$ are associated with a single approximate Floquet multiplier, they have the same dynamical dependence. One might call these ensemble Floquet modes. To reduce the effects of noise we will average these ensemble Floquet modes to obtain a better mode *shape*. Before the average of the ensembles may be taken, each ensemble must be corrected because of the phase difference between the data taken from the first conceptual Poincaré section and subsequent ones. In other words, each ensemble must have the phase shifted in such a way that it represents the same portion of the oscillation.

In this method, the ensemble phase correction and averaging was performed in the following manner. First, as we have discussed, the real and imaginary parts of the modes that have a positive modal frequency are sufficient for a basis to use in a decomposition. Taking the first ensemble as

phase, $\theta = 0$, this ensemble does not need phase correction and the real and imaginary parts of the ensembles may be found as:

$$\boldsymbol{\phi}_A^+ = \mathrm{Re}\{\boldsymbol{\phi}_A\} = \frac{1}{2}\left[\boldsymbol{\phi}_A + \boldsymbol{\phi}_A^*\right] \quad \text{and} \quad \boldsymbol{\phi}_A^- = \mathrm{Im}\{\boldsymbol{\phi}_A\} = \frac{i}{2}\left[\boldsymbol{\phi}_A - \boldsymbol{\phi}_A^*\right]. \tag{165}$$

Each of the other ensembles must have the phase corrected by the amount, $\theta = \exp[-i\omega t]$, where ω and t are the modal angular frequency ($\mathrm{Im}\{\rho\}$) and the time difference between the initial snapshots used to generate the first ensemble and the current ensemble, respectively. Note that the angular frequencies for the complex conjugate pair of modes $\boldsymbol{\phi}_A$ and $\boldsymbol{\phi}_A^*$ are ω and $-\omega$, respectively. Consequently, the phase correction for the second ensemble is obtained from the following expression:

$$\boldsymbol{\phi}_B^+ = \mathrm{Re}\{\boldsymbol{\phi}_B\} = \frac{1}{2}\left[\boldsymbol{\phi}_B e^{-i\omega\Delta tr/j} + \boldsymbol{\phi}_B^* e^{i\omega\Delta tr/j}\right] \quad \text{and} \quad \boldsymbol{\phi}_B^- = \mathrm{Im}\{\boldsymbol{\phi}_B\} = \frac{i}{2}\left[\boldsymbol{\phi}_B e^{-i\omega\Delta tr/j} - \boldsymbol{\phi}_B^* e^{i\omega\Delta tr/j}\right], \tag{166}$$

and for the third ensemble:

$$\boldsymbol{\phi}_C^+ = \mathrm{Re}\{\boldsymbol{\phi}_C\} = \frac{1}{2}\left[\boldsymbol{\phi}_C e^{-i2\omega\Delta tr/j} + \boldsymbol{\phi}_C^* e^{i2\omega\Delta tr/j}\right] \quad \text{and} \quad \boldsymbol{\phi}_C^- = \mathrm{Im}\{\boldsymbol{\phi}_C\} = \frac{i}{2}\left[\boldsymbol{\phi}_C e^{-i2\omega\Delta tr/j} - \boldsymbol{\phi}_C^* e^{i2\omega\Delta tr/j}\right], \tag{167}$$

and so on.

The final, low noise modes are found by averaging each phase corrected ensemble:

$$\boldsymbol{\phi}^+ = \mathrm{mean}(\boldsymbol{\phi}_A^+, \boldsymbol{\phi}_B^+, \boldsymbol{\phi}_C^+, \ldots) \quad \text{and} \quad \boldsymbol{\phi}^- = \mathrm{mean}(\boldsymbol{\phi}_A^-, \boldsymbol{\phi}_B^-, \boldsymbol{\phi}_C^-, \ldots). \tag{168}$$

This technique has been applied to the experimental data and will be discussed in Section 6.1.

5.6 Examples

While the FD method may appear to simply be the DMD method with a modified sampling frequency, the analysis period plays a critical role in the FD method allowing the study of more complex evolution operators. As a result, we expect there are many cases where the FD method will provide better results than the DMD method with a sampling frequency either higher or lower than the FD analysis frequency. For example, we expect the FD to more accurately decompose the data from parametric instabilities and systems with mainly narrow band noise. In this section, we give a number of examples that show how the FD method can be applied to simple systems and how to interpret the

results. This will aid in our ability to interpret results obtained from the analysis of more complex systems, such as those obtained from the analysis of our experimental data (presented in Section 6.1).

5.6.1 Linear Mathieu Equation

In Section 5.2 we discussed the following linear Mathieu equation:

$$\ddot{u} + [\kappa + \epsilon \cos(t)]\, u = 0, \tag{169}$$

as an example of a system capable of exhibiting parametric instabilities. Let's assume that Eq. (169) is the governing equation for a spring-mass system, where κ is the mass specific stiffness and for small values of ϵ, $\epsilon \cos(t)$ is a harmonic perturbation to the stiffness. Rewriting Eq. (169) in state space with $\boldsymbol{x} = \{u \quad \dot{u}\}^T$, yields:

$$\dot{\boldsymbol{x}} = \begin{bmatrix} 0 & 1 \\ -\kappa - \epsilon \cos(t) & 0 \end{bmatrix} \boldsymbol{x}. \tag{170}$$

The stability of Eqs. (169) and (170) for various values of the parameters κ and ϵ are given by the diagram shown in Fig. 44. These regions of instability (marked: U) are sometimes referred to tongues.

As an aside, the narrow stability tongues for low amplitude parametric forcing (small ϵ) may explain an observation about the stability of the experimental facility. Specifically, under almost all

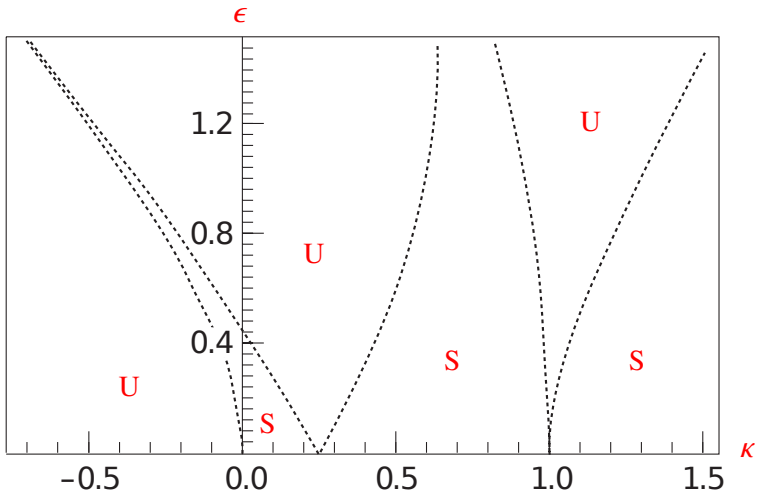

Figure 44: Linear Mathieu equation stability tongues, adapted from Sinha and Butcher [1]. U: unstable and S: stable

configurations the rig was stable. By which we mean that the acoustic spectra showed peaks, some of which were large amplitude, but all of the peaks were of low quality (wide) and not likely due to acoustically coupled CIs. For the rig to go unstable, the transverse length ducts had to be tuned closely to our *unstable* configuration described in Chapter 2. The narrow bands of frequency tuning (κ) of instability for low amplitude forcing for parametric systems like the one shown in Fig. 44 may explain why the rig was stable under almost all configurations.

The system of ODEs, Eq. (170), was numerically integrated from initial conditions $\boldsymbol{x}_0 = \{1 \quad 0\}^T$ for 50 s with three different combinations of κ and ϵ. The values of these parameters were chosen to be near the fundamental unstable tongue, with two cases inside the unstable region and one inside the stable region. The parameters for the three cases (Cases 1 to 3) are shown in Table 8. The fourth case in Table 8 will be discussed in Section 5.6.2. The phase-space diagrams for cases 1 to 3 are shown in Fig. 45.

For Cases 1 to 3, in addition to the numerical integration, the fundamental matrix was integrated to find the monodromy matrix, which was used to find the Floquet multipliers, μ, and Floquet exponents, ρ. These values are also listed in Table 8. The modulus of the largest Floquet multiplier, $|\mu_1|$ is also listed. For Cases 1 and 2 the modulus is larger than one, indicating the system is unstable, as also shown by the growth of the solution in the phase-diagram, Figs. 45a and 45b. For Case 3 the modulus is equal to one within the calculation's numerical precision, thus indicating that it is Lyapunov stable, not asymptotically stable. But, from the phase-diagram, Fig. 45c, it appears the solution is growing and growing quicker than Case 2. To see the difference in the true nature of Case 2 and 3 we must observe the phase space of the systems for a longer period of time.

If we integrate the solution for five times as long, i.e., for 250 s, the behavior of Case 2 and 3 becomes clearer. The phase diagrams for these longer simulations are shown in Fig. 46. In Case 2, Fig. 46a, the exponential growth is evident, while in Case 3, Fig. 46b, there is different behavior. It shows that the solution initially grows, then stops growing, and then decays. In this longer-term observation, the stability predicted by the Floquet multipliers is confirmed. This is an example of what is sometimes called *transient amplification* [64]. Interestingly, Floquet theory predicts that Case 3 is Lyapunov stable, all of which is found from the fundamental matrix solution for one time period, $\tau = 2\pi$ s.

Table 8: Floquet multipliers for the Mathieu equation

Case	1	2	3	4
κ	0.25	0.25	0.26	0.25
ϵ	0.1	0.01	0.01	0.1
α	0.0	0.0	0.0	0.1
μ_1	-1.36709975	-1.03191360	$-0.9985518 + 0.05383583i$	-
μ_2	-0.73148135	-0.96908384	$-0.9985518 - 0.05383583i$	-
$\lvert\mu_1\rvert$	1.36709975	1.03191360	1.0000019969	-
ρ_1	$0.04976640 + 0.5i$	$-0.00499813 + 0.5i$	$3.17617388 \times 10^{-7} + 0.49142763i$	-
ρ_2	$0.00499984 + 0.5i$	$-0.04976513 + 0.5i$	$3.17617388 \times 10^{-7} - 0.49142763i$	-
Lyapunov stability	Unstable	Unstable	Stable	Stable
$\tilde{\mu}_1$	-1.36710476	-1.03197541	$-0.99852864 + 0.0537927i$	$-0.91765101 + 0.22096103i$
$\tilde{\mu}_2$	-0.73087982	-0.96896407	$-0.99852864 - 0.0537927i$	$-0.91765101 - 0.22096103i$
$\lvert\tilde{\mu}_1\rvert$	1.36710476	1.03197541	0.9999765495	0.9438787808
Error: $\lvert\frac{\mu_1-\tilde{\mu}_1}{\mu_1}\rvert$	3.66×10^{-6}	5.99×10^{-5}	4.90×10^{-5}	-

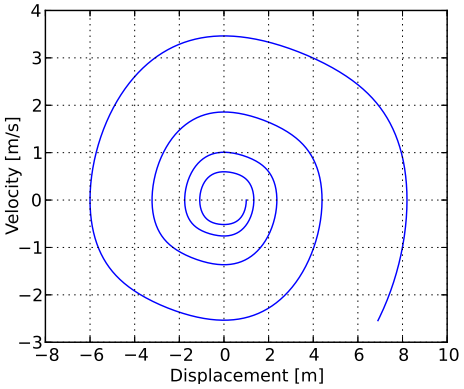

(a) Case 1: $\kappa = 0.25, \epsilon = 0.1$, unstable

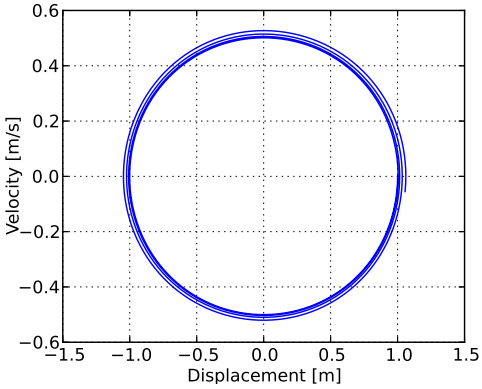

(b) Case 2: $\kappa = 0.25, \epsilon = 0.01$, unstable

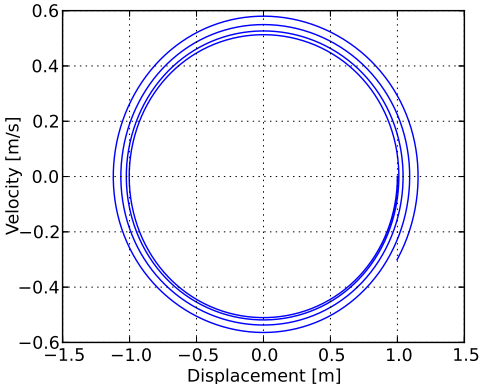

(c) Case 3: $\kappa = 0.26, \epsilon = 0.01$, stable

Figure 45: Linear Mathieu equation phase space diagrams for $t = [0, 50]$ s

Another example of how it may be difficult to tell the difference between a stable and an unstable case is shown in Fig. 47. In Figs. 47a and 47c we have plotted PSD of the displacement and Figs. 47b and 47d shows the L^2 norm as a function of time, where this norm is defined as:

$$E \equiv \left[\sum_k x_k^2 \right]^{1/2} . \tag{171}$$

The Case 2 and Case 3 PSDs are remarkably similar, but the long-term stability is different, as shown by the time evolution of the energy-like, L^2, norms. Thus, the spectra contributes little to the determination of the stability of the system in this case.

We simulated Eq. (170) with a Python code using the SciPy algorithm: Complex-valued Variable-coefficient Ordinary Differential Equation solver (zvode). The solution is reported at 1 ms (the integration time-step is set by the algorithm to achieve desired accuracy, here the relative and absolute tolerances were set to $rtol = 1.49012 \times 10^8$ and $atol = 1.49012 \times 10^8$, respectively). The FD method

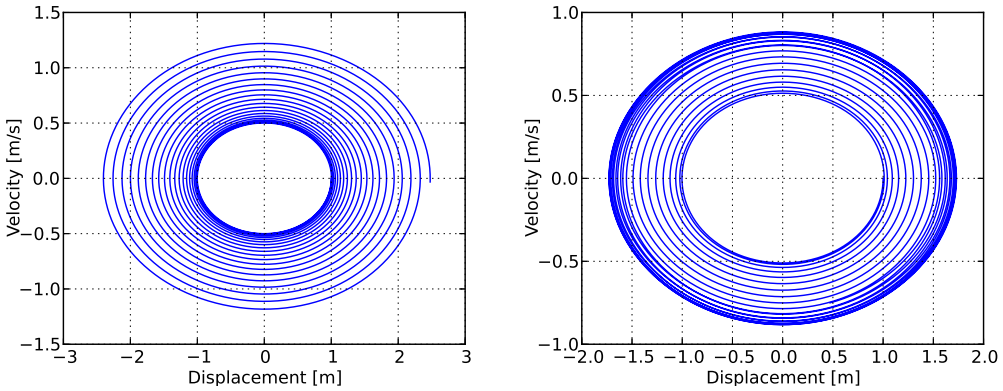

(a) Case 2: $\kappa = 0.25, \epsilon = 0.01$ (b) Case 3: $\kappa = 0.26, \epsilon = 0.01$

Figure 46: Linear Mathieu equation phase space diagrams for $t = [0, 250]$ s

is then applied to the first 50 s of state-space vector data consisting of the position and velocity data. For the data presented here we have used the analytical period, $\tau = 2\pi$ s. The results from the $\tau = 2\pi$ s analysis are very similar to those found by estimating the period via autocorrelation of the state vector, although the period of the coefficient matrix and the orbit are somewhat different in nature and this approach is not alway appropriate. Often, in physical systems, there may be additional clues that help find the appropriate period. We will discuss the choice of τ in more detail in Section 5.7.

Notably, the FD method determined the approximate Floquet multipliers and, equivalently, the Floquet exponents of the system without knowledge of the governing equations. These approximate multipliers $\tilde{\mu}$ are listed in Table 8. Comparing the Floquet multipliers calculated with the monodromy matrix (μ) and the FD based estimation ($\tilde{\mu}$) shows a very good agreement. In fact,we estimate that the error in the largest multiplier, $\tilde{\mu}_1$, for Case 1 to be $3.7\times10^{-4}\%$. The application of the FD method for Cases 2 and 3 have slightly larger estimated errors of $6.0\times10^{-3}\%$ and $4.9\times10^{-3}\%$, respectively.

The traditionally calculated multipliers (circles) and those obtained by the FD method (crosses) for the first three cases are plotted relative to the unit circle in Fig. 48. For Case 1, the black markers, we see there is one Floquet multiplier inside the unit circle and one outside. As another check of our calculated Floquet multipliers, from theory, e.g., Magnus and Winkler [58], we know the product $\mu_1\mu_2 = 1$. We find this product for both the monodromy matrix and FD based Floquet multipliers, for example, for Case 1, $\mu_1\mu_2 = (-1.36709975) \cdot (-0.73148135) = 1.0000079707$ and $\tilde{\mu}_1\tilde{\mu}_2 = (-1.36710476) \cdot (-0.73087982) = 0.99918928$, respectively. The product of the monodromy

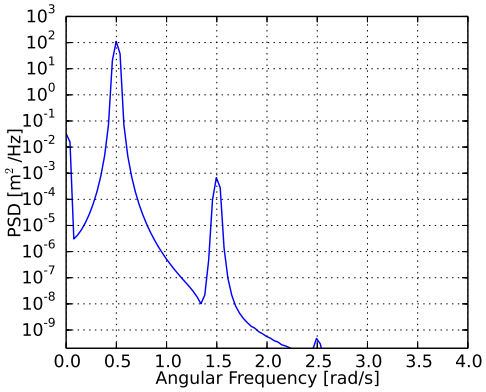

(a) Case 2: PSD of x_1

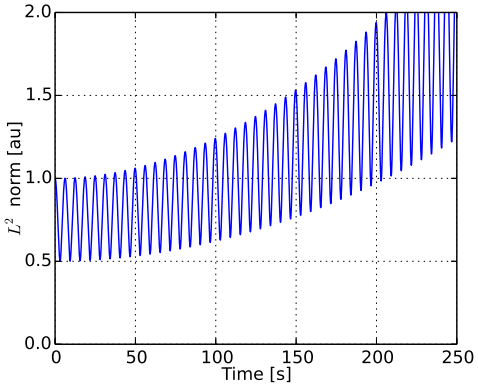

(b) Case 2: L^2 norm

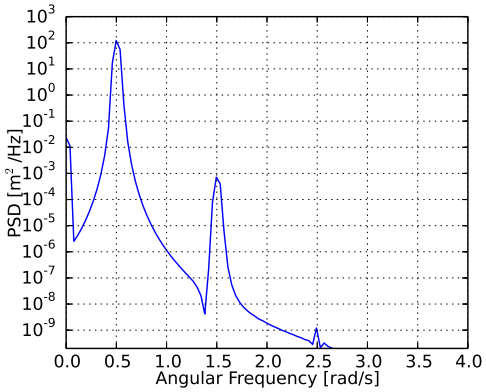

(c) Case 3: PSD of x_1

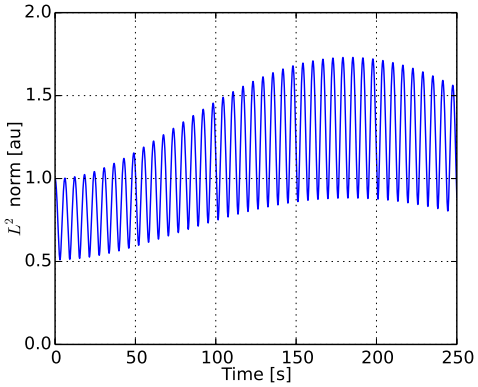

(d) Case 3: L^2 norm

Figure 47: Linear Mathieu equation power spectrum and L^2 norm

matrix based multipliers is closer to 1.0 than the FD based product, but both are within our expected precision.

While the parameters chosen for Case 2 also produce an unstable system, it is much closer to the stability boundary. This is apparent in Fig. 48—the red markers—where the pair of Floquet multipliers are much closer to the unit circle. For Case 3, the green markers, the parameters chosen produce a stable system, which is near the stability boundary. Again, the stability is not asymptotic. In other words, the Floquet multipliers are on the unit circle, indicating a stable toroidal type orbit. From Table 8 and Fig. 48 we see the FD method approximates the Floquet multipliers well.

The FD method predicts that Case 3 is Lyapunov stable and accurately approximates the Floquet multipliers long before the stability could be inferred from the phase diagram in Fig. 45c. To see the proper stability of Case 3 from a phase diagram, Fig. 46b, or the energy-like, L^2 norm

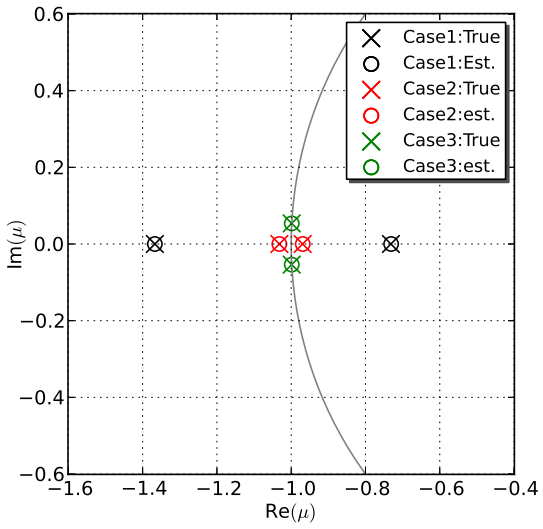

Figure 48: Linear Mathieu equation Floquet multipliers and estimated Floquet multipliers

diagram, Fig. 47d, we must observe the system for over 25 periods to see that the solution does not unboundedly grow—considerably longer than the eight periods used in the FD analysis.

5.6.2 Nonlinear Mathieu Equation

The unbounded growth being a physical impossibility, we are interested in nonlinear equations that exhibit parametric instabilities, whose amplitudes are bounded. One possible nonlinear addition to the Mathieu equation is a cubic damping term. When we supplement Eq. (169) with this damping term we obtain the following nonlinear equation:

$$\ddot{u} + [\kappa + \epsilon \cos(t)]\, u + \epsilon\alpha u^3 = 0. \tag{172}$$

In order for this equation to behave similarly to its linear counterpart, we will require the ratio of damping to driving, α, be much less than one. The presence of this nonlinear term limits the solution growth due to the instability, producing limit cycle like behavior.

Rewriting Eq. (172) as a system of first order ODEs (i.e., state space) yields:

$$\dot{\boldsymbol{x}} = \begin{bmatrix} 0 & 1 \\ -\kappa - \epsilon\cos(t) - \epsilon\alpha x_1^2 & 0 \end{bmatrix} \boldsymbol{x}, \tag{173}$$

where the state vector is $\boldsymbol{x} = \{u \quad \dot{u}\}^T$. This system of ODEs was integrated for 150 s using the techniques discussed in the previous section. The phase diagrams of the linear equation, Case 1, and

the nonlinear case, Case 4, are shown in Figs. 49a and 49b, respectively. In Figs. 49c and 49d we have plotted the time history of the displacement and velocity. The first 2 or 3 periods of both solutions are very similar, but as the displacements become larger the nonlinear term exerts a damping like effect. Notably, the displacement plot in Fig. 49d is qualitatively similar to the pressure measurements made in the experimental system, e.g., see Figs. 8a and 8b. Also the solution plotted in Fig. 49b does not exhibit a limit cycle in the traditional sense, although the solution is bounded.

The FD method analysis was performed using the first 50 s of state space data, with the period estimated to equal $\tau = 6.265$ s, nearly 2π s, by the autocorrelation. The appropriate period deviates more and more from 2π s as α becomes larger. The resulting approximations for the Floquet multipliers are listed in Table 8. Note that in this case we have not listed monodromy based Floquet multipliers and exponents as the Floquet theory is strictly limited to linear systems. The FD based

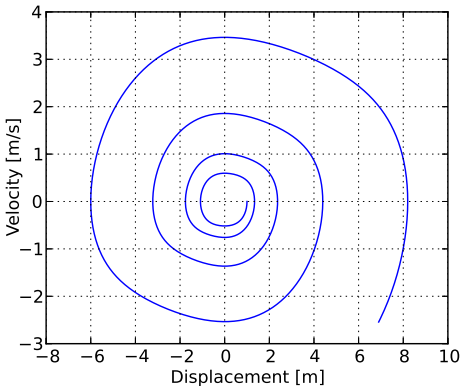

(a) Case 1: $\kappa = 0.25, \epsilon = 0.1, \alpha = 0$

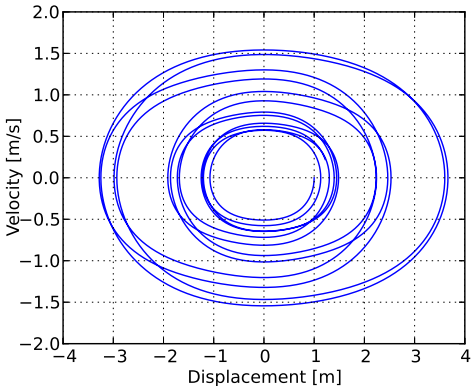

(b) Case 4: $\kappa = 0.25, \epsilon = 0.1, \alpha = 0.1$

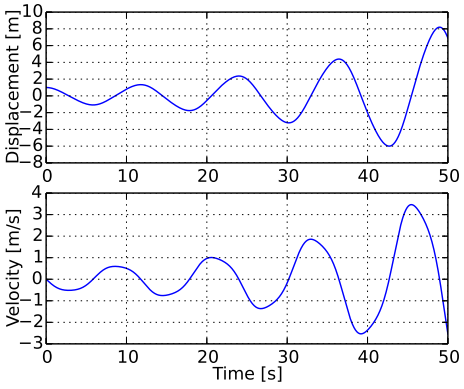

(c) Case 1: $\kappa = 0.25, \epsilon = 0.1, \alpha = 0$

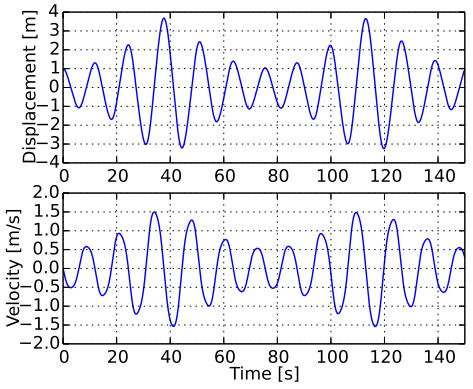

(d) Case 4: $\kappa = 0.25, \epsilon = 0.1, \alpha = 0.1$

Figure 49: Nonlinear Mathieu equation phase space diagrams (a and b) and time histories (c and d)

multipliers are $-0.918 \pm 0.221i$, the modulus of which is less than one, predicting the system is asymptotically stable, although, from the available phase diagram the system appears only to be Lyapunov stable. This result can be explained by recalling that Case 1 has the same system parameters except for the nonlinear term and we found that case to be linearly unstable. As the displacements become small the system is linearly unstable, but the orbit is nonlinearly asymptotically stable—and as these effects balance the system exhibits a complex toroidal like orbit.

5.6.3 Nonlinear Mathieu like System of Equations

Our experiments appear to represent a system of coupled oscillators, i.e., the hydrodynamic/ combustion system and the transverse acoustic system. This example shows how coupled subsystems, which are autonomous, can exhibit behavior very similar those discussed in the previous examples.

Specifically, we will examine a couple system composed of two subsystems where the first subsystem is a Mathieu equation that has had the autonomous term, $\cos(t)$, replaced by the *displacement* like variable from a harmonic oscillator subsystem, u_2; this system of equations was suggested by Holmes and Rand as a close analog to Eq. (172) [70]:

$$\begin{cases} \ddot{u}_1 + [\kappa + \epsilon u_2]\, u_1 + \epsilon\alpha u_1^3 = 0 \\ \ddot{u}_2 + u_2 = \frac{1}{2}\epsilon u_1^2 \end{cases} . \tag{174}$$

We will refer to these two subsystems as Subsystem 1 and 2, respectively. The second subsystem is coupled back to the modified Mathieu subsystem by feedback through the u_1^2 term and we have changed the sign of the feedback term in the second equation from that given by Holmes and Rand; this change will be discussed after we have presented the results. Although the specific form of the equations may be different, this type of system of equations might describe our CI experiments because presumably the two experimental subsystems are linked through a similar feedback cycle.

Rewriting Eq. (174) into state space, where $\boldsymbol{x} = \{u_1 \quad u_2 \quad \dot{u}_1 \quad \dot{u}_2\}^T$, yields:

$$\dot{\boldsymbol{x}} = \begin{bmatrix} 0 & 0 & 1 & 0 \\ 0 & 0 & 0 & 1 \\ -\kappa - \epsilon x_2 - \epsilon\alpha x_1^2 & 0 & 0 & 0 \\ \frac{1}{2}\epsilon x_1 & -1 & 0 & 0 \end{bmatrix} \boldsymbol{x}. \tag{175}$$

This system describes an autonomous, homogeneous, coupled set of oscillators that behave similarly to those described by Eq. (173); specifically, u and $\dot{u}$ in Eq. (173) can be similarly interpreted as u_1 and $\dot{u}_1$ in Eq. (175).

Similarly to the previous examples, we have integrated the system, Eq. (175), for 150 s with the initial conditions $\boldsymbol{x}_0 = \{1 \quad 1 \quad 0 \quad 0\}^T$. The composite phase diagrams and time history plots are shown in Fig. 50, where the solid and dashed lines represent the state variables of Subsystem 1 and 2, respectively.

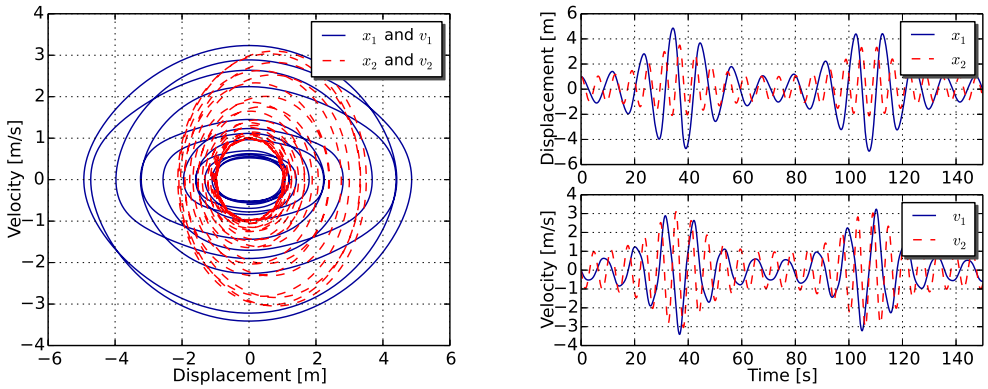

(a) Phase space diagram (b) Time history

Figure 50: Nonlinear autonomous Mathieu system of equations phase space and time histories, $\kappa = 0.25, \epsilon = 0.1, \alpha = 0.1$

To determine whether the coupled system, Eq. (175), mimics the dynamics produced by the nonlinear Mathieu equation presented as Case 4, we compare the displacement and velocity solution components from Case 4 with those from Subsystem 1 in Fig. 51. While these two systems are different, their amplitudes and frequencies differ somewhat, their dynamics are qualitatively similar. This comparison shows that the subsystems of the coupled, autonomous system behave much like a periodic, nonautonomous system and can exhibit parametric instabilities.

If we analyze the data generated for this coupled system with the FD method, we find two complex conjugate pairs of estimated Floquet multipliers, $\eta_{1,2} = -0.83955138 \pm 0.42069237i$ and $\eta_{3,4} = 0.90310260 \pm 0.2720392i$. The magnitudes of these pairs are $|\eta_{1,2}| = 0.93905729$ and $|\eta_{3,4}| = 0.94318589$, respectively, indicating that the system is asymptotically stable. These multipliers are compared with the calculated pair from Case 4 in Fig. 52, where the modulus of the multipliers was 0.944. Figure 52 also shows that we find four multipliers and associated angular

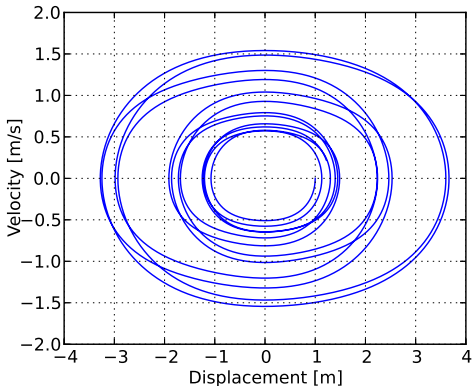

(a) Case 4: Phase diagram

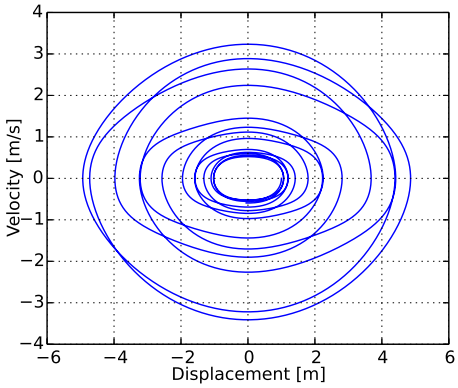

(b) Autonomous system: Phase diagram

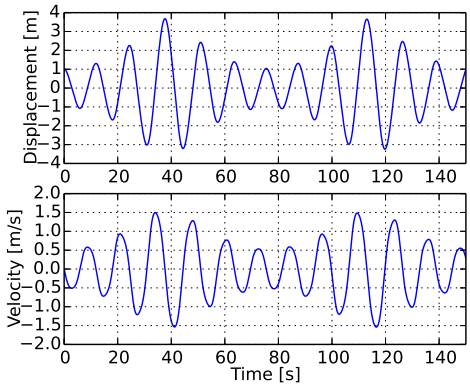

(c) Case 4: Time history

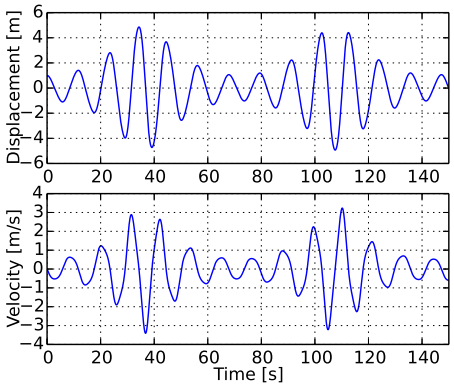

(d) Autonomous system: Time history

Figure 51: Nonlinear Mathieu equation and autonomous system (plotted is Subsystem 1 data only), phase space diagrams and time histories, $\kappa = 0.25, \epsilon = 0.1, \alpha = 0.1$

frequencies in the coupled system and only two for Case 4. This does not imply, however, that we have introduced new oscillatory frequencies into the system. First, we examine the angular frequencies found in the system solution/FD analysis. Using Eq. (144) and accounting for the logarithmic branch cuts, we find the angular frequencies $\omega_{1,2} = \pm 0.576$ and $\omega_{3,4} = \pm 1.05\,\text{rad/s}$, when the integer in the equation is, $k = 2$. Comparing these frequencies to Case 4, we find $\omega_{1,2} = \pm 0.539\,\text{rad/s}$ using $k = 1$, a similar result to 2 of the 4 frequencies we found from the system of equations. In addition, there is another implicit frequency in Case 4, the frequency of the $\cos(t)$ term, $\omega = 1.0\,\text{rad/s}$. Again showing that the differences in these two solutions are small when we compare the angular frequencies and modulus of the multipliers. Ultimately, it appears the FD method yields the stability of the system and the complex frequencies of the system whether the system is parametrically forced and nonautonomous, or an autonomous set of coupled subsystems that exhibits a parametric instability.

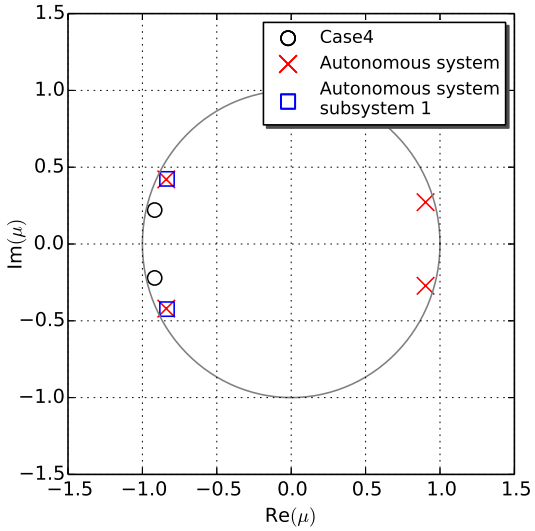

Figure 52: Estimated Floquet multipliers for nonlinear Mathieu equation (black circles), the autonomous, nonlinear Mathieu system (red crosses), and the autonomous, nonlinear Mathieu system using only Subsystem 1 data in FD (blue squares)

The examples presented thus far have utilized the full state vector in the FD analyses, but in most experimental situations we will are unable to obtain data that fully describes the state vector. Due to the 4-dimensional nature of the system example, we can explore whether the FD method properly analyzes the system when only a portion of the state vector is used in the analysis. We will examine a number of cases where we analyze the system using incomplete state data in the next section. But first, to demonstrate that full state data may not be required to find important modes, we have analyzed data take from only Subsystem 1 and compared the results to those obtained using the full state information. Analyzing the system using only data from Subsystem 1, $x_1 = u_1$ and $x_3 = \dot{u}_1$, we found the estimated Floquet multipliers are $\eta_{1,2} = -0.83470232 \pm 0.42400283i$. These values have been included in Fig. 52 as blue squares. Notably, these multipliers are nearly identical to the first pair of multipliers from the analysis using the full system state data (left two red crosses). This result adds support to our claim that we may not need the entire set of state data to find the largest modulus Floquet multiplier.

As we found in Case 4, the coupled system is linearly unstable and nonlinearly stable, again producing limit cycle like behavior. In Fig. 53a we have plotted the total L^2 norm of the system and the L^2 norm of each subsystem. Again, if we had only observed this system for a short period of

time, we might have come to the conclusion that this system was unstable due to the large growth of the L^2 norm. Nevertheless, the FD analysis of the system correctly shows otherwise.

At this point we would like to comment on our choice of sign for the right hand side of Eq. (174). If we keep the negative sign used by Holmes and Rand on the feedback term and the use the same initial conditions, the resulting solution is also similar to that found for Case 4, but from the FD analysis the system appears to be Lyapunov stable; the modulus of the approximated Floquet multipliers are 1.001, 1.001, 0.966, 0.966. This study also determined the period was $\tau = 12.13$ s, approximations to the Floquet multipliers were $\mu_{1,2} = 0.9658 \pm 0.2648i$ and $\mu_{3,4} = 0.7079 \pm 0.6568i$, and corrected frequencies were $\omega_{1,2} = \pm 0.5400$ and $\omega_{3,4} = \pm 1.0976$ rad/s for this case. Choosing to remove the negative sign from Holmes and Rand's system yields a system that is linearly unstable and nonlinearly stable—which mimics Case 4 and the behavior of many unstable combustors.

5.7 Choice of Sampling Period

In the last example, Section 5.6.3, how did we choose the FD analysis time period? And, did we choose correctly? Our choice for the period for the analysis was based on the peak autocorrelation for time delays near the linear system's period of 2π s—knowing that 2π s is the correct period in the linear case. If we examine the PSD of a state variable from each subsystem, shown in Fig. 53b, we see that Subsystem 1 and 2 have peak angular frequencies near 0.5 rad/s and 1.0 rad/s, respectively. As a result, we might conjecture that the correct analysis period is close to either 4π s or 2π s, respectively.

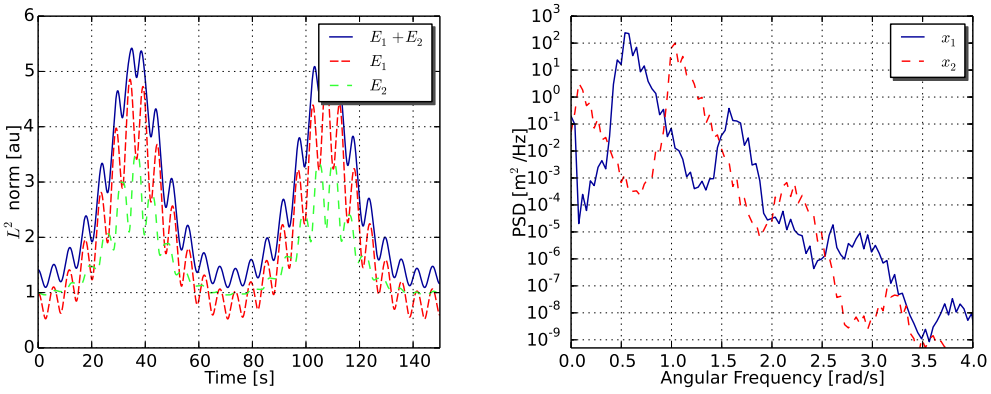

(a) L^2 norms (b) PSD of x_1

Figure 53: Nonlinear Mathieu system of equations, power spectrum and L^2 norms

Given that the proper period is near either 2π s or 4π s, which should we use? Imagine, for example, a system in $\mathbb{R}^3$ whose solutions lie on an invariant torus as shown in Fig. 54a. This system has two important periods; one associated with the travel time around the loop of the torus and another associated with the travel time around the cross-section of the torus. In this figure, the solution's first time around the loop of the torus has been colored dark red; then, the solution's second time around the loop, the trajectory's color is a lighter shade of red, and so on, until the last full loop of the solution is nearly white. Choosing which period to use in the FD analysis is similar to picking the transverse Poincaré section on which to analyze the periodic system. The two possible periods correspond to slicing the torus through its cross-section somewhere along the loop or slicing the torus perpendicular to the axis of revolution of the torus, as shown in Figs. 54b and 54c, respectively. In these figures we have shown only half of each trajectory for clarity. While the slicing plane may be infinite in extent, in defining the Poincaré section we only include the solution intersections with the plane when the solution passes through the plane in one direction, e.g., from back to front in Fig. 54b or bottom to top in Fig. 54c. In other words, we require the Poincaré section to transversely intersect the trajectories and that the trajectories pass through the section in the same direction. First, the system shown in Fig. 54b corresponds to the period associated with the trajectory around the loop of the torus. Since the frequency of the solution around the loop of the torus has been removed, in this case, the frequencies associated with the Floquet multipliers would be the reciprocal of the time period of the trajectory around the torus cross-section. Conversely, Fig. 54c, corresponds to performing the FD analysis with the period associated with the trajectory around the torus's cross-section, yielding frequencies from the Floquet multipliers that are the reciprocal of the time period of the trajectory around the torus's loop.

It might appear that using either analysis period the FD method would be capable of analyzing the coupled system and finding the two principal time periods. But, as we will show, this is not always the case.

Our third example problem, the Mathieu like system of equations, Eq. (175), is four dimensional and would thus, allow us to determine how the analysis methods perform when we do not have measured data from the entire state vector. Here we performed six analyses: 4 using the FD method, analyzing either Subsystem 1 or Subsystem 2 and using a time period of 2π or 4π s; and 2 using

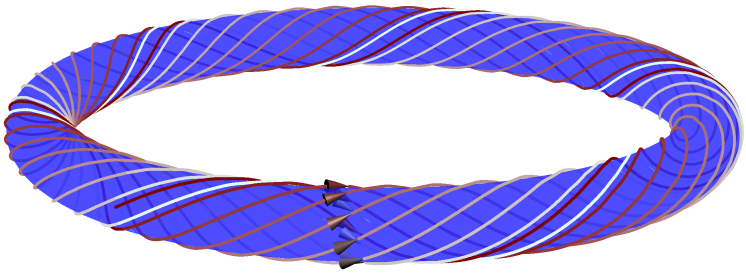

(a) Solution trajectory from dark to light on invariant torus

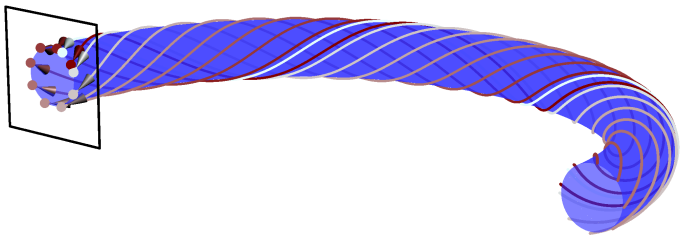

(b) Poincaré section associated with time period for trajectory around the torus loop or axis of revolution

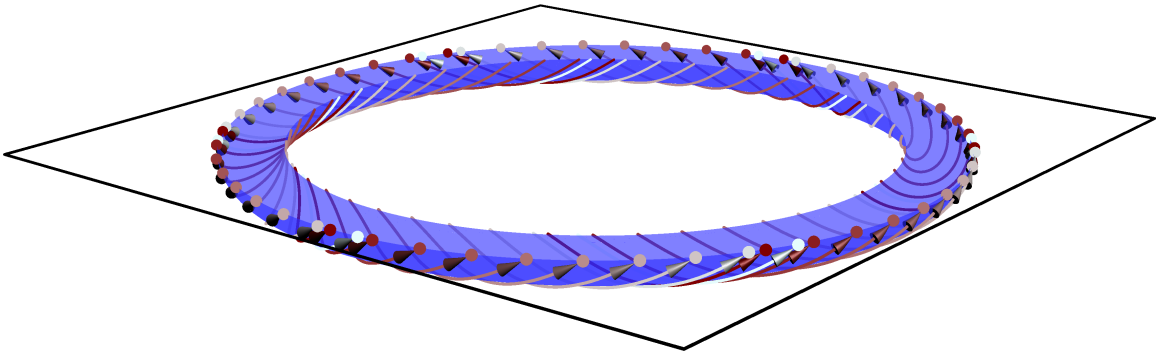

(c) Poincaré section associated with time period for trajectory around the torus cross-section

Figure 54: Conceptual solution trajectories on an invariant torus and possible Poincaré sections associated with different time periods for the FD analysis

the DMD method, with a sampling frequency of $\Delta t = 1$ ms. The resulting frequencies given by the imaginary parts of the Floquet exponents (or the time stepper Ritz value in the case of the DMD) are presented in Table 9.

Examination of Fig. 53b showed that the primary angular frequency content of Subsystem 1 and Subsystem 2 were nearly 0.5 and 1.0 rad/s, respectively. In each of the three cases where we performed the FD or DMD on Subsystem 1, the analyses returned an angular frequency of approximately 0.57 rad/s. Likewise, the three analyses performed on Subsystem 2 with either the FD or DMD method yielded an angular frequency of approximately 1.04 rad/s. In each of these

cases, given full state information from either subsystem, the natural mode of that system was found regardless of the time period used. This result is not surprising due to the similarity, by design, of the subsystems with a parametrically unstable mathematical equation, as shown in Figs. 51a and 51b.

Table 9: Predicted frequencies from subsystem analyses with different periods

Frequency [rad/s]	$\tau = 2\pi$ s	$\tau = 4\pi$ s	$\tau = \Delta t = 1$ ms
FD($u_1, \dot{u}_1$)	±0.5757388	±0.57150715	—
FD($u_2, \dot{u}_2$)	±1.0502751	±1.04495498	—
DMD($u_1, \dot{u}_1$)	—	—	±0.57761352
DMD($u_2, \dot{u}_2$)	—	—	±1.02212689

A more complex situation is encountered when the limited state information comes from different subsystems. For example, if we could only measure the displacement like variables, u_1 and u_2, then the available phase plot would be considerably more complex than that from either subsystem. This displacement only phase portrait is shown in Fig. 55a.

Using only these data, we have performed the FD analysis with periods of 2π and 4π s and also applied the DMD method. The resulting Floquet multipliers or exponential style Ritz value are listed in Table 10 and the associated angular frequencies are listed in Table 11. The DMD calculated Ritz value is nearly 1.0; in other words, the mode is nearly steady. We may interpret this result as the time period is so short that the DMD method is unable to *see* appreciable movement in the solution from one time step to the next. The predicted angular frequency in this case was approximately 0.005 rad/s, far from either of the important frequencies of the system. Given this limited information, the DMD has failed to find any useful information about our system. Turning to the FD method with a time period of 2π s, the approximate Floquet multipliers are both real, indicating non-oscillatory behavior of the orbit; in other words, the orbit is exponentially decaying, although we know that this is incorrect. Performing the FD analysis again with time period 4π s, the approximate Floquet multipliers are a complex conjugate pair. The associated angular frequency of this pair is 1.02 rad/s, one of the frequencies we hoped to find in the system. In fact, in this case we have both frequencies of interest and have found the proper coupled mode. In addition to the 1.02 rad/s angular frequency of the mode, the second important angular frequency comes from the reciprocal of the time period multiplied by 2π, or 0.5 rad/s.

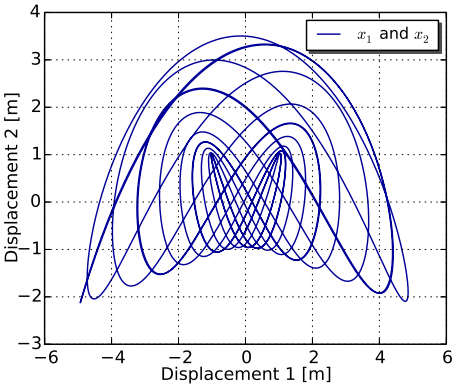

(a) Displacement like data (u_1 and u_2) phase diagram from Mathieu system

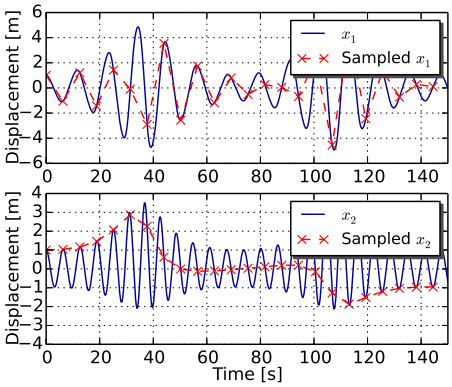

(b) Time history of displacements and sampled signals with $\tau = 2\pi$ s

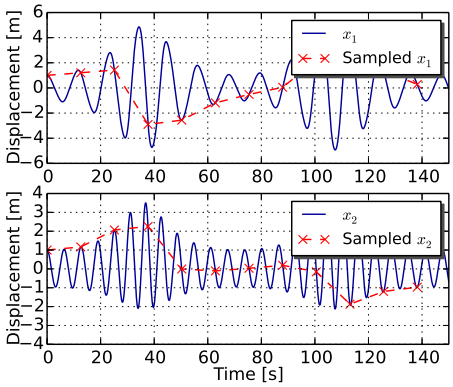

(c) Time history of displacements and sampled signals with $\tau = 4\pi$ s

Figure 55: Limited state data example for the Mathieu like system

Table 10: Approximate Floquet multipliers (for the FD method) and Ritz values (for the DMD method) from mixed subsystem data (displacements only) analyses with different periods

η	$\tau = 2\pi$ s	$\tau = 4\pi$ s	$\tau = \Delta t = 1$ ms
FD(u_1, u_2)	-0.849831, 0.903189	$0.62054 \pm 0.140714i$	—
DMD(u_1, u_2)	—	—	$0.999999 \pm 5.43538 \times 10^{-6}i$

To visualize the effects of the different time periods on the FD method we have plotted the two displacement like variables and the 2π and 4π s sampled displacements in Figs. 55b and 55c. In the case of the 2π s analysis period, the oscillations in x_1 are still resolved, while the oscillations in x_2 have been *removed* by the sampling. In the case of the 4π s analysis period, the oscillations in both variables have essentially been *removed* by the sampling. Interestingly, this second case yields the correct results and this may appear counterintuitive. But, in fact, what we have done is by analyzing

Table 11: Predicted frequencies from mixed subsystem data (displacements only) analyses with different periods

Frequency [rad/s]	$\tau = 2\pi$ s	$\tau = 4\pi$ s	$\tau = \Delta t = 1$ ms
FD(u_1, u_2)	Non-dynamic	±1.01774489	—
DMD(u_1, u_2)	—	—	±0.00543538

the data with the proper time period, we have exchanged details of the quasiperiodic portion of the solution for clearer information about how the orbit changes from cycle to cycle.

For this case it appears that the correct analysis period is approximately $\tau = 4\pi$ s. Having identified the *correct* time period, what are the techniques that yield this period? If we can develop methods for finding the correct period in this simple system, it may help us in the analysis of our complex experimental system. Two techniques are considered here; one using the frequencies found in the PSD of the measured data and another using the autocorrelation of the measured data.

By using the PSD in Fig. 53b, finding the maximum of $\hat{u}_1$ and $\hat{u}_2$ and taking the reciprocal of these peak frequencies gives possible periods of 11.53923077 s and 6.25041667 s, respectively. The former is around 8% smaller than 4π s. Using $\tau = 11.539$ s in the FD analysis, the Floquet multipliers give frequencies of $\omega = \pm 1.09622661$ rad/s, which are close to the values we expect, but the damping factor from these multipliers are considerably smaller than the previous results. This difference is visible in the difference in the modulus of the multipliers, $|\eta| = 0.63629398$ for this period, compared to $|\eta| = 0.7634348$ previously. It appears that the PSD is useful locating the frequency ranges that may be important, but that the frequencies themselves may need refinement from additional analyses.

Perhaps we can use the autocorrelation function to refine the time periods found with the PSD. Recalling that to apply the Floquet theory we are actually trying to find the period of the operator $A(t)$, let's first discuss how we could find the correct period given the time varying system matrix data. There are number of possibilities. For example, we could find the autocorrelation of each component of the time varying matrix $A(t)$ and look for the correct time delay that simultaneously maximizes all of the correlations. For very large systems this would be impractical, so we relax the requirement of component-wise periodicity in exchange for a simpler method. To find the time period we take the autocorrelation of the Frobenius norm [36] of the system matrix and find the peak

correlation over the time range of interest, or:

$$\tau \approx \max(\text{autocorr}(A(t_k))), \quad t_k = [0, 5\pi]\, s\,. \tag{176}$$

Using a 10 step window for the autocorrelation, we find the approximate time period to be $\tau = 12.582$ s, only 0.124% different from 4π s. In fact, our example problem is designed to be nearly a 4π-periodic system, but we do not know the exact period. The small difference in period has very little effect on the FD method results, $\eta = 0.62270087 \pm 0.16825226i$ for the autocorrelation based period, compared to $\eta = 0.62053988 \pm 0.14071352i$ for period of 4π s.

While autocorrelation of the system matrix provides us with a method to find the period, the intent of the FD method is to be able to analyze systems where the system matrix is not known. In some cases the periodicity of the system matrix is not necessarily related to the periodicity of the state vector, e.g., the Mathieu equation, Eq. (170). But, in the case of coupled subsystems causing parametric instabilities, e.g., Eq. (175), the system periodicity is reflected in the state vector. So in this case, the autocorrelation of the state vector may yield the proper time period without knowledge of the system matrix. Specifically, we have normalized the time history of each available state variable, found the L^2 norm, taken the autocorrelation with a 10 step window, and found the maximum autocorrelation within the time range of interest. For our example using displacement like data, we approximated the period by:

$$\tau \approx \max\left(\text{autocorr}\left(\frac{u_1(t_k)}{|u_1|} + \frac{u_2(t_k)}{|u_2|}\right)\right), \quad t = [0, 5\pi]\, s\,. \tag{177}$$

With this technique we find the approximate time period to be $\tau = 12.555$ s, only 0.09048% different from 4π s. Again, this time period yields nearly identical Floquet multipliers, $\eta = 0.61889718 \pm 0.12346955i$.

We know that in this data there are two important time periods/frequencies. The time periods directly give one set of important frequencies. The angular frequencies corresponding to the time periods of $\tau = 4\pi$, $\tau = 12.582$, and $\tau = 12.555$ s are $\omega = 0.5$, $\omega = 0.4993789$, and $\omega = 0.50045283$ rad/s, respectively. Each of these frequencies are are good agreement.

The second set of frequencies comes from the FD analyses. While the angular frequencies are calculated from the imaginary part of η, see Eq. (144), the difference in the imaginary part

of η for the three cases is exaggerated by the different analysis time periods. So, comparing the calculated frequencies may be a better one-to-one check of these analyses. The approximate angular frequencies from the FD method with time periods of $\tau = 4\pi$, $\tau = 12.582$, and $\tau = 12.555$ s are $\omega = 1.01774489$, $\omega = 1.01973189$, and $\omega = 1.01658978$ rad/s, respectively—the second set of important frequencies. The total range of angular frequencies is about 0.3%. Thus, it appears our autocorrelation of the normalized state variables based technique provides a viable option for finding the correct FD analysis time period.

5.8 Conclusions

In this chapter we have developed tools for analyzing experimental systems that exhibit behavior similar to that of a linear periodic system. In Chapter 4, we saw that the DMD method was unable to identify the link between the hydrodynamic/combustion modes and the observed CI, likely due to the oscillatory nature of the system. The appropriate method for analyzing many oscillatory systems is the Floquet theory. By combining the concepts of Floquet theory with the DMD method we developed the FD method, which we showed to accurately approximate the Floquet multipliers (at least the largest in modulus)—key to the stability of the periodic orbits. In addition, by applying the FD method to systems that were nearly linear and periodic, we saw that these techniques may be applicable to some nonlinear systems. We showed how two or more subsystems can couple to create a parametric instability and that the FD method can be used to analyze either the full system, a single subsystem (for example, if we can only make measurements of one subsystem), or limited mixed subsystem data (for example, if we can only make measurements of the displacement variable). Lastly, a technique for finding the time period to be used in the FD analysis was developed. In the next chapter, we will use the techniques developed in this chapter, i.e., the FD and EFD methods, to analyze experimental data measured in stable and unstable combustor configurations.

CHAPTER VI

STUDY OF COMBUSTION INSTABILITY MECHANISMS WITH THE FLOQUET DECOMPOSITION AND ENSEMBLE-AVERAGE FLOQUET DECOMPOSITION METHODS

This chapter describes the results of an investigation of the application of the FD and EFD methods to elucidate the driving mechanisms found in the unstable combustors. Specifically, this chapter discusses the results obtained when these methods were used to analyze the stable and unstable experiment datasets.

As discussed in Sections 4.2 and 4.3.3, the DMD/SDD analyses were unable to identify 170 Hz mode oscillations in the measured unstable experiment dataset in spite of the fact that it was present in the PSD analysis of the dynamic pressure. One possible explanation for the inability of these methods to identify the unsteady mode is that the evolution operator, A in Eq. (55), is assumed to be a constant, which may not be the case. In Chapter 5 we developed a DMD/SDD based technique to analyze systems whose evolution operator varied periodically with time, i.e., $A(t) = A(t + \tau)$. This newly developed technique, which we refer to as the FD method, allows us to approximately determine the largest Floquet multipliers, which control the stability of the periodic system, from measured data alone.

To investigate the FD analysis, we apply the technique to the unstable experiment dataset in Section 6.1. Next, to demonstrate the advantages of the ensemble averaged version of the FD analysis, we apply the EFD method to the datasets from both the stable and unstable experiments in Section 6.2.

6.1 FD Analysis of the Unstable Experiment Dataset

To apply the FD/EFD methods, we must first determine the period, τ, of the evolution operator, $A(t) = A(t + \tau)$, see Eq. (141). In Section 5.7, we discussed approaches for determining the proper analysis period. Specifically, we determined the analysis period by looking at the acoustic PSD,

autocorrelation, and the SDD results discussed in Section 4.3.3. First, the acoustic PSD, see Fig. 8, shows that the largest amplitude oscillations for both the stable and unstable experiment datasets occurs at approximately 1000 Hz. Performing autocorrelation on the combustion chamber acoustic pressure and finding the frequency of the peak autocorrelation, see Fig. 56, suggests the evolution operator may be nearly periodic at a frequency near 990 Hz, which corresponds to a period of 1.01 ms. Finally, the SDD analysis results, presented in Section 4.3.3, show the presence of a strong mode near 1017 Hz, which has a period of 0.9833 ms. While the measured data have been sampled at discrete times, preventing us from using either 1.01 ms or 0.9833 ms, taking every 10^{th} data snapshot of our 10 kHz data, allows us to employ an analysis period of $\tau = 1$ ms. In Section 6.2.3, we will show that the FD/EFD method is relatively insensitive to small differences in this analysis period.

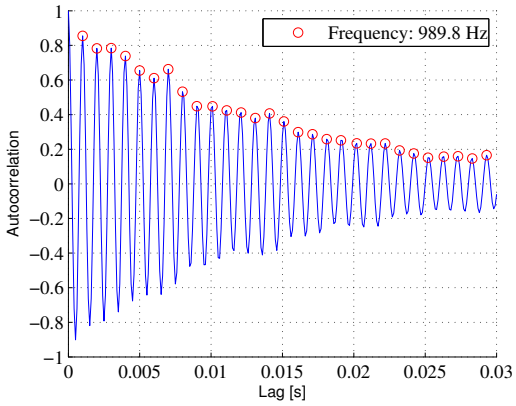

Figure 56: Autocorrelation of combustion chamber acoustic pressure; frequency: 989.9 Hz; period: 1.01 ms

Since we want to find the physical processes associated with the 170 Hz CI, we will focus on the analysis of the unstable experiment dataset. Applying the FD analysis, developed in Section 5.4, to this unstable dataset, we find the approximate Floquet multipliers and Floquet exponents that are shown in Figs. 57a and 57b, respectively. As we found in the DMD/SDD analyses in Chapter 4, there is a non-dynamic mode—a Floquet multiplier on the x-axis with modulus 1.0, see Fig. 57a—which in the DMD analysis represented the steady component of the solution. The interpretation of this mode in the FD analysis is now slightly different, as this mode represents the steady portion of the periodic trajectory at the analysis period, i.e., the fixed point on the Poincaré section on which the

analysis is being performed. Conceptually, analyzing the system with the same analysis period, but different starting phases or a different Poincaré sections could yield a different *steady* mode.

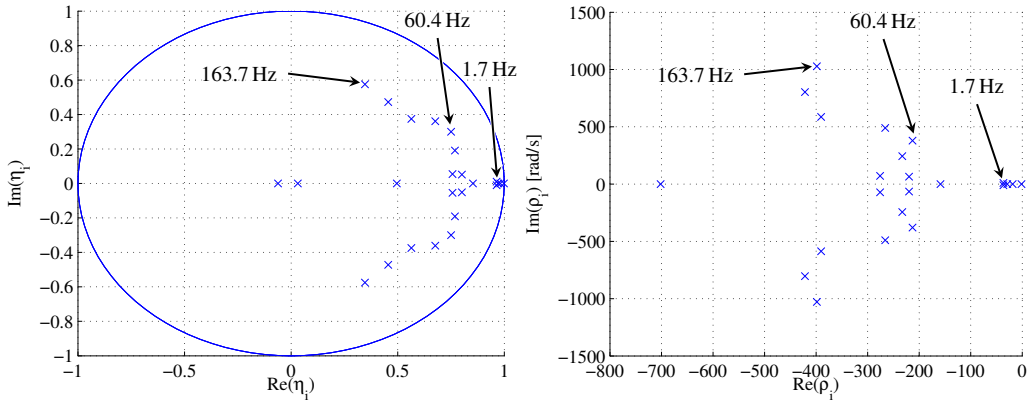

(a) Estimated Floquet multipliers (b) Estimated Floquet exponents

Figure 57: FD based approximate Floquet multipliers and exponents

The largest modulus complex conjugate pair of dynamic modes in this analysis occurs at an extremely low frequency of 1.668 Hz. This low frequency mode could be an artifact of the experimental conditions or the measurement systems changing slowly due to, e.g., heating or PIV seed accumulating on the windows.

The next largest modulus dynamic mode pair—depending on the logarithmic branch cut we choose, as discussed in Section 5.3, see Eq. (144)—has a frequency of 60.41 Hz or 1000 ± 60.41 Hz or 2000 ± 60.41 Hz and so forth. The real and imaginary parts of the PIV, PLIF, and chemiluminescence components of this mode are shown in the left and right columns of Fig. 58, respectively. Comparing the 170.9 Hz PIV velocity PSD, Fig. 20a, with the axial velocity for this FD mode, Fig. 58a, shows similar vertically oriented velocity band. But, at this point, the relationship of this mode to the previous findings is unclear and it appears that this mode is not directly related to the instability of interest.

The next FD mode pair that we will discuss is the 163.65 Hz mode shown in Fig. 59. While the frequency of this mode differs from the measured combustion instability frequency, the difference is relatively small and, thus, we conjecture that this mode is related to the observed CI. Physically, this mode appears to represent a highly asymmetric annular or helical hydrodynamic wave—along with

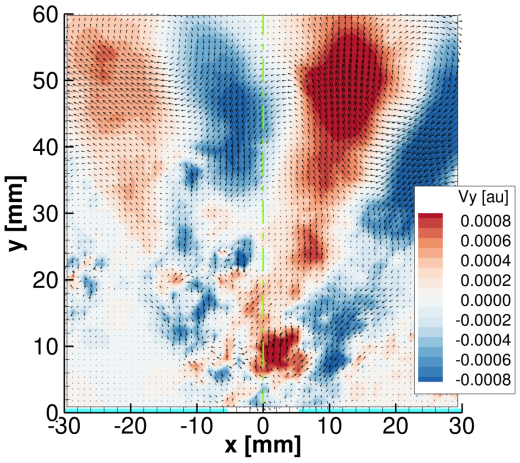

(a) Real part of PIV component of FD mode

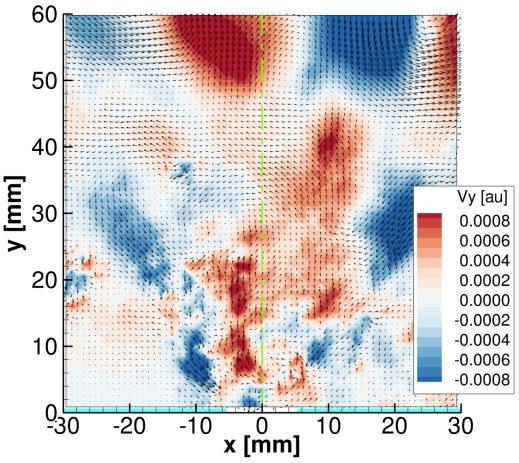

(b) Imaginary part of PIV component of FD mode

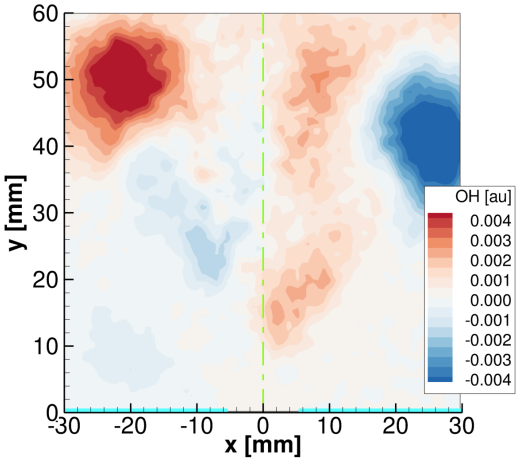

(c) Real part of PLIF component of FD mode

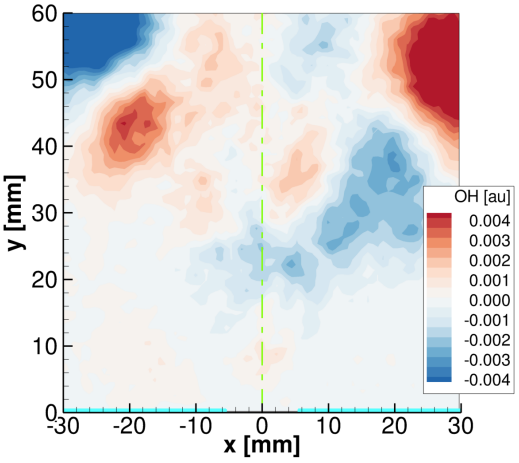

(d) Imaginary part of PLIF component of FD mode

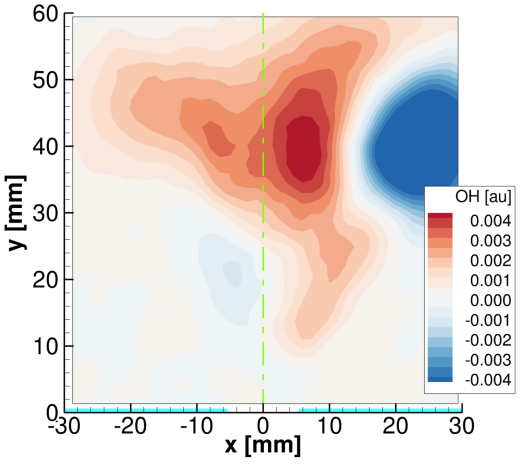

(e) Real part of chemiluminescence component of FD mode

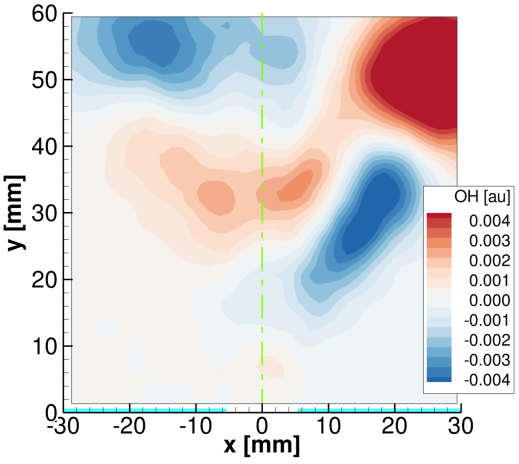

(f) Imaginary part of chemiluminescence component of FD mode

Figure 58: Unstable dataset FD mode. Period: 1 msec, frequency: 60.41 Hz

its coupled, oscillating reaction zone shown in the PLIF and chemiluminescence components of the mode.

In addition to the PIV, PLIF, and chemiluminescence components of the FD modes shown in, e.g., Fig. 59, the FD mode also contains acoustic pressure information associated with the three dynamic pressure sensors. To graphically display the modal acoustic information, we have plotted the normalized acoustic pressure amplitudes against the modal frequency for each of the 25 FD modes, see Fig. 60 (p'_1, p'_3, and p'_5, blue, red, and green crosses, respectively). Interestingly, the modes that have zero or very low frequencies have substantial *acoustic* energy while the non zero frequency modes have relatively low acoustic amplitude. Thus, it would be difficult to conclude that the 164 Hz mode is closely related to the 170 Hz CI, which is prominent in the acoustic spectra.

6.2 EFD Analyses of the Stable and Unstable Experiment Datasets

In the previous section, the FD analysis identified a mode whose frequency was near the measured CI frequency, but the mode did not appear to be coupled with the measured acoustic oscillations. In this section, we will employ the ensemble averaged version of the FD method, the EFD method, to determine if it could identify the dynamic mode associated with the observed CI. The objective of this study is to determine whether the ensemble averaging and the additional state data available when using the EFD method improves upon the results found in Section 6.1.

6.2.1 Comparison of the FD and EFD Method Results

As we discussed in Section 5.5, if the evolution operator governing the measurements was both linear and periodic, and, the measurements provided a complete description of the state variable at each time, then the set of normalized singular values from each conceptual Poincaré section would be identical. As a result, upon assembly, the normalized singular value plot generated by the EFD method would have the appearance of stair steps, as shown in Fig. 43. However, the EFD analysis singular value data, plotted in Fig. 61, do not exhibit this stair step appearance. This finding makes sense due to the fact that our planar measurements do not provide complete state information.

While the EFD singular values do not exhibit a stair step character, comparing the FD and EFD generated singular values, the EFD singular values decrease at a much slower rate than the decrease in the FD singular values. In each of the analyses, we retained 25 singular values in the Moore-Penrose

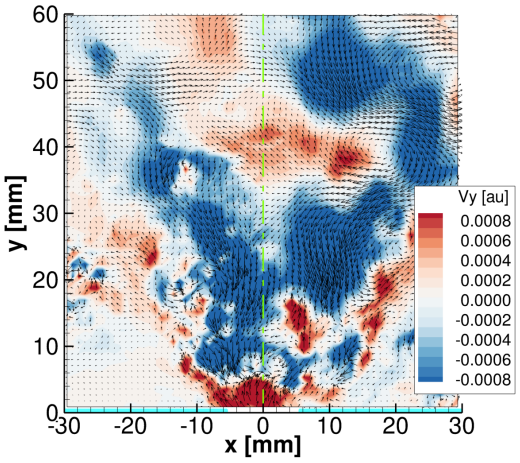

(a) Real part of PIV component of FD mode

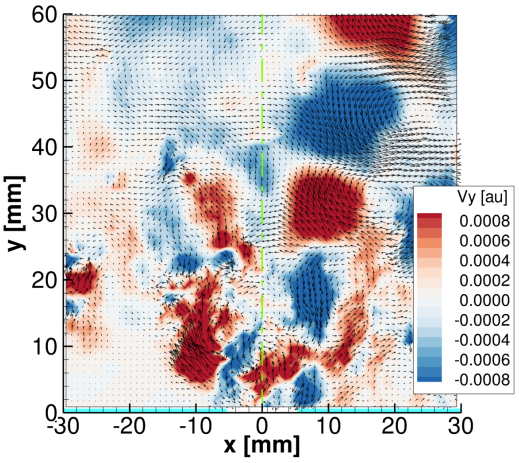

(b) Imaginary part of PIV component of FD mode

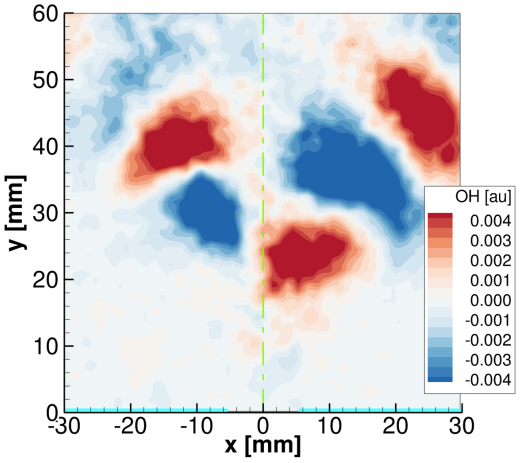

(c) Real part of PLIF component of FD mode

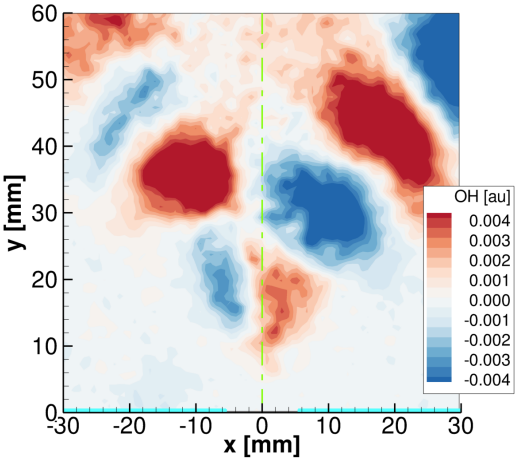

(d) Imaginary part of PLIF component of FD mode

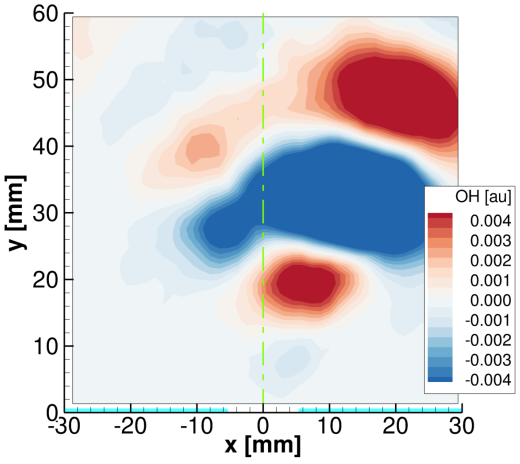

(e) Real part of chemiluminescence component of FD mode

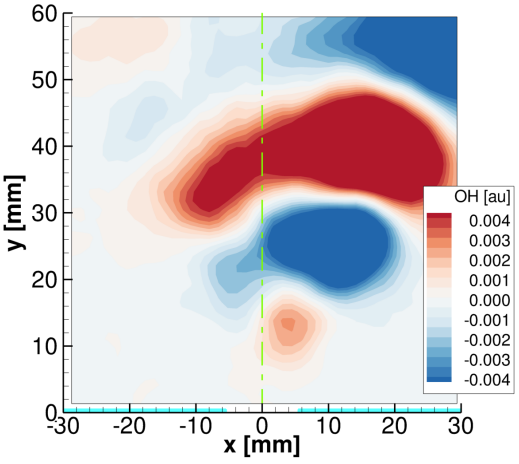

(f) Imaginary part of chemiluminescence component of FD mode

Figure 59: Unstable dataset FD mode. Period: 1 ms, frequency: 163.65 Hz

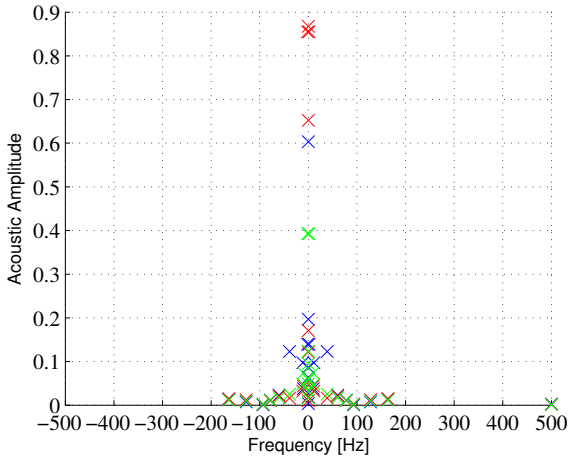

Figure 60: Predicted modal acoustic amplitudes from FD analysis. Dynamic pressure sensor location: p'_1 at $x = 0.336$ m (blue), p'_3 at $x = 0.0263$ m (red), p'_5 at $x = -0.0263$ m (green)

pseudoinverse and, interestingly, the 25$^{\text{th}}$ singular value in the EFD method is nearly an order of magnitude larger than the 25$^{\text{th}}$ singular value in the FD analysis. The larger singular values found with the EFD method are likely due to increased state information available within the analysis. While more analysis is needed, it appears this method may be more resilient to noise contamination, while also providing more information about the complete state of the system than the FD method.

Figure 62 shows the FD (blue crosses) and EFD (black circles) approximate Floquet multipliers and Floquet exponents for the unstable experiment dataset. The set of approximate Floquet multipliers/exponents associated with the EFD method shows four pairs of dynamic modes that are less damped than all but the insipid (uninteresting?) 1.7 Hz FD based dynamic modes. The increased

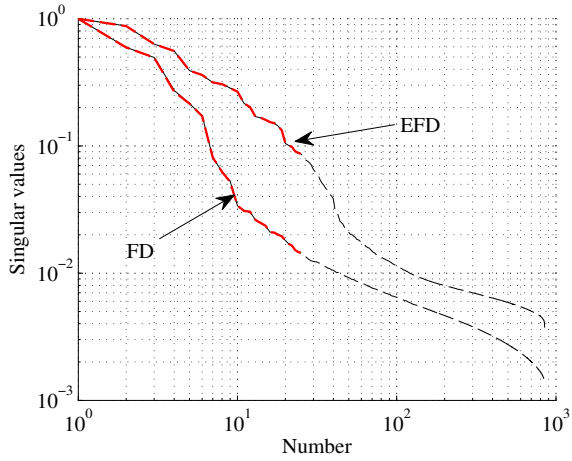

Figure 61: SDD based FD and EFD Normalized Singular Values

modulus of the approximate Floquet multipliers towards the unit circle suggests the presence of nearly constant amplitude oscillations in the experiment, i.e., the extracted modes are closer to being Lyapunov stable. Conversely, there are four pairs of dynamic modes whose approximate Floquet multipliers have smaller modulus than most of the FD modes. These modes have been deemphasized by the EFD method and they likely represent dynamics contained in only a small portion of the ensembles. In addition, these modes are sensitive to small changes in the data or processing and likely do not play an important role in the CI driving mechanism and, can be, thus, ignored.

From Fig. 62a, it can be seen that there are two pairs of modes that nearly lie on the unit circle. The pair of modes with the highest modulus approximate Floquet multiplier has a frequency of 169.57 Hz and modulus of $|\eta| = 0.9855$. The second pair of modes, with only a slightly smaller magnitude approximate Floquet multiplier, has a frequency of 258.15 Hz and modulus of $|\eta| = 0.9675$. Again, to display the modal acoustic information, we have plotted the normalized acoustic pressure amplitudes against the modal frequency for the 25 FD (crosses) and 25 EFD (circles) modes generated by the analyses, see Fig. 63. Recalling in Section 6.1, the FD method found a nearly 170 Hz mode, but this mode's acoustic amplitude was insignificant—only the non-dynamic or very low frequency modes appeared to have acoustic content in the FD results. In contrast to the acoustic content from the FD analysis, the EFD analysis results show the two largest modulus pair of modes also have the largest acoustic amplitudes and the frequencies are consistent with the observed acoustic PSD

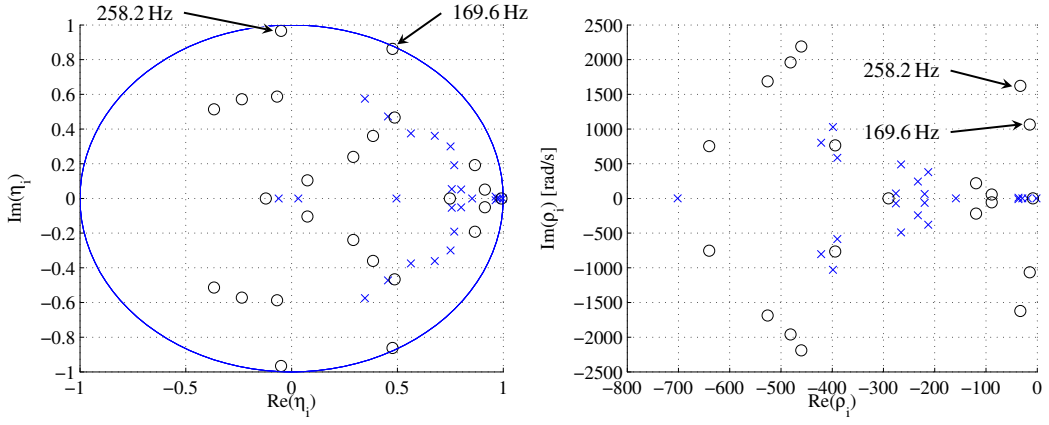

(a) Estimated Floquet multipliers

(b) Estimated Floquet exponents

Figure 62: Estimated Floquet multipliers and exponents: FD analysis (blue crosses) and EFD analysis (black circles)

shown in Fig. 8d. With frequencies closely related to the natural acoustic modes, details of these large modulus EFD modes will be explored in the following section.

6.2.2 Discussion of the Unstable Experiment EFD Modes

During the development of the EFD method, in Eqs. (165) to (168), we discussed the complex conjugate pair of modes, the phase correction that must be made to each of these modes during the process, and the ensemble averaging of these phase corrected modes. Figures 64 to 69 show the imaginary parts of the PIV, PLIF, and chemiluminescence for the 170 Hz EFD mode, before and after the phase correction has been applied. The phase shift for the 10 ensembles, each separated by 0.1 ms, represents approximately a total shift of 1/6 of a cycle. The phase shift between ensembles for the PIV data, Fig. 64, is fairly subtle, whereas the shift is clearly apparent in the PLIF and chemiluminescence data, Figs. 66 and 68, respectively. For example in Fig. 68, the chemiluminescence mode for ensemble 1, Fig. 68a, has a strong, positive value to the right of the centerline of the injector and this region becomes smaller and weaker as we proceed towards the 10^{th} ensemble. By ensemble 10, Fig. 68j, the positive region is nearly absent. Comparing the uncorrected chemiluminescence ensembles, Fig. 68, to the phase corrected chemiluminescence ensembles, Fig. 69, we see that the right-hand sides of all the phase corrected ensembles are quite similar. In spite of the slight differences between the images

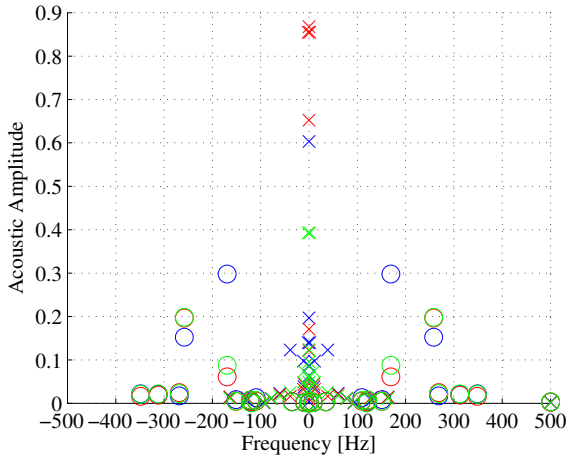

Figure 63: Predicted modal acoustic amplitudes: FD analysis (crosses) and EFD analysis (circles). Dynamic pressure sensor location: p'_1 at $x = 0.336\,\text{m}$ (blue), p'_3 at $x = 0.0263\,\text{m}$ (red), p'_5 at $x = -0.0263\,\text{m}$ (green)

in Fig. 69, they appear to be 10 different representations of the same mode—at approximately the same phase.

The averages of the phase corrected real and imaginary parts of the PIV, PLIF, and chemiluminescence descriptions of the 170 Hz EFD mode are shown in Fig. 70. By comparing the ensembles of imaginary part from the chemiluminescence component of the mode and their ensemble average, Fig. 69 and 70f, respectively, we see that the averaging process has smoothed the results, but overall the differences are relatively small. The situation is somewhat different when we compare the ensembles from the imaginary PIV component of the mode and their ensemble average, Fig. 64 and 70b, respectively. In each of the ensembles in Fig. 64 there appears to be an organized hydrodynamic structure as indicated by the alternating blue and red regions in the top half of each frame and, additionally, there are smaller blue and red regions in the bottom half of each ensemble. In contrast, the ensemble average of these images, Fig. 70b, shows a much clearer description of the hydrodynamic structure in the upper portion of the frame and little content in this mode near the injector plane. In other words, much of the velocity content in the lower half of the field was averaged out, leading us to believe that these fluctuations were either random fluctuations in the velocity field (i.e., turbulence) or the result of random errors in the measurements. In either case, the fact that they were removed from the ensemble average mode helps us interpret the physical results by removing the random noise while retaining the coherent dynamical behavior.

To elucidate the physical processes involved in the 170 Hz CI, we will utilize the spatial information contained within Fig. 70, keeping in mind that the acoustic phase of the real and imaginary parts of the mode were -29.6° and 60.4°, respectively. This pressure phasing indicates that the peak pressure in the combustion chamber occurs just after the moment when the structure of the 170 Hz oscillation resembles the real part of the EFD mode, i.e., the left column of Fig. 70. Conversely, the peak acoustic velocities occur just after the moment when the structure of the 170 Hz oscillation resembles the imaginary part of the EFD mode, i.e., the right column of Fig. 70. While the transverse acoustic velocities are orders of magnitude smaller than the steady fluid dynamic velocities—thus not likely resolved within the PIV measurements—in Fig. 70b there appears to be a bulk transverse velocity from left to right in phase with the acoustic velocity. Similarly to our discussion in Section 4.3.2, this unexplained transverse velocity field at 170 Hz is perhaps due to the nonlinear

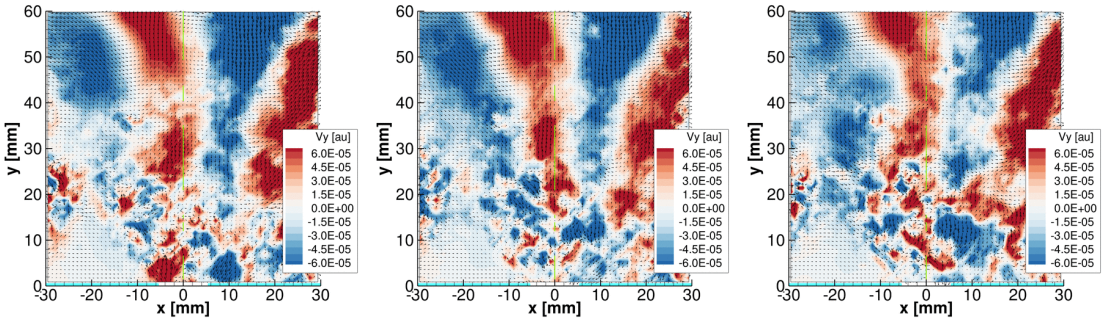

(a) Ensemble 1; PIV component of mode

(b) Ensemble 2; PIV component of mode

(c) Ensemble 3; PIV component of mode

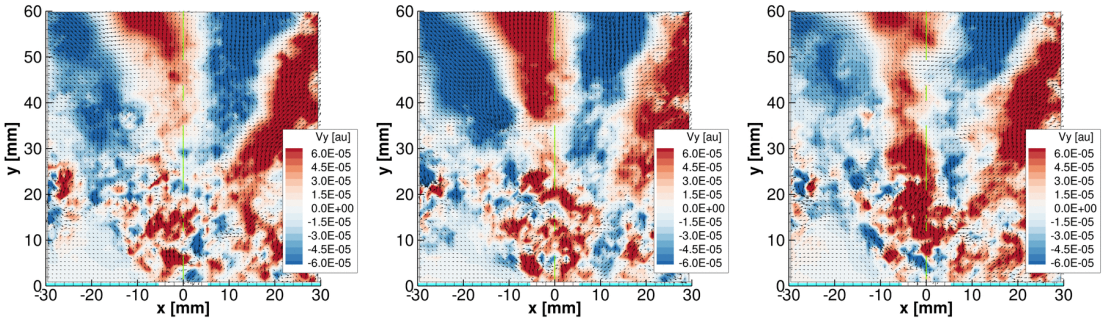

(d) Ensemble 4; PIV component of mode

(e) Ensemble 5; PIV component of mode

(f) Ensemble 6; PIV component of mode

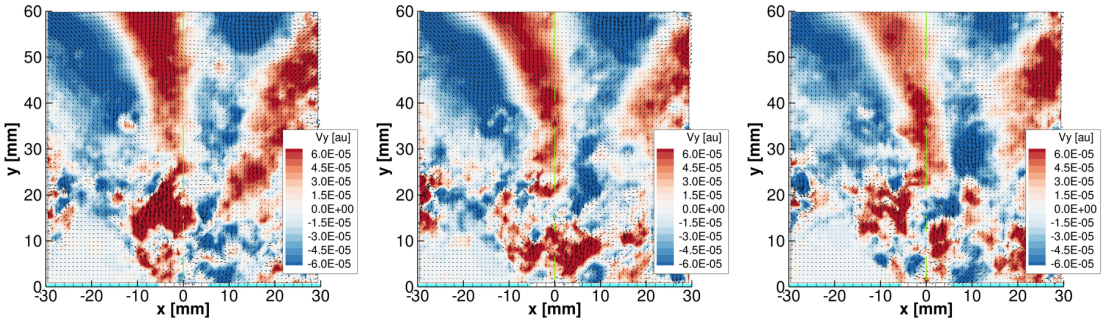

(g) Ensemble 7; PIV component of mode

(h) Ensemble 8; PIV component of mode

(i) Ensemble 9; PIV component of mode

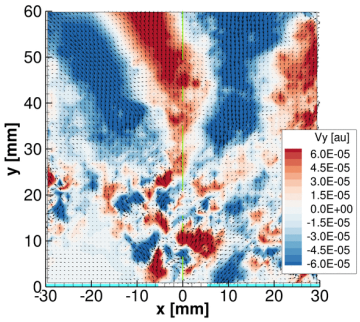

(j) Ensemble 10; PIV component of mode

Figure 64: Unstable dataset non-phase corrected EFD modes. Period: 1 ms, frequency: 169.6 Hz; Only imaginary part of ensembles plotted

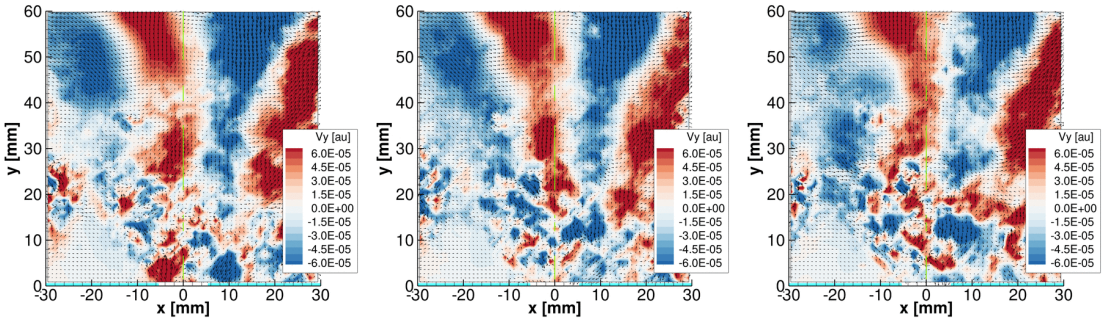

(a) Phase corrected ensemble 1; PIV component of mode

(b) Phase corrected ensemble 2; PIV component of mode

(c) Phase corrected ensemble 3; PIV component of mode

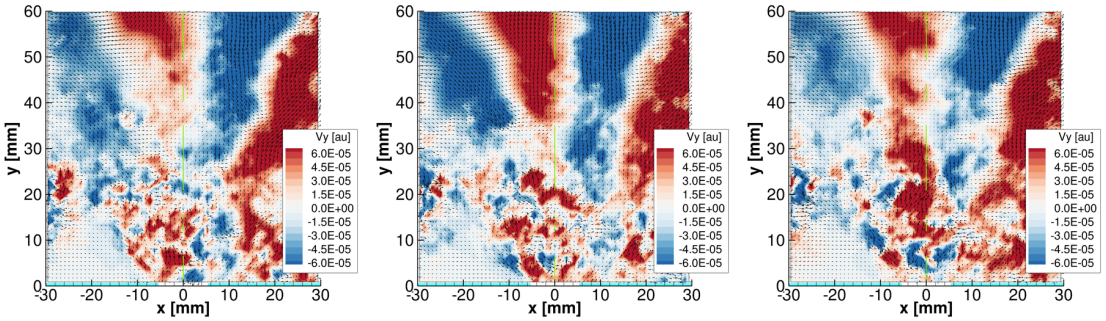

(d) Phase corrected ensemble 4; PIV component of mode

(e) Phase corrected ensemble 5; PIV component of mode

(f) Phase corrected ensemble 6; PIV component of mode

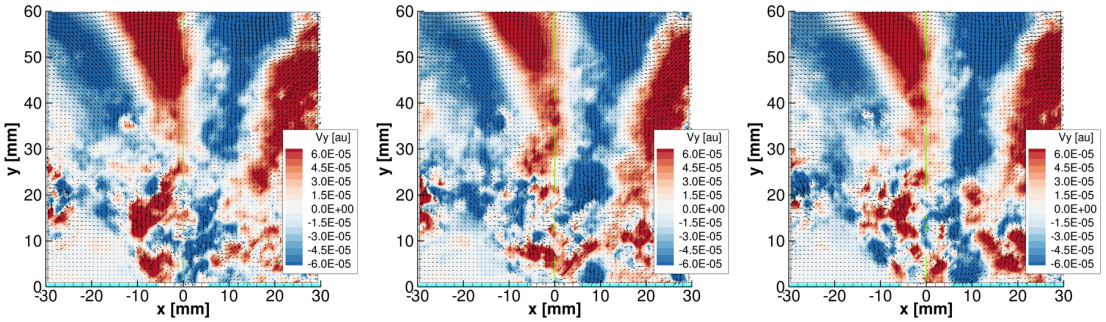

(g) Phase corrected ensemble 7; PIV component of mode

(h) Phase corrected ensemble 8; PIV component of mode

(i) Phase corrected ensemble 9; PIV component of mode

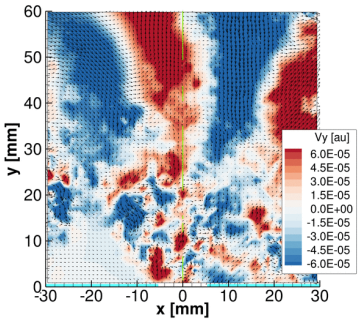

(j) Phase corrected ensemble 10; PIV component of mode

Figure 65: Unstable dataset phase corrected EFD modes. Period: 1 ms, frequency: 169.6 Hz; Only imaginary part of ensembles plotted

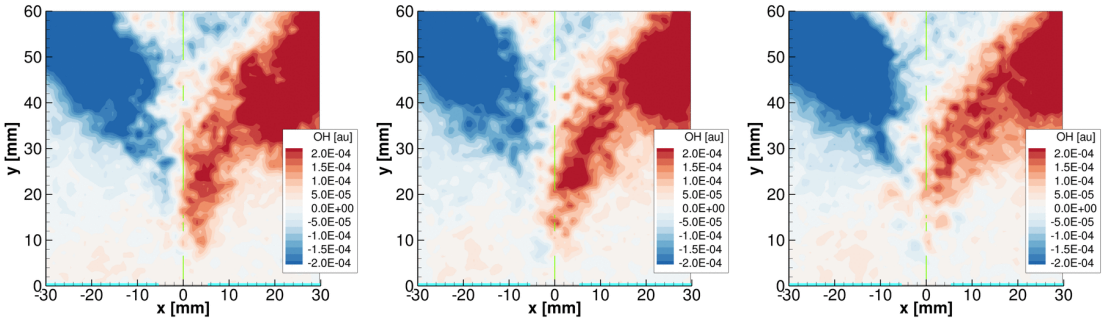

(a) Ensemble 1; PLIF component of mode

(b) Ensemble 2; PLIF component of mode

(c) Ensemble 3; PLIF component of mode

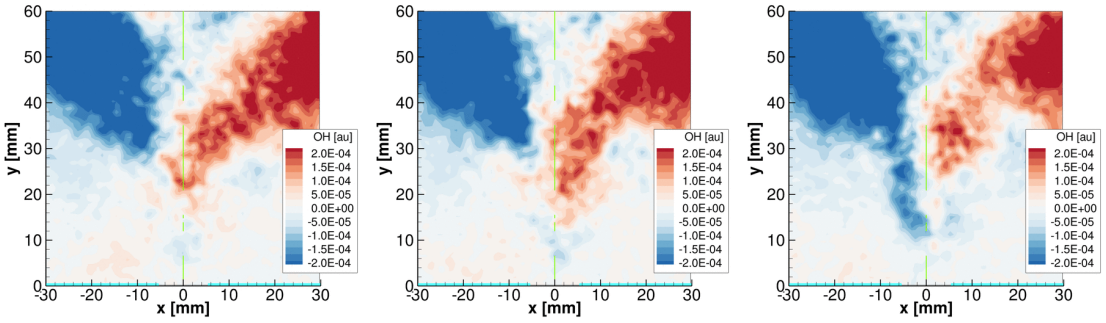

(d) Ensemble 4; PLIF component of mode

(e) Ensemble 5; PLIF component of mode

(f) Ensemble 6; PLIF component of mode

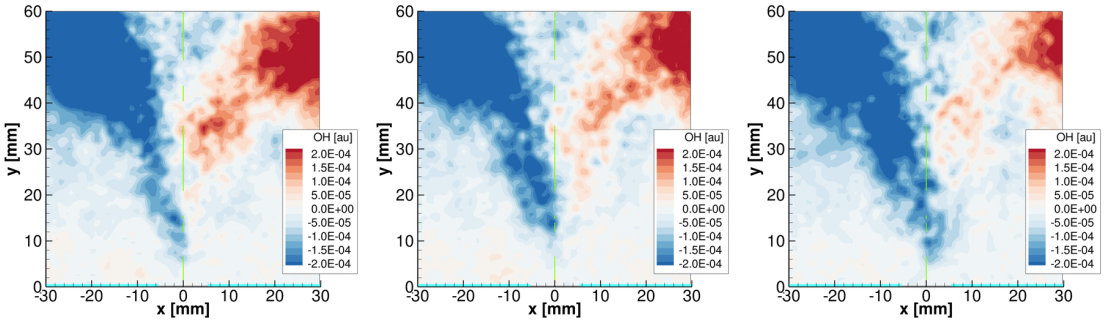

(g) Ensemble 7; PLIF component of mode

(h) Ensemble 8; PLIF component of mode

(i) Ensemble 9; PLIF component of mode

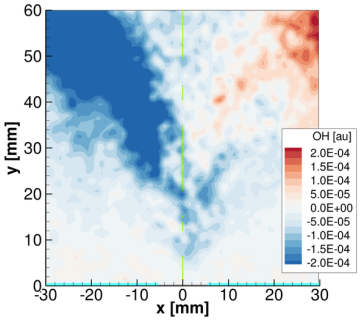

(j) Ensemble 10; PLIF component of mode

Figure 66: Unstable dataset non-phase corrected EFD modes. Period: 1 ms, frequency: 169.6 Hz; Only imaginary part of ensembles plotted

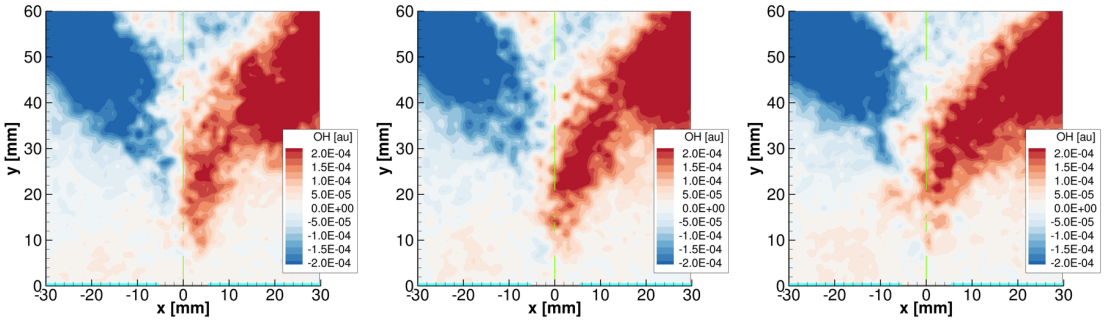

(a) Phase corrected ensemble 1; PLIF component of mode

(b) Phase corrected ensemble 2; PLIF component of mode

(c) Phase corrected ensemble 3; PLIF component of mode

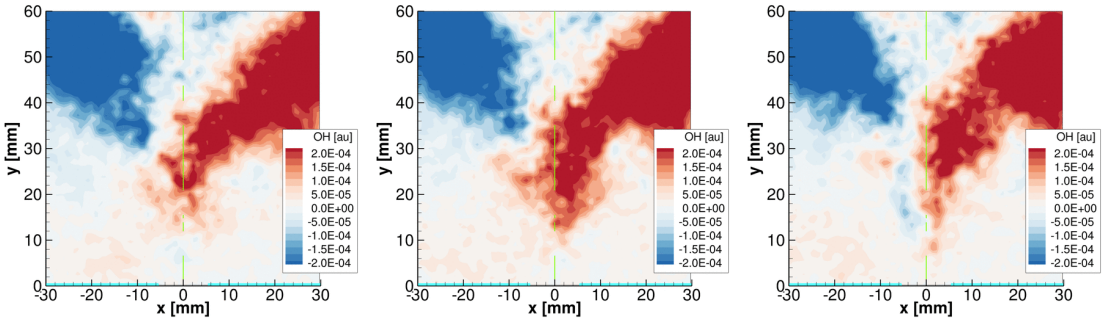

(d) Phase corrected ensemble 4; PLIF component of mode

(e) Phase corrected ensemble 5; PLIF component of mode

(f) Phase corrected ensemble 6; PLIF component of mode

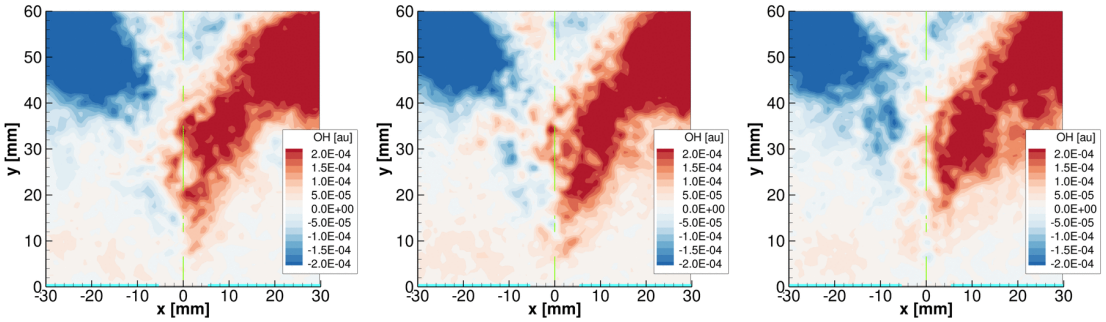

(g) Phase corrected ensemble 7; PLIF component of mode

(h) Phase corrected ensemble 8; PLIF component of mode

(i) Phase corrected ensemble 9; PLIF component of mode

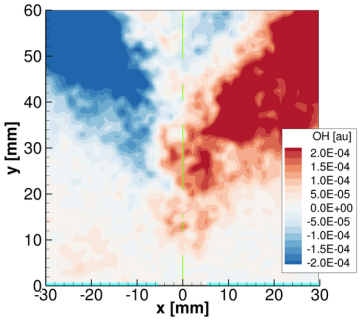

(j) Phase corrected ensemble 10; PLIF component of mode

Figure 67: Unstable dataset phase corrected EFD modes. Period: 1 ms, frequency: 169.6 Hz; Only imaginary part of ensembles plotted

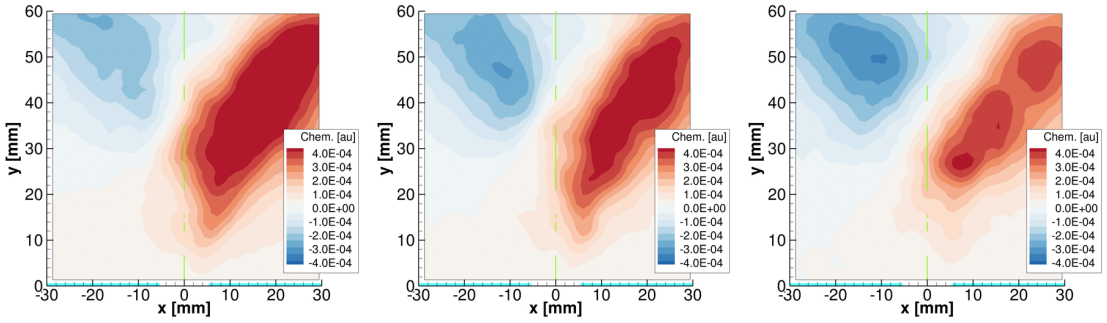

(a) Ensemble 1; chemilum. part of mode

(b) Ensemble 2; chemilum. part of mode

(c) Ensemble 3; chemilum. part of mode

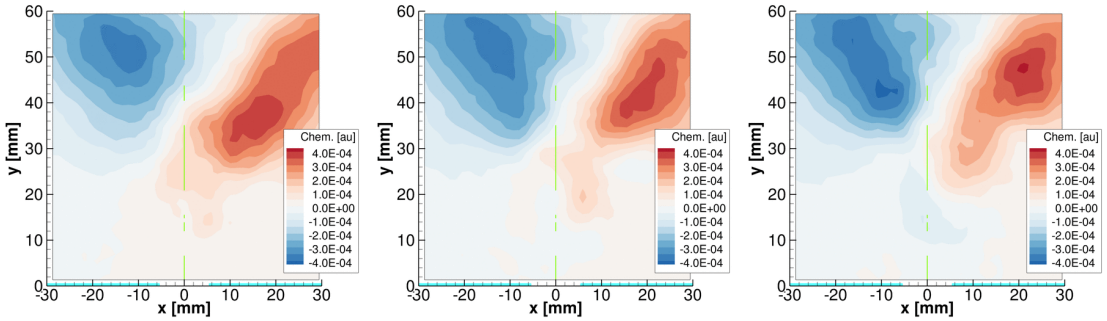

(d) Ensemble 4; chemilum. part of mode

(e) Ensemble 5; chemilum. part of mode

(f) Ensemble 6; chemilum. part of mode

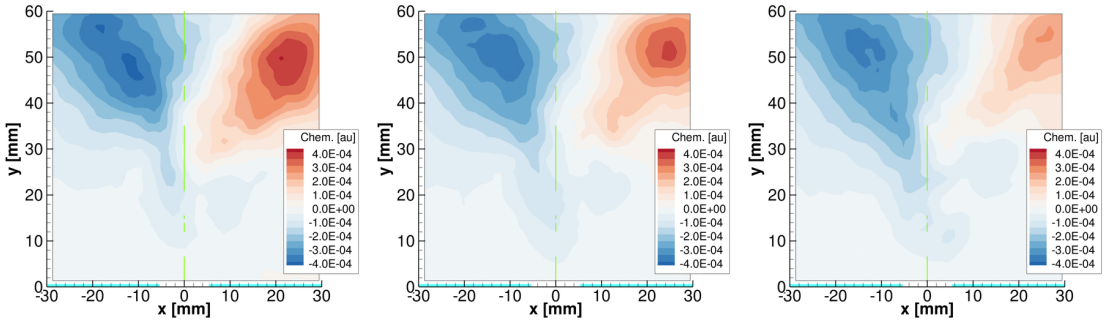

(g) Ensemble 7; chemilum. part of mode

(h) Ensemble 8; chemilum. part of mode

(i) Ensemble 9; chemilum. part of mode

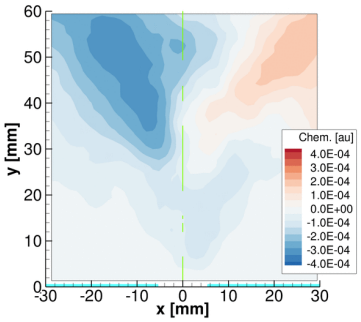

(j) Ensemble 10; chemilum. part of mode

Figure 68: Unstable dataset non-phase corrected EFD modes. Period: 1 ms, frequency: 169.6 Hz; Only imaginary part of ensembles plotted

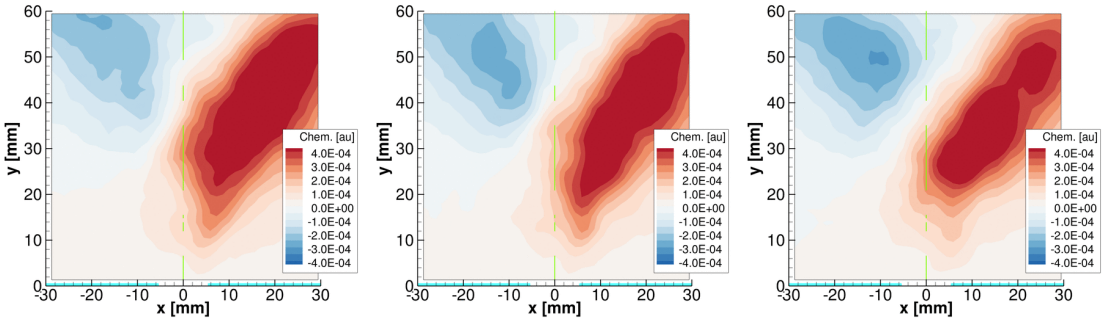

(a) Phase corrected ensemble 1; chemilum. part of mode

(b) Phase corrected ensemble 2; chemilum. part of mode

(c) Phase corrected ensemble 3; chemilum. part of mode

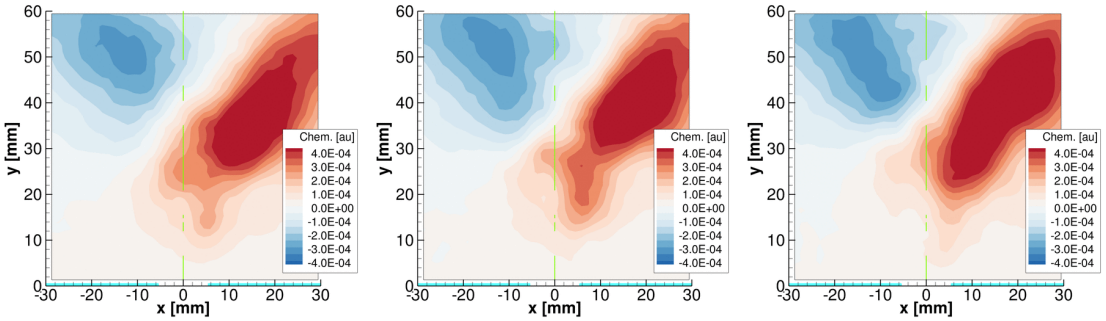

(d) Phase corrected ensemble 4; chemilum. part of mode

(e) Phase corrected ensemble 5; chemilum. part of mode

(f) Phase corrected ensemble 6; chemilum. part of mode

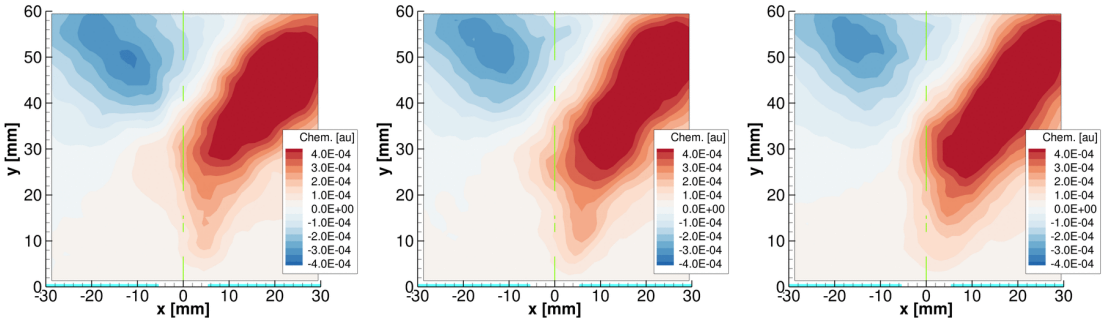

(g) Phase corrected ensemble 7; chemilum. part of mode

(h) Phase corrected ensemble 8; chemilum. part of mode

(i) Phase corrected ensemble 9; chemilum. part of mode

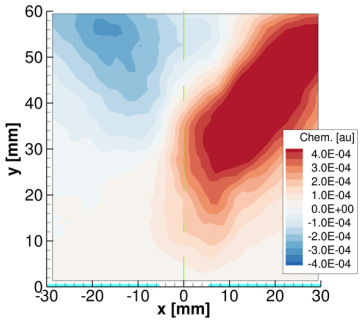

(j) Phase corrected ensemble 10; chemilum. part of mode

Figure 69: Unstable dataset phase corrected EFD modes. Period: 1 ms, frequency: 169.6 Hz; Only imaginary part of ensembles plotted

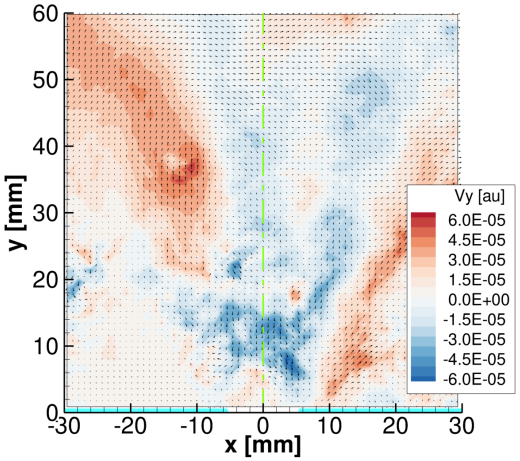

(a) Mean of real part of PIV component of EFD mode

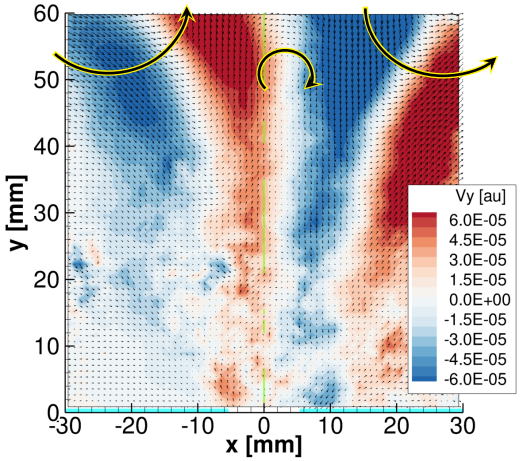

(b) Mean of imaginary part of PIV component of EFD mode

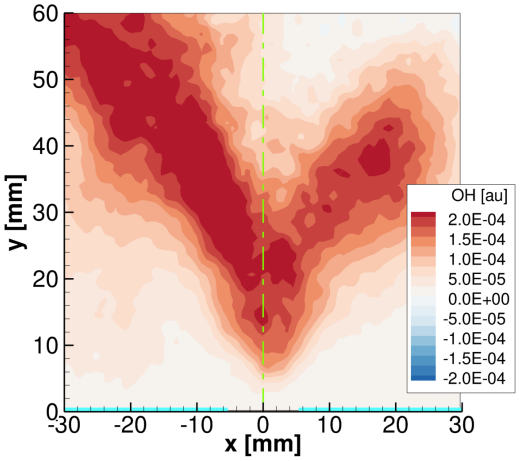

(c) Mean of real part of PLIF component of EFD mode

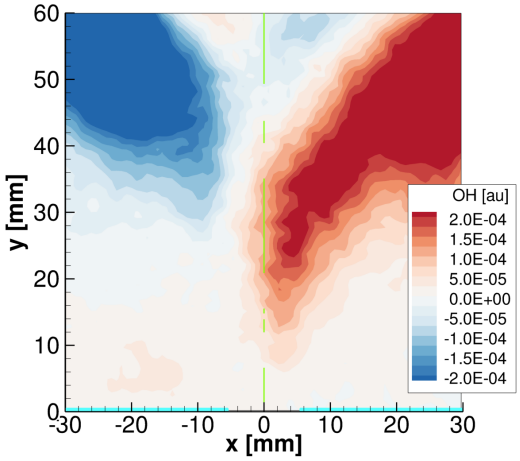

(d) Mean of imaginary part of PLIF component of EFD mode

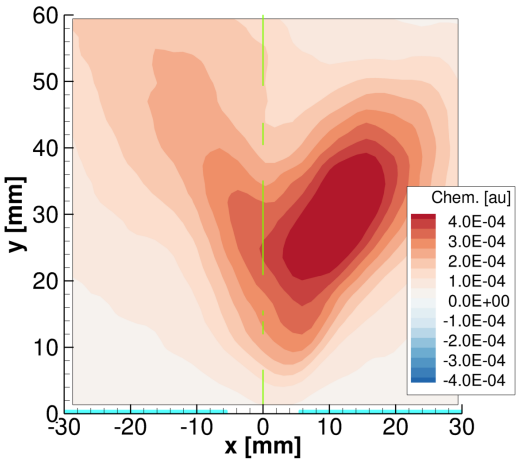

(e) Mean of real part of chemiluminescence component of EFD mode

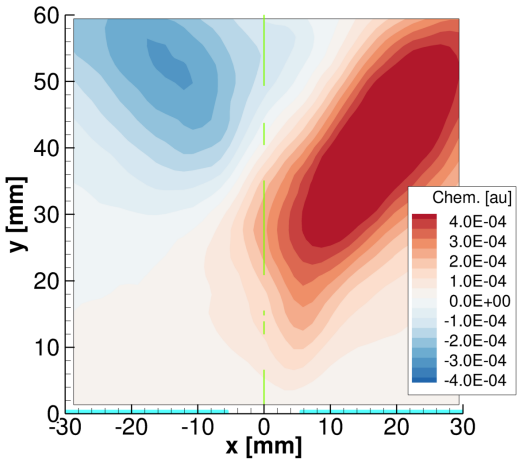

(f) Mean of imaginary part of chemiluminescence component of EFD mode

Figure 70: Averages of unstable dataset EFD mode components. Period: 1 ms, frequency: 169.5 Hz. Acoustic phase of real and imaginary parts (left and right columns, respectively): −0.5160 rad (−29.56°) and 1.0548 rad (60.44°), respectively.

interaction between the transverse acoustics perturbing the low velocity inner recirculation zone and the unstable hydrodynamic shear layer.

Figure 70b suggests that the portion of the 170 Hz EFD mode when the acoustic velocity peaks is related to a complex vortical structure, as highlighted by the arrows in Fig. 70b. This vortical structure might consist of a precessing vortex core pair, which originates near the inner recirculation zone, but further study—perhaps with stereoscopic PIV—is needed to fully describe the coherent structure. What we can see is that this vortex structure occurs substantially downstream of the injector and could serve as an acoustic source when it impinges on the exhaust nozzles/wall.

There are two possible mechanisms that can generate sound when a vortex interacts with the nozzles or walls. The first mechanism, which we were referred to as *vortex sound generation*, occurs when the vorticity within the structure is accelerated as it enters the nozzle [71–73]. The second mechanism is due to the vigorous mixing that occurs when a vortical structure interacts with an obstruction, which, in turn, enhances the combustion. The enhanced combustion appears as unsteady heat release and sound is generated; we believe this mechanism dominates the vortex sound generation. A number of authors have suggested CI feedback mechanisms that include acoustic sound generation through vortex interactions [74–76].

While measured acoustic pressure data strongly suggest the presence of a 170 Hz CI, the only evidence we have presented so far was the narrow spectral peak in Fig. 8d, which indicates a low damped, high quality oscillation. Now, by utilizing the coupled 170 Hz EFD mode data the modal Rayleigh criterion may be checked, see Eqs. (102) and (103). Assuming that the CH^*-chemiluminescence is proportional to heat release, the line of sight integrated Rayleigh index is constructed by multiplying the chemiluminescence component of the mode with the combustion chamber acoustic pressure (taken here as the average of the modal content from sensors p'_3 and p'_5. Specifically, for the j^{th} mode we can define the local Rayleigh index as the instantaneous heat release times the acoustic chamber pressure:

$$\mathcal{LR}_j = \dot{q}'_j p'_j \propto I_{\text{chemi}} p'_j \tag{178}$$

For the 170 Hz mode, this local Rayleigh index is plotted for one complete cycle of the 170 Hz mode in Fig. 71. In addition, the combustion chamber acoustic pressure and the spatially integrated

Rayleigh index (defined by Eq. (106)) are plotted versus one period of the wave in Fig. 72 (170 Hz mode: blue line). Figure 72 shows that the acoustic pressure peaks at a phase of approximately 30°, as does the total spatially integrated Rayleigh index. The line of sight integrated Rayleigh index for this maximum (phase of 30°) is shown in Fig. 71b, and a minimum occurs at a phase of approximately 120°, where the acoustic pressure is nearly zero, Fig. 71e. Since the Rayleigh index is the product of the acoustic pressure and the unsteady heat release, both of which change sign during the cycle, the total spatially integrated Rayleigh index peaks twice within one acoustic cycle. As a result, the line of sight Rayleigh index plots in Figs. 71g to 71l are identical to those given in Figs. 71a to 71f. Interestingly, the Rayleigh index in Fig. 71 shows that this mode drives the CI at nearly all spatial locations and all phases of the mode. By integrating the total Rayleigh index with respect to time/phase we find that the Rayleigh integral/criterion, listed in Table 12, is 0.0122 AU—a positive value indicating that the 170 Hz mode is driven by the combustion process. While the approximate Floquet multiplier for this mode indicates the mode is Lyapunov stable or even slightly stable, this mode is, in fact, *unstable* in the CI sense of the word—meaning that net energy is added to the 170 Hz acoustic mode by the combustion heat release process.

Let us now turn our attention to the 258 Hz dynamic mode pair with the second-largest modulus approximate Floquet multiplier. The ensemble averages of the real and imaginary parts of the PIV, PLIF, and chemiluminescence descriptions of this mode are shown in Fig. 73. Since the phases of the real and imaginary parts of the acoustic pressure for this mode are approximately $-39.07°$ and 50.93°, respectively. As a result, the real part of the mode shown in Fig. 73 (i.e., the left column) is nearly in phase with the acoustic pressure.

Comparing the 170 Hz and 258 Hz EFD modes, Figs. 70 and 73, respectively, we observed that some of the spatial structures are similar. Specifically, the imaginary part of the 170 Hz mode is quite similar to the negative of the real part of the 258 Hz mode. While this similarity may imply

Table 12: EFD predicted combustion stability based on modal Rayleigh integral for the unstable experiment dataset

f [Hz]	169.57	258.15
Rayleigh Integral [AU]	0.0122	−0.0041
Modal combustion stability	Unstable	Stable

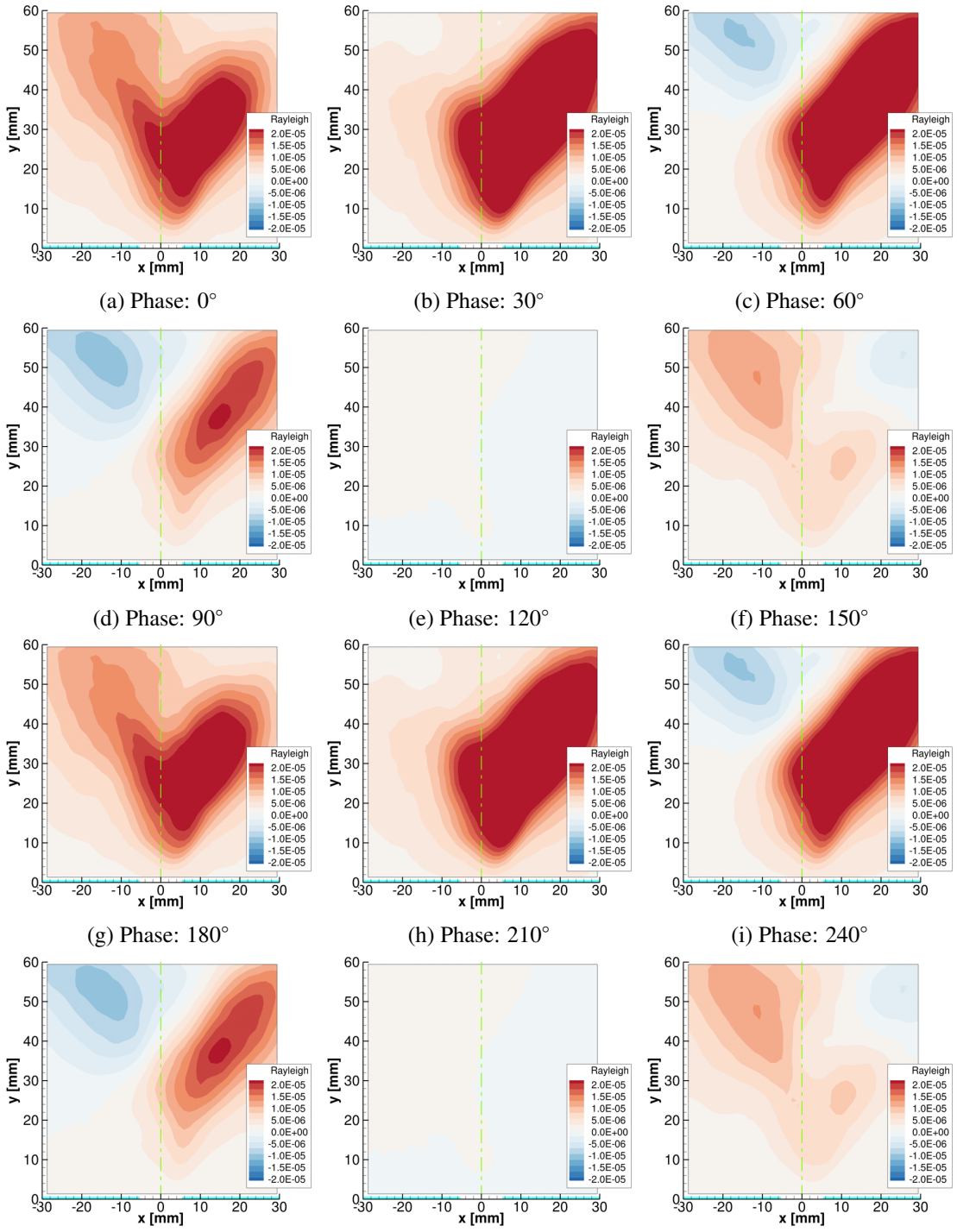

(a) Phase: 0° (b) Phase: 30° (c) Phase: 60°

(d) Phase: 90° (e) Phase: 120° (f) Phase: 150°

(g) Phase: 180° (h) Phase: 210° (i) Phase: 240°

(j) Phase: 270° (k) Phase: 300° (l) Phase: 330°

Figure 71: Unstable dataset local Rayleigh index. Period: 1 ms, frequency: 169.6 Hz

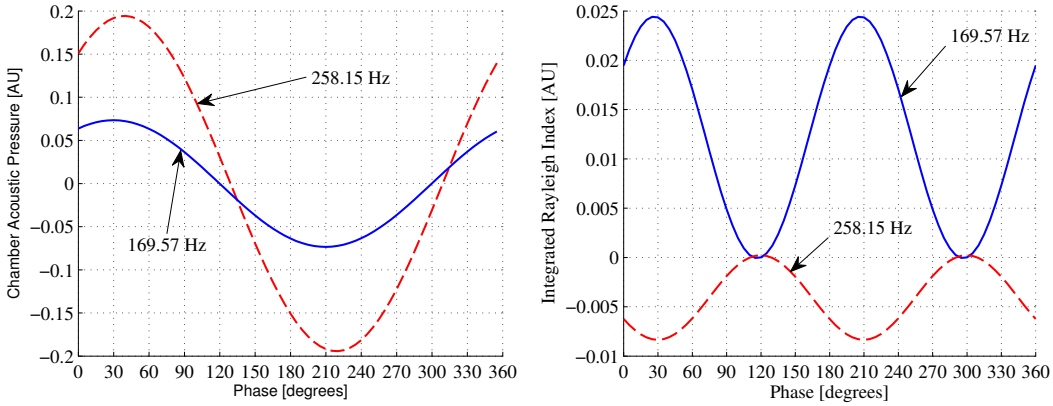

(a) Combustion chamber acoustic pressure

(b) Spatially integrated Rayleigh index

Figure 72: Combustion chamber acoustic pressure and spatially integrated Rayleigh index versus mode phase for the unstable experiment at 169.57 and 258.15 Hz

that these modes represent coupled physical oscillations, their phase with respect to the combustion chamber acoustic pressure is substantially different. We will see that this difference in phase results in significant difference between the Rayleigh integrals of the 170 Hz and 258 Hz modes.

As an aside, let's compare the present results with what we might expect from a POD based analysis. Since the POD method maximizes the L^2 norm within a spatially orthonormal basis, without placing any constraints on the temporal evolution of the modes, eigenmodes of the system that have similar physical structure would be lumped into a single POD mode. As a result, the POD analysis of the unstable experiment dataset could not separate the contributions of the 170 Hz and 258 Hz modes, shown in Figs. 70 and 73, due to their similar spatial structure. Furthermore, while these two modes are spatially similar, but not identical, the POD analysis would likely lump the common component of the 170 Hz and 258 Hz modes into one POD mode and the remainder into other POD modes. Here, not only has the POD mixed physical modes, it has also broken a single physical mode into multiple POD modes and, as a result, it may be difficult to make physical interpretations of the POD modes.

Returning to the EFD analysis, the chemiluminescence and acoustic chamber pressure were used to calculate the line of sight, local Rayleigh index for the 258 Hz mode, see Fig. 74. Additionally, the acoustic pressure and total spatially integrated Rayleigh index for a cycle of the 258 Hz mode are shown in Fig. 72 (red dashed lines). Figure 74 shows that during much of the cycle, the 258 Hz

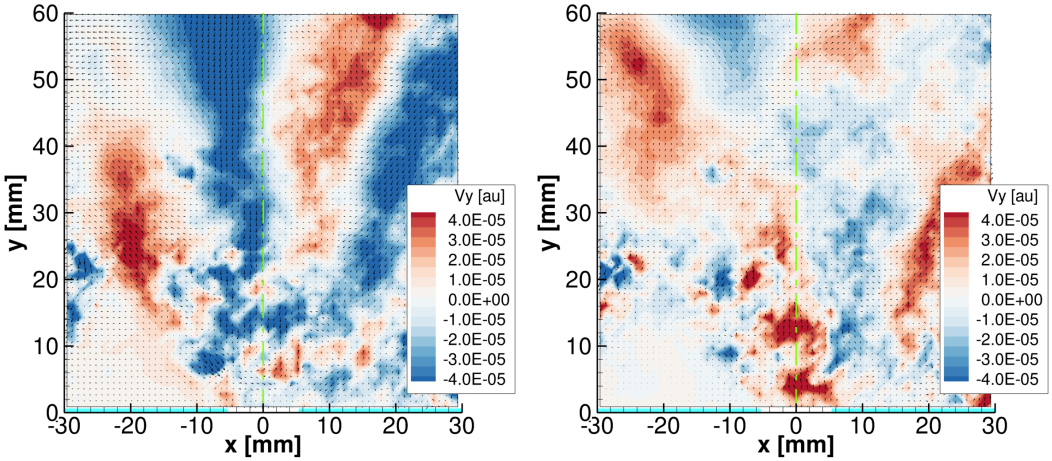

(a) Mean of real part of PIV component of EFD mode

(b) Mean of imaginary part of PIV component of EFD mode

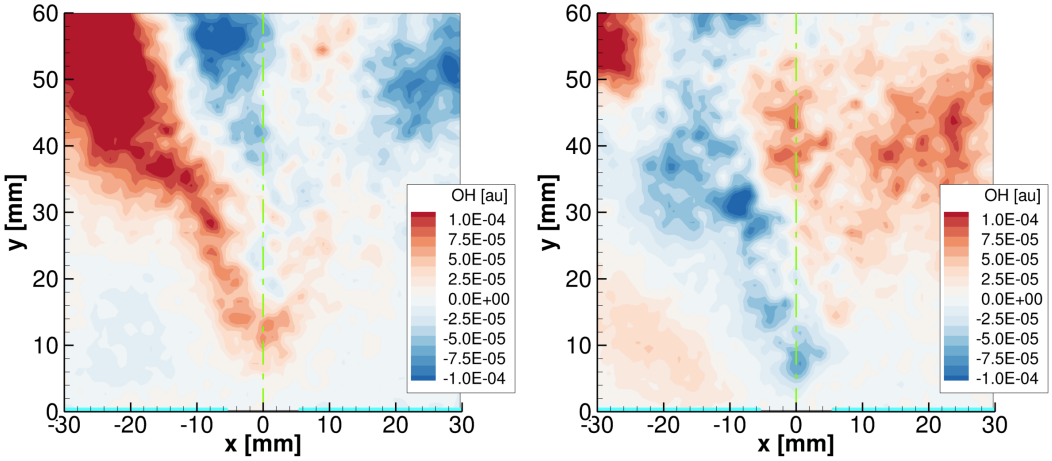

(c) Mean of real part of PLIF component of EFD mode

(d) Mean of imaginary part of PLIF component of EFD mode

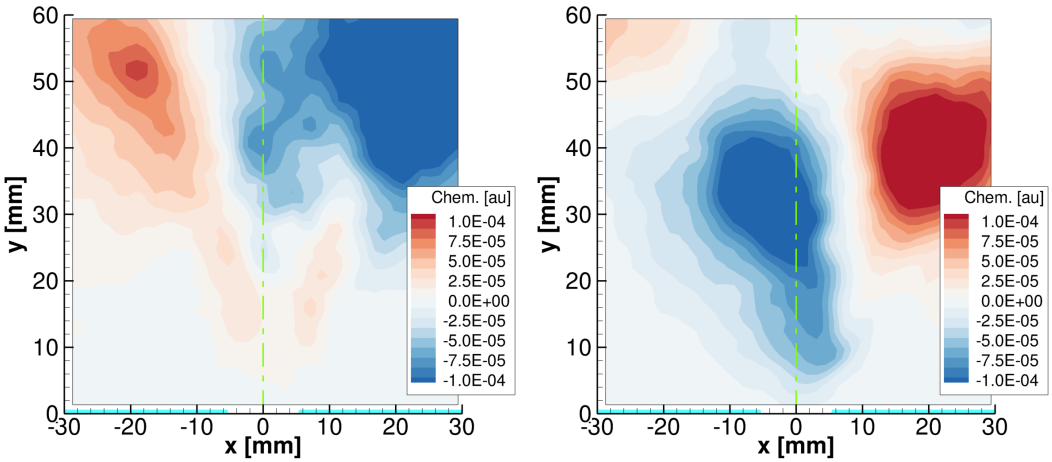

(e) Mean of real part of chemiluminescence component of EFD mode

(f) Mean of imaginary part of chemiluminescence component of EFD mode

Figure 73: Averages of unstable dataset EFD mode components. Period: 1 ms, frequency: 258.15 Hz. Acoustic phase of real and imaginary parts (left and right columns, respectively): −0.6819 rad (−39.07°) and 0.8889 rad (50.93°), respectively.

mode has regions that are positive and negative, indicating local driving and damping of the acoustic mode. It should be noted, however, that spatial integration of the Rayleigh index shown in Fig. 74 yields substantial cancellation of the total spatially integrated Rayleigh index shown in Fig. 72b. This figure shows that for this mode the index is negative for nearly the entire cycle and that the Rayleigh integral value for this mode is -0.0041 AU. These results show that while the combustion process drives the 170 Hz mode, it tends to damp the 258 Hz mode. It, thus, appears that the 258 Hz mode is driven by some process other that the combustion—likely the flow noise coupling with the 2 W transverse acoustic mode—and is then damped by the combustion process.

We will discuss the surprising fact that we observe a mode with negative Rayleigh integral further in Section 6.2.4.

6.2.3 Sensitivity Analysis

Now that we have demonstrated that the EFD method is capable of finding modes whose approximate Floquet multipliers have a large magnitude—analysis of the unstable experiment dataset showed the presence of two complex conjugate pairs of dynamic modes whose moduli are nearly one—we want to make certain that these findings are physical and not an artifact of the analysis technique. To explore whether the EFD technique does, in fact, robustly find the approximate Floquet multipliers, we investigated the modes' dependence upon: 1. the scaling of the input data, 2. different analysis periods, 3. the number of modes retained in the SVD inversion, and 4. the ranges of data within the dataset used to ensure repeatability of the results. In each case, we present the frequency and modulus of the approximate Floquet multiplier corresponding to the 170 Hz and 258 Hz modes to quantify the influence of the analysis parameter on the results.

Our first sensitivity study examines the influence of data scaling on the EFD modes. As we discussed in Section 4.3.3, the scale of the average vector norm for one data type may be considered arbitrary. Thus, in this study we may keep the PLIF norm scaled to one. Also, at this point we have not found a need to vary the chemiluminescence data scaling and, therefore, we will also keep the norm of these data set to one. Nominally, we have chosen the PIV data norm to be three times smaller and the acoustic data norm to be three times larger than the PLIF and chemiluminescence data types' norm, respectively. In this sensitivity study, we have both increased and decreased the 3x scale factor,

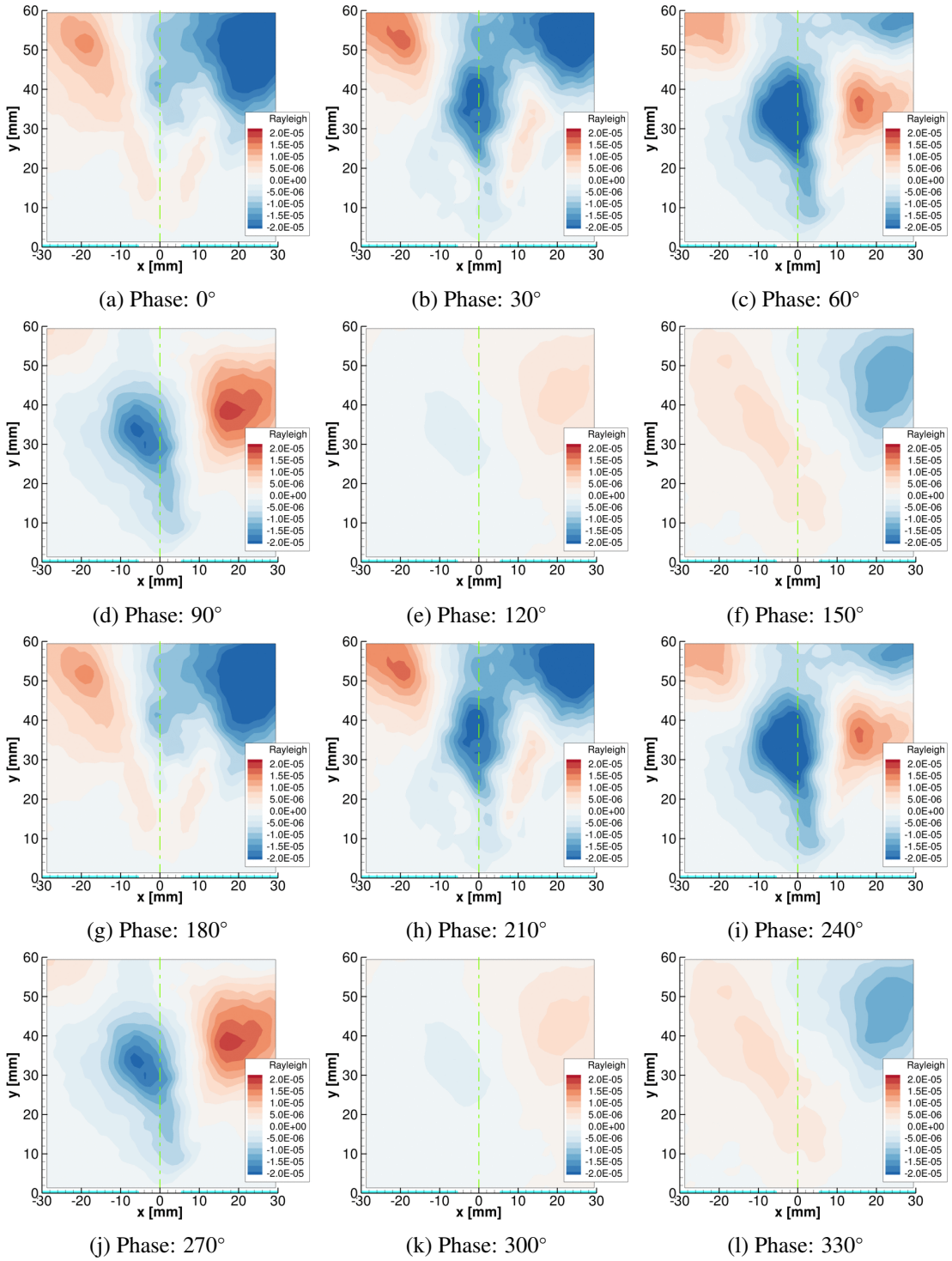

(a) Phase: 0° (b) Phase: 30° (c) Phase: 60°

(d) Phase: 90° (e) Phase: 120° (f) Phase: 150°

(g) Phase: 180° (h) Phase: 210° (i) Phase: 240°

(j) Phase: 270° (k) Phase: 300° (l) Phase: 330°

Figure 74: Unstable dataset local Rayleigh index. Period: 1 ms, frequency: 258.15 Hz

instead using values of 10x and 1x. We ran a total of four analyses with different data scaling sets; each set is listed as a column in Table 13. The third column represents the baseline scaling that we have used to this point, the first column uses the same scale for each type of data, and the second and third column represent lower PIV data emphasis and higher acoustic data emphasis than the baseline case, respectively.

Table 13: EFD predicted frequencies and moduli of estimated Floquet multipliers of two leading dynamic modes from analysis using different data scaling

PIV data norm	1	1/10	1/3	1
PLIF data norm	1	1	1	1
Chemiluminescence data norm	1	1	1	1
Acoustic data norm	1	1	3	10
f [Hz]	169.52	169.62	169.57	169.60
$\|\eta\|$	0.9686	0.9787	0.9855	0.9864
f [Hz]	258.75	258.73	258.15	258.15
$\|\eta\|$	0.9542	0.9593	0.9675	0.9678

The approximate Floquet multipliers and exponents for the four cases are plotted in Figs. 75a and 75b, respectively, and key values are listed in Table 13. While the Floquet multipliers whose moduli are less than 0.6 differ substantially, these are not the modes of interest or the modes we expect Krylov subspace methods to accurately approximate. On the other hand, the larger moduli EFD modes appear to be nearly unchanged by the different scaling values. To show the general trends with different dataset scaling, we have scaled the real axis (growth/decay coefficient) of the Floquet exponents, shown in Fig. 75b, to show only the modes closest to the real axis. In this figure and Table 13 we see that in each of the cases the EFD analysis reproduces the two largest moduli complex conjugate pairs of dynamic modes well, e.g., the largest change from the baseline case in frequency and $|\eta|$ for the 170 Hz mode is 0.02949% and 1.7149%, respectively. For the two leading dynamic mode pairs, the case with equal scale factors for each data type, the blue squares in Fig. 75, has the lowest moduli Floquet multiplier. The baseline and high acoustic scale factor analyses, cases 3 (black circles) and 4 (red crosses), yield the largest moduli for these two complex conjugate pairs of modes. We expect that physically observable modes will have Floquet multipliers with moduli of approximately one and the scaling that yields higher moduli approximate Floquet multipliers are

likely better approximations to the true Floquet multipliers. In addition, these last two cases yield two additional relatively high moduli dynamic pairs, where as the uniformly scaled analysis found only a non-dynamic mode—another sign of the improved results with the higher acoustic norm scaling. While we observe some dependence of the scale factors on the results, the overall qualitative results and the quantitative values for the leading EFD modes are nearly unchanged.

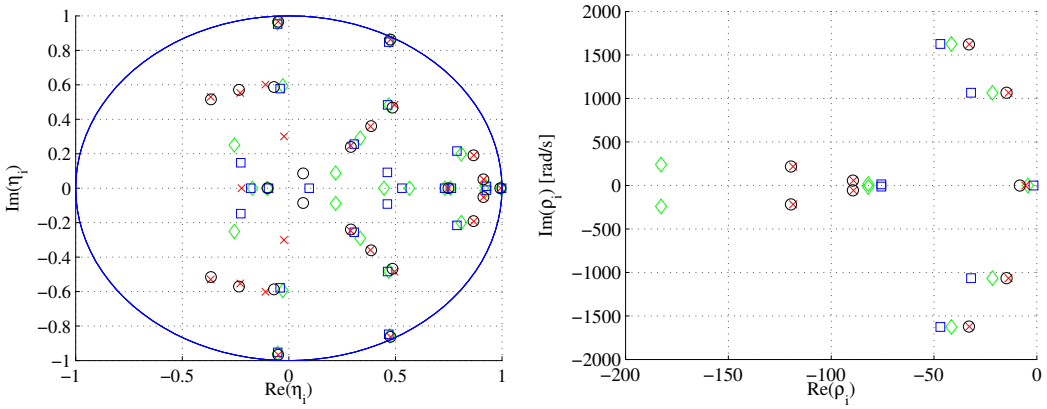

(a) Norm study Floquet multipliers

(b) Norm study Floquet exponents

Figure 75: Sensitivity of EFD results on different data scalings; norms of PIV, PLIF, Chemiluminescence, and acoustic data: (1,1,1,1) blue squares, (1/10,1,1,1) green diamonds, (1/3,1,1,3) black circles, and (1,1,1,10) red crosses

Our second sensitivity study examines the influence of non-exact EFD analysis period on the EFD modes. As we discussed in Section 6.1 there are number of possible values for the Floquet theory time period, each of them close to 1 ms. Since the diagnostic data was sampled at 10 kHz we cannot examine the system at an arbitrary time period, e.g., 0.9833 ms. To test the sensitivity of the EFD results to this inability to both definitively predict the correct time period and the inability to observe the system at this correct time period, we have run three analyses with time periods of 0.9 ms, 1.0 ms, and 1.1 ms, i.e., every 9^{th}, 10^{th}, and 11^{th} snapshot. It should be noted that this also changed the number of ensembles in each analysis, 9, 10, and 11, respectively. For each of the three analyses the frequency and modulus of the two leading dynamic complex conjugate mode pairs are listed in Table 14. The estimated Floquet multipliers are plotted in Fig. 76a. In this case the multipliers are difficult to compare because an EFD mode with the same frequency but different analysis period would appear at a different azimuthal location in this plot. A direct comparison may be made by examining the equivalent approximate Floquet exponents, shown in Fig. 76b. From Table 14 and

Fig. 76b it is clear that the largest modulus EFD modes are nearly unchanged by the use of the three different analysis periods, e.g., the 170 Hz mode's frequency and $|\eta|$ are changed from the baseline case at most 0.09436% and 0.14206%, respectively. From Fig. 76b we see that the lower moduli EFD modes differ from one another more substantially, but again, these modes are not the primary focus of the analysis.

Table 14: EFD predicted frequencies and moduli of estimated Floquet multipliers of two leading dynamic modes from analysis using different FD analysis periods

Analysis period [ms]	0.9	1	1.1
Number of time steps/ensembles	9	10	11
Equivalent frequency [Hz]	1111.1	1000	909.09
f [Hz]	169.73	169.57	169.57
$\|\eta\|$	0.9841	0.9855	0.9855
f [Hz]	258.00	258.15	258.39
$\|\eta\|$	0.9710	0.9675	0.9630

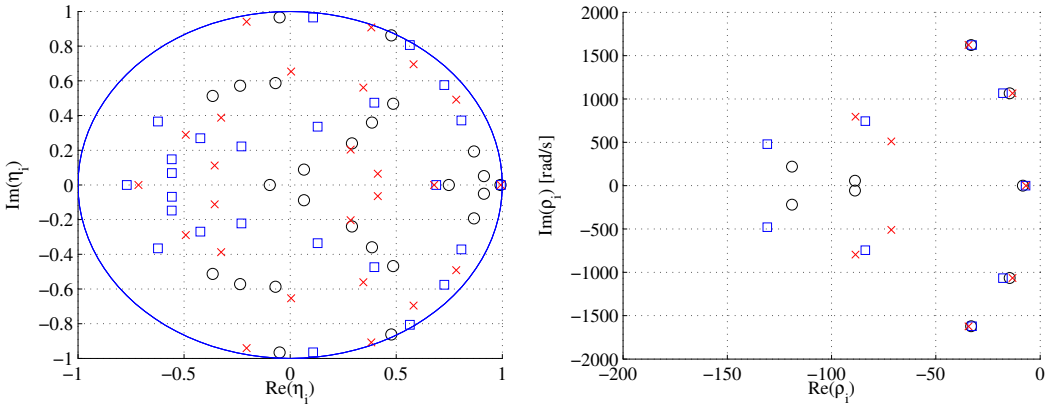

(a) Analysis period (b) Analysis period

Figure 76: Sensitivity of EFD results on different FD analysis periods; analysis period: 0.9 ms blue squares, 1 ms black circles, 1.1 ms red crosses

Our third sensitivity study examines the influence of the number of retained modes during the singular value inversion process on the EFD modes. As discussed in Sections 3.1.4 and 5.4, we do not invert the singular value matrix, Σ, in for example Eq. (155). Instead, we form a Moore-Penrose pseudoinverse—keeping a specific number of the largest singular values, taking the reciprocal of these values, and zeroing the other diagonal entries. As a result, the pseudoinverse is a low rank, least squares approximation to the inverse. By choosing the number of singular values and equivalently

EFD modes retained in this process we can balance the noise rejection with how completely the original measurements can be reconstructed. For our baseline case, to this point, we have retained 25 singular values/modes in an attempt to retain enough dynamic modes to identify the physical processes, while rejecting noise. To examine the effects of retaining a higher or lower number of singular values on the EFD modes we also performed EFD analyses retaining 10, 15, and 100 singular values. The results for the 10 singular values case are not presented here as they did not produce either the 170 or 258 Hz modes—this severe restriction in the number of modes cannot accurately represent the dynamics of the system. The leading dynamic modes' frequencies and moduli for the 15, 25, and 100 retained singular values cases are listed in Table 15 and the approximate Floquet multipliers and exponents are plotted in Fig. 77. From Fig. 77a it is clear that the 100 singular value case, red crosses, has far more complex conjugate dynamic mode pairs then either the 25 or 15 singular value cases, black circles and blue squares, respectively. But, this figure also shows that all of the additional modes have estimated Floquet multiplier moduli less than approximately 0.8. In fact, above a modulus of 0.8 there appears to be little difference between the 25 and 100 singular value cases and for the two highest moduli complex conjugate pairs even the 15 mode results are approximately the same as the other two cases. In Fig. 77b it can be seen that the retention of more singular values brings the approximate Floquet exponents for the 170 Hz and 258 Hz modes closer to the imaginary axis, but the modal frequencies are approximately unchanged, e.g., for the 170 Hz mode the largest frequency difference occurs between the 25 singular value baseline case and 15 singular value case of 0.4128% and the largest difference in the multiplier modulus was between the 100 and 15 singular values cases and was 2.139%. From this result, we see that retaining more modes likely yields better approximations of the frequencies and growth/decay rates for the system, at the expense of the amount of noise rejected from the spatial mode shapes. Depending on the goals of the analyses, the number of singular values retained must be balanced between accurately approximating the Floquet multipliers and rejecting enough noise from the mode shapes. For our current data and goals, 25 retained singular values/modes appears to be a good compromise.

Our final sensitivity study examines the influence of the data itself on repeatability of the EFD modes. We want to ensure the modes that the EFD analysis identifies are physically significant and that we are not simply correlating noise. The baseline analysis has been performed using

Table 15: EFD predicted frequencies and moduli of estimated Floquet multipliers of two leading dynamic modes from analysis using 15, 25, and 100 largest singular values

Number of modes	15	25	100
f [Hz]	170.27	169.57	169.85
$\|\eta\|$	0.9700	0.9855	0.9912
f [Hz]	259.37	258.15	260.49
$\|\eta\|$	0.9461	0.9675	0.9859

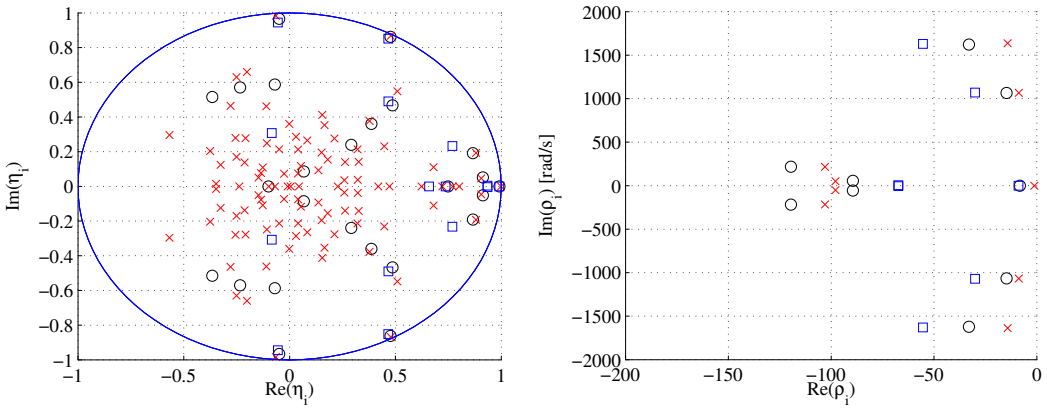

(a) Number of EFD modes

(b) Number of EFD modes

Figure 77: Sensitivity of EFD results on number of modes/rank of SVD; number of modes: 15 blue squares, 25 black circles, 100 red crosses

8500 snapshot of simultaneous data. Here, we ran two additional analyses, one using the first 4000 snapshots and a second using the second 4000 snapshots. The leading dynamic EFD modes' frequencies and approximate Floquet multipliers moduli are listed in Table 16 and the approximate Floquet Multipliers and exponents are plotted in Fig. 78.

Table 16: EFD predicted frequencies and moduli of estimated Floquet multipliers of two leading dynamic modes from analysis using full dataset, first 4000 snapshots, and second 4000 snapshots

Data range/snapshot numbers	1:8500	1:4000	4001:8000
f [Hz]	169.57	169.44	169.43
$\|\eta\|$	0.9855	0.9732	0.9901
f [Hz]	258.15	254.87	261.29
$\|\eta\|$	0.9675	0.9472	0.9840

In these three EFD analyses, for the 170 Hz mode, the largest difference in predicted frequency was 0.082562%. The difference in predicted modulus of the multiplier was slightly larger, with a

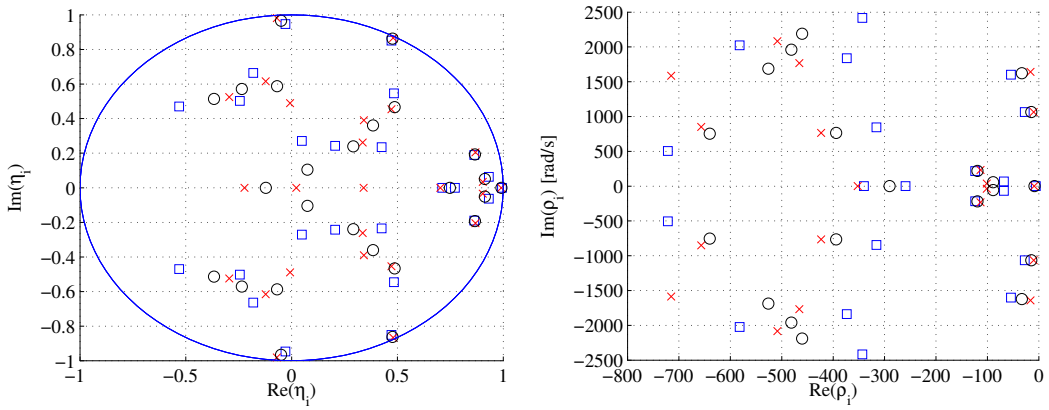

(a) Data range (b) Data range

Figure 78: Sensitivity of EFD results on the data range used; data range/snapshot numbers: 1:8500 black circles, 1:4000 blue squares, 4001:8000 red crosses

1.7069% difference between the first and second 4000 snapshot analyses. The analysis with the complete dataset may be a slightly better approximation to the frequency due to the longer data record. On the other hand, the highest modulus modes were found using the data from the 4001st to 8000th snapshots. One possible explanation of the higher moduli in the latter case is that there was a slightly change in conditions during the data acquisition window. Another possibility may be due in part to the high-speed laser data acquisition setup used in the experiment. The PIV and PLIF laser systems were initially in a standby mode (not firing—pumping is happening, but q-switch is not being triggered) and when a master trigger was pressed, the laser systems began to fire and the acquisition systems began recording data. Due to the high energy nature of the laser systems there is a rapid transient within the systems before the lasers reach a steady temperature and energy per pulse. For example, the first few times the PIV laser fires, substantially more energy is released than when it has been in operation for a few hundred cycles. As a result, the first few images associated with the bright laser pulses are unusable. On the other hand, due to memory limitations within the high-speed cameras, we were only able to store about nine tenths of a second worth of images. To balance these limitation and maximize the dataset length, the first 36 images have been discarded from all of the datasets. These discarded images would be labeled -35 to 0 in our current numbering scheme. We choose to discard 36 images because beyond 25 or 30 laser firings the images did not appear to be affected by this transient. At this point we can only conjecture, but perhaps, the *better* EFD results using only the later data indicates that the transient, while not visually perceptible, was

present in some of the first 4000 snapshots, reducing the quality of this dataset. All this being said, the differences in the all important largest moduli dynamic EFD modes are very small for these three cases. First, this shows that the method is not sensitive to dataset length, although there is some minimum length required to obtain adequate results. Second, it appears the method is not just finding modes as a result of random fluctuations in the data. We can conclude this because there is no common data between the two shortened data range analyses and, thus, the random variations due to noise in the measurements and turbulent fluctuations are not the same in these two datasets.

The sensitivity studies presented in this section demonstrate that the EFD method is not only capable of finding the largest moduli dynamic modes, but also that these results are insignificantly changed by the user specified analysis parameters.

6.2.4 Comparison of the EFD Results from the Stable and Unstable Experimental Datasets

In this section we will examine the EFD modes from the stable experiment and attempt to identify the relevant relationships to the unstable experiment EFD modes shown in Section 6.2.2.

The approximate Floquet multipliers and exponents for the stable and unstable experimental conditions are plotted in Fig. 79. Similarly to the unstable dataset's 258 Hz mode, the EFD analysis of the stable experimental case yields a complex conjugate pair of Floquet multipliers with modulus nearly 1, at 257 Hz. The stable case also yields a mode at 65 Hz with a modulus of nearly one. Additionally, in the stable case, there are a number of slightly lower modulus modes, e.g., 141 Hz and three from 300 to 400 Hz. The relative acoustic amplitudes for the EFD modes, for both stable and unstable experiments, are shown in Fig. 80.

First, we will examine the 257 Hz mode, for which the ensemble averaged mode is shown in Fig. 81. Perhaps surprisingly, both the estimated Floquet multipliers and acoustic mode content are very similar between the stable experiment 257 Hz mode and the unstable experiment 258 Hz mode, as shown in Figs. 79 and 80. In addition, the mode structure for each of these modes is similar in nature, see Fig. 81 and 73, respectively. For example, the real part of the vertical velocity for each mode, Fig. 81a and 73a, have a similar structure with alternating bands of positive and negative y-velocity in a wave structure, oriented transverse to the mean flow. It also turns out that the modes' frequencies are near natural acoustic mode frequencies of their respective configurations.

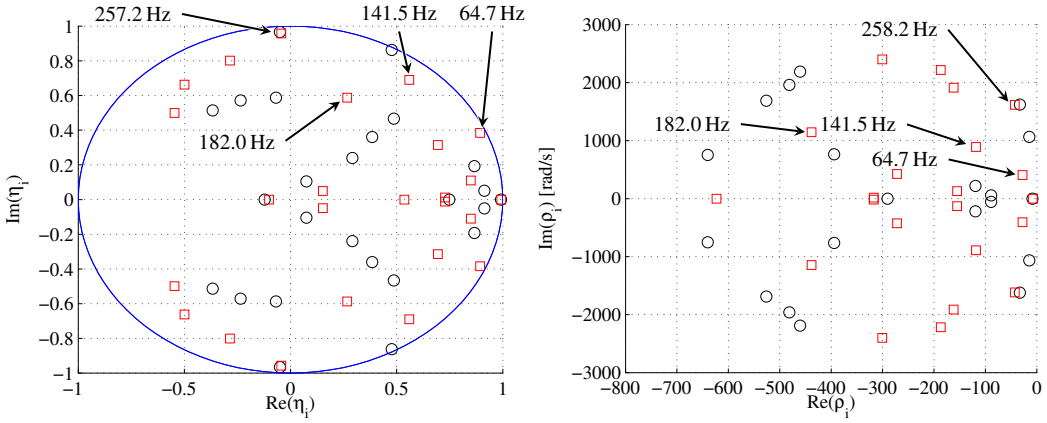

(a) Estimated Floquet multipliers

(b) Estimated Floquet exponents

Figure 79: EFD estimated Floquet multiplier and exponent estimation for stable (red squares) and unstable (black circles) experiments

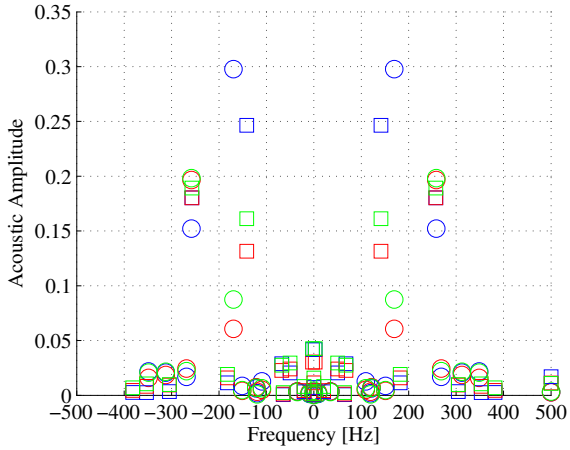

Figure 80: EFD based modal acoustic amplitude for stable (squares) and unstable (circles) experiments

Furthermore, we showed in Section 2.3.2 that in each of these two modes that the injector is located near a pressure anti-node, i.e., near a velocity node, where the modal transverse acoustic velocity is small. Since the air injection orifices are choked, see Appendix B, we do not expect substantial mass flow induced combustion response to pressure perturbations in this case. So, these modes are unlikely to cause acoustically coupled CIs. We also believe that the appearance of these modes is due to broadband excitation from the injector fluid flow. Specifically, the driving energy may be supplied from the fluid flow oscillations associated with the approximately 1000 Hz mode shown in Fig. 35. This type of natural frequency *filtering* often occurs in confined combustion systems. Overall, the 257 Hz and 258 Hz modes appear to represent the same physical phenomena.

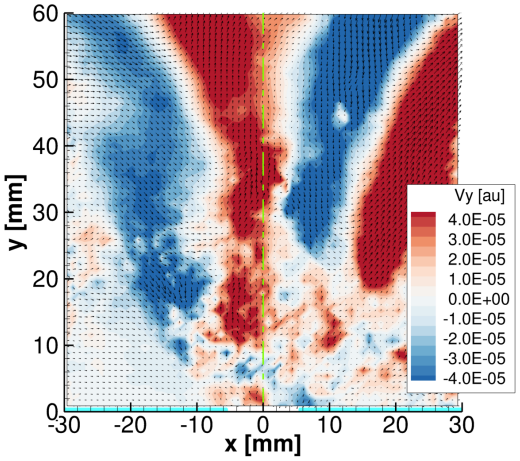

(a) Mean of real part of PIV component of EFD mode

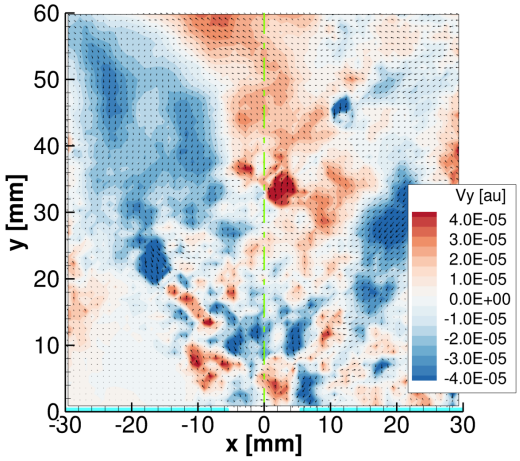

(b) Mean of imaginary part of PIV component of EFD mode

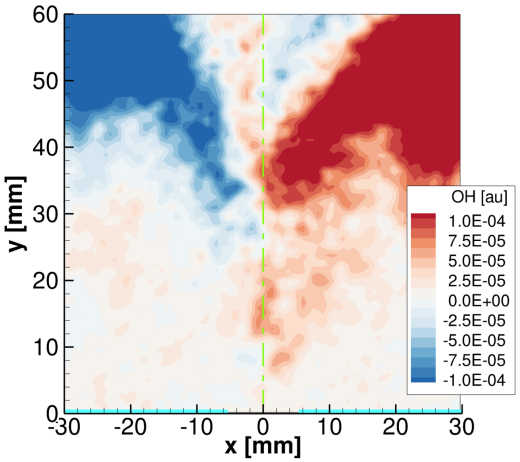

(c) Mean of real part of PLIF component of EFD mode

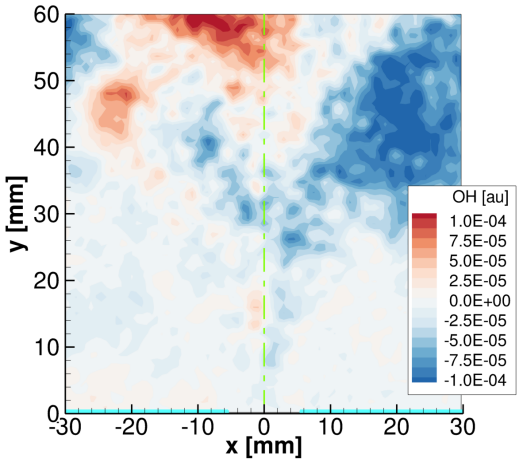

(d) Mean of imaginary part of PLIF component of EFD mode

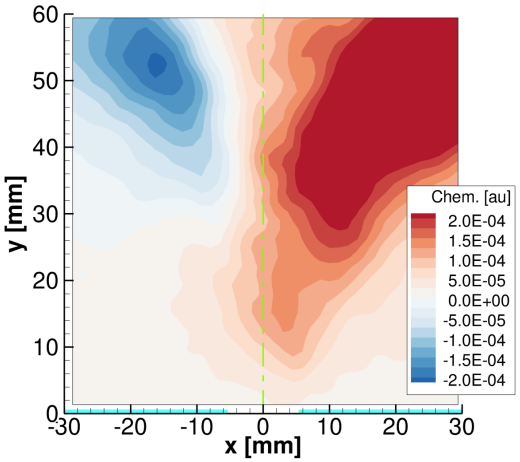

(e) Mean of real part of chemiluminescence component of EFD mode

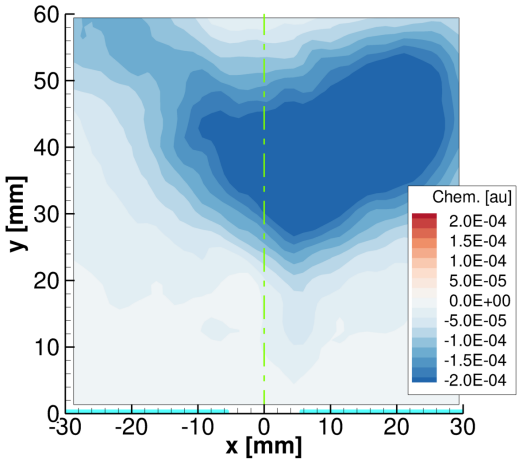

(f) Mean of imaginary part of chemiluminescence component of EFD mode

Figure 81: Averages of stable dataset EFD mode components. Period: 1 ms, frequency: 257.24 Hz

Turning to what is the largest modulus dynamic mode found in the stable experimental dataset, the 65 Hz mode is shown in Fig. 82. From the imaginary part of this mode, Figs. 82b, 82d, and 82f, it appears that this mode captures the lifting and dropping of the inner recirculation zone and, with it, the flame anchor point. Further, this mode appears to be unrelated to the approximately 60 Hz mode that was found in the unstable experimental dataset with the FD analysis, Fig. 58. While the mode has a large modulus approximate Floquet multiplier, the acoustic amplitude of this mode, shown in Fig. 80, is very low. This makes sense as the mode is far from a natural acoustic mode. At least with respect to CIs, we are not interested in this mode.

In attempt to find related modes between the 170 Hz unstable mode and the stable experiments, we finally turn our attention to the 142 Hz mode, as shown in Fig. 83. While the 142 Hz mode has a considerably lower modulus approximate Floquet multiplier than the previously discussed 170 Hz mode, the modal acoustic amplitude for the two modes are similar. This is an unexpected result due to the fact that for this experimental configuration 142 Hz is not near any natural acoustic mode. There is no clear explanation for the substantial acoustic content of this mode.

Comparing the mode shapes shows some qualitative similarities between the 170 and 142 Hz modes, e.g., Figs. 83a and 70b both show similar velocity structures, all be it somewhat different. The 142 Hz mode appears to have more y-component velocity content near the inner recirculation zone. Even if this mode represents the same physical phenomena as the 170 Hz mode, all be it more heavily damped, this EFD mode is far from any of the acoustic modes in this configuration and thus is incapable of coupling to form a CI. In the future, it would be interesting to study the 142 Hz mode to explore how it is related to the observed CI at 170 Hz. This could perhaps be accomplished by analyzing the measured PIV, PLIF, and chemiluminescence data, while replacing the measured acoustic pressure data with various frequency and phase synthetic signals. The resulting modes could be post analyzed to examine which configurations might yield positive Rayleigh integrals and these configurations could then be tested experimentally for verification of the predictions.

6.3 Conclusions

In this chapter we have shown the FD and EFD methods, developed in Chapter 5, applied to experimental data, are capable of locating physical phenomenon that was beyond the reach of

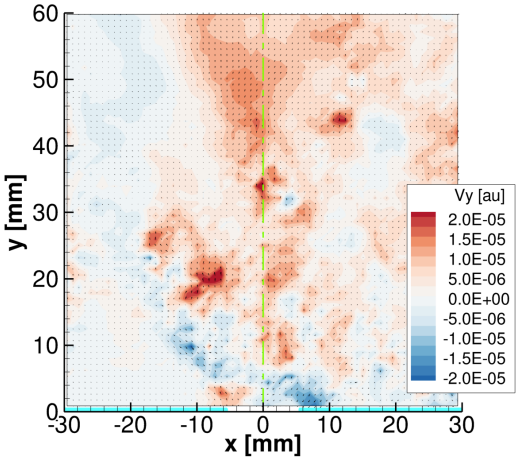

(a) Mean of real part of PIV component of EFD mode

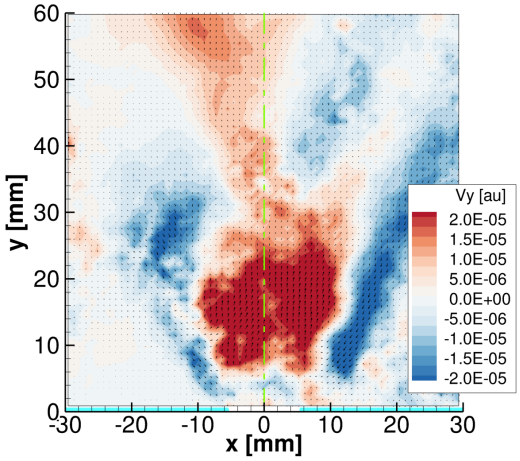

(b) Mean of imaginary part of PIV component of EFD mode

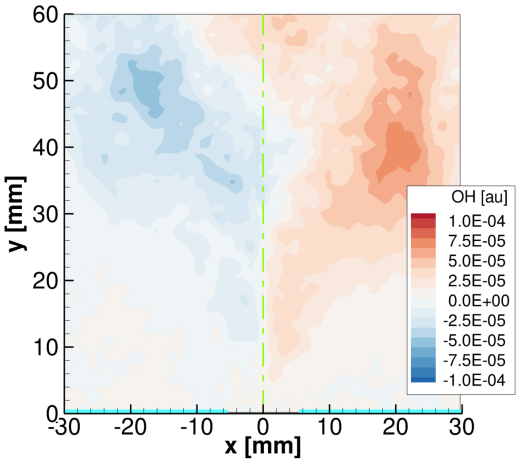

(c) Mean of real part of PLIF component of EFD mode

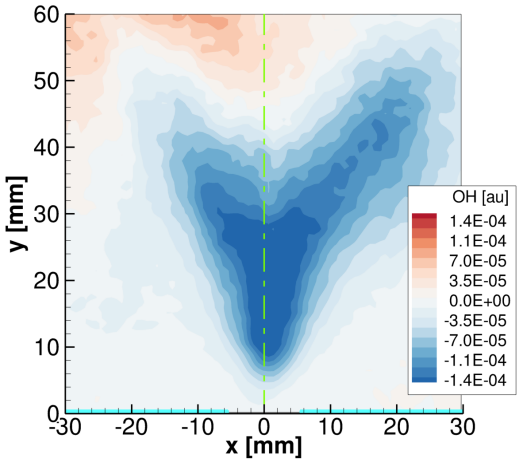

(d) Mean of imaginary part of PLIF component of EFD mode

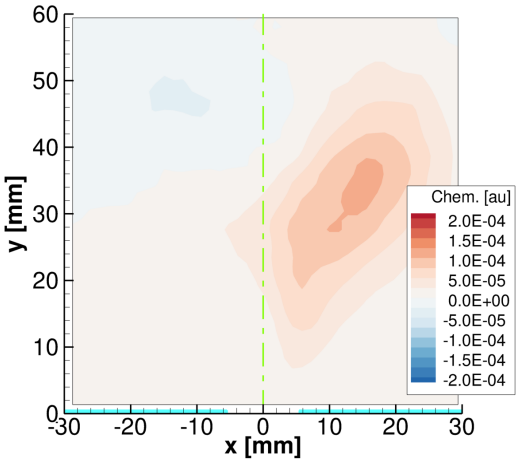

(e) Mean of real part of chemiluminescence component of EFD mode

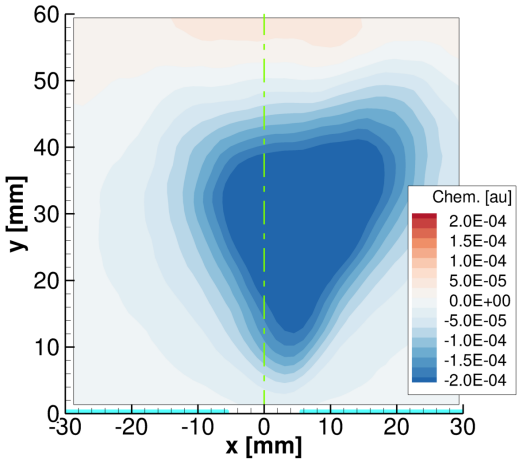

(f) Mean of imaginary part of chemiluminescence component of EFD mode

Figure 82: Averages of stable dataset EFD mode components. Period: 1 ms, frequency: 64.68 Hz

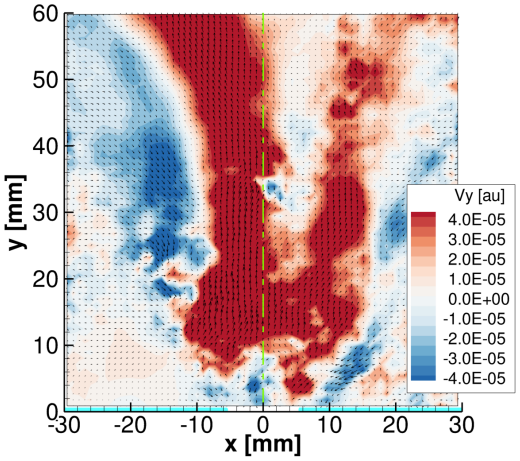

(a) Mean of real part of PIV component of EFD mode

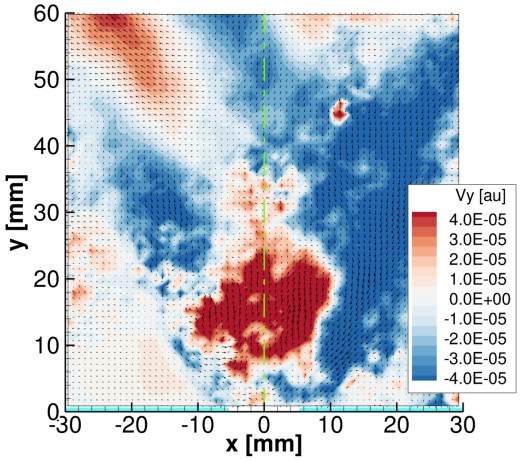

(b) Mean of imaginary part of PIV component of EFD mode

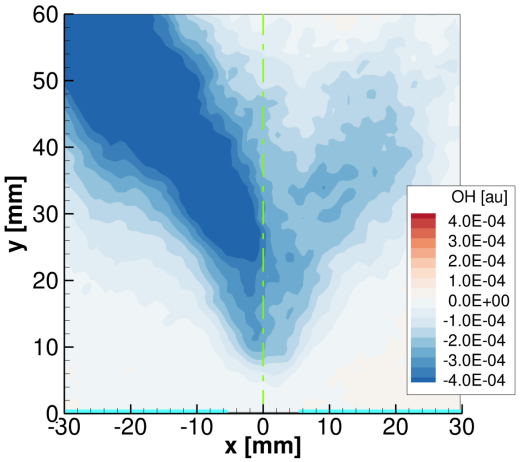

(c) Mean of real part of PLIF component of EFD mode

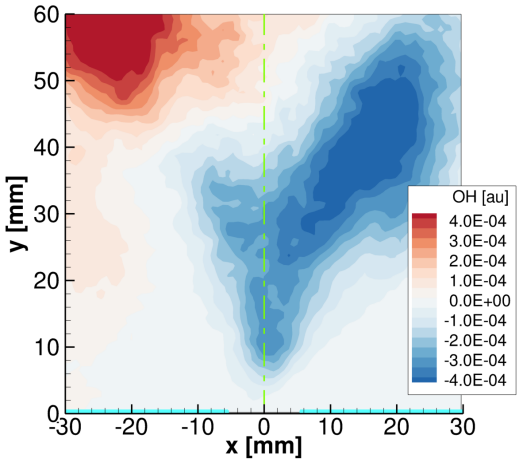

(d) Mean of imaginary part of PLIF component of EFD mode

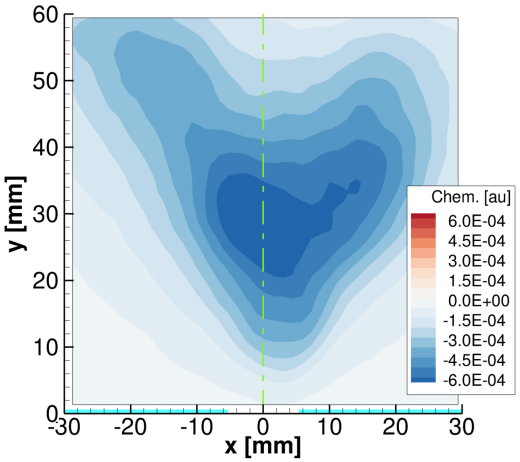

(e) Mean of real part of chemiluminescence component of EFD mode

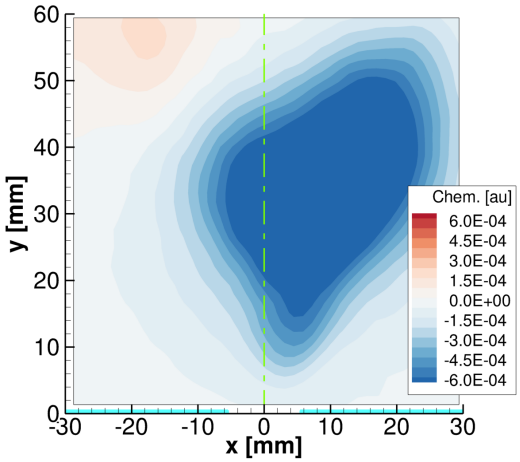

(f) Mean of imaginary part of chemiluminescence component of EFD mode

Figure 83: Averages of stable dataset EFD mode components. Period: 1 ms, frequency: 141.54 Hz

DMD/SDD techniques. Although, to apply these new techniques, we must now select the length of time at which it is believed that the governing operator is periodic. Again, in the previous chapter we established a number of techniques to possible identify the proper time period, leading us to use a time period of 1 ms for the analyses presented in this chapter. While there is no way to prove that this is the proper period beyond the fact that when used, the analyses returns a number of modes whose approximate Floquet multipliers have a modulus of nearly one—nearly undamped or Lyapunov stable modes. Furthermore, these large moduli modes' complex frequencies appear to relatively insensitive to small changes ($\pm 10\%$) in the analysis period used. All signs indicate that the chosen period is indeed appropriate for the current experiment.

In addition, we also showed that compared to the FD method that the EFD method yielded an enhanced ability to locate key modes from the experimental data. This enhanced ability is due to the added state information from the multiple time steps being included—yielding improved approximate Floquet multipliers—and the phase correction/ensemble averaging of the modes—resulting in improved spatial structures with lower random noise.

There were additional improvements found by moving from the FD to the EFD analysis. While the FD analysis found some modes, which look similar to the EFD modes, these FD modes had insignificant acoustic amplitude. On the other hand, the EFD analysis of the unstable experimental data shows large acoustic mode amplitudes at 170 Hz and 258 Hz. We were also able to use the EFD mode data and the Rayleigh index/integral concept to show that the 170 Hz mode was, in fact, a CI, while the other analyzed modes were not.

CHAPTER VII

CONCLUSION

The objective of this work was to develop methods that can improve our understanding of the underlying physical processes involved in the mechanisms that drive CIs in LREs. In particular, this work sought to accomplish three goals: (i) to develop a small-scale, optically accessible LRE simulator; (ii) to apply modern, high-speed diagnostic techniques to characterize the reacting flow and acoustic field; (iii) and, to develop approaches to reduce the large quantities of data, extracting key physics involved in the CI driving mechanism. Based on the idea that the CI problem could be characterized by an approximately linear constant coefficient system of equations, the experimental data were analyzed by the DMD method. When the DMD's assumed constant operator approach failed to locate the modes of interest, we developed a new data analysis technique based on the DMD and Floquet theory that assumes that the system is governed by a linear, periodic system of equations. The new periodic analysis technique allowed us to identify a mode corresponding to the observed CI. The remainder of this chapter will summarize the key contributions of this research in more detail and suggests a number of future studies to further the understanding of detrimental CIs.

7.1 Summary of Findings/Accomplishments

The first major contribution of this work was the development of a laboratory-scale combustor that was capable of simulating full-scale like CIs. The facility had to have natural acoustic resonant frequencies that are much lower than typical sub-scale rigs to properly emulate full-scale CIs. In addition, the facility's acoustic field must be oriented transverse to the mean flow direction as is the case in the most destructive LRE instabilities. The rig reproduces transverse acoustic fields with adjustable resonant frequencies as low as 150 Hz. Together with the correct acoustic field and the dynamic pressure measurements, the facility needed to be highly accessible for modern optical diagnostic data collection such as PIV, OH-PLIF, and CH^*-chemiluminescence to characterize the reaction zone dynamics. With this newly developed facility, a natural (unforced) CI was excited

at the relatively low frequency of 170 Hz, corresponding to a large full-scale engine. While this instability was occurring, we acquired simultaneous 10 kHz diagnostic data.

The second major contribution of this work was the development of a consistent approach to analyze the simultaneously acquired diagnostic data. This data analysis technique needed to be capable of reducing the large volume of diagnostic data into a small number of fundamental modes, which can then be interpreted by the user. Furthermore, based on model CI problems and the ability to rewrite these problems as a linear system of equations, we selected the DMD to process the experimental data. To accomplish the analysis goals, we took the data corresponding to each diagnostic measure at each time and combined the data into a larger composite vector or snapshot that became the input into the DMD algorithm (the SDD method). The increased quantity of descriptive data used in the analysis improves the quality of the approximated eigenvalues of the governing system. For each approximate eigenvalue, the associated approximate eigenvectors from the DMD can be separated into components, corresponding to the input diagnostic measurements, allowing us to plot, e.g., the PLIF component of the calculated dynamic mode.

We applied the SDD method to the PIV and PLIF data. The resulting modes showed that the reaction zone oscillations were closely coupled with the inner shear layer hydrodynamic oscillations. In addition, by comparing the stable and unstable experiment datasets, it was found that the combustion/hydrodynamics were not substantially changed by the CI.

Next, we applied the SDD method to the simultaneously acquired PIV, PLIF, chemiluminescence, and dynamic pressure data from the unstable experiment. In this case, the analysis showed that the data was dominated by a nearly neutrally stable mode, with large acoustic amplitude, at 1017 Hz. Not only was the acoustic amplitude high, but the PIV, PLIF, and chemiluminescence components of the mode suggested the presence of an annular or a helical hydrodynamic structure. By using the CH^*-chemiluminescence as an approximation to the heat release and the Rayleigh criterion, we were able to determine that this mode was stable with respect to CIs. We believe that this mode, whose frequency is near the 7 W natural acoustic mode for this configuration, is driven by the high-speed fluid flow. On the contrary, the SDD analysis was unable to locate the acoustically observed, apparent CI near 170 Hz. This observation led us to hypothesize that the governing physics were not well described by a constant evolution operator, as prescribed by the DMD method. Physically, our results

suggest that the often assumed—and sometimes successful—constant relationship between heat release and either p' or u' is unrealistic in some combustors.

The third major contribution of this work came when we relaxed the DMD requirement that the unknown, governing evolution operator be constant with respect to time. Rather, we developed a new approach for analyzing data in which we allowed the operator to be periodic in time. By combining the theory for periodic, linear systems of equations, the Floquet theory, with mathematical manipulations paralleling those of the DMD, we were able to develop a technique to approximate, from experimental data, the largest moduli Floquet multipliers. The Floquet multipliers play a similar role to that of the eigenvalues in linear, constant coefficient systems, in that the multipliers determine the stability of the periodic solution trajectories of the system. This new technique, the FD method, requires an estimation of the time period of the governing system of equations. We outlined several techniques to estimate the period. Specifically, for our experiments, we believe that the correct time period is approximately 1 ms. The FD method and estimated period was used to process the data from the unstable experiment. Much like the results from the SDD analysis, the FD analysis was unable to locate any modes near the 170 Hz observed CI with large acoustic amplitudes. This led us to further develop an ensemble average version of the time-periodic operator analysis technique, which we have called the EFD method. This method combines the sampled data from different phases within the operator's period into large composite data vectors to improve its ability to estimate the system's stability and frequencies. Next, the EFD analysis proceeds similarly to the FD analysis to calculate the largest moduli approximate Floquet multipliers and their associated modes. Then, from each composite mode, the differently phased components are separated and shifted to correct for their different initial phases. Finally, the EFD analysis takes the time-average of the phase corrected components to yield improved spatial mode structures.

The EFD method was used to analyze the unstable experiment dataset. Interestingly, we found a nearly neutrally stable/Lyapunov stable mode with a frequency of 169.6 Hz, which also had a large acoustic amplitude. Furthermore, again approximating the heat release by the intensity of the CH^*-chemiluminescence, the Rayleigh criterion indicated that this mode was driven by the oscillatory combustion process.

Taken together, an unstable combustion mode at 170 Hz shown in Section 6.2.2 with the operator's periodic frequency near 1000 Hz, we believe that the 1017 Hz mode shown in Section 4.3.3 parametrically forces the 170 Hz mode. Given these results, we might call these coupled modes a parametric CI. Furthermore, we believe that this type of CI occurs in full-scale LREs and with the techniques developed within this thesis and related future work we might be able to remedy previously unexplained CIs and prevent CIs in new designs.

7.2 Recommendations for Future Work

7.2.1 Improved Simultaneously Acquired Datasets

Confined swirling flows are notoriously complex and the system in this study is no different. The 169.6 Hz unstable mode appears to be related to vortical structures, perhaps a helical vortex pair, interacting with the downstream wall and exhaust nozzles with a transverse natural acoustic mode. But, to verify that these physical phenomena are responsible for the instability, we will require more information. To properly elucidate the mode of interest, we need information about the full 3-dimensional flow field. Ideally, the system should be studied with volumetric PIV, which is likely unrealistic with current capabilities, but may be obtainable soon. In the mean time, we recommend that data be taken under similar conditions as used in this study employing an improved particle seeder, window anti-fogging system, and stereoscopic PIV, along with PLIF, chemiluminescence, and dynamic pressure measurements. While stereoscopic PIV is still a planar measurement, it does resolve all three velocity components on that plane. Similarly, we recommend that the planar diagnostics also be applied to planes perpendicular to the injector axis. These measurements would allow for more insight into the vortical structures as they precess around the axis and potentially explain how the 1017 Hz mode parametrically drives the 169.6 Hz mode.

7.2.2 Analysis Technique Verification and Improvement

Towards further validation and improvement of the FD/EFD methods, we suggest that data be taken at higher acquisition rates and, rather than scaling data by its data type alone, that a point-by-point data scaling technique be developed. The higher acquisition rate data would allow for more flexibility in the testing of the EFD algorithm. Specifically, with a 10 kHz sampling rate and a governing time period of 1 ms, there are 10 data points taken during a period. In this work, the sampling rate and

period led us to use all 10 possible *ensembles* in the analysis to improve the EFD results. If data were available at a much higher rate, the number of ensembles and chosen time period could be studied independently. For example, if 20 kHz data was available, we could retain 10 ensembles, but we could test analysis periods as low as 0.5 ms. Also in the present work, different scale factors have been applied to the different diagnostic method types, but within one type of data, say OH-PLIF, all of the data was scaled by the same factor. This is a good approach if all of the data of a specific type is of equal quality, which may be the case for the PLIF data. On the other hand, there are regions of the PIV data where the reported velocities are of better or worse quality. Ideally, we would like to analyze all of the data, but place less emphasis on data that is believed to be of low quality. This goal could be accomplished withing the SDD framework by applying point-by-point data scaling proportional to the estimated data quality. The resulting analyses should improve the approximation to the system's eigenvalues or Floquet multipliers.

7.2.3 Predictive Models for Parametric Combustion Instabilities

Having identified an experimentally observed CI as a parametric instability, new models are needed to predict their behavior and see how they are affected by the engine design.

An example of a typical CI model was given in Eq. (114) and is repeated here for reference:

$$\frac{\partial}{\partial x}\left(c^2\frac{\partial p'}{\partial x}\right) - \frac{\partial^2 p'}{\partial t^2} = N_u\frac{\partial p'}{\partial x}. \tag{179}$$

Again, expanding in a Galerkin mode expansion and assuming that N_u is harmonic in time, then Eq. (179) may be written as Eq. (126), which is also repeated here for reference:

$$\ddot{\boldsymbol{a}} + \left(M^{-1}K + \epsilon\cos\left(\hat{\omega}t\right)M^{-1}G\right)\boldsymbol{a} = 0. \tag{180}$$

A very simple parametric CI model could be completed by specifying the geometry, local speed of sound, and boundary conditions to calculate the Galerkin modes, ϕ_i, and, thus, K, M, and G, and the parametric frequency and amplitude, $\hat{\omega}$ and ϵ, respectively. In spite of the simple form of this model, the issue is correctly specifying $\hat{\omega}$ and ϵ. To overcome this issue and create improved models, we recommend that the coupled hydrodynamic/combustion/acoustic system be viewed as two coupled subsystems. One subsystem should be the combined hydrodynamic and combustion dynamics due to

their close relationship—as demonstrated in this work. The other subsystem would naturally be the acoustics.

As we showed for Eq. (174), two or more coupled subsystems can exhibit parametric instabilities. Equation (174) is repeated here for reference:

$$\begin{cases} \ddot{u}_1 + [\kappa + \epsilon u_2]\, u_1 + \epsilon\alpha u_1^3 = 0 \\ \ddot{u}_2 + u_2 = \frac{1}{2}\epsilon u_1^2 \end{cases} . \tag{181}$$

Using Eq. (181) as an example of the form of the coupled subsystems that are responsible for the observed CI, we might expect a model of the system to take the form:

$$\begin{cases} \ddot{\boldsymbol{a}} + \left(M^{-1}K + f(u_h')M^{-1}G\right)\boldsymbol{a} + \mathcal{N}(\boldsymbol{a}) = 0 \\ \ddot{u}_h' + \kappa u_h' = g(p') \end{cases} , \tag{182}$$

where the second equation in Eq. (182) represents the governing equations for the hydrodynamic/combustion subsystem, u_h' is some characteristic hydrodynamic velocity, κ is the hydrodynamic subsystem frequency or wavenumber, $\mathcal{N}(\boldsymbol{a})$ is the acoustic system nonlinearity (e.g., nonlinear acoustic damping), and $f(u_h')$ and $g(p')$ are the unknown coupling functions between the two subsystems. At this point we cannot speculate on the functional forms of the coupling functions. On the other hand, once they have been identified, this system could be analyzed by advanced techniques for dynamical systems of equations. One such technique is the continuation method, which allows for the identification of different parametric solution regions and branch/bifurcation point types. This information could yield deep understanding of the system's physics and the system's dependence on operational/design parameters.

APPENDIX A

COMPARISON OF THE FOURIER TRANSFORM, PROPER ORTHOGONAL DECOMPOSITION, AND DYNAMIC MODE DECOMPOSITION

The DMD method is conceptually similar to two widely used data analysis techniques: the Fourier decomposition [77] and the proper orthogonal decomposition (POD) [78]. These three methods are compared in Fig. 84. In this discussion the input to each method is a set of data that represents numerical or experimental observations at multiple locations and evenly spaced time intervals; the desired output is the *reconstructed* data from the decomposition and as much spatial/temporal information about the system as is possible.

The Fourier based techniques, see Fig. 84a, rely on projection of the original data into a series of spatially orthogonal functions/vectors, i.e., *Fourier modes*, that are determined from the system geometry and boundary conditions. In other words, the modes must be known before the decomposition is performed. Common Fourier modes for rectangular and cylindrical geometries take the form of trigonometric and Bessel functions, respectively. The Fourier decomposition is performed by *projecting* the original data, at each time step, into these predetermined modes to find the time varying modal coefficients, e.g. in one spatial dimension:

$$\boldsymbol{c}_n(t_k) = \frac{1}{2\pi}\int_{-\pi}^{\pi} f(x,t_k)e^{-inx}\,\mathrm{d}x, \tag{183}$$

where $f(x,t_k)$ and $\boldsymbol{c}_n(t_k)$ are the original data and the n^{th} Fourier coefficient, respectively, at time step t_k. The original data at each time step can be *reconstructed* (or *synthesized*) by taking the sum of the coefficient-weighted modes, at least in an approximate sense:

$$\tilde{f}(x,t_k) = \sum_{n=-\infty}^{\infty} \boldsymbol{c}_n(t_k)e^{inx}. \tag{184}$$

If we performed a spatial Fourier mode decomposition in this way, each time step can be thought of as independent/uncoupled because the modal coefficients at any time step do not depend on data from any other time step. In other words, this approach does not directly incorporate any temporal features, so the dynamical information from the Fourier decomposition is held within the time varying

coefficients $\boldsymbol{c}_n(t_k)$. To extract dynamical information from these coefficients a secondary analysis must be performed; typically, the time history of the coefficients are plotted to see how the modal content changes with time and the time histories are processed with the fast Fourier transform (FFT) to see their spectral content. It should be noted that with this approach it is difficult to quantify the rate at which an oscillatory mode is growing or decaying, i.e., only the frequency and phase are found and not the growth or decay coefficient. Further, these FFT based methods assume the time history data is periodic, which is not the case in many situations.

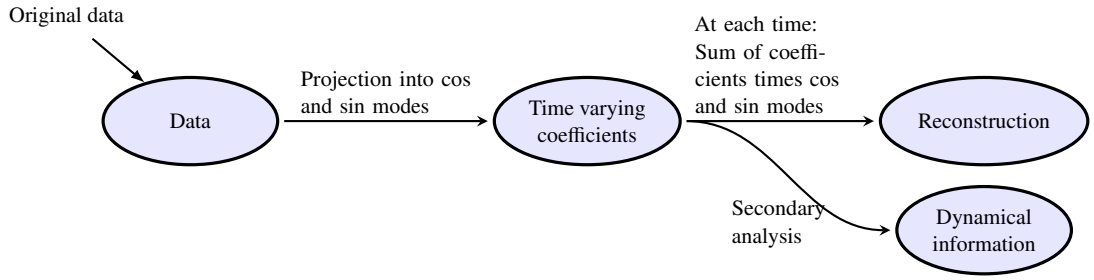

(a) Fourier series

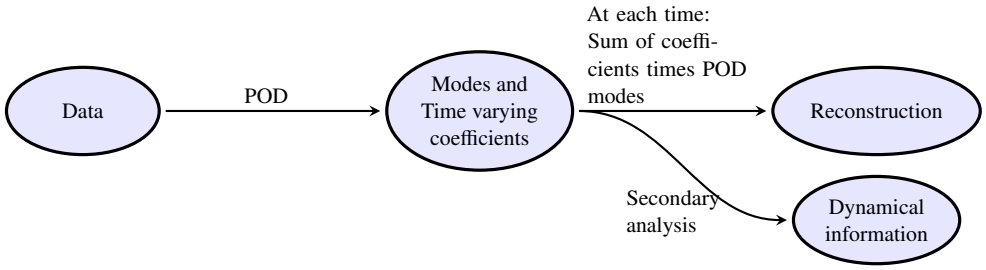

(b) POD

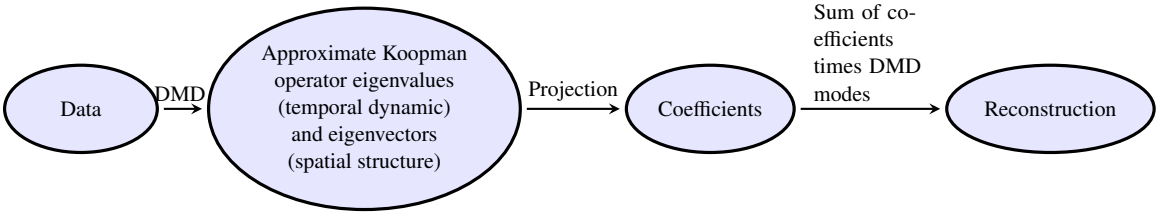

(c) DMD

Figure 84: Data processing/reduction concepts

It may be difficult or impossible to construct the Fourier modes in many situations, e.g., in complex geometries such as those commonly found in experiments, thus restricting the practical usefulness of the Fourier based method. One method that addresses this issue is the POD, see Fig. 84b, which still bears many similarities to the Fourier decomposition approach, including the

projection of the data into a set of orthogonal modes to find time varying modal coefficients and data reconstruction via a weighted sum of the modes. The major conceptual difference is that in the POD method, the orthogonal modes are not known *a priori*, rather, the modes are determined as part of the analysis. The modes may be found by a number of techniques, but they all essentially build a series of orthogonal modes that maximize the variance that each successive mode accounts for, in a least squares sense. Again, like the Fourier decomposition, the POD method does not explicitly include the temporal dynamics, thus the POD shares the coefficient post processing steps with the Fourier based approach.

As in the POD method, the DMD modes are determined from the input data rather than beforehand, thus yielding many of the advantages of the POD method, but additionally the DMD method makes available new information about the temporal dynamics. This dynamical information is contained in a linear, potentially infinite dimensional, operator that represents the governing physics of the system. This operator transforms measurements from the system at any time to the repeated measurements at the next time step and thus the evolution of the system is governed by the eigenvalues of this operator. Through a series of linear algebra based steps the DMD method allows for a data-centric algorithm to extract approximations to some of these eigenvalues and associated eigenvectors, which represent the temporal and spatial character of the DMD mode, respectively. Hence, the DMD method allows us to extract spatial/temporal behavior of the system without requiring knowledge of the system's governing equations. Because of its ability to extract the coherent spatial/temporal behavior from complex geometrical domains based on measurements only, we use the DMD method rather that the more common POD and Fourier based techniques for our data analysis.

APPENDIX B

INJECTOR DEVELOPMENT

The injector designed and used in this study is similar to bi-propellant swirl injectors, which have a long heritage in Russian LRE but are relatively new in American engines [79]. Examples of these bi-propellant injectors may be found in Woodward et al., see Fig. 85, and Rubinsky [79, 80].

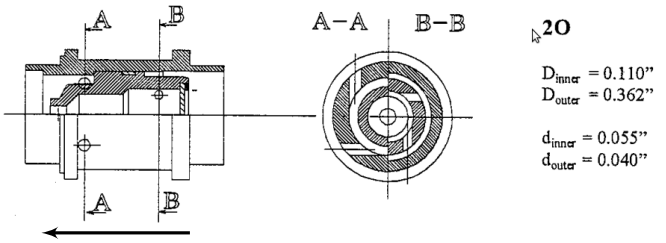

Figure 85: Bi-propellant swirl injector concept [79]

While similar in concept to a bi-propellant injector, more flexibility was desired for a research facility, such as easily adjustable swirl. Essentially, the typical bi-propellant design was modified by using both propellant paths (previously fuel and oxidizer) instead for two paths of gaseous oxidizer. Then, the fuel was introduced through a new annular gaseous fuel supply that was located between the two oxidizer paths, see Fig. 86. Therefore, the developed injector is essentially a gas-gas-gas co-axial injector where the fuel is introduced between two swirling oxidizer flows. This leads to fast mixing and a compact combustion zone, allowing for the rig height, i.e., the distance from the injector to the exhaust ports, to be relatively short. The oxidizer swirl was introduced via two tangential swirlers, each with four orifices, one for the outer path and one for the inner path. The orifices sizes, supply pressure, and mass flow rates were chosen to chock the flow though each orifice. This chocking prevents mass flow rate oscillations due to pressure fluctuations in the combustion chamber. This type of mass flow oscillation, *injector coupling*, is known to drive CI [12] and, hence, must be avoided to allow the study other driving mechanisms. Note that each swirler is symmetric relative to the orifices and may, thus, be flipped end for end during the assembly process. This allows us to

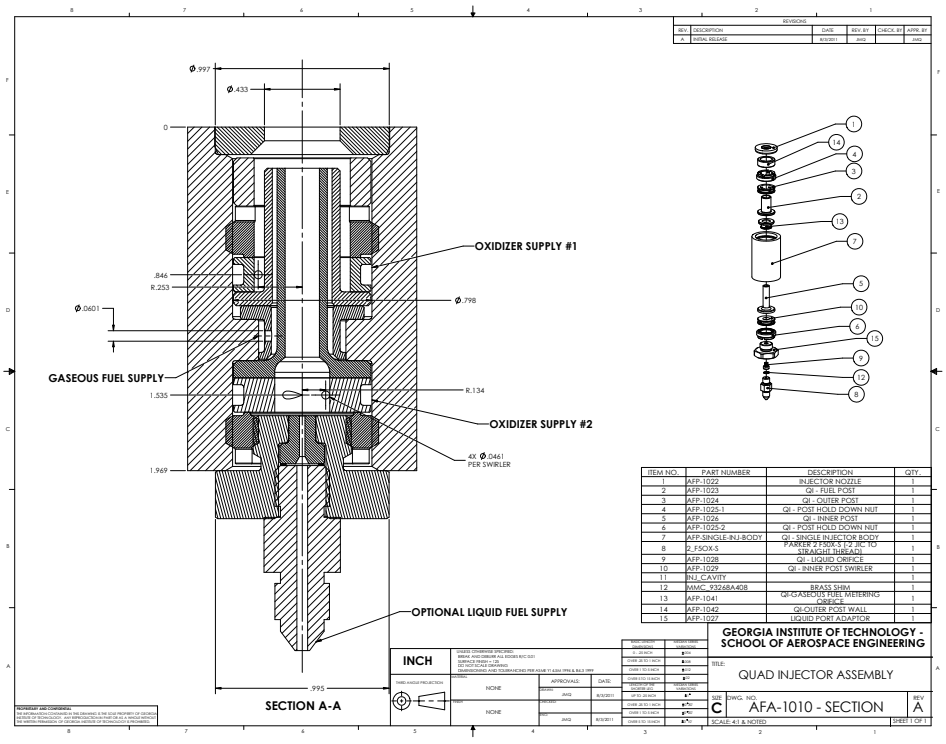

Figure 86: Adjustable swirl injector design

reverse the direction of the swirl to obtain both co-swirl and counter-swirl configurations. In all tests presented here, the counter-swirl arrangement was employed. Additionally, the split of mass flow rates through the two oxidizer paths is controllable. This allows for the adjustment of the reaction zone shape and total swirl because of the unequal geometric swirl number of the two paths.

Specifically, defining the geometric swirl number as [81]:

$$S_g \equiv \frac{\pi r_0 r_\theta}{A_\theta} \left(\frac{\dot{m}_\theta}{\dot{m}_\theta + \dot{m}_z} \right)^2, \tag{185}$$

where r_0, r_θ, A_θ, $\dot{m}_\theta$, and $\dot{m}_z$ are the radius of the injector exit, the radius of the tangential orifice centerlines from the injector axis, the total area of the tangential orifices, the mass injected tangential, and the mass injected axially, respectively. Since, this injector does not use axial injection, the geometric swirl number for each swirl path reduces to:

$$S_g = \frac{\pi r_0 r_\theta}{A_\theta}. \tag{186}$$

Using Eq. (186) and the geometry shown in Fig. 86, the geometric swirl numbers were calculated to be 13.7 and −25.8 for the inner and out swirl paths, respectively. The negative sign for the outer path

indicates that the swirl is in the counter-clockwise direction when viewing the injector from the exit, towards the swirler generators. The dimensions used to calculate the geometric swirl numbers are listed in Table 17.

Table 17: Geometric swirl number and required dimension for the inner and outer swirl paths of injector

	Inner path	Outer path
r_0 [in]	0.217	0.217
r_θ [in]	0.134	0.253
A_θ [in^2]	6.676×10^{-3}	6.676×10^{-3}
S_g [-]	13.68	−25.83

While the gaseous fuel supply system is not chocked, its annular supply area is small and its length long to create a relatively high resistance and pressure drop, thus limiting detrimental mass flow oscillations. It is also worth noting that the developed injector has an optional liquid fuel supply port and orifice that allows the injection of liquid fuel into the inner oxidizer swirl chamber. Finally, the injector was designed utilizing metal to metal seals to allow for a wide range of reactant supply temperatures.

APPENDIX C

MODERN DIAGNOSTIC TECHNIQUES

A combustor that is highly accessible for diagnostics has been presented in Section 2.1. In this section, the specific diagnostics applied to this combustor will be reviewed conceptually and details of the equipment utilized will be given.

C.1 Dynamic pressure

To measure the pressure fluctuations that are important to the CI coupling, a total of six piezoelectric dynamic pressure sensors, Kistler 211B5, were used. Four of the sensors are located along the length of the sensing section and the remaining two sensors are located in standoff tubes attached to the combustion chamber. These standoffs tubes are ø6.35 mm and approximately 85 mm in length. The duct cutoff frequency varies along the length of the transverse duct due to temperature variations. But, in the sensing section it is near 2400 Hz and thus any waves that are not traveling in the duct in a one dimensional fashion, below this frequency, are evanescent and decay exponentially along the duct's length from the combustor. So, well below the cutoff frequency, by the time the acoustic wave reach the first pressure sensor in the sensing section, the evanescent waves may be assumed completely damped.

The signals from the six sensors are conditioned with Kistler amplifiers, then low-pass filtered with Krohn-Hite 4-pole Butterworth filters with a cutoff frequency of 8 kHz, and digitized via a National Instruments NI cDAQ-9172 rack with an NI 9215 voltage module at a sampling frequency of 20 kHz. Thus aliasing is avoided and for the frequencies of interest, below approximately 2400 Hz, there are at least eight data points per period. For each of the datasets presented here, acoustic data was taken for 3 second, yielding 60000 data points per set. This length data record allows for noise rejecting ensemble averaging techniques to be applied to the signals spectra while maintaining adequate frequency resolution. An example of the pressure measurements and other acquired data is presented in Section 2.3.

C.2 Particle image velocimetry

PIV is a diagnostic technique by which the velocity of fluid may be found in an laser illuminated volume. Typically, this volume takes the form of a *sheet*, which is actually a parallelepiped with one dimension small relative to the the other two[1]. The PIV technique requires the interrogated flow to be *seeded* with some type of particle. The seed particles could be anything from bubbles naturally occurring in the fluid, to smoke particles, to plastic, metal, or ceramic particles specifically added to the flow. For combustion type experiments ceramic particles remain one of the only viable choices, primarily Al_2O_3, SiO_2, and TiO_2. There are competing constraints when selecting the size of the particles. The amount of light scattered from the particle, at least in the range of sizes of interest, is quadratically related to its diameter. On the other hand, the heavier the particle becomes, the less it will follow the flow because the viscous forces may be overcome by the momentum forces. This momentum/viscous trade-off also depends on the density and viscosity of the fluid and density of the seed particle and this trade-off is usually quantified in terms of a Stokes number. For good flow following, the particle Stokes number should be small, this implies the particle should be light and small in size. It is found for many combustion experiments there is an acceptable compromise between illumination and flow following by using ceramic particles with a mean size on the order of $0.1 - 5\,\mu$m. In this work TiO_2 particles with a mean diameter of $1\,\mu$m were used.

In the most widely applied version of the technique, once the flow is seeded, the laser is pulsed twice per cycle with a known separation in time between the laser pulses. An image of the scattered light from the particles is acquired for each of the laser pulses. This pair of images is processed through an algorithm based on cross-correlation to find the spatial movement of the particles. This movement represents the motion of the particles in the illuminated volume projected onto a plane perpendicular to the axis of the camera lens. Hence, for standard two-dimensional PIV effort should be made to position the camera perpendicular to the laser *sheet*. Having determined the planar displacement of regions of the flow, using many particles, the velocity of the fluid may be found approximately using Eq. (187).

$$\boldsymbol{v}_{PIV} = \frac{\Delta \boldsymbol{x}}{\Delta t} \tag{187}$$

[1] Henceforth, the word *sheet* will refer to this high aspect ratio parallelepiped.

The laser used was a high-speed two cavity Litron nd:YLF laser system. Image pairs separated by $\Delta t = 9\,\mu$s, collected at 10 kHz, were acquired through a Semrock FF01-527/20-72-1 filter and Nikkor Macro 55 mm F2.8 lens with F stop set to F8. The high-speed camera used was a Photron FASTCAM SA1.1.

C.3 Planar laser induced fluorescence

PLIF is the thin *sheet*, as discussed previously, version of a broader class of technique known as laser induced fluorescence (LIF). LIF based approaches rely on molecules absorbing and emitting light on the quantum mechanical level. The first step of this process is the stimulated absorption of a specifically tuned photon by a molecule to a well defined excited state. Due to equilibrium arguments, the molecule will not stay in this excited state. The deactivation occurs though the process of spontaneous emission of a photon, in other words, fluorescence [82]. This photon is the light that will be collected by optics, intensified, and read by a digital sensor.

This technique is not applicable to arbitrary molecules, actually there are very few species found in combustion devices that can be imaged via PLIF. Some common combustion species that PLIF has been applied to are: hydroxyl (OH), methylidyne (CH), nitric oxide (NO), formaldehyde (CH_2O), and acetone ($(CH_3)_2CO$). Here OH-PLIF will be employed to highlight the region of active combustion, as the OH radical is created in the reaction zone and has a relatively short lifetime. The OH excitation laser was an ultraviolet beam tuned to a wavelength of approximately 283.95 nm, pulsed at 10 kHz. This laser was generated by a frequency doubled Sirha Credo dye laser. The dye laser was pumped by a 532 nm wavelength, 42 W, Edgewave IS series slab diode laser. The ultraviolet beam had a total power approximately 2.1 W and the sheet width and thickness were approximately 60 mm and 1 mm respectively.

Images were collected, at 10 kHz, with a NAC GX3 high-speed camera using a Lambert Instrument HiCatt intensifier with a 160 ns open gate. A quartz 45 mm F1.8 LaVision VZ-UV-Objective lens, with a LaVision ‘Vz-Image Filter LIF for OH, Enhanced’ filter was employed at F1.8. To reduce noise and the data size, a sliding minimum was used for background subtraction, a 9 by 9 median filter applied, then each 4 by 4 pixel region was binned into a super-pixel.

C.4 Chemiluminescence

Similarly to PLIF, chemiluminescence is sensed by a spontaneous emitted photon being collected by a lens, intensified, and converted to a digital signal via a camera. The key difference is how the molecule becomes electronically excited. LIF processes require a preexisting molecule to undergo stimulated absorption of energy from a laser source to become excited. While in chemiluminescence, the excited molecule is a product of a chemical reaction. Again like PLIF, few species are viable for detection via chemiluminescence. The main species that exhibit chemiluminescence in typical hydrocarbon based systems are CH^*, OH^*, and C_2^*, and there is some broadband emission from H_2O and CO_2. Here the focus will be on the emission from the CH^* radical, which has a wavelength centered around 431 nm. As shown by Hall et al., the chemical reactions in Eq. (188) are important in the formation of the CH^* species [83].

$$\begin{aligned} C_2H + O &\rightleftharpoons CH^* + CO \\ C_2 + OH &\rightleftharpoons CH^* + CO \end{aligned} \tag{188}$$

The last, and very important, difference between PLIF and chemiluminescence is that the former is a sheet based technique, collecting essentially two dimensional information, while the latter collects signal from the entire thickness of the reaction zone. Thus, chemiluminescence images represent a line-of-sight integrated signal. Often, the line-of-sight property has been viewed as a disadvantage; although, the recent work by Moeck et al. has used this property to their advantage, at least for a nearly axisymmetric flame, by applying tomographic concepts with a single camera [84].

For the experiments performed during this research, CH^* emissions from the rig have been filtered with a CVI F10 430, bandpass filter centered at 430 nm with a FWHM = 10 ± 2 nm, then collected through a Nikon Nikkor 50 mm F1.4 lens used at F1.4, intensified by a LaVision High-Speed IRO with a gate open time of 90 μs, and digitized by a Photron FASTCAM SA3 high-speed camera. Data was collected at 10 kHz. As an aside, this filter has a transmission of 25% in the bandpass; this is quite poor when compared to available interference filters with similar band location and widths.

C.5 Simultaneous high-speed PIV, OH-PLIF, CH^*-chemiluminescence, and acoustic measurements

To ensure the data from each diagnostic system was recorded at the proper time, *simultaneous*, each system had to be triggered properly. Note, the word *simultaneous* must be interpreted carefully as each diagnostic has a different acquisition time, e.g., the Δt between the PIV image pair or the chemiluminescence exposure/gate time. To begin recording, a master TTL trigger is sent to a dual channel signal generator Tektronix AFG 3022. Next, this signal generator output two TTL start signals, the first to the PIV High-Speed Controller, the National Instruments data acquisition system, and the dSPACE system that controls the experiment and the second to the PLIF High-Speed Controller. The PLIF start trigger was delayed to place its Q-switch directly between the pair of Q-switch signals for the two cavities of the PIV laser. The proper delay was found to be $36\,\mu$s. The chemiluminescence gate opening was synchronized with the gate opening of the PLIF system.

APPENDIX D

STUDY OF NONLINEAR SYSTEMS USING THE DYNAMIC MODE DECOMPOSITION

There is an obvious need to develop DMD like methods to analyze nonlinear systems. The DMD method assumes that the system is well represented by a constant linear operator, A in Eq. (55), but in reality many system are nonlinear and, typically, when measurements from these nonlinear systems are taken they are exhibiting limit cycle like behavior. To improve our understanding of nonlinear systems a different approach is needed. In this appendix we discuss a new technique for studying nonlinear systems with the DMD/SDD method.

The DMD algorithm approximates a nonlinear system by a linear/tangent approximation. Furthermore, it is well established that Krylov subspace methods—like the DMD—can approximate the largest magnitude eigenvalue well from a very short sequence. These two points suggest we try to use the DMD algorithm to approximate the largest eigenvalue (and potentially others) of the nonlinear operator. To make this approximation we apply the DMD algorithm to a short sequence of measurements, $\widetilde{V}$, e.g., $\widetilde{V} = V_{1:20}$. The resulting largest Ritz value, λ_{10}, from the DMD method forms a linear/tangent approximation to the nonlinear system over the time sequence, so it can be thought of as the tangent approximation at the sequence midpoint, here step 10. Shifting the data used by one time step later we can approximate λ_{11}. By continuing this process we can build a time history of the approximate eigenvalue, which can be thought of as an approximation to the continuously varying true eigenvalue of the nonlinear system. In other words, we can estimate the largest magnitude nonlinear eigenvalue of the governing equation as a function of time as:

$$\begin{array}{ccccccc} V_{1:20} & \rightarrow & \widetilde{V} & \rightarrow & DMD & \rightarrow & \lambda_{10} \\ V_{2:21} & \rightarrow & \widetilde{V} & \rightarrow & DMD & \rightarrow & \lambda_{11} \\ & & \vdots & & & & \end{array} \tag{189}$$

To demonstrate the concept, we will present two simple example problems, each of which exhibits nonlinear system behavior. The first example is a single spring-mass-damper system that has

what is known as a strain-hardening spring and as a result the angular frequency during a cycle is not constant. The second example is a single van der Pol oscillator. In this case the frequency remains nearly constant over the cycle, but the system is self excited by the *damping* term and therefor the real part of the eigenvalue varies with time.

D.1 Strain-Hardening Spring Example

The first example to which we will apply the sequential DMD algorithm to short sections of measurements, which we will refer to as the nonlinear eigenvalue estimation (NEE), is a simple single degree of freedom spring-mass-damper system where the spring stiffens nonlinearly as the displacement increases. Specifically, we have chosen to examine a case where the spring is linear asymptoticly as the displacement goes to zero and is cubic for large displacements. The mass specific governing equation is:

$$\ddot{u} + 2\zeta\dot{u} + \kappa\left(u + \beta u^3\right) = 0, \tag{190}$$

where u is the displacement of the mass from equilibrium, $\dot{}$ represents differentiation with respect to time, ζ is the mass specific damping coefficient (decay coefficient), κ is the mass specific stiffness coefficient, and β is the mass specific spring strain-hardening coefficient.

We may write this system in state space as:

$$\dot{\boldsymbol{x}} = \begin{bmatrix} 0 & 1 \\ -\kappa\left(1 + \beta x_1^2\right) & -2\zeta \end{bmatrix} \boldsymbol{x}, \tag{191}$$

where $\boldsymbol{x} = \{u \quad \dot{u}\}^T$.

The eigenvalues of this system are:

$$\lambda_{12} = -\zeta \pm \sqrt{\zeta^2 - \kappa\left(1 + \beta x_1^2\right)}. \tag{192}$$

Assuming the damping is small, the eigenvalues form a complex conjugate pair with a small real part that represents the exponential growth/decay coefficient and an oscillator imaginary part, which is equal to the damped natural frequency when the displacement is zero and increases as the amplitude of the displacement increases.

We have run a numerical simulation with $k = m = 1$, $c = 0.1$, $\beta = 1$, and time step of 0.01 and used the calculated displacements and velocities as input into our NEE approach. Specifically, we ran

the DMD algorithm on a sequence of these data from the first time step to the 20^{th} time step, forming the first approximation of the nonlinear eigenvalue at the 10^{th} time step (tangent approximation at the center of our window). The second approximation is obtained by analyzing the 2^{nd} to the 21^{st} time step data and so on. We call this the NEE method of order 20, i.e., the number of time steps over which the nonlinear system is approximated by a linear operator. We will study the effects of including noise in the measurements and so the DMD algorithm employed included the noise reducing technique where both Krylov sequences in Eq. (59) are approximated with the SVD, keeping only the 10 largest singular values.

Recall that the NEE method is rigorously applicable to only the largest eigenvalue, but since the two eigenvalues of the operator in Eq. (191) are complex conjugate pairs we can examine either one as they are both *largest* in magnitude. Note, when we say largest we are referring to the largest DMD Ritz value μ, what we might call the logarithmic form of the eigenvalue/Ritz value, not the converted time-stepping eigenvalue form from Eq. (88), λ. Although, typically we will plot and discuss the results in the latter form.

The results of the NEE method and the positive frequency exact eigenvalue are plotted in Fig. 87. The first plot, Fig. 87a shows the real part of the Ritz value or eigenvalue, i.e., the growth rate. The real part of the exact eigenvalue is simply a constant, $-\zeta = -0.1$, while the NEE method predicts an oscillator value. It is not clear yet why the NEE method does a poor job with this prediction, but at this point we conjecture that the linear contribution varies, but is balanced by a higher-order term, yielding a constant value. In fact, in this case the more standard DMD approach, taking a single longer dataset, would yield a better result.

The NEE method proves to be much more useful in predicting the imaginary part of the eigenvalue for this case. Figure 87b shows the imaginary part—the real angular frequency of the system—of the exact eigenvalue and the NEE tangent approximation. At each time where the displacement is zero the true angular frequencies drops to the damped natural frequency of the linear system, here 0.99499 rad/s. As the displacement becomes large, in either the positive or negative direction, the spring becomes stiffer, raising the natural frequency of the system proportionally to the strain hardening coefficient, β. Turning to the NEE approximation, the method appears to capture much of the dynamics of the changing angular frequency. In fact, it appears to correctly predict the value

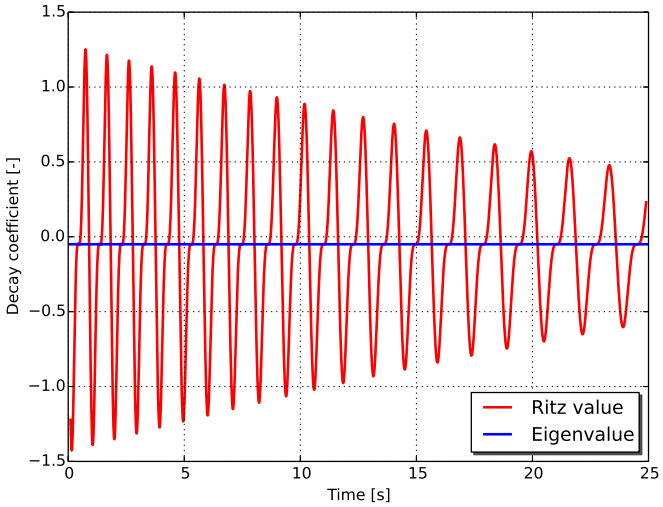

(a) Growth rate

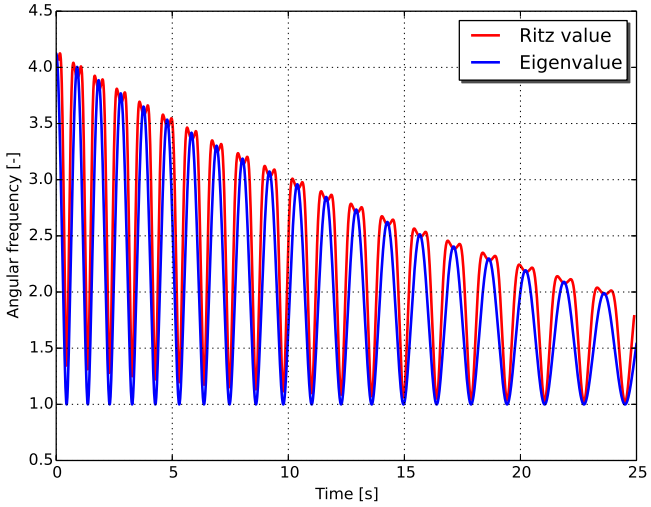

(b) Angular frequencies

Figure 87: Exact eigenvalue and NEE calculated Ritz values

when the displacement is at a local extremum, consequently where the derivative of the eigenvalue with respect to time is zero. We are making an linear approximation to the system and intuitively the approximation should work well near these points, where the neglected higher-order terms are zero or small.

We repeated this analysis adding Gaussian noise to the displacement and velocity measurements of peak-to-peak amplitude of 0.01 m and 0.01 m/s, respectively. The real and imaginary parts of the exact eigenvalue and NEE approximated Ritz value for this *noisy* case are shown in Fig. 88. The plots

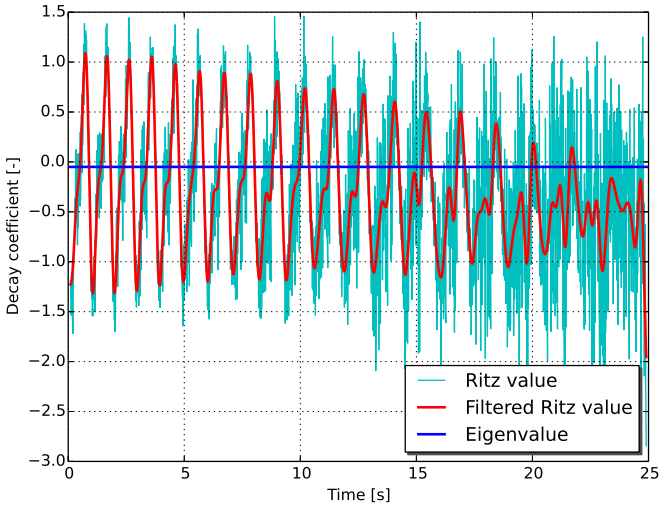

(a) Short DMD decay coefficients

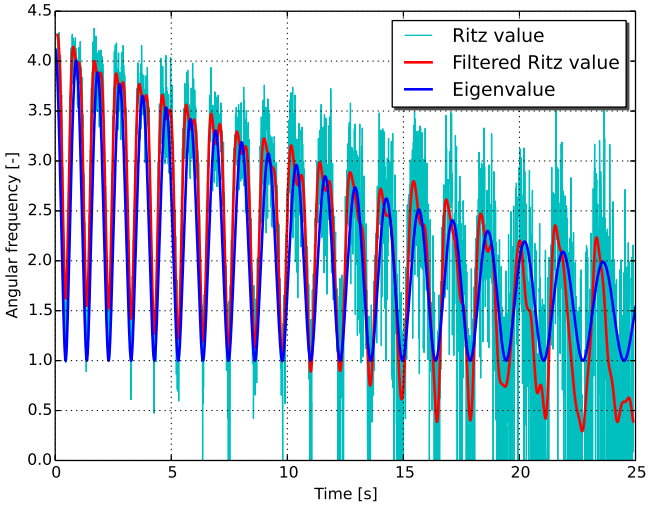

(b) Short DMD angular frequencies

Figure 88: Exact eigenvalue and NEE calculated Ritz values with added Gaussian noise (0.01 peak to peak amplitude)

now have three lines each. The raw NEE predicted values, shown by thin cyan lines, indicate that the noise has substantial influence on the prediction. Due to the fact that we are forming a linear tangent approximation over 20 points, we do not expect to be able to resolve high-frequency oscillations. Furthermore, since we have assumed that the eigenvalues of the nonlinear system change smoothly over time, we may low-pass filter the Ritz value time history without loss of the system's physical behavior. We have low-pass filtered these data via a fourth-order Butterworth filter with a cutoff

frequency of 2.5 Hz (≈ 15.7 rad/s). The filtering appears to improve the results and the process yields plots (thick red lines) that resemble the noise free predictions from Fig. 87. Interestingly, the prediction becomes worse as the magnitude of the oscillations diminish. This is expected from the viewpoint that the added noise is larger with respect to the amplitudes, but the system becomes closer to linear, apparently not improving the methods results.

While the decay coefficient prediction does not represent the true eigenvalue well, it appears that the nonlinear change in frequency over the cycle for a strain-hardening spring system can be predicted from measured data and the NEE method.

D.2 Van der Pol Oscillator

The second example we will analyze is a single degree of freedom van der Pol oscillator. Where the previous example had a cubic stiffness nonlinearity and was damped, this example has a quadratic nonlinearity in the damping term and is perhaps the simplest of self-excited systems. In this case the mass-specific equation governing the system is:

$$\ddot{u} - 2\zeta\left(1 - \beta u^2\right)\dot{u} + \kappa u = 0. \tag{193}$$

This system has a stable limit cycle where both the velocity and displacement amplitudes are equal to two.

In many ways, this example reflects the experimental measurements that we have studied. The systems are both self-excited, meaning that there is an internal feedback mechanism that drives the oscillations, and the systems are oscillating near a limit cycle, so we might expect similar behavior if we perform the NEE method on the measured data from either case.

Writing this system in state space yields:

$$\dot{\boldsymbol{x}} = \begin{bmatrix} 0 & 1 \\ -\kappa & 2\zeta\left(1 - \beta x_1^2\right) \end{bmatrix} \boldsymbol{x}, \tag{194}$$

the eigenvalues of which are:

$$\lambda_{12} = \zeta\left(1 - \beta u^2\right) \pm \sqrt{\zeta^2\left(1 - \beta u^2\right)^2 - \kappa}\,. \tag{195}$$

Much like in the last example, we ran a numerical simulation with $k = m = 1$, $c = 0.1$, $\beta = 1$, and time step of 0.01 and used the calculated displacements and velocities as input into our NEE

approach. Now, β is the damping nonlinearity coefficient, rather that the strain hardening coefficient. The data from the numerical integration became the input into our NEE algorithm, which again used 20 time steps to for a linear tangent approximation to the operator found in Eq. (194) (actually it is the exponential of this operator and then we take the natural log of the eigenvalue). The resulting estimated eigenvalues and the exact eigenvalues are plotted in Fig. 89.

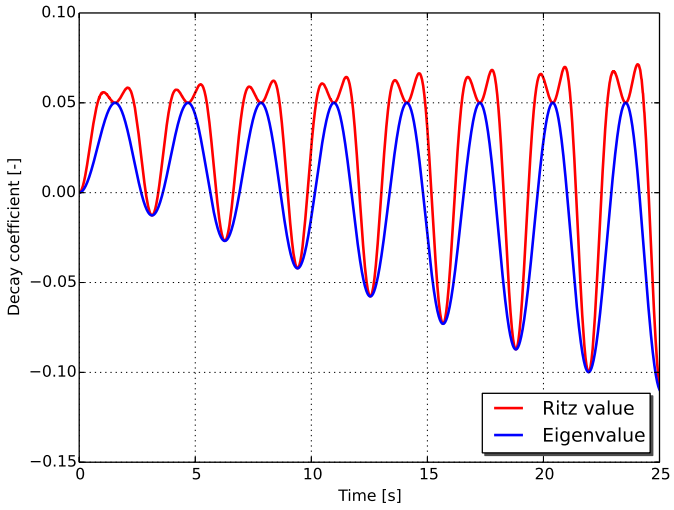

(a) Growth rate

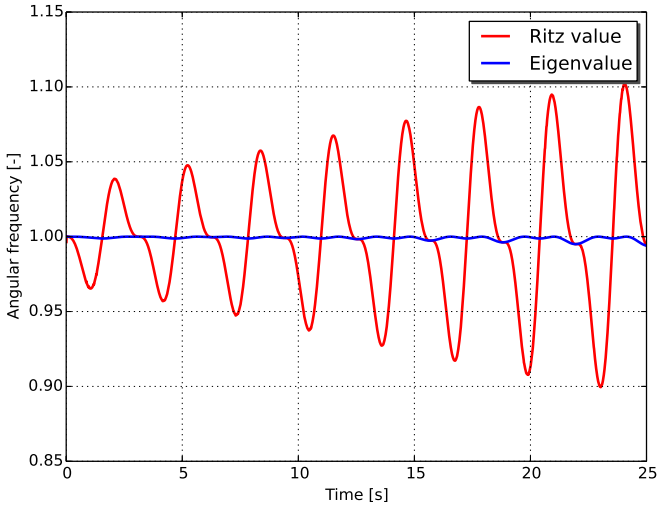

(b) Angular frequencies

Figure 89: Exact eigenvalue and NEE calculated Ritz values

The first plot, Fig. 89a shows the real part of the eigenvalue (Blue) and Ritz value (Red) for the van der Pol oscillator case. We can see how for the chosen initial condition ($u = 1$ and $\dot{u} = 0$) that

the derivative term in Eq. (193) drives the system most of the cycle, causing the amplitude to grow. While near the end of the simulation, there are nearly equal driving and damping portions of the cycle, resulting in the observed approach to limit cycle (it takes infinite time to get to the limit cycle). Also from this plot, we see that the NEE approximates the real part of the exact eigenvalue behavior well, and near where the derivative of the eigenvalue time history is zero, the estimation appears very good. Again, we suspect the portions of the plot where the NEE approximation deviates from the true values is due to contributions from a higher-order term.

The imaginary part of the exact and approximate eigenvalues are plotted in Fig. 89b. From this plot we see the NEE method over predicts the change in angular frequency due to the nonlinearity, but the magnitude of this error is relatively small. The exact eigenvalue is near 1.0 everywhere (the orbit is nearly circular in phase space), while the NEE method predict up to 10% oscillations around 1.0.

Adding noise to the van der Pol oscillator case shows mixed results. Figure 90 shows the resulting predictions when we add 0.002 m and 0.002 m/s peak to peak amplitude Gaussian noise to the displacement and velocity, respectively. Much like the previous example, the raw unfiltered output of the NEE is substantially corrupted by the noise addition and the low-pass filtering improves the results. Although, the filtered results are still lackluster. Examining the details of these plots, we see that the growth/decay coefficient appear to be less effected by noise in this case and both the real and imaginary parts are closer to the noise free case later in the simulation when the relative amplitude of the noise diminishes. Overall this example appears to be more sensitive to the addition of noise. The low-pass filter cutoff frequency was again 2.5 Hz, well above the approximately 0.159 Hz oscillator frequency, so we could lower the cutoff and the NEE algorithm results would likely improve.

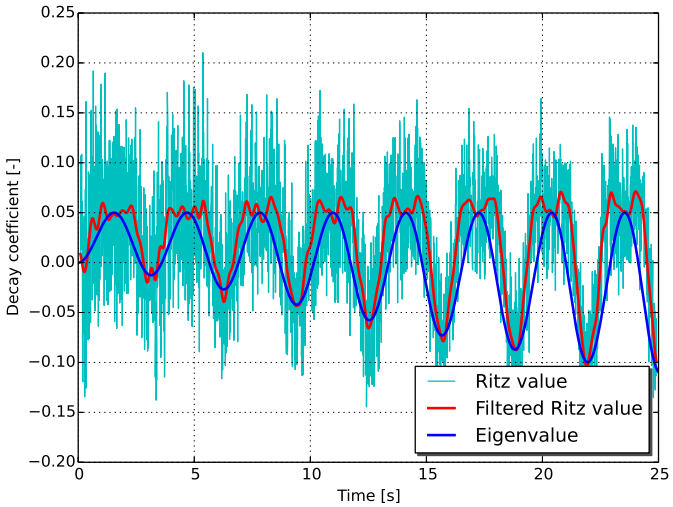

(a) Short DMD decay coefficients

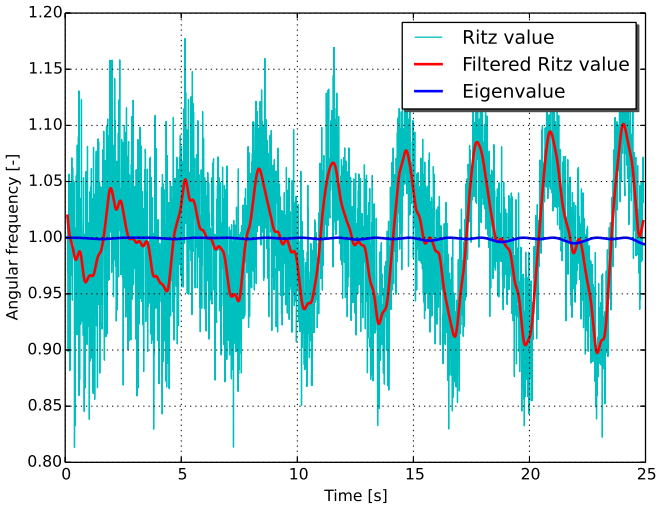

(b) Short DMD angular frequencies

Figure 90: Exact eigenvalue and NEE calculated Ritz values with added Gaussian noise (0.002 peak to peak amplitude)

REFERENCES

[1] Sinha, S. and Butcher, E., "Symbolic computation of fundamental solution matrices for linear time-periodic dynamical systems," *Journal of Sound and Vibration*, vol. 206, no. 1, pp. 61–85, 1997.

[2] Oefelin, J. C. and Yang, V., "Comprehensive review of liquid-propellant combustion instabilities in F-1 engines," *Journal of Propulsion and Power*, vol. 9, no. 5, pp. 657–677, 1993.

[3] Goy, C., James, S., and Rea, S., "Monitoring combustion instabilities: E.ON UK's experience," *Progress in Astronautics and Aeronautics*, vol. 210, pp. 163–175, 2005.

[4] Crocco, L. and Cheng, S.-I., *Theory of combustion instability in liquid propellant rocket motors*. Butterworths Scientific Publications, 1956.

[5] Harrje, D. T. and Reardon, F. H., eds., *Liquid propellant rocket combustion instability. NASA SP-194*, vol. 194. NASA, 1972.

[6] Yang, V. and Anderson, W., eds., *Liquid rocket engine combustion instability*, vol. 169. AIAA, 1995.

[7] Natanzon, M. S., *Combustion instability*, vol. 222. AIAA, 1999.

[8] O'Connor, J., Acharya, V., and Lieuwen, T., "Transverse combustion instabilities: Acoustic, fluid mechanic, and flame processes," *Progress in Energy and Combustion Science*, vol. 49, pp. 1–39, Aug. 2015.

[9] Schmid, P. J., "Dynamic mode decomposition of numerical and experimental data," *Journal of Fluid Mechanics*, vol. 656, pp. 5–28, 2010.

[10] Elam, S., "Subscale LOX/hydrogen testing with a modular chamber and a swirl coaxial injector," in *Joint Propulsion Conferences*, American Institute of Aeronautics and Astronautics, June 1991.

[11] Hulka, J. and Jones, G., "Performance and stability analyses of rocket combustion devices using liquid oxygen/liquid methane propellants," in *Joint Propulsion Conferences*, American Institute of Aeronautics and Astronautics, July 2010.

[12] Hutt, J. J. and Rocker, M., *High-frequency injection-coupled combustion instability*, vol. 169, ch. 12, pp. 345–356. AIAA, 1995.

[13] Schmid, P., Violato, D., and Scarano, F., "Decomposition of time-resolved tomographic PIV," *Experiments in Fluids*, vol. 52, no. 6, pp. 1567–1579, 2012.

[14] Roy, S., Hua, J.-C., Barnhill, W., Gunaratne, G. H., and Gord, J. R., "Deconvolution of reacting-flow dynamics using proper orthogonal and dynamic mode decompositions," *Physical Review E*, vol. 91, no. 1, 2015.

[15] Zinn, B. T. and Powell, E. A., "Nonlinear combustion instability in liquid-propellant rocket engines," in *Symposium (International) on Combustion*, vol. 13, pp. 491–503, Elsevier, 1971.

[16] Culick, F., "Non-linear growth and limiting amplitude of acoustic oscillations in combustion chambers," *Combustion Science and Technology*, vol. 3, no. 1, pp. 1–16, 1971.

[17] Culick, F., "Some recent results for nonlinear acoustics in combustion chambers," *AIAA journal*, vol. 32, no. 1, pp. 146–169, 1994.

[18] Jahnke, C. C. and Culick, F. E., "Application of dynamical systems theory to nonlinear combustion instabilities," *Journal of Propulsion and Power*, vol. 10, no. 4, pp. 508–517, 1994.

[19] Culick, F. E. and Yang, V., "Overview of combustion instabilities in liquid-propellant rocket engines," *Liquid Rocket Engine Combustion Instability*, vol. 169, pp. 3–37, 1995.

[20] Peracchio, A. A. and Proscia, W. M., "Nonlinear heat-release/acoustic model for thermoacoustic instability in lean premixed combustors," *Journal of Engineering for Gas Turbines and Power*, vol. 121, pp. 415–421, July 1999.

[21] Lieuwen, T. C., "Experimental investigation of limit-cycle oscillations in an unstable gas turbine combustor," *Journal of Propulsion and Power*, vol. 18, no. 1, pp. 61–67, 2002.

[22] Culick, F. and Kuentzmann, P., "Unsteady motions in combustion chambers for propulsion systems," tech. rep., DTIC Document, 2006.

[23] Kabiraj, L., Saurabh, A., Wahi, P., and Sujith, R. I., "Route to chaos for combustion instability in ducted laminar premixed flames," *Chaos: An Interdisciplinary Journal of Nonlinear Science*, vol. 22, no. 2, 2012.

[24] Quinlan, J. M. and Zinn, B. T., "Simulating full-scale transverse combustion instabilities in a lab-scale facility," in *Joint Propulsion Conferences*, American Institute of Aeronautics and Astronautics, July 2013.

[25] Reddy, J. N., *An introduction to the finite element method*. McGraw-Hill Higher Education, 2006.

[26] Golub, G. and Reinsch, C., "Singular value decomposition and least squares solutions," *Numerische Mathematik*, vol. 14, no. 5, pp. 403–420, 1970.

[27] Mezić, I., "Analysis of fluid flows via spectral properties of the Koopman operator," *Annual Review of Fluid Mechanics*, vol. 45, no. 1, pp. 357–378, 2013.

[28] Mezić, I., "Spectral properties of dynamical systems, model reduction and decompositions," *Nonlinear Dynamics*, vol. 41, no. 1-3, pp. 309–325, 2005.

[29] Koopman, B. O., "Hamiltonian systems and transformation in Hilbert space," *Proceedings of the National Academy of Sciences*, vol. 17, no. 5, pp. 315–318, 1931.

[30] Rowley, C. W., Mezić, I., Bagheri, S., Schlatter, P., and Henningson, D. S., "Spectral analysis of nonlinear flows," *Journal of Fluid Mechanics*, vol. 641, pp. 115–127, 11 2009.

[31] Saad, Y., *Numerical methods for large eigenvalue problems*, vol. 158. SIAM, 1992.

[32] Watkins, D. S., *The matrix eigenvalue problem: GR and Krylov subspace methods*, vol. 101. Siam, 2007.

[33] Ruhe, A., "Rational Krylov sequence methods for eigenvalue computation," *Linear Algebra and its Applications*, vol. 58, pp. 391–405, 1984.

[34] Duke, D., Soria, J., and Honnery, D., "An error analysis of the dynamic mode decomposition," *Experiments in fluids*, vol. 52, no. 2, pp. 529–542, 2012.

[35] Strang, G., *Introduction to Linear Algebra*. Wellesley Cambridge Press, 2003.

[36] Golub, G. H. and Van Loan, C. F., *Matrix Computations*, vol. 3. Johns Hopkins University Press, 1996.

[37] Eckart, C. and Young, G., "The approximation of one matrix by another of lower rank," *Psychometrika*, vol. 1, no. 3, pp. 211–218, 1936.

[38] Golub, G., Hoffman, A., and Stewart, G., "A generalization of the eckart-young-mirsky matrix approximation theorem," *Linear Algebra and its Applications*, vol. 88/89, pp. 317–327, 1987.

[39] Campbell, S. L. and Meyer, C. D., *Generalized Inverses of Linear Transformations*. Society for Industrial and Applied Mathematics, 2009.

[40] Meirovitch, L., *Fundamentals of Vibrations*. New York: McGraw-Hill Higher Education, 2001.

[41] Hale, J. K., *Ordinary Differential Equations*. Krieger, Malabar, Florida, 1980.

[42] Richecoeur, F., Hakim, L., Renaud, A., and Zimmer, L., "DMD algorithms for experimental data processing in combustion," *Center for Turbulence Research Proceeding of the 2012 Summer Program*, pp. 459–468, 2012.

[43] Emerson, B., O'Connor, J., Juniper, M., and Lieuwen, T., "Density ratio effects on reacting bluff-body flow field characteristics," *Journal of Fluid Mechanics*, vol. 706, pp. 219–250, 9 2012.

[44] Valera-Medina, A., Syred, N., and Griffiths, A., "Visualisation of isothermal large coherent structures in a swirl burner," *Combustion and Flame*, vol. 156, no. 9, pp. 1723–1734, 2009.

[45] Bendat, J. S. and Piersol, A. G., *Random data: analysis and measurement procedures*. John Wiley & Sons, 2010.

[46] Steinberg, A. M., Boxx, I., Stöhr, M., Meier, W., and Carter, C. D., "Effects of flow structure dynamics on thermoacoustic instabilities in swirl-stabilized combustion," *AIAA journal*, vol. 50, no. 4, pp. 952–967, 2012.

[47] Roux, S., Lartigue, G., Poinsot, T., Meier, U., and Bérat, C., "Studies of mean and unsteady flow in a swirled combustor using experiments, acoustic analysis, and large eddy simulations," *Combustion and Flame*, vol. 141, no. 1, pp. 40–54, 2005.

[48] Pope, S. B., *Turbulent flows*. Cambridge university press, 2000.

[49] Chicone, C., *Linear Systems and Stability of Nonlinear Systems*, vol. 34 of *Texts in Applied Mathematics*. Springer New York, 2006.

[50] Faraday, M., "On a peculiar class of acoustical figures; and on certain forms assumed by groups of particles upon vibrating elastic surfaces," *Philosophical Transactions of the Royal Society of London*, vol. 121, pp. 299–340, 1831.

[51] Melde, F., "Über die erregung stehender wellen eines fadenförmigen körpers," *Annalen der Physik*, vol. 187, no. 12, pp. 513–537, 1860.

[52] Rayleigh, L., "Xvii. on the maintenance of vibrations by forces of double frequency, and on the propagation of waves through a medium endowed with a periodic structure," *The London, Edinburgh, and Dublin Philosophical Magazine and Journal of Science*, vol. 24, no. 147, pp. 145–159, 1887.

[53] Mumford, W., "Some notes on the history of parametric transducers," *Proceedings of the IRE*, vol. 48, no. 5, pp. 848–853, 1960.

[54] Lieuwen, T. and Zinn, B. T., "The role of equivalence ratio oscillations in driving combustion instabilities in low NO_x gas turbines," in *Symposium (International) on Combustion*, vol. 27, pp. 1809–1816, Elsevier, 1998.

[55] Gelb, A. and Vander Velde, W. E., *Multiple-input describing functions and nonlinear system design*. New York: McGraw-Hill, 1968.

[56] Noiray, N., Durox, D., Schuller, T., and Candel, S., "A unified framework for nonlinear combustion instability analysis based on the flame describing function," *Journal of Fluid Mechanics*, vol. 615, pp. 139–167, 2008.

[57] Verhulst, F., "Perturbation analysis of parametric resonance," in *Mathematics of Complexity and Dynamical Systems* (Meyers, R. A., ed.), pp. 1251–1264, Springer New York, 2011.

[58] Magnus, W. and Winkler, S., *Hill's equation*. Courier Dover Publications, 2013.

[59] Chicone, C., "Stability theory of ordinary differential equations," in *Mathematics of Complexity and Dynamical Systems* (Meyers, R. A., ed.), pp. 1653–1671, Springer New York, 2011.

[60] Floquet, G., "Sur les équations différentielles linéaires à coefficients périodiques," *Ann. Ecole Normale Sup. Palaiseau*, vol. 12, pp. 47–82, 1883.

[61] Meiss, J., *Differential Dynamical Systems*. Society for Industrial and Applied Mathematics, 2007.

[62] Kelley, W. G. and Peterson, A. C., *The theory of differential equations: classical and qualitative*. Springer, 2010.

[63] Gantmacher, F., *The Theory of Matrices*. Chelsea Publishing Co., 1959.

[64] Schmid, P. J. and Henningson, D. S., *Stability and transition in shear flows*, vol. 142. Springer, 2001.

[65] Feigenbaum, M. J., "Quantitative universality for a class of nonlinear transformations," *Journal of statistical physics*, vol. 19, no. 1, pp. 25–52, 1978.

[66] Feigenbaum, M. J., "The universal metric properties of nonlinear transformations," *Journal of Statistical Physics*, vol. 21, no. 6, pp. 669–706, 1979.

[67] Gollub, J. and Benson, S., "Many routes to turbulent convection," *Journal of Fluid Mechanics*, vol. 100, no. 03, pp. 449–470, 1980.

[68] Feigenbaum, M. J., "Universal behavior in nonlinear systems," *Physica D: Nonlinear Phenomena*, vol. 7, no. 1, pp. 16–39, 1983.

[69] Swinney, H. L., "Observations of order and chaos in nonlinear systems," *Physica D: Nonlinear Phenomena*, vol. 7, no. 1, pp. 3–15, 1983.

[70] Holmes, C. A. and Rand, R. H., "Coupled oscillators as a model for nonlinear parametric excitation," *Mechanics Research Communications*, vol. 8, no. 5, pp. 263–268, 1981.

[71] Chu, B.-T. and Kovásznay, L. S., "Non-linear interactions in a viscous heat-conducting compressible gas," *Journal of Fluid Mechanics*, vol. 3, no. 05, pp. 494–514, 1958.

[72] Marble, F. and Candel, S., "Acoustic disturbance from gas non-uniformities convected through a nozzle," *Journal of Sound and Vibration*, vol. 55, pp. 225–243, Nov. 1977.

[73] Howe, M., "Indirect combustion noise," *Journal of Fluid Mechanics*, vol. 659, pp. 267–288, 2010.

[74] Poinsot, T. J., Trouve, A. C., Veynante, D. P., Candel, S. M., and Esposito, E. J., "Vortex-driven acoustically coupled combustion instabilities," *Journal of Fluid Mechanics*, vol. 177, pp. 265–292, 1987.

[75] Candel, S. M., "Combustion instabilities coupled by pressure waves and their active control," *Symposium (International) on Combustion*, vol. 24, pp. 1277–1296, 1992.

[76] Smith, R., Xia, G., Anderson, W., and Merkle, C., "Computational simulations of the effect of backstep height on nonpremixed combustion instability," *AIAA journal*, vol. 48, no. 9, pp. 1857–1868, 2010.

[77] Lighthill, M. J., *Introduction to Fourier analysis and generalised functions*. New York: Cambridge University Press, 1958.

[78] Berkooz, G., Holmes, P., and Lumley, J. L., "The proper orthogonal decomposition in the analysis of turbulent flows," *Annual Review of Fluid Mechanics*, vol. 25, no. 1, pp. 539–575, 1993.

[79] Woodward, R., Miller, K., Bazarov, V., Guerin, G., Pal, S., and Santoro, R., "Injector research for shuttle oms upgrade using lox/ethanol propellants," *AIAA Paper*, pp. 98–3816, 1998.

[80] Rubinsky, V., *Combustion instability in the RD-0110 engine*, vol. 169, ch. 4, pp. 89–89. Washington, DC, USA: AIAA, 1995.

[81] Feikema, D., Chen, R.-H., and Driscoll, J. F., "Enhancement of flame blowout limits by the use of swirl," *Combustion and Flame*, vol. 80, no. 2, pp. 183–195, 1990.

[82] Seitzman, J. M. and Hanson, R. K., "Comparison of excitation techniques for quantitative fluorescence imaging of reacting flows," *AIAA Journal*, vol. 31, pp. 513–519, Mar. 1993.

[83] Hall, J., de Vries, J., Amadio, A., and Petersen, E., "Towards a kinetics model of CH chemiluminescence," in *Aerospace Sciences Meetings*, American Institute of Aeronautics and Astronautics, Jan. 2005.

[84] Moeck, J., Bourgouin, J.-F., Durox, D., Schuller, T., and Candel, S., "Tomographic reconstruction of heat release rate perturbations induced by helical modes in turbulent swirl flames," *Experiments in Fluids*, vol. 54, no. 4, pp. 1–17, 2013.